

UNIVERSITAT POLITÈCNICA DE VALÈNCIA

Institute of Mechanical and Biomechanical Engineering



PhD THESIS

Development of hybrid optimization
techniques of mechanical components
employing the Cartesian Grid Finite
Element Method

Presented by: David Muñoz Pellicer

Supervised by: Ph.D. Juan José Ródenas García

Ph.D. Enrique Nadal Soriano

Valencia, November 2023

PhD THESIS

**Development of hybrid optimization
techniques of mechanical components
employing the Cartesian Grid Finite Element
Method**

for the degree of

Doctor in Industrial Engineering and Production

presented by

David Muñoz Pellicer

at the

Institute of Mechanical and Biomechanical Engineering
of Universitat Politècnica de València

Supervised by

Ph.D. Juan José Ródenas García

Ph.D. Enrique Nadal Soriano

Valencia, November 2023

PhD THESIS

**Development of hybrid optimization
techniques of mechanical components
employing the Cartesian Grid Finite Element
Method**

Presented by: David Muñoz Pellicer

Supervised by: Ph.D. Juan José Ródenas García

Ph.D. Enrique Nadal Soriano

QUALIFYING TRIBUNAL

PRESIDENT: Dr. _____

VOCAL: Dr. _____

SECRETARY: Dr. _____

Valencia, November 2023

Abstract

This thesis explores innovative approaches for structural optimization, encompassing a variety of commonly used optimization algorithms in this field. It specifically focuses on shape optimization (SO) and topology optimization (TO). The first contribution of this research revolves around ensuring and maintaining a desired level of accuracy throughout the TO process and the proposed solution. By establishing confidence in the suggested components of the TO algorithm, our attention can then shift to the subsequent contribution.

The second contribution of this thesis aims to establish effective communication between TO and SO algorithms. To achieve this, our goal is to directly convert the optimal material distribution proposed by the TO algorithm into geometry. Subsequently, we optimize the geometry using SO algorithms. Facilitating seamless communication between these two algorithms presents a non-trivial challenge, which we address by proposing a machine learning-based methodology. This approach seeks to extract a reduced number of geometric modes that can serve as a parameterization for the geometry, enabling further optimization by SO algorithms.

Lastly, the third contribution builds upon the previous idea, taking it a step forward. The proposed methodology aims to derive new components through knowledge-based approaches instead of relying solely on physics-based TO processes. We argue that this knowledge can be acquired from the historical designs employed by a given company as they retain invaluable immaterial know-how. This methodology also relies on machine learning algorithms, but we also consider techniques for analyzing high-dimensional data and more suitable interpolation strategies.

Resumen

Esta tesis explora enfoques innovadores para la optimización estructural, abarcando una variedad de algoritmos de optimización comúnmente utilizados en el campo. Se centra específicamente en la optimización de forma (SO) y la optimización de topología (TO). La primera contribución de esta tesis gira en torno a garantizar y mantener un nivel deseado de precisión durante todo el proceso de TO y la solución propuesta. Al establecer confianza en los componentes sugeridos por el algoritmo de TO, nuestra atención puede centrarse en la siguiente contribución.

La segunda contribución de esta tesis tiene como objetivo establecer una comunicación efectiva entre los algoritmos de TO y SO. Para lograr esto, nuestro objetivo es convertir directamente la distribución óptima de materiales propuesta por el algoritmo de TO en geometría. Posteriormente, optimizamos la geometría utilizando algoritmos de SO. Facilitar una comunicación fluida entre estos dos algoritmos presenta un desafío complejo, que abordamos proponiendo una metodología basada en aprendizaje automático. Este enfoque busca extraer un número reducido de modos geométricos que pueden servir como parametrización para la geometría, lo que permite su optimización mediante algoritmos de SO.

Por último, la tercera contribución recoge algunas de las ideas previas y las lleva un paso hacia delante. La metodología propuesta tiene como objetivo derivar nuevos componentes a través de enfoques basados en el conocimiento existente en lugar de depender únicamente de procesos de TO basados en la física. Sostenemos que este conocimiento se puede obtener del histórico de diseños empleados por una determinada empresa, ya que retienen un valioso conocimiento inmaterial. Esta metodología también se basa en algoritmos de aprendizaje automático, pero también consideramos técnicas para analizar datos de alta dimensionalidad y estrategias de interpolación más adecuadas.

Resum

Aquesta tesi explora enfocaments innovadors per a l'optimització estructural, abastant una varietat d'algorismes d'optimització comunament utilitzats en el camp. Se centra específicament en l'optimització de forma (SO) i l'optimització de topologia (TO). La primera contribució d'aquesta tesi gira entorn de garantir i mantenir un nivell desitjat de precisió durant tot el procés de TO i la solució proposada. En establir confiança en els components suggerits per l'algorisme de TO, la nostra atenció pot centrar-se en la següent contribució.

La segona contribució d'aquesta tesi té com a objectiu establir una comunicació efectiva entre els algorismes de TO i SO. Per a aconseguir això, el nostre objectiu és convertir directament la distribució òptima de materials proposada per l'algorisme de TO en geometria. Posteriorment, optimitzem la geometria utilitzant algorismes de SO. Facilitar una comunicació fluida entre aquests dos algorismes presenta un desafiament complex, que abordem proposant una metodologia basada en aprenentatge automàtic. Aquest enfocament busca extreure un nombre reduït de maneres geomètriques que poden servir com a parametrització per a la geometria, la qual cosa permet la seua optimització mitjançant algorismes de SO.

Finalment, la tercera contribució recull algunes de les idees prèvies i les porta un pas cap endavant. La metodologia recomanada té com a objectiu derivar nous components a través d'enfocaments basats en el coneixement existent en lloc de dependre únicament de processos de TO basats en la física. Sostenim que aquest coneixement es pot obtenir de l'històric de dissenys emprats per una determinada empresa, ja que retenen un valuós coneixement immaterial. Aquesta metodologia també es basa en algorismes d'aprenentatge automàtic, però també considerem tècniques per a analitzar dades d'alta dimensionalitat i estratègies d'interpolació més adequades.

Preface

The work presented in this thesis has been carried out at the Institute of Mechanical and Biomechanical Engineering (I2MB) at the Universitat Politècnica de València, under the supervision of Juan José Ródenas García and Enrique Nadal Soriano. This thesis consists of a summary report and the following appended papers:

- A D. Muñoz, J. Albelda, J.J. Ródenas and E. Nadal. *Improvement in 3D Topology Optimization with h-adaptive refinement using the Cartesian Grid Finite Element Method (cgFEM)*, International Journal for Numerical Methods in Engineering, **Volume 123** (2021).
- B D. Muñoz, E. Nadal, J. Albelda, F. Chinesta and J.J. Ródenas. *Allying topology and shape optimization through machine learning algorithms*. Finite Elements in Analysis and Design, **Volume 204** (2022).
- C D. Muñoz, F. Chinesta, E. Nadal, O. Allix and J. J. Ródenas. *Manifold learning for coherent design interpolation based on geometrical and topological descriptors*. Computer Methods in Applied Mechanics and Engineering, **Volume 405** (2023).

Acknowledgements

First of all, I would like to thank my supervisors Juan José Ródenas and Enrique Nadal for their advice and support during these years. They not only provided the technical guidance necessary to pull this Thesis off but a work environment based on patience, trust and comprehension. I would like to extend my gratitude to all my colleagues and staff of the Institute of Mechanical and Biomechanical Engineering. It was a pleasure to share this stage of my life with all of them.

I have to thank very particularly Francisco Chinesta for letting me be part of his research group in the Laboratoire Procédés et Ingénierie en Mécanique et Matériaux (PIMM) at École Nationale Supérieure d'Arts et Métiers. In addition, I will never forget the contributions made by Olivier Allix. Definitely his help has made my work more powerful.

I would also like to express my gratitude to the Spanish society for funding the public education system which provided me the opportunity of growing as a scientist in the framework of the FPU scholarship program.

Finally, I would like to express my very special thanks to my family and friends, for bringing me to this world, providing the best life I could ever imagined and supporting me unconditionally always.

To all of you, thank you so much.

Contents

Abstract	vii
Resumen	ix
Resum	xi
Preface	xiii
Acknowledgements	xv
I Thesis report	1
1 Introduction	3
1.1 Motivation	3
1.2 Objectives	5
1.3 Outline of the thesis	7
2 State of the art	9
2.1 Structural optimization	9
2.1.1 Topology optimization	9
2.1.2 Shape optimization	12
2.1.3 Hybrid optimization	13
2.2 Immersed boundary methods	15
2.2.1 Cartesian grid Finite Element Method (<i>cgFEM</i>)	15
2.2.1.1 Topology optimization in <i>cgFEM</i>	18
2.3 Advanced techniques for high-dimensional data analysis	19
2.3.1 Manifold learning	19

2.3.2	Topological data analysis	21
2.3.3	Optimal transport	24
3	Contributions	27
3.1	Advances in structural optimization: topology optimization and hybrid Techniques	27
3.1.1	Benchmark problem	28
3.1.2	Improvement strategies in topology optimization	32
3.1.2.1	Voxel-type independent integration mesh	32
3.1.2.2	Solution-based refinement strategies	34
3.1.3	Hybrid optimization	38
3.1.3.1	STEP 1: Topology optimization	40
3.1.3.2	STEP 2: The ML-based TO-SO interface	42
3.1.3.3	STEP 3: Shape optimization	45
3.2	Knowledge-driven design generation	48
3.2.1	Benchmark Problem	49
3.2.2	Methodology	50
3.2.2.1	Geometrical characterization	50
3.2.2.2	Topological characterization	51
3.2.2.3	Modifications in LLE to consider geometry and topology	52
3.2.2.4	Optimal transport-based interpolation to recover di- mensionality	55
3.2.2.5	Methodology to propose suitable designs	57
4	Closure	61
4.1	Summary	61
	Bibliography	63
II	Articles	71
	Paper A: Improvement in 3D Topology Optimization with h-adaptive refinement using the Cartesian Grid Finite Element Method	73
	Paper B: Allying topology and shape optimization through machine learning algorithms	125
	Paper C: Manifold learning for coherent design interpolation based on geometrical and topological descriptors	171

Part I

Thesis report

Chapter 1

Introduction

1.1. Motivation

Optimization techniques are ubiquitous across various industrial and scientific domains, as they facilitate the identification of the best alternative from a given set of individuals. In this context, individuals are evaluated based on their ability to perform a specific task, with their performance typically quantified using an objective or loss function, a commonly employed metric in optimization. Moreover, optimization problems typically entail a set of constraints that delineate the design space's feasibility, thereby reducing the number of individuals under consideration. Although optimization techniques find application in numerous fields, our research is specifically focused on structural optimization.

Structural optimization aims to identify the most suitable component from a given set based on their performance, which is evaluated through an objective function. The optimal component is the one that minimizes or maximizes the objective function while fulfilling a set of constraints. In the field of structural optimization, two of the most common pairs of objective function and constraints are the minimization of mass/volume while satisfying yield stress constraints, and the maximization of stiffness while fulfilling a volume fraction constraint. Various approaches exist for solving structural optimization problems, and we will primarily focus on techniques that alter the shape of the component, namely topology optimization and parametrized shape optimization (hereafter referred to as shape optimization).

Topology optimization algorithms are extensively employed for manipulating the material topology within the design space through the manipulation of various design variables [1–3]. For example, the Solid Isotropic Material Penalization (SIMP) method adjusts the relative density of individual elements, while the Level-Set approaches utilize auxiliary functions to define the evolving boundary of the shape [4–6]. During the optimization process, the finite element method (FEM) is commonly used to determine the current state of the design domain. However, FEM calculations can be **computationally expensive**, making computational efficiency a crucial factor in topology optimization due to its iterative nature. Moreover, the accuracy of FEM results strongly relies on the mesh quality, which in turn affects the performance of the optimization techniques. **Inaccurate FEM solutions** can lead to suboptimal designs that may fail to satisfy the imposed constraints [7].

Shape optimization techniques involve utilizing a computer-aided design (CAD) model to determine objective functions and constraints commonly employing FEM calculations. The CAD representation can employ various types of geometric entities, such as splines or NURBS. In this study, we will employ the STL format to represent the boundary as a triangular tessellation, which is commonly used in additive manufacturing processes. One of the primary advantages of shape optimization lies in the precision in terms of boundary definition. Additionally, the number of design variables required to parameterize the boundary is typically small, allowing for the effective exploration of the design space using a wide range of optimization algorithms. However, it is important to note that this parametrization requires **user intervention** and is limited to a fixed topology, thus **hindering the exploration of alternative topologies**.

The previous strategies rely on a physics-based methodology for designing structural components, which may not always align with industry practices. The design procedure in industry may be driven by various objectives that do not necessarily prioritize the structural behavior of the component. Consequently, the design process may not adhere to a predefined set of rules or steps. Instead, the expertise and intuition of different professionals, such as engineers and designers, play a crucial role in the design process. However, this reliance on individual expertise poses a potential risk. If a member of the design team leaves, it can result in a substantial **loss of knowledge**, which will require significant investments of both time and money to recover, if possible.

1.2. Objectives

This thesis aims to make a substantial contribution to the field of structural optimization by proposing innovative solutions that address current limitations. The primary objective is to advance the automation of structural design through the development of new methodologies based on optimization techniques. By doing so, we aim to overcome the existing limitations, which are highlighted in bold, and enable more efficient and effective structural design processes. To achieve this overarching goal, we have defined a set of specific objectives outlined below. Each of these objectives is designed to address one or more of the highlighted limitations:

- 1. Enhancing the computational efficiency of topology optimization algorithms.**

To enhance computational efficiency, it is preferable to use meshes consisting of elements with the same shape. Cartesian elements are commonly employed for rectangular or cuboidal domains due to their ease of meshing with regular shapes. However, practical applications often extend beyond such domains. Standard boundary-conforming finite element (FE) meshes struggle to ensure uniform element shapes. Immersed boundary methods (IBM), including the Finite Cell Method (FCM) [8–10], the CutFEM [11], and the Cartesian grid Finite Element Method (cgFEM) [12, 13], do not conform to the domain’s geometry. In this thesis, we adopt the cgFEM approach, developed by the supervisors of this thesis, due to its numerous advantages in terms of computational cost, especially when applied in iterative processes like optimization algorithms. The improved efficiency can be attributed to the hierarchical structure of the meshes and the uniformity of element shapes within them. Further details regarding these benefits are thoroughly addressed in *Paper A*.

- 2. Improving the solution quality of topology optimization algorithms**

To address inaccuracies in FE calculations, various mesh refinement techniques based on error estimation have been developed, such as h -adaptive mesh refinement [14–18]. These techniques refine the mesh in regions where the FE solution is less accurate, thereby enhancing the quality of the solution. Additionally, traditional topology optimization algorithms suffer from a significant drawback - they do not provide a clear geometric definition of the optimal material layout. To overcome these limitations, we have devised several strategies than the FE mesh including the incorporation of an integration mesh with higher resolution, or an additional mesh refinement strategy guided by the density distribution. Further details on these strategies can be found in *Paper A*.

- 3. Reducing user intervention in shape optimization algorithms and enabling topology exploration.**

To address this objective, a hybrid optimization methodology is desirable. Initially, topology optimization is employed to explore various topological alternatives and generate a preform. Subsequently, this preform is transformed into an optimal material distribution layout. An interface is then utilized to establish a connection between the topology and shape optimization algorithms. This interface generates a parametric geometrical model derived from the topology optimization process, which is later utilized by the shape optimization algorithm. The aim of the shape optimization algorithm is to identify the optimal combination of parameters that minimizes a given objective function while adhering to specified constraints. The outcome of this step is a CAD-like representation of the optimal geometry. The interface can be created using various techniques and approaches, as demonstrated in previous studies [19–30]. In this work, we propose employing manifold learning (ML) strategies [31, 32] to deduce the geometrical characterization of the interface using a set of parameters representing the principal geometric modes of the preform. ML algorithms are utilized to create the parametric model that characterizes the implicit boundary of the interface using a combination of geometric modes. The extracted geometric features may encompass simple entities such as radius or thickness, although they are generally more complex. Nonetheless, the ML tool identifies the geometric modes, providing a parametric geometrical representation. This parametric characterization is then employed to generate new geometries by manually adjusting the parameter values or by utilizing an external algorithm for guidance. In our case, these parameters are introduced as design variables utilized by a shape optimization algorithm. Further details regarding the proposed hybrid optimization algorithm can be found in *Paper B*.

4. Knowledge preserving tool for generative design.

Changes in the design team of an industrial company can lead to potential loss of knowledge. To avoid this invaluable and intangible asset from being lost, we propose a methodology for extracting this know-how. The main advantage of this strategy, apart from enabling us to store the knowledge, is that we can utilize it to generate new components that meet the same criteria as the existing designs of the company. To achieve this objective, we propose a comprehensive framework that allows for the incorporation of new components based on user-defined criteria. We introduce new tools to implement this idea. For example, topological data analysis (TDA) techniques [33, 34] can be employed to extract topological features that characterize a given component, such as the number and size of holes. Thus, a component can be characterized by its geometry and topology, providing sufficient information to describe the similarity between individuals in the database using an appropriate metric. This metric can then be used to obtain the corresponding projection onto a low-dimensional manifold, employing manifold learning techniques. By exploring the inherent structure of the database, one can navigate within this manifold and use the

current database as a basis for generating new components. However, standard interpolation techniques based on the Euclidean metric may introduce artifacts and yield non-physical components. Therefore, we propose using metrics from the field of optimal transport (OT) [35–38] to address topological changes when generating new components, thereby preserving the original dimensionality. The construction of the knowledge-based generative tool is detailed in *Paper C*.

1.3. Outline of the thesis

This document consists of two parts: the Thesis report and the Scientific Articles. After this brief introduction, the first part follows with Chapter 2 that provides an overview of the current state of the art. Chapter 3 summarizes the work conducted in this thesis, accompanied by illustrative numerical examples. Finally, Chapter 4 presents the conclusions of this research and proposes directions for future studies.

The second part comprises a compilation of three papers that extensively discuss the scientific contributions of this work. All papers have already been published in high-quality, peer-reviewed journals. The contributions are presented in this document without any journal editing, and each paper is preceded by a cover page containing a citation to the corresponding journal.

Paper A introduces a 3D topology optimization methodology within the framework of *cgFEM*. It explores various strategies to enhance the quality of the solution proposed by the topology optimization algorithm. *Paper B* proposes a hybrid optimization strategy that integrates topology and shape optimization algorithms by automatically parameterizing the shape's boundary. *Paper C* take a step forward and proposes the generation of new components through a fully knowledge-based approach, where the knowledge can be derived from the analysis of previous designs.

Chapter 2

State of the art

2.1. Structural optimization

Structural optimization techniques play a critical role in the design process of mechanical components, as they can determine an optimal structural design based on a given set of applied loads. This optimal design can be obtained by minimizing or maximizing an objective function while satisfying a set of constraints. In the field of structural optimization, the most common pairs of objective function and constraints are the minimization of mass/volume while satisfying a yielding stress constraint, and the maximization of stiffness while satisfying a volume fraction constraint. Various approaches exist to solve the structural optimization problem, but in this work, we will focus on two of the most commonly used techniques: topology optimization and parametrized shape optimization (hereafter referred to as shape optimization).

2.1.1. Topology optimization

TO is a structural optimization technique that seeks to determine the optimal distribution of material within a given physical design domain. The problem involves minimizing or maximizing an objective function subject to a set of constraints that depend on the applied loads. To solve the TO problem, the design domain is discretized using the FEM, resulting in a large set of design variables, where each point can be either a solid material or void. TO has gained popularity due to its capacity to extensively explore the design space with a reduced computation time.

Among the different approaches, we found those based on strictly 0-1 values of relative density [39–42]. On the other hand, some TO algorithms applied to structural problems make use of a fictitious material that exhibits composite behavior [43], which is defined by a characteristic function that specifies the elastic properties. One widely used approach to regularize the material properties is the SIMP method [1–3], which penalizes the density interpolation function. Other techniques have also been proposed in the literature, including the level-set methods that use nodal values of an implicit function that defines the boundary [44–48] and those based on phase-field methods [49].

As previously indicated, structural TO is a technique used to determine the optimal distribution of material in a design domain Ω . The SIMP method aims to minimize the compliance c subject to constraints regarding the volume fraction of material used in the design space. To solve the optimization problem, the SIMP method considers the relative density ρ as a continuous variable, rather than a binary (0-1) variable. The method uses a penalization parameter p to penalize intermediate density values of ρ and enforce material-void segregation as much as possible. Therefore, a typical TO problem using the SIMP method can be formulated as follows:

$$(\text{TO}(v_f)) = \left\{ \begin{array}{ll} \min_{\rho} : & c(\rho; \mathbf{u}) = \frac{1}{2} \int_{\Omega} \boldsymbol{\varepsilon}(\mathbf{u}) \mathbf{D}(\rho) \boldsymbol{\varepsilon}(\mathbf{u}) d\Omega, & (2.1a) \\ & \text{with } \mathbf{D}(\rho) = \rho^p \mathbf{D}_0, & (2.1b) \\ \text{subject to:} & V(\rho) = \int_{\Omega} \rho d\Omega = \bar{V}_e \sum \rho_e = v_f V_0, & (2.1c) \\ & a(\mathbf{u}, \mathbf{u}; \rho) = l(\mathbf{u}) \text{ where,} & (2.1d) \\ & a(\mathbf{u}, \boldsymbol{\nu}; \rho) = \int_{\Omega} \boldsymbol{\varepsilon}(\mathbf{u}) \mathbf{D}(\rho) \boldsymbol{\varepsilon}(\boldsymbol{\nu}) d\Omega, & (2.1e) \\ & l(\boldsymbol{\nu}) = \int_{\Omega} \mathbf{b}^T \boldsymbol{\nu} d\Omega + \int_{\Gamma_N} \mathbf{t}^T \boldsymbol{\nu} d\Gamma_N, & (2.1f) \\ & 0 \leq \rho_{min} \leq \rho \leq 1, & (2.1g) \end{array} \right.$$

where $\boldsymbol{\varepsilon}$ is the strain field and \mathbf{u} the displacement field. The matrix \mathbf{D} represents Hook's law, which relates strains $\boldsymbol{\varepsilon}$ and stresses $\boldsymbol{\sigma}$. It is important to note that, according to the SIMP method, the relation between \mathbf{D} and \mathbf{D}_0 is given by $\mathbf{D}(\rho) = \rho^p \mathbf{D}_0$. Here, \mathbf{D}_0 is the matrix of Hook's law for the fully dense material. When $p > 1$, intermediate densities in elements are penalized because they contribute with little stiffness relative to their volume fraction. For isotropic materials with non-negative Poisson's ratio, a penalization parameter of $p = 3$ provides intermediate materials

that lie between the H-S bound and have physical meaning [50]. The parameter v_f is a prescribed volume fraction, and V_0 is the total volume of the design domain. Finally the lower bound in ρ is set in order to prevent ill conditioning issues [51]. One important factor to consider when using the parameter p is its impact on the optimization algorithm's convergence. To address the problem of local minima, a continuation strategy is often employed. As such, the SIMP method suggests starting with $p = 1$ and gradually increasing it to $p = 3$ [52] as the optimization process converges.

To optimize the layout of material distribution, it is necessary to obtain the sensitivities of the compliance. As recommended in [51], a low-pass filter should be applied to the sensitivities to prevent numerical instabilities [53,54] like the checkerboard pattern. The filtering of sensitivities can be computed as follows:

$$\widehat{\frac{\partial c}{\partial \rho_e}} = \frac{1}{\rho_e \sum_{k=1}^N \widehat{H}_k} \sum_{k=1}^N \widehat{H}_k \rho_k \frac{\partial c}{\partial \rho_k}, \quad (2.2)$$

with the filter \widehat{H}_k defined as:

$$\begin{aligned} \widehat{H}_k &= r_{min} - dist(e, k), \\ &\{k \in N \mid dist(e, k) \leq r_{min}\}, \\ &e = 1, 2, \dots, N, \end{aligned} \quad (2.3)$$

where e is the element to be filtered and k are each of the neighbors of element e . We define neighbors, denoted by N , as the elements located within a distance of r_{min} , which is commonly referred to as the filter size. We chose this filtering technique due to its simplicity, as opposed to other approaches that require solving differential equations, such as those based on the Helmholtz equation [55].

The topology optimization algorithm uses the filtered sensitivities to obtain the new material distribution ρ . In [51], the optimality criteria (OC) algorithm is used. Other alternatives like the method of moving asymptotes (MMA) [56] and the sequential quadratic programming (SQP) [57] could also be used. The iterative procedure is repeated until a convergence criterion is accomplished.

The previous TO problem in (2.1a–2.1g) finds the material distribution given an amount of material. However, in some situations is interesting to find the quantity of material for not surpassing certain stress limit indicator. For achieving that, the problem (2.4a–2.4c) is presented. This consists in an optimization problem that tries to minimize v_f subjected to the final solution of (2.1a–2.1g) providing stresses below a certain limit.

$$\begin{aligned}
(\mathbb{T}\mathbb{O}(v_f(S_y))) = \begin{cases} \text{find:} & v_f, & (2.4a) \\ \text{subjected to:} & \max(\sigma_{eq}^*) \equiv S_{crit}, & (2.4b) \\ & \mathbb{T}\mathbb{O}(v_f), & (2.4c) \end{cases}
\end{aligned}$$

where S_{crit} is the limit value of σ_{eq}^* . In this work we considered S_{crit} as the yield limit S_y and σ_{eq}^* represents an equivalent uniaxial stress value. In this work, we used as σ_{eq}^* the recovered von Mises stress field σ_{vm}^* evaluated from σ^* , the so called recovered stress field, more accurate than the stress field σ^h provided by the FEM. There are different procedures to obtain σ^* . Because of their accuracy, the most commonly used techniques are the superconvergent patch recovery (SPR) technique (proposed by Zienkiewicz and Zhu [58]) and enhanced versions of this technique, like the SPR-C technique [59]. This method provides satisfactory results if no singular points appear in the domain.

In order to obtain σ^* from the raw FE results, we consider that the use of the density field ρ in topology optimization implies a particular definition of the stress field to keep consistency with the expression of the strain energy (compliance) in (2.1a). We can rewrite equation (2.1a) as:

$$\sigma_e^{h\rho} = \mathbf{D}(\rho_e)\varepsilon_e^h = \rho_e^p \mathbf{D}_0 \varepsilon_e^h = \rho_e^p \sigma_e^{h_0}, \quad (2.5)$$

where $\sigma_e^{h_0} = \mathbf{D}_0 \varepsilon_e^h$ would represent the original FE stress field at the element, before considering the density correction. The penalization parameter p in (2.5) is consistent with equation (2.1b) [60, 61]. Taking into account equation (2.5), we propose to smooth the original stress field at elements, σ^{h_0} , for the evaluation of the recovered stress field and then to modify the resulting recovered stress field using the density correction.

2.1.2. Shape optimization

SO techniques involve the use of CAD models to determine objective functions and constraints for optimizing geometries. These CAD representations are based on various geometrical entities such as splines, NURBS or other entities. One of the primary advantages of shape optimization techniques is the precision and smoothness of the boundary definition. This benefit is particularly significant because the number of design variables required to parameterize the boundary is usually low. As a result, a wide range of optimization algorithms can be used to explore the design space. In this work, we consider the shape optimization where the boundary is defined *a priori* employing a set of parameters, also known as design variables \mathbf{a} , as shown in Figure 2.1.

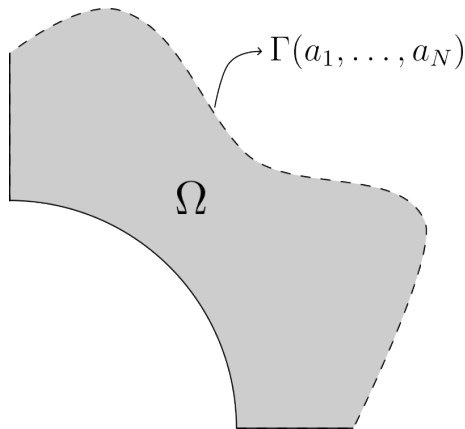


Figure 2.1: Parametrized boundary of the design domain.

In the context of structural optimization, the objective function typically involves optimizing for volume or mass, while the constraints involve ensuring that certain measures of stress remain within acceptable limits. For example, one common constraint is to keep the maximum von Mises stress ($\max(\sigma_{vm}^*)$) below the yield stress limit (S_y). This can be expressed mathematically as follows:

$$(\mathbb{SO}_\sigma(S_y)) = \begin{cases} \min_{\mathbf{a}} : & \text{Volume}(\mathbf{a}), & (2.6a) \\ \text{subjected to:} & \max(\sigma_{vm}^*(\mathbf{a})) \leq S_y. & (2.6b) \end{cases}$$

2.1.3. Hybrid optimization

After a thorough analysis of the characteristics of the two primary structural optimization techniques, it is clear that a hybrid optimization methodology would be beneficial, which consists in bridging both techniques by creating an interface that allows to jump from the TO results to the SO problem. This approach would leverage the advantages of topology and shape optimization techniques while addressing their respective weaknesses, which are more pronounced when these techniques are used independently.

Several approaches have been proposed in the literature. In this section, we will discuss some of the main contributions found in the literature. The approach described in [20, 21] involves parameterizing the optimal material distribution of a 2D design domain using curve fitting algorithms. The shape optimization algorithm then modifies the parameters defining those curves to find the optimal geometry. Artificial neural networks were also used in [22] to find the set of simple entities that reproduce the material distribution provided by the topology optimization algorithm. In [23], an

edge detection technique is used to identify the structural elements provided by the topology optimization algorithm. In [24], the Canny algorithm is used to detect edges, and a B-spline representation of the model is manually created. In [25], the mesh for the shape optimization algorithm is manually created using the material distribution layout indicated by the topology optimization algorithm. In [26], both optimization algorithms are simultaneously evaluated, and the shape is modified by considering the variation of the nodal coordinates of the mesh through weights, acting as design variables, and predefined perturbation vectors. In [27, 28], a two-stage algorithm is created where the general geometric definition is achieved in the topology optimization step. Then the result is represented with deformable simplicial complexes entities whose vertices' positions can be modified by the shape optimization algorithm. Additionally, [29] presented a new level-set algorithm that reduces the dimension of the functional by employing the radial basis functions. Finally, the work developed in [30] proposes using a shape optimization algorithm first to define the design domain and then using a topology optimization algorithm to find the optimal material distribution. Overall, several approaches have been proposed to tackle the challenge of combining topology and shape optimization. Each approach has its strengths and weaknesses. These approaches can be useful in different scenarios, and choosing the most suitable one depends on the specific problem being addressed. However, the automation of this step is not straightforward: they may need of human intervention, they constrain excessively the design space or they are not suitable for 3D design domains, for instance.

Precisely, when implementing a hybrid algorithm that combines topology and shape optimization, the most significant challenge is creating an interface to combine the two algorithms. As in most of the previous works, we employ an algorithm composed by of three main steps:

1. **TO.** In the first step, the algorithm will generate a preform of the optimal component, which exhibits topological characteristics defined by an optimal material distribution layout. The design domain described by the analyst will be taken into consideration.
2. **Interface.** The second step will involve communication between the topology and shape optimization algorithms. An interface will be designed to provide a parametric geometrical model, defined by a reduced number of design variables, obtained from the intermediate results of the topology optimization process, and required by the shape optimization algorithm.
3. **SO.** In the final step, the shape optimization algorithm will use the parametric geometric model to find the optimal combination of parameters that minimize/-maximize a given objective function while satisfying the prescribed constraints. The output of this step will be a CAD-like representation of the optimized geometry, in STL format which will be directly suitable for additive manufacturing.

By following this three-step process, the proposed hybrid optimization strategy will generate a geometrically optimized design, taking into account both topological

and shape optimization considerations.

2.2. Immersed boundary methods

IBM have gained popularity in the computational mechanics community due to their ability to achieve geometry-mesh independence, which significantly reduces the burden of meshing [8, 11, 12]). In many cases, the meshing process becomes trivial as a result. Furthermore, certain IBM implementations have been successfully adapted to problems where the object under analysis is described by an image, such as medical images. The FCM [8–10] and the *cgFEM* [12, 13] have both demonstrated their efficacy in dealing with such problems [62, 63].

The IBM approaches offer attractive advantages. Apart from simplifying the meshing process, they allow the simple definition of efficient data structures to reuse calculations. However, it also presents some challenges that must be considered. In particular, the computational cost with these techniques shifts from the expensive meshing algorithm towards the need for:

- a) More complex numerical integration schemes for the elements cut by the boundary, so that only the part of the element lying within the physical domain is considered in the evaluation of volume integrals; and
- b) The use of special formulations to impose boundary conditions [64–69]. In the standard FEM procedures to impose boundary conditions is assumed that the domain’s boundary is represented by element sides described by nodes placed on the boundary. These procedures are not suitable for IBM because, in general, the boundaries will cut the elements, and there will be no nodes on the boundaries.

2.2.1. Cartesian grid Finite Element Method (*cgFEM*)

There are various IBM approaches, and among them, we select the *cgFEM* method, developed by the supervisors of this thesis. The *cgFEM* method involves embedding the physical domain Ω_{Phys} within a cuboid that defines the fictitious domain Ω_{Fic} . The fictitious domain is meshed with elements of varying levels, with the *Level-0* mesh considered as a single element that encompasses the entire cuboid. We then split this mesh into eight new Cartesian elements to create the *Level-1* mesh, and recursively repeat the process to generate meshes with higher refinement levels, resulting in a

hierarchical structure. The final mesh for the FE analysis comprises elements of different refinement levels. To ensure C^0 continuity between contiguous elements from different levels, multi-point constraints are utilized [70].

In Figure 2.2a, we present an example of a physical domain, denoted as Ω_{Phys} , with boundary Γ that is smooth enough for our purposes. This physical domain is embedded within a larger domain, referred to as Ω_{Fic} . The boundary Γ of Ω_{Phys} can be divided into two non-overlapping parts: Γ_D and Γ_N . These regions respectively impose the Dirichlet and Neumann conditions. Figure 2.2b depicts the embedding domain Ω_{Fic} , which we discretize using Cartesian elements, Ω_e . Finally, we note that the following expression relates these domains:

$$\Omega_{Phys} \subseteq \Omega_{Fic} = \bigcup_{e=1}^{n_e} \Omega_e. \quad (2.7)$$

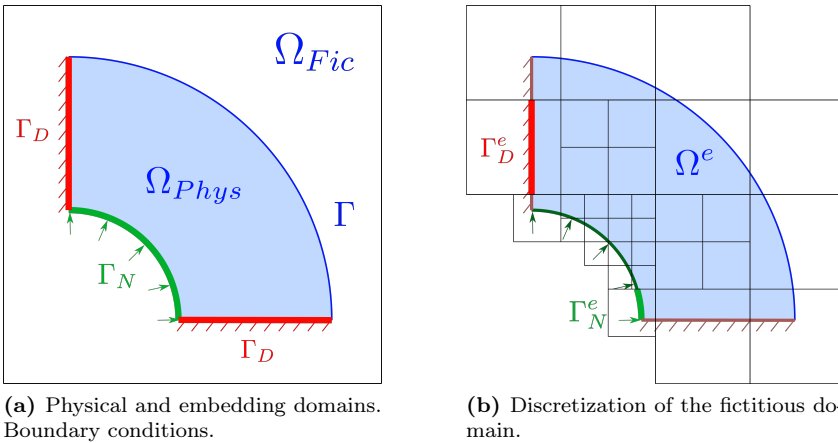
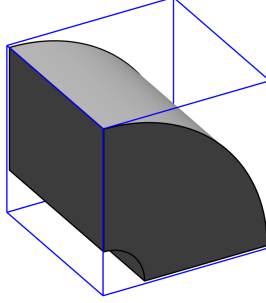


Figure 2.2: Representation of the physical domain and the discretization of the fictitious domain in *cgFEM*.

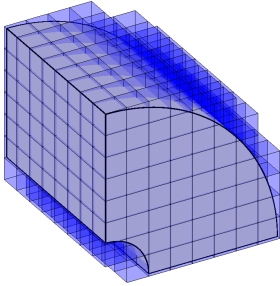
The efficiency and main characteristics of the *cgFEM* methodology are summarized in Figure 2.3, which illustrates a 3D example analyzed using this technique.

- *cgFEM* is an efficient FE analysis technique that employs a Cartesian discretization of the embedding domain, as depicted in Figure 2.3a.
- The analysis mesh utilized by *cgFEM* to model the physical domain Ω_{Phys} can include elements of different refinement levels. These elements can be entirely situated within Ω_{Phys} , cut by its boundary Γ , or be placed outside of it. The latter are excluded from the analysis mesh, as shown in Figure 2.3b.

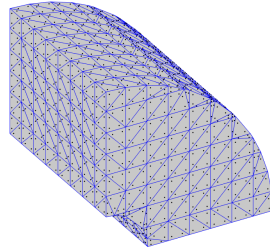
- *cgFEM* relies on a specially designed integration mesh (Figure 2.3c), based on the NEFEM integration approach [71]. This approach enables the exact boundary representation, such as in the form of NURBS or T-Splines [72], to be taken into account in the integration process.



(a) Physical domain Ω_{Phys} ($\frac{1}{4}$ of a hollow cylinder) embedded in the fictitious domain Ω_{Fic} (cube).



(b) Discretization of the fictitious domain: analysis mesh.



(c) Integration Mesh.

Figure 2.3: *cgFEM*. Different domains involved in a finite element analysis.

To impose the boundary conditions regarding the *cgFEM* framework some considerations should be done. In the case of Neumann boundary conditions, it is only necessary to consider that the surface of integration is in the interior of the element, as it will not generally coincide with any element face. In contrast, the case of Dirichlet boundary conditions requires more complex techniques. A common approach to impose the essential boundary conditions in a weak form consists on using the Lagrange multipliers technique [73]. However, the choice of an appropriate Lagrange multiplier space is not trivial, as a wrong choice could produce oscillations in the Lagrange multipliers field and thus in the FEM solution. Hence, stabilization techniques are

needed, and an adaptation of Nitsche’s method is one of the most popular ways of stabilization [74]. This approach results in the replacement of equation (2.1d) with the following equation:

$$a(\mathbf{u}, \mathbf{u}) + \frac{k}{h} \int_{\Gamma_D} \mathbf{u} \cdot \mathbf{u} d\Gamma = l(\mathbf{u}) + \frac{k}{h} \int_{\Gamma_D} \mathbf{g} \cdot \mathbf{u} d\Gamma + \int_{\Gamma_D} \mathbf{T}(\bar{\mathbf{u}}) \cdot \mathbf{u} d\Gamma. \quad (2.8)$$

A detailed description of the equation’s derivation and its behavior is available in [65]. The proposed stabilized Lagrange multipliers formulation is notable for its stabilization term \mathbf{T} , which is evaluated as a recovered [58, 59] traction field. Since this traction field depends on the FE solution, an iterative process using Richardson iterations is used to solve (2.8). However, this is merely a technical detail since the stabilization terms given ρ does not play any role in the TO procedure.

2.2.1.1. Topology optimization in *cgFEM*

We propose utilizing the *cgFEM* framework for TO, which requires adapting the algorithm accordingly. The original version of the SIMP method, as presented in [51], assumed that all mesh elements were of the same shape and size. To implement the SIMP method within the *cgFEM* framework, we need to consider two essential features: (a) elements of different sizes, i.e., from different levels, are used to construct the analysis mesh; and (b) only the portion of the element within the physical domain should be considered for elements intersecting the boundary. Therefore, the volume of the physical domain after discretization should be determined as the sum of the volumes of each element e within the physical domain:

$$V(\rho) = \sum_e \rho_e \cdot V_e \quad \text{where} \quad V_e = \int_{\Omega_e \cap \Omega_{Phys}} d\Omega. \quad (2.9)$$

To ensure compliance with the volume constraint during the material distribution ρ update, it is necessary to evaluate the volume sensitivities. The computation of volume sensitivities follows the expression:

$$\frac{\partial V(\rho)}{\partial \rho_e} = V_e \quad (2.10)$$

Furthermore, in order to incorporate the volume of each element V_e into the computation of the filtered sensitivities (2.2), the corresponding expression must be revised as shown below:

$$\widetilde{\frac{\partial c}{\partial \rho_e}} = \frac{1}{\rho_e \sum_{f=1}^N \hat{H}_f V_f} \sum_{f=1}^N \hat{H}_f \rho_f V_f \frac{\partial c}{\partial \rho_f}. \quad (2.11)$$

Hence, it is necessary to modify the topology optimization formulation. Firstly, equation (2.1c) should be replaced by equation (2.9) to account for the fact that each element has a different volume V_e , either due to the mesh being h -adapted or because the element is intersected by the domain's boundary. Secondly, to impose boundary conditions in elements cut by the Dirichlet boundary, a stabilized Lagrange multipliers formulation is employed. Consequently, equation (2.1d) is substituted by equation (2.8).

2.3. Advanced techniques for high-dimensional data analysis

In recent years, data analysis has become an increasingly important area of research, with applications ranging from natural language processing to genomics and neuroscience. While traditional statistical methods remain valuable, the growing complexity and scale of data sets have led to a need for new approaches that can capture their underlying structure and patterns. This section explores three related areas of research that offer promising avenues for analyzing complex data sets: manifold learning, topological data analysis, and optimal transport. ML aims to discover the intrinsic low-dimensional structure of high-dimensional data, allowing for effective visualization and analysis. TDA, on the other hand, seeks to extract topological features from data, such as holes and voids, to reveal its underlying structure. Finally, OT provides a powerful framework for comparing and transforming probability distributions, enabling efficient data alignment and analysis. While these three areas of research are distinct, they share a common goal: to provide geometric and topological insights into complex data sets. By combining these approaches, we can gain a deeper understanding of the underlying structure of data and develop more effective techniques for analysis and modeling. In the following sections, we will explore each of these areas in more detail, highlighting their unique features and potential applications.

2.3.1. Manifold learning

ML algorithms are commonly used to extract the underlying structure of high-dimensional data by identifying a set of low-dimensional parameters. In the ML field, there are a plethora of techniques available, with the principal component analysis (PCA) [31] being one of the earliest linear techniques, widely used in the past. However, with the development of ML, non-linear techniques have been introduced that can preserve the non-linear nature of the original dataset, such as locally linear embedding (LLE) [32]. These techniques are particularly important when dealing with

information from the component's topology, which is considered highly non-linear [75].

In this study, we have used the LLE algorithm to extract the low-dimensional parameters of the dataset. Here, each high-dimensional point or snapshot, denoted as \mathbf{X}_i , can be obtained as a linear combination of its K nearest neighbors, with weights represented by $W_{ij}, j \in [1, K]$. The number of neighbors K is a user-defined parameter, and the weights are obtained by minimizing the functional represented in Equation (2.12):

$$e(\mathbf{W}) = \sum_i \|\mathbf{X}_i - \sum_j W_{ij} \mathbf{X}_j\|^2. \quad (2.12)$$

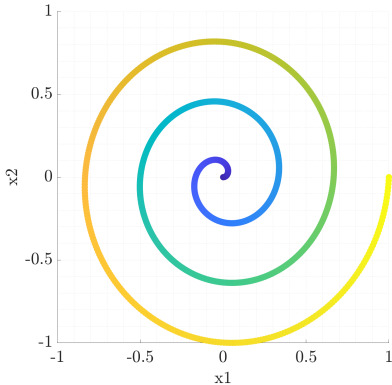
The weights W_{ij} are subjected to the constraint $\sum_j W_{ij} = 1$. The LLE algorithm hypothesizes that these weights are invariant to space transformations, and their values are preserved when changing between spaces. The low-dimensional parameters can be obtained by minimizing the functional in (2.13):

$$\varphi(\mathbf{Y}) = \sum_i \|\mathbf{Y}_i - \sum_j W_{ij} \mathbf{Y}_j\|^2, \quad (2.13)$$

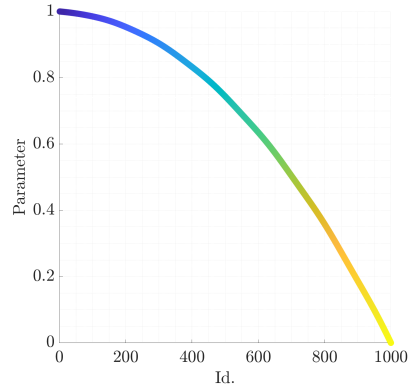
where \mathbf{Y}_i represents each of the points projected to the embedded space. This equation can be represented in the form shown in (2.14):

$$\varphi(\mathbf{Y}) = \mathbf{Y}^T \mathbf{M} \mathbf{Y}, \quad (2.14)$$

where $\mathbf{M} = (\mathbf{I} - \mathbf{W})^T (\mathbf{I} - \mathbf{W})$. The minimization problem can be considered an eigenvalue problem, where the eigenvectors represent the low-dimensional points \mathbf{Y} .



(a) Original sampled dataset.



(b) Reduced coordinates proposed by the LLE algorithm.

Figure 2.4: LLE example of an analytic database. Just one dimension is enough to characterize the database, as illustrated with the preservation of the color distribution.

The dimension of the embedded space can be a user-defined parameter, but it is convenient to study the eigenvalues of \mathbf{M} . As we minimize (2.14), the target eigenvectors are related to the smallest eigenvalues. The detailed mathematical procedure to obtain the low-dimensional embedded space is explained in [32].

To illustrate the LLE technique, we apply it to an analytical example and present the results in Figure 2.4. Figure 2.4a shows the original sampled dataset, which is reduced to the space illustrated in Figure 2.4b, showing that one of its dimensions was not relevant.

2.3.2. Topological data analysis

The characterization of the component's topology relies on TDA [33,34]. TDA is a set of tools used in high-dimensional data analysis to extract topological information from a group of points, including persistent homology [76]. These techniques are directly applicable to our work as any signed distance function (SDF) can be converted into a cloud of points using the coordinates of the nodes in the Cartesian grid and their respective function values. TDA tools are particularly useful because they employ methodologies developed for algebraic topology, allowing them to be used over data represented as a set of points. In Figure 2.5a, we demonstrate an example of a component's geometry, and in Figure 2.5b, we illustrate how this information is transformed into a set of points using TDA.

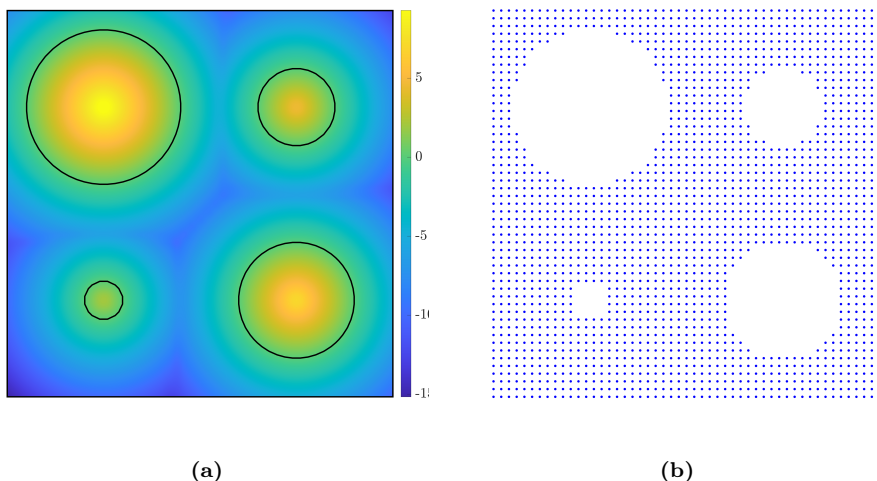


Figure 2.5: Example of the particularized SDF that represents a geometry (a) and the points used for the TDA tools (b).

To provide an intuitive understanding of the method, we refer to Figure 2.6 and consider a set of points denoted by A, B, C, D . In general, these points exist in a high-dimensional space where the intrinsic topology is not visible. To address this, we introduce a distance parameter r at each point to define the connectivity. By varying the value of r , we alter the connectivity of the point set, resulting in the emergence of different k -simplexes. It is worth noting that a 0-simplex corresponds to a point, a 1-simplex to an edge, a 2-simplex to a triangle, a 3-simplex to a tetrahedron, and so on.

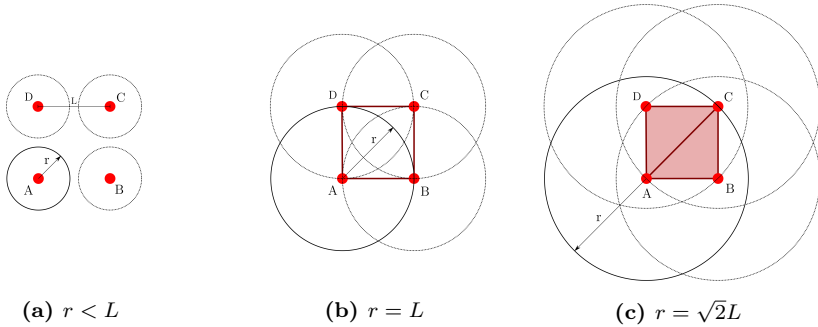


Figure 2.6: Intuitive description of the methodology in TDA tools, (a) with $r < L$ the set of points A, B, C, D remains disconnected, (b) with $r = L$ the edges AB, BC, CD, DA appear and also a hole, (c) with $r = \sqrt{2}L$ the triangles ABC and ACD appear, therefore the hole is covered.

Figures 2.6a, 2.6b, and 2.6c show the strategy for extracting topological features from an unconnected set of points. As the value of r increases, the connectivity of the points changes, allowing the creation of higher-order simplices, such as 1-simplices or edges. These edges form a hole in $r = L$ that persists until $r = \sqrt{2}L$, at which point even higher-dimensional simplices, such as 2-simplices or triangles, are created, covering the hole and causing it to disappear. Persistent features that are detected over a wide range of spatial scales r are more likely to represent true topological features of the underlying point cloud, rather than sampling artifacts or noise. The value of r at which a persistent feature appears and disappears is used to construct the persistence diagram (PD) shown in Figure 2.7a, which represents the birth x and death y of each topological feature found along the growth of r . Since the birth of any persistent feature, such as a hole, precedes its death, all the points in the persistence diagram lie above the diagonal $y = x$. Points near the diagonal may represent noise or small-scale features, whereas points far from the diagonal represent topological features that persist and define the overall topology of the component. The persistence diagram belongs to a non-metric space, so it is not directly suitable for comparing or evaluating distances between different persistence diagrams, to do so the space must be equipped with a metric. Other representations of persistent

homology that contain the same information but are displayed differently are also available. For instance, applying the mapping $f : (x, y) \rightarrow (x, y - x)$ to the PD yields the lifetime diagram (LD) shown in Figure 2.7b. In the LD, points far from the x -axis represent more relevant topological features. The same information may also be displayed in a barcode format, as shown in Figure 2.7c.

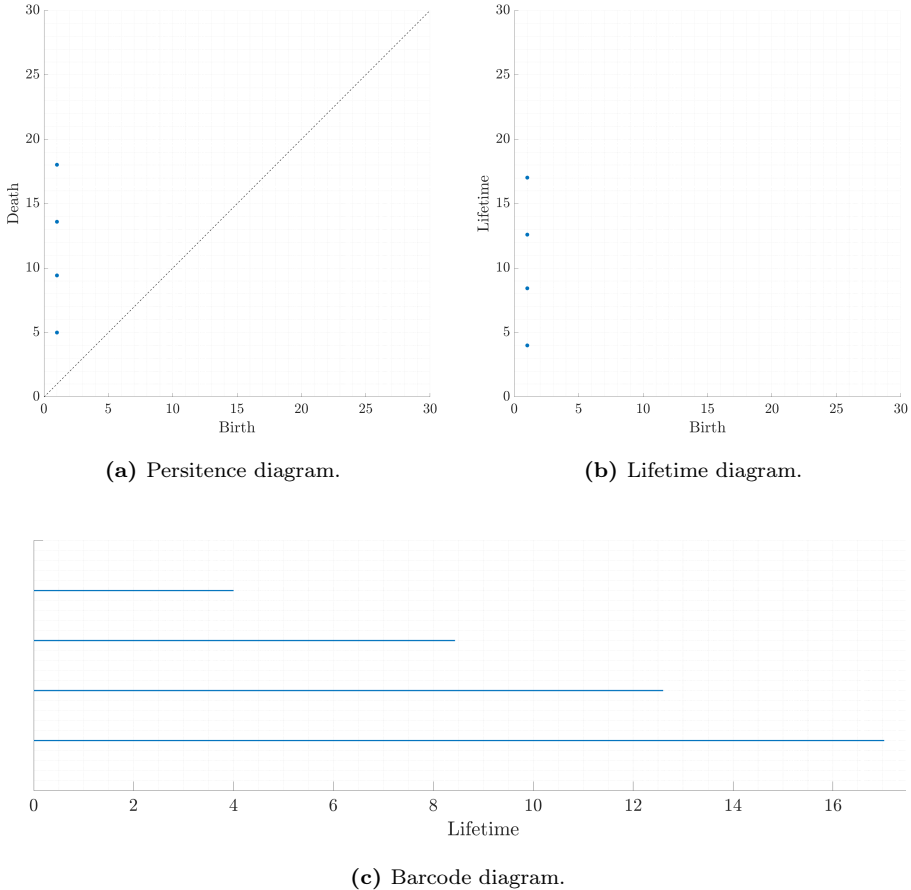


Figure 2.7: Different representations of the persistent homology for the example in Figure 2.5.

One limitation of using certain spaces, like the previous representations of the topology, is that they have non-Euclidean norms, such as the commonly used L_2 norm in many machine learning applications. Hence, it's necessary to transform the current descriptor of topological features using a space transformation. To do this,

a persistence surface is defined based on a Gaussian kernel evaluated in the space of the LD. The resulting surface is then converted into a finite-dimensional discretized space by fixing a grid with $n \times n$ subdomains (pixels) in the plane. Integrating the persistence surface over each pixel results in the so-called persistence image (PI) $\in R^2$, as shown in Figure 2.8b [77]. By framing the persistence features in this space, we can leverage a wide range of machine learning algorithms. However, it's worth noting that there are limitations to the PI approach, such as sensitivity to the choice of kernel and the number of pixels $n \times n$ in the grid. These limitations should be taken into consideration when applying this technique.

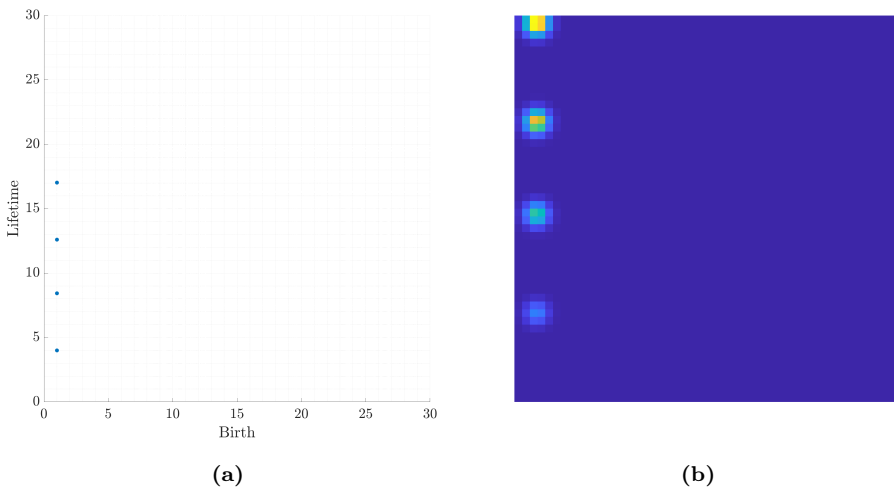


Figure 2.8: Space transformation of the persistent homology from the lifetime diagram (a) to the persistence image (b).

2.3.3. Optimal transport

Probability distributions are widely used in many scientific fields as they often encapsulate uncertain information related to geometric domains. Comparing two or more probability distributions requires an appropriate notion of similarity or discrepancy. OT techniques [35–37] provide a way to evaluate the similarity between distributions. The main problem in OT is computing the Wasserstein (also known as Earth Mover's) distance between probability distributions. These distance represent the geometric likeness between two objects by measuring the minimal amount of "work" needed to move the mass contained in one object onto the other. Recent developments show that incorporating these distances yields powerful tools for manipulating distributions, which can be useful for tasks such as geometric domain

interpolation [38].

To understand OT, we need some background information. We consider a manifold M representing the domain where the geometric domains are located. Then, we define $d : M \times M \rightarrow \mathbb{R}_+$ to specify the geodesic distance function, so $d(\mathbf{X}_i, \mathbf{X}_j)$ is the shortest distance from \mathbf{X}_i to \mathbf{X}_j along M . We use $\text{Prob}(M)$ to indicate the space of probability measures on M and $\text{Prob}(M \times M)$ to refer to probability measures on the product space of M with itself. We refer to elements $\mu_i, \mu_j, \dots \in \text{Prob}(M)$ as *marginals* and the joint probabilities $\pi_{ii}, \pi_{ij}, \pi_{jj}, \dots \in \text{Prob}(M \times M)$ as *couplings*. We consider that μ_i represents the probabilistic distribution of the general function \mathbf{X}_i , which may contain geometric information, such as the distance level-set.

Formally, the 2-Wasserstein distance between μ_i and μ_j is defined as

$$W_2(\mu_i, \mu_j) := \sqrt{\inf_{\pi} \int \int_{M \times M} d(x, y)^2 d\pi(x, y)}, \quad (2.15)$$

where π represents the transportation plan, which is a coupling in $\text{Prob}(M \times M)$ that describes the amount of mass to be displaced.

On the other hand, the Wasserstein barycenter problem aims to find the probabilistic distribution $\hat{\mu}$ that minimizes the weighted functional described in (2.16). This problem has applications in shape interpolation, where the resulting μ corresponds to the probabilistic functions that describe a geometric domain. In Figure 2.9, we compare the resulting distributions obtained through linear interpolation and the barycenter interpolation.

$$\hat{\mu} = \arg \min_{\mu} \sum_{i=1}^k \alpha_i W_2^2(\mu, \mu_i). \quad (2.16)$$

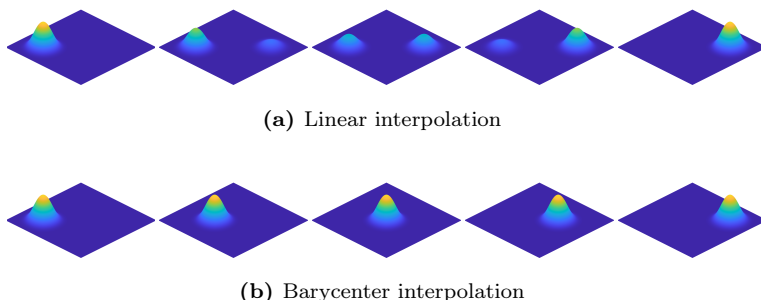


Figure 2.9: Comparison of linear and barycenter interpolation. Left and right figures are the reference distributions while the middle ones show its weighted interpolation.

Chapter 3

Contributions

The purpose of this chapter is to provide an overview of the contributions made, while the extended explanation can be found in the scientific papers attached. The contributions relate to two fields: structural optimization and generative design, that are closely related to each other. Structural optimization involves the process of minimizing or maximizing a specific quantity while adhering to a set of constraints and algorithmic rules. Generative design, on the other hand, focuses on leveraging the stored knowledge in a component database to replicate designs for other components with varying parameters.

This chapter highlights the contributions made in the thesis and presents a summary of the novelties introduced in each publication. The contributions are categorized into two sections based on the aforementioned fields of knowledge. Each section includes a reference problem to showcase the various contributions.

3.1. Advances in structural optimization: topology optimization and hybrid Techniques

In this chapter, we present our work on improving TO and a hybrid optimization methodology for structural design. We first describe our advances in topology optimization, where we developed novel algorithms that overcome some of its limitations

and allow for the design of more practical and manufacturable structures. We then discuss our contributions to hybrid optimization, where we combined topology optimization with shape optimization techniques to achieve even greater improvements in structural performance and efficiency.

3.1.1. Benchmark problem

We first define a benchmark problem to evaluate the behavior of the proposed methodologies. The problem, illustrated in Figure 3.1, consists of a beam with a constant hollowed cross-sectional area, featuring two perpendicular planes of symmetry at $x = 0$ and $z = 0$. The beam is subjected to a pressure P on its internal cylindrical surface under a plane strain condition, simulated by symmetry boundary conditions at $y = -10$ and $y = 10$.

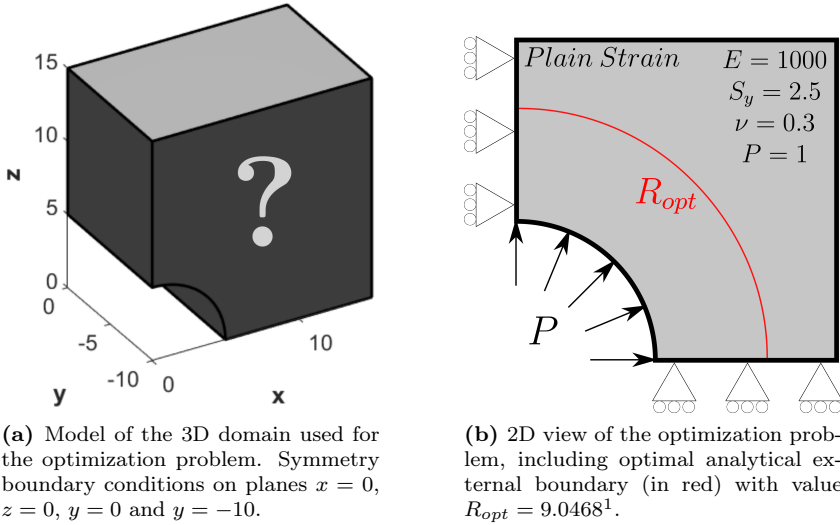


Figure 3.1: Reference problem.

The aim of the optimization problem is to minimize the material usage while ensuring that $\sigma_{vm} \leq S_y$. It is known that the optimal shape will take the form of a thick-walled cylinder. The analytical solutions for displacements (3.1) and stresses (3.2) of thick-walled cylinders subjected to internal pressure are available in [78]. These equations provide a useful basis for optimizing the design of such cylinders.

¹Value truncated to 4 decimal places.

$$\mathbf{u} = \begin{Bmatrix} u_R \cos(\theta) \\ 0 \\ u_R \sin(\theta) \end{Bmatrix} \quad u_R = \frac{P(1+\nu)}{E(\kappa^2-1)} \left[(1-2\nu)r + \frac{r_{ext}^2}{r} \right], \quad (3.1)$$

$$\boldsymbol{\sigma} = \begin{Bmatrix} \sigma_R \cos(\theta)^2 + \sigma_H \sin(\theta)^2 \\ \nu(\sigma_x + \sigma_z) \\ \sigma_R \sin(\theta)^2 + \sigma_H \cos(\theta)^2 \\ 0 \\ 0 \\ (\sigma_R - \sigma_H) \sin(\theta) \cos(\theta) \end{Bmatrix} \quad \begin{aligned} \sigma_R &= \frac{P}{\kappa^2-1} \left[1 - \left(\frac{r_{ext}}{r} \right)^2 \right], \\ \sigma_H &= \frac{P}{\kappa^2-1} \left[1 + \left(\frac{r_{ext}}{r} \right)^2 \right], \end{aligned} \quad (3.2)$$

where $r = \sqrt{x^2 + z^2}$ is the radius of the point, r_{ext} and r_{int} are the external and internal radii, $\kappa = r_{ext}/r_{int}$, $\theta = \arctan(z, x)$, P is the internal pressure, E is the Young Modulus and ν is the Poisson's ratio.

The maximum von Mises stress in the cylinder can be determined by evaluating the exact solution for stresses as a function of the external radius. By finding the value of the minimum external radius that satisfies $\sigma_{vm} \leq S_y$, we can identify the optimal external radius. Using the data presented in Figure 3.1, the optimal radius is determined to be $R_{opt} = 9.0468$ (as shown in Figure 3.1b), which results in an optimal volume of $V_{opt} = 446.4545$. This corresponds to a volume fraction $V/V_0 = 0.2174$, taking into account the dimensions of the design space illustrated in Figure 3.1. Topology optimization can also be used to solve the reference problem. We solve the problem (2.4a-2.4c) with uniform element size of $h_{ref} = 0.9563$, a filtering radius of $r_0 = 1.5 \times h_{ref} = 1.4345$, and a penalization parameter of $p = 3$. Figure 3.2 shows the evolution of the optimization algorithm, and Figure 3.3 shows 3D and 2D views of the resulting solution.

Figure 3.3 demonstrates that the TO process generates a solution that resembles a cylinder, which closely matches the optimal analytical solution. Figure 3.3.b) displays the optimal analytical radius R_{opt} alongside the iso-contours of relative densities $\rho = 0.01$, $\rho = 0.5$ and $\rho = 0.99$. To produce these iso-contours, we applied nodal averaging [79] to the original discontinuous topology optimization solution, which had a constant ρ value for each element. These iso-contours reveal a problem with the solution: it fails to provide a clearly defined representation of the edges, instead offering a diffuse representation characterized by intermediate ρ values over a region approximately twice the filtering radius thick ($2 \times r_0$).

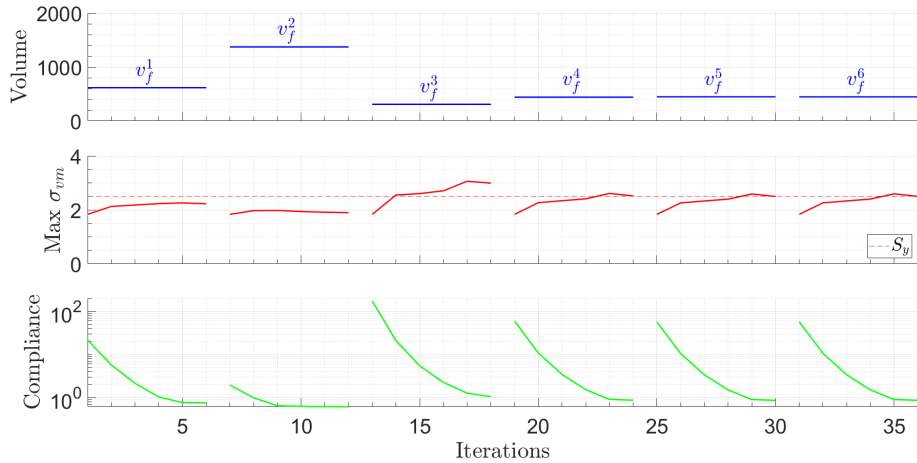


Figure 3.2: Reference Problem: Convergence curves of volume (Top), maximum von Mises stress (Middle) and compliance (Bottom). These curves represent the evolution of problem (2.4a–2.4c), where for a given value of v_f we solve the problem in (2.1a–2.1g) then this value is updated looking for the satisfaction of the stress constraint. Each time the v_f is updated, the problem (2.1a–2.1g) is initialized with a uniform distribution of densities.

To manufacture a component from the solution presented in Figure 3.3, a reasonable choice would be a hollowed cylinder. The external radius of the cylinder can be defined as a function of a threshold value of relative density ρ , which would be selected by the user. Let \bar{R}_ρ denote the mean value of the external radius, evaluated from the iso-contour of the relative density ρ chosen by the user. As the object to be manufactured is a thick-walled cylinder subjected to internal pressure, we can use the exact solutions given in Equations (3.1) and (3.2) to determine the maximum von Mises stress, denoted by $\hat{\sigma}_{vm}(\rho)$, that would occur in the object. Table 3.1 displays the values of \bar{R}_ρ and $\hat{\sigma}_{vm}(\rho)$ for three different values of ρ , along with the relative errors of these magnitudes, denoted by $e(R)$ and $e(\hat{\sigma}_{vm})$, respectively, with respect to the optimal analytical solution of this problem.

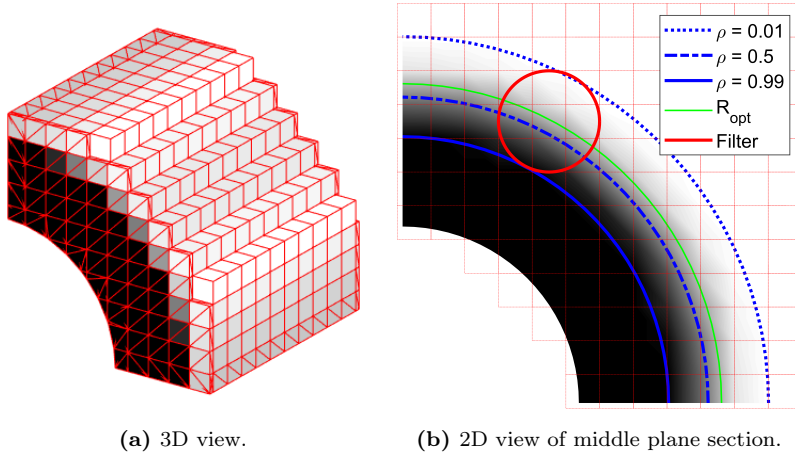


Figure 3.3: Reference solution of the reference optimization problem. Elements with relative density $\rho \leq 0.01$ have not been represented in (a). The 2D view in (b) includes the optimal analytical radius R_{opt} and the iso-contours $\rho = 0.01$, $\rho = 0.5$ and $\rho = 0.99$ and an example of the area covered by the filter radius.

Threshold	\bar{R}_ρ	$e(R)$	$\hat{\sigma}_{vm}(\rho)$	$e(\hat{\sigma}_{vm})$
$\rho = 0.01$	10.3804	14.7408%	2.2586	-9.6579%
$\rho = 0.5$	8.6663	-4.2057%	2.6039	4.1570%
$\rho = 0.99$	7.5457	-16.5922%	3.1037	24.1470%

Table 3.1: Reference Problem. Comparison between the solution obtained and the analytical solution, including the relative error.

where $e(R) = 100 \cdot \frac{\bar{R}_\rho - R_{opt}}{R_{opt}}$ and $e(\sigma_{vm}) = 100 \cdot \frac{\hat{\sigma}_{vm}(\rho) - S_y}{S_y}$.

Table 3.1 highlights a second issue with the proposed solution: the imprecise representation of the boundary may result in the choice of an external radius that deviates significantly from the optimal value R_{opt} . Specifically, opting for a smaller external radius than R_{opt} would give rise to a component that violates the stress constraint $\sigma_{vm} \leq S_y$, thereby leading to failure.

3.1.2. Improvement strategies in topology optimization

In this section, we present a series of methodologies that utilize the *cgFEM* technique to enhance the quality of the solution provided by the topology optimization algorithm based on the SIMP approach.

3.1.2.1. Voxel-type independent integration mesh

One of the practical applications of *cgFEM* is in the automated generation of FE meshes from medical images, where the data is stored in a Cartesian format [80]. This approach is particularly useful for creating FE models of bone tissues. The fundamental concept involves placing a Cartesian grid (either uniform or *h*-adapted) over the medical image. The voxels within each element are linked to the element and treated as integration subdomains, with associated integration points for each voxel. By establishing relationships between the material properties and the values used to represent the medical image, such as Hounsfield values for bone structures, it is possible to identify correlations between Young's modulus and these values [80,81]. By incorporating these relationships during the numerical integration stage of the stiffness matrix for each element, homogenized stiffness matrices can be produced, which take into account various voxel values (and their corresponding material properties). As a result, this modeling technique entails the consideration of two meshes:

- a) The **analysis mesh**, used for the FE analysis, and
- b) The **integration mesh**, a finer discretization of the model embedded in the analysis mesh. This mesh is composed of voxels and enables a higher resolution representation of the material distribution within the model than the analysis mesh.

The proposed method is depicted in Figure 3.4, where it can be observed that our approach offers a more accurate representation of the material distribution compared to the standard approach. The advantages of our voxel-type integration approach are twofold. Firstly, it provides a more detailed representation of the material distribution, which allows for a better control of the topology optimization process. Secondly, it reduces the computational cost associated with the FE analysis, as the integration mesh is finer only where it is necessary, and the analysis mesh is used only for the FE analysis.

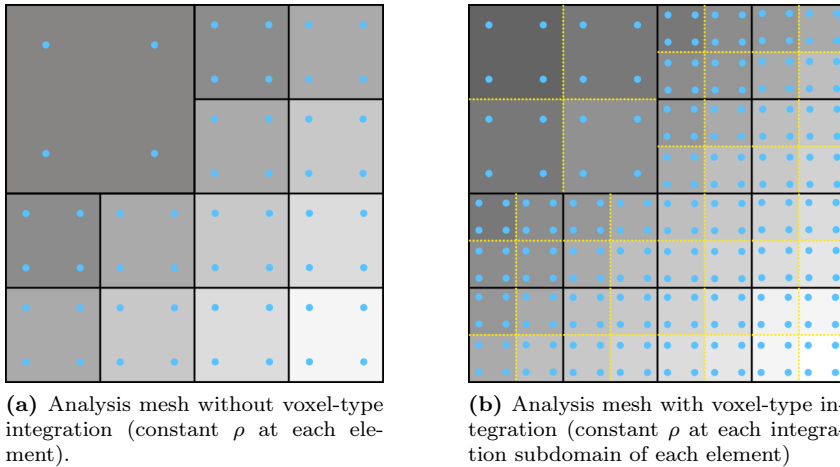


Figure 3.4: Standard vs. Voxel Integration Mesh: representation of ρ and distribution of Gauss Points (in blue).

It is important to note that in the proposed voxel-type integration approach, the design variables used by the TO algorithm are not associated with the individual elements. Rather, they are associated with the integration of subdomains into the elements. Therefore, in order to compute the sensitivities of the compliance, they must be determined at the level of the integration subdomains (voxels). Additionally, the filter radius must be related to the size of the integration subdomains.

We conducted numerical analyses on the reference problem to evaluate the performance of the proposed voxel-integration technique. For comparison with the optimal analytical solution, we utilized the SIMP method algorithm in the analyses without any iterations on the volume fraction. We set the volume fraction to the same value as the optimal analytical solution, i.e., $V/V_0 = 0.2174$. Figure 3.5 and Table 3.2 present the comparison of three types of results: the reference results (Figure 3.5.a), the results obtained through the proposed voxel-type integration approach (Figure 3.5.b), and the reference results that would have been achieved with a one order finer mesh (Figure 3.5.c). The results demonstrate that the total execution time of the voxel-type integration approach is only slightly higher than that of the reference solution. Additionally, the boundary definition considerably improves and reaches the accuracy obtained with finer meshes. The proposed technique enables us to obtain a boundary definition of the same quality as that obtained with a mesh of elements of size $h/2$ at a marginally higher computational cost than with a mesh of elements of size h .

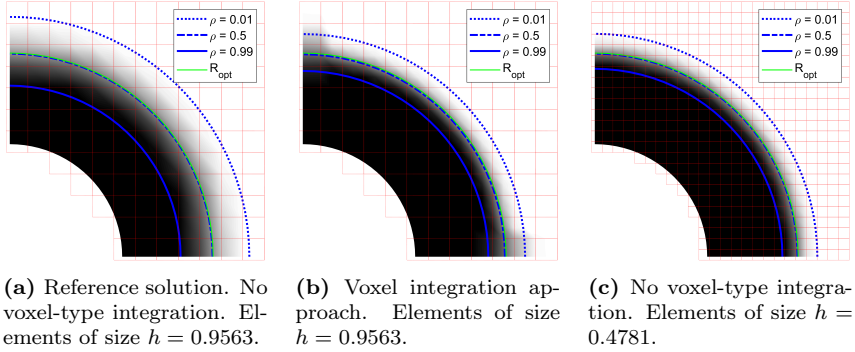


Figure 3.5: Effect of voxel-type integration.

Threshold	Coarse Mesh				Fine Mesh	
	No voxel-integration		Voxel-integration		No voxel-integration	
	\bar{R}_ρ	$e(R)$	\bar{R}_ρ	$e(R)$	\bar{R}_ρ	$e(R)$
$\rho = 0.01$	10.6583	17.8136%	9.8911	9.3332%	9.9026	9.4596%
$\rho = 0.5$	9.0221	-0.2731%	8.9931	-0.5936%	9.0211	-0.2840%
$\rho = 0.99$	7.5988	-16.0059%	8.2537	-8.7662%	8.3473	-7.7321%

Table 3.2: Results obtained for the Reference problem with a coarse mesh, a coarse mesh with the voxel-integration technique and a fine mesh.

3.1.2.2. Solution-based refinement strategies

The accuracy of edge definition in topology optimization is influenced by the element size used and the filter radius employed. Generally, smaller elements and/or smaller filter radii result in sharper geometries, but also in more complex topologies. To address this issue, we propose using h -adapted meshing techniques, which are more efficient than uniform meshes, to decouple the effects of element size and filter radius. This enables us to obtain a sharp edge representation of controlled topological complexity. We also employ two mesh refinement strategies to enhance boundary sharpness and accuracy of the solution:

- a) **Density-based refinement**, where the mesh is refined in regions with intermediate values of relative density, and
- b) **Error-based refinement**, where the mesh is refined in regions where the estimated discretization error is higher.

In both cases, we refine the mesh using element splitting, whereby each parent Cartesian brick element of size h is subdivided into 8 children Cartesian elements of size $h/2$.

Filtering techniques are commonly employed in topology optimization to mitigate the occurrence of checkerboard patterns. However, the size of the intermediate density region is usually around twice the size of the filtering radius r_f . To address this issue, we propose an adaptive filtering approach, wherein the filter radius at each element is proportional to the element size, and the proportionality constant is defined by the analyst. This allows for different filter sizes within the same mesh and can limit the minimum size of the features that define the solution, thereby improving the boundary definition.

We use a relaxed stopping criterion to reduce the computational burden. Specifically, we propose the computation of the relative variation of the objective function (the compliance in the SIMP method), given by:

$$\frac{c_{i-1} - c_i}{c_{i-1}} \times 100 \leq SC, \quad (3.3)$$

where c represents the compliance, i stands for the iteration number, and SC is the user-defined stopping criterion. In our case, we selected $SC = 0.01\%$.

Using filtering techniques with an h -adapted mesh can be computationally expensive in standard FE implementations. This is because the elements surrounding the filtering radius must be localized at each iteration step. The computational cost can become even greater when a set of voxels is included within an element to improve the representation's accuracy. However, the Cartesian structure of *cgFEM* meshes helps to reduce this cost. Hence, we propose the virtual filtering technique based on the hierarchical structure of the Cartesian grid, that is characterized as follows:

- The Cartesian structure allows to select those elements whose center is within a cuboid larger than the radius of the filter.
- Based on the hierarchical structure of the meshes we found those elements that are active in the current mesh.
- The computation of the distance is just carried out within those elements instead of the whole mesh.

As previously mentioned, we propose a refinement criterion that focuses on refining elements with intermediate values of relative density ρ , specifically elements with $1 > \rho > \rho_{min}$. The effectiveness of this density-based refinement procedure is evaluated on the reference problem, as shown in Figure 3.6b. Although the representation of the boundary is improved, the lack of quality in the solution leads to radii far from the optimal. Therefore, the refinement strategy based on the error in the solutions

also results necessary.

The error-based refinement criterion is based on h -adaptivity, which considers the accuracy of the numerical solution in terms of the estimation of the discretization error in the energy norm. This criterion is particularly relevant for volume minimization problems with stress constraints, where inaccurate stress evaluations could lead to non-optimal solutions. Although error estimation techniques have been used to improve the performance of FE simulations in various fields, their use in topology optimization algorithms remains limited. Previous studies that considered the accuracy of the solution as a mesh refinement criterion in topology optimization used residual-based error estimators [82]. In this work, we propose to estimate the discretization error in the energy norm using the approach suggested by Zienkiewicz and Zhu [83]. This involves estimating the error in the energy norm using the following equation:

$$\|\mathbf{e}^*\| = \sqrt{\int_{\Omega} (\boldsymbol{\sigma}^* - \boldsymbol{\sigma}^h) \mathbf{D}^{-1} (\boldsymbol{\sigma}^* - \boldsymbol{\sigma}^h) d\Omega} \quad (3.4)$$

The integral in equation (3.4) is taken over the domain Ω , but it can be restricted to a single element's domain Ω_e to obtain an estimate at the element level. However, the accuracy of the estimate depends on the accuracy of the $\boldsymbol{\sigma}^*$ field. To evaluate an error indicator ζ_e of the discretization error at the element level, we propose the use of the following expression, which is consistent with equation (2.1b) for this type of problem:

$$\zeta_e = \sqrt{\int_{\Omega_e} \rho_e^p (\boldsymbol{\sigma}_e^* - \boldsymbol{\sigma}_e^{h_0}) \mathbf{D}_0^{-1} (\boldsymbol{\sigma}_e^* - \boldsymbol{\sigma}_e^{h_0}) d\Omega_e} \quad (3.5)$$

In [82] the authors argue that recovery-based error estimators are ineffective over material interfaces. As a result, they caution against using recovery-based error estimation in topology optimization since it would unnecessarily over-refine the material/non-material interface. However, in our study, we do not use a binary representation of the material, but rather a regularized representation through the relative density ρ . In fact, in Eq. (3.5), elements with intermediate ρ values typically result in low ζ_e values due to the penalization induced by the term ρ_e^p . Therefore, the mesh optimality criterion utilized for mesh refinement is less likely to refine these elements, instead concentrating on fully dense elements ($\rho = 1$) with high-stress gradients.

The current refinement technique based on error will not lead to the refinement of elements with intermediate values of ρ . Consequently, it will not be useful in enhancing the boundary representation. Therefore, we suggest combining the error-based refinement and the density-based refinement. These two techniques will play different roles: the error-based refinement will enhance the accuracy of the finite element results while the density-based refinement will be used to improve the boundary rep-

resentation.

We performed volume optimization with stress constraints on the reference problem to evaluate the impact of the proposed refinement criteria. The results are illustrated in Figure 3.6, which compares the optimal analytical solution with the results obtained using the enhancements proposed in this study. The reference result, obtained using uniformly-sized elements and none of the proposed enhancements, is shown in Figure 3.6a. As previously mentioned, the most notable feature of this solution is the blurry representation of the exterior surface. When considering the isocontour $\rho = 0.5$, the maximum stress value is underestimated, resulting in an incorrect reduction in the amount of required material, as error estimation is not activated in this case. Even with voxel integration and density-based refinement, as shown in Figure 3.6b, the material quantity is still underestimated for the isocontour $\rho = 0.5$. However, Figure 3.6c illustrates the result obtained when using the proposed voxel-type integration approach in conjunction with the proposed density-based and error-based refinement strategies. The synergistic effect of these techniques results in a sharply-defined external boundary with a radius close to the optimal analytical value.

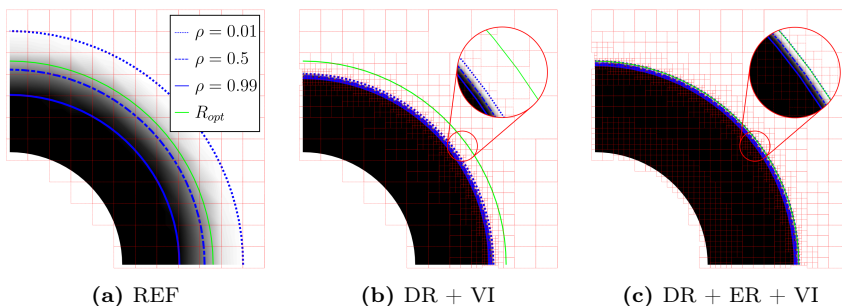


Figure 3.6: Reference problem: Effect of the proposed improvement strategies on the final result of the topology optimization process. The acronyms stand for: reference solution (REF), voxel-type integration (VI), density-based refinement (DR), and error-based refinement (ER).

Even though the use of voxel-type integration reduces the size of the region with intermediate values of ρ , the most significant improvement in the sharp definition of the boundary is achieved through the use of density-based mesh refinement. It is essential to note that this improvement in the sharp definition of the boundary does not necessarily correspond to the accurate placement of the boundary. The latter requires the use of error-based refinement.

In this study, we aim to investigate the impact of the prescribed error level on topology optimization. To achieve this goal, we conducted three different simulations with varying values of the prescribed relative value of the indicator of the relative discretization error in the energy norm, specifically 10%, 5%, and 2%. The results of the simulations were analyzed in terms of the external radius, and the findings are presented in Figure 3.7. The figure illustrates how the prescribed error of the FE analyses affects the external radius, considering both error-based and density-based refinement strategies. As shown, the results converge to the optimal analytical solution as the accuracy of the FE analyses increases.

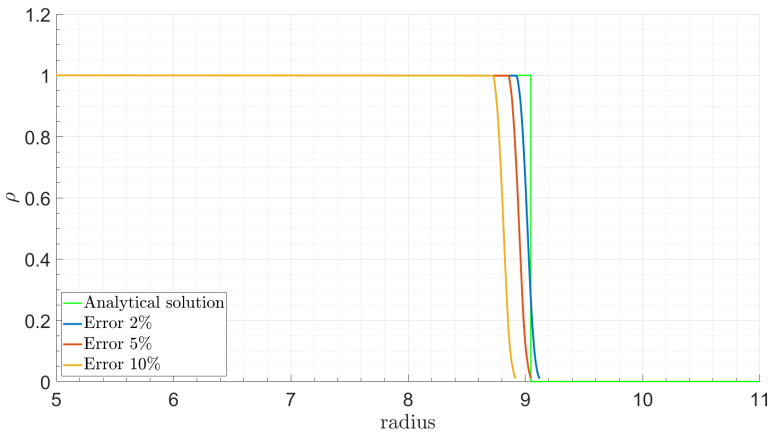


Figure 3.7: Reference Problem: Effect of prescribed error in energy norm on the external radius of the solution.

3.1.3. Hybrid optimization

This section describes the proposed hybrid optimization methodology, that combines topology and shape optimization algorithms, developed to create an efficient structural optimization framework. In the proposed algorithm, topology optimization is used to create a predesign of the solution and shape optimization is used to refine the design. The main feature of the algorithm is the method developed to automatically communicate these two optimization algorithms avoiding user intervention. This interface algorithm is based on the used of machine learning techniques to automatically extract, from intermediate results of the TO, the geometrical modes that represent the TO solution and to use them to create a parametric model that will be used by the SO algorithm. Figure 3.8 shows the main steps of the proposed strategy.

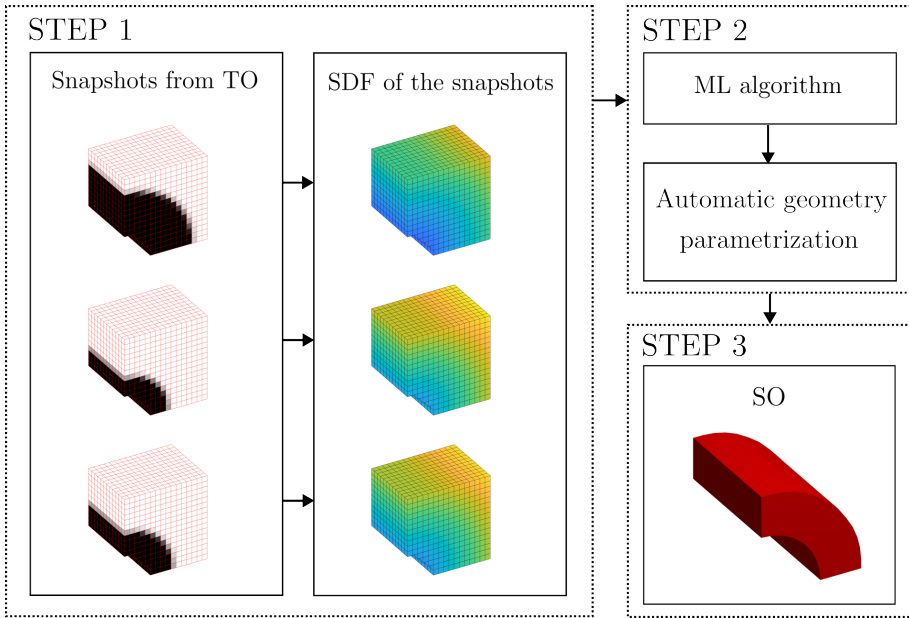


Figure 3.8: Workflow of the hybrid optimization methodology.

STEP 1. The TO algorithm solves the problem defined in (2.4a–2.4c). Intermediate and converged results are gathered and processed. We convert the logical material distribution into SDF using the level-set method. These functions store the distance between each node on the Cartesian grid to the implicit boundary (represented as the 0-isolevel).

STEP 2. The database composed by the SDFs is then used to extract the main geometrical modes through the manifold learning tool, in our case, the LLE algorithm. This process is based on the procedure presented in [75], where a set of \mathbf{X} segmented images of livers were used to train a ML technique to infer the shape of livers. This technique provided a parameterized model to represent livers based on just two parameters.

STEP 3. Using the reduced parametric geometrical model, the procedure can reconstruct new geometries and, thus, use a standard parametric shape optimization tool to obtain the final optimal geometry, both topologically and structurally optimized, as described in (2.6a–2.6b).

3.1.3.1. STEP 1: Topology optimization

A TO algorithm, the SIMP method, is used to determine the optimal material distribution layout in the design domain, specifying the material/void status of each element in the discretization. To reduce the number of parameters required to describe the solution’s geometry, we will use a ML algorithm to extract the inherent structure from the data. The training process for a ML algorithm necessitates a sufficiently large set of snapshots, each representing the geometry to be inferred. As with most optimization techniques, TO is an iterative method, resulting in the availability of material distribution information for each iteration. As the TO process converges, minor changes to the material distribution occur, which are similar to the final solution and therefore possess the same topology. The ML tool will then infer a description of the geometry considering a reduced number of parameters, each associated with a geometrical mode, by leveraging these intermediate material distributions obtained with the TO algorithm. Because all snapshots maintain the same topology, their selection is arbitrary. We propose to employ the last iterations of the topology optimization process to ensure topology invariance. As each snapshot might have been obtained with a different mesh, we project each snapshot’s information onto a shared uniform mesh of elements sized identically to the smallest element used in the definition of the snapshots. The use of a Cartesian grid and the hierarchical data structure of *cgFEM* makes this projection process costless and straightforward.

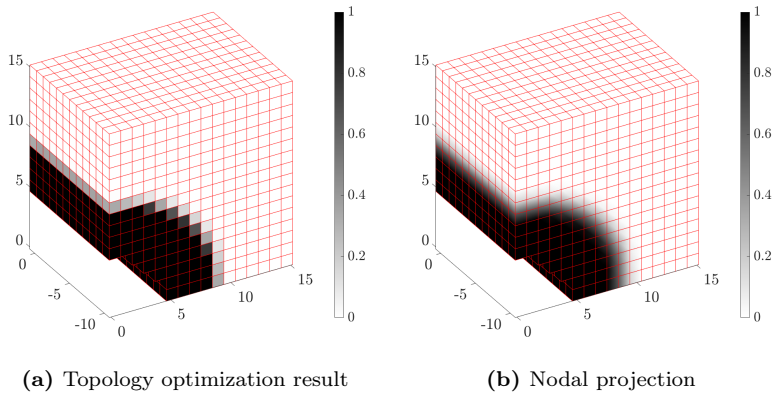


Figure 3.9: Reference problem. Optimal topology optimization material distribution (a) with its nodal projection equivalent (b).

The optimal material distribution layout obtained through the algorithm for the Benchmark problem is shown in Figure 3.9a. This figure serves to illustrate the procedure, although no changes in the topology are expected in this particular example. To obtain a nodal representation, the element-wise solution provided by the

TO algorithm will be smoothed using a nodal averaging procedure. The result of this smoothing process is presented in Figure 3.9b.

Level-set description of the snapshots

As shown in Figure 3.9b, the field represented over the design domain is quasi-boolean, providing minimal information. Post-processing is required to obtain a smoother and richer information, using the distance of each node to the implicit boundary. As the boundary in the regions with intermediate values of ρ is not explicitly defined, an explicit geometrical definition must be generated. To achieve this, the marching cubes (MC) algorithm is used [84]. This algorithm provides a polygonal mesh from the isosurfaces defined by an isovalue ρ_c existing in the material distribution with $\rho_c \in [0, 1]$. Figure 3.10 shows the polygonal mesh obtained from the MC algorithm for different values of v_f for an isovalue $\rho_c = 0.5$ in both cases. The final volume is represented by the isosurface of a selected value of ρ_c in the regions with intermediate values of ρ (red surface in Figure 3.10), and by the regions of the CAD surface that define the design space with $\rho = 1$ (green transparent surfaces in Figure 3.10).

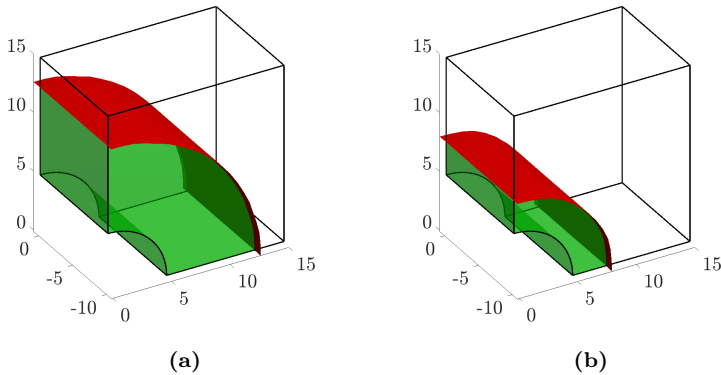
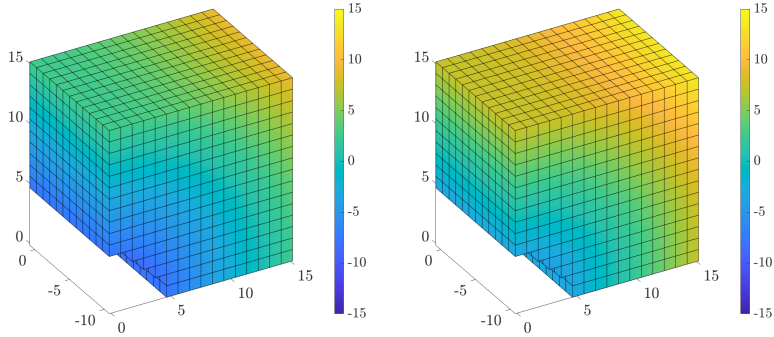


Figure 3.10: MC polygonal meshes representing the external cylindrical shape of the solution obtained from the material distribution considering an isovalue $\rho_c = 0.5$, for v_f equal to 0.5 (a) and 0.15 (b).

Once the surface that defines the volume has been evaluated, the nodal densities representing the solutions are replaced with level-set information, which represents the distance of each node to the surface. Figure 3.10 shows the cases used to obtain the distance level-set represented in Figure 3.11. Using this procedure, the quasi-boolean information of the material distribution is transformed into a smooth and monotonic level-set.



(a) Distance function obtained from the boundary shown in Figure 3.10a (b) Distance function obtained from the boundary shown in Figure 3.10b

Figure 3.11: Distance function to the boundary, represented as a value equal to 0, obtained from Figure 3.10.

In order to increase the richness of the dataset, different volume fractions are considered. To do so, the TO-based problem (2.4a–2.4c) is solved. Additionally, we suggest increasing the number of snapshots artificially by repeating the same strategy but considering different values of ρ_c for each material/void layout. The snapshots must preserve the topology, and their selection is arbitrary.

3.1.3.2. STEP 2: The ML-based TO-SO interface

The LLE algorithm is used to reduce the dimensionality of the snapshots dataset. LLE is a ML technique that extracts the latent structure embedded in the high-dimensional manifold. In our case, the high-dimensional data is constituted by the SDF of each individual. We hypothesize that the parameters extracted by the LLE algorithm define a geometrical basis corresponding to the main geometrical modes of the resulting component.

The dimension of the embedded space may be a user-defined parameter, but it is convenient to study the eigenvalues of the matrix \mathbf{M} in (2.14). As we minimize (2.14), the target eigenvectors are related to the smallest eigenvalues. Figure 3.12 shows that the first eigenvalue is significantly larger than the others, indicating that $d = 1$ is a suitable choice for the dimensionality of the embedded space. This is consistent with this benchmark problem, defined by only one parameters, the external radius. For a detailed mathematical procedure on how to obtain the low-dimensional embedded space, please refer to [85].

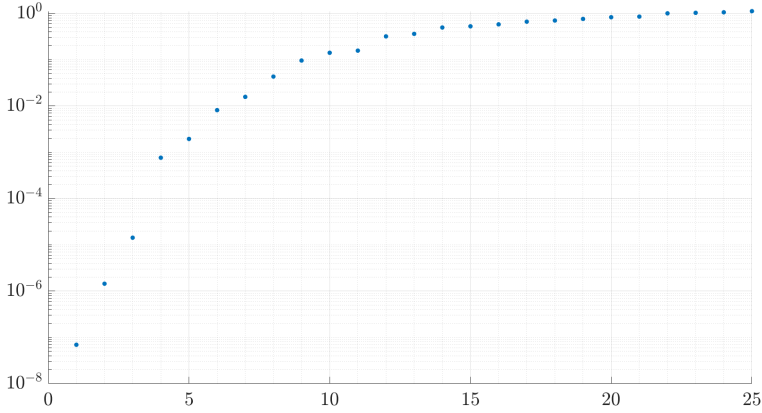


Figure 3.12: Reference Problem. First 25 eigenvalues of \mathbf{M} (see (2.14)), in the LLE procedure.

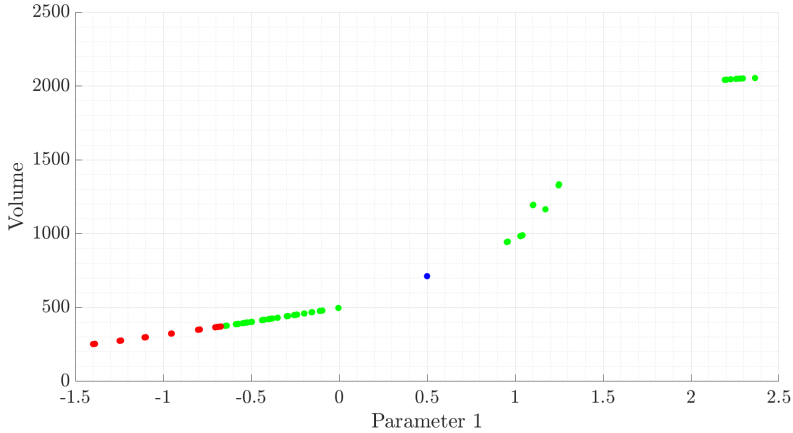


Figure 3.13: Reference problem. Embedded space² for the reference problem considering $K = 21$ neighbours and $d = 1$ parameters. The y-axis represents the volume of each individual, while the colour represents if the maximum stress value is below (green) or above (red) the yield stress limit.

²The representation of the design space in this study is limited by the exploration performed by the topology optimization algorithm. It is important to note that the algorithm explores a subset of the design space, and therefore, the results obtained in this study may not fully represent the entire design space.

Figure 3.13 displays the embedded space resulting from applying the technique to the reference problem. The y -axis corresponds to the volume of the final geometry, and the x -axis represents the extracted low-dimensional parameter. In this case, $K = 21$ neighbors were used from a total of 101 individuals (snapshots). The feasibility of the individuals is represented by the colors in the graph. Green points indicate structures with maximum stress below the yield stress limit, while red points correspond to solutions with von Mises stresses above S_y .

We have obtained a low-dimensional embedded manifold that defines the geometrical characteristics of the material distribution. Our objective is to use this information to create CAD representations of the geometry. Therefore, we define the value of a set of parameters $\widehat{\mathbf{Y}}_i$ in the embedded space \mathbf{Y} . Although this point may be user-defined, the interesting part of this approach is that it can also be automatically defined by an algorithm, such as a shape optimization algorithm. We hypothesize that $\widehat{\mathbf{Y}}_i$ is a weighted interpolation between a set of \widehat{K} neighbors. The value of interpolation weights \widehat{W}_{ij} is obtained by minimizing the functional:

$$e(\widehat{W}) = \sum_i \|\widehat{\mathbf{Y}}_i - \sum_j \widehat{W}_{ij} \mathbf{Y}_j\|^2 \quad (3.6)$$

In this case, we assume, as in the LLE technique, that weights \widehat{W}_{ij} are invariant to spatial transformations. As we have computed the neighbors \mathbf{Y}_j , we gather the matching high-dimensional points \mathbf{X}_j . Finally, we apply the following weighted interpolation to compute $\widehat{\mathbf{X}}_i$, which is a level-set of the new geometry defined in the high-dimensional space:

$$\widehat{\mathbf{X}}_i = \sum_{j=1}^{\widehat{K}} \widehat{W}_{ij} \mathbf{X}_j \quad (3.7)$$

To illustrate the generation of geometries, we begin by selecting a point $\widehat{\mathbf{Y}}_i = 0.5$ that belongs to the embedded space formed by \mathbf{Y} . In Figure 3.13, the individual $\widehat{\mathbf{Y}}_i$ is depicted in blue within its space \mathbf{Y} . This procedure results in a new point $\widehat{\mathbf{X}}_i$ located in the high-dimensional space \mathbf{X} , which contains distance information of each node to the boundary of the geometry, as illustrated in Figure 3.14a. We use this information to compute the boundaries that define the new geometry, as shown in Figure 3.14b.

Note that this procedure allows to define a set of coordinates $\widehat{\mathbf{Y}}_i$ (in this particular case one unique value, but several in the general case) and obtain the corresponding geometry. Hence, this is parametrization of the geometry where the parameters are the coordinates of the reduced space. This is not a conventional parametrization as the coordinates of the reduced space will not have, in general, a geometrical meaning. Even though, in this case, we could assume that the coordinate $\widehat{\mathbf{Y}}_i$ is related to the external radius of the cylinder, but not in a linear fashion.

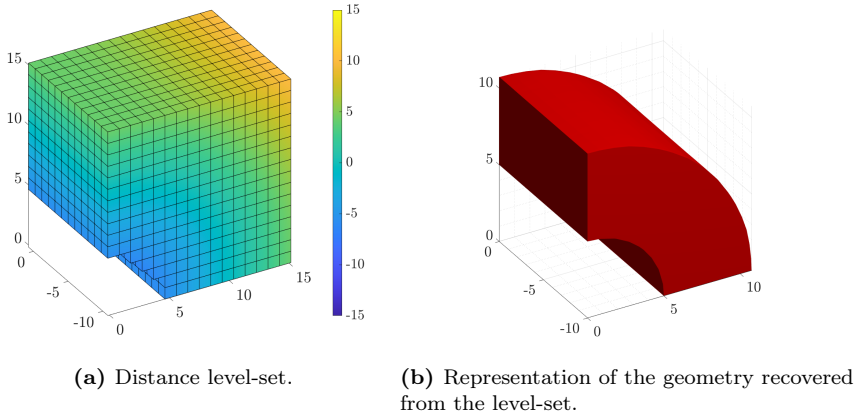


Figure 3.14: Reference problem. New geometry obtained from the space transformation of $\widehat{\mathbf{Y}}_i$ into $\widehat{\mathbf{X}}_i$.

3.1.3.3. STEP 3: Shape optimization

We suggest a final step that guides the modification of the parameter $\widehat{\mathbf{Y}}_i$ using a shape optimization algorithm. Specifically, we minimize the volume in the region of feasible designs, where the maximum von Mises stress value is below the prescribed yield limit, using the updating scheme of the shape optimization algorithm.

As we have defined an implicit parametrization of the design domain's boundary, we can express our shape optimization problem as follows:

$$(\text{SO}_\sigma(Sy)) = \begin{cases} \min_{\widehat{\mathbf{Y}}} : & \text{Volume}(\widehat{\mathbf{Y}}) & (3.8a) \\ \text{subject to:} & \max(\sigma_{eq}(\widehat{\mathbf{Y}})) \leq S_{cr} & (3.8b) \end{cases}$$

where, σ_{eq} represents the equivalent stress value, and S_{cr} denotes the limit value of σ_{eq} . Here, we use the recovered von Mises stress σ_{vm}^* as the equivalent stress value and the yield limit S_y as the limit value.

After expressing the geometry as a function of a reduced set of design variables, a variety of shape optimization algorithms can be used, similar to using a parametrized CAD model. In our study, we employed the Bayesian optimization algorithm, although other methods such as genetic algorithms or gradient-based algorithms would also be adequate. Figure 3.15a displays the optimal geometry of the reference problem,

while Figure 3.15b illustrates the recovered von Mises stress field. Both optimization algorithms were run using a mesh with an element size of $h_{\text{TO}} = h_{\text{SO}} = 0.9563$.

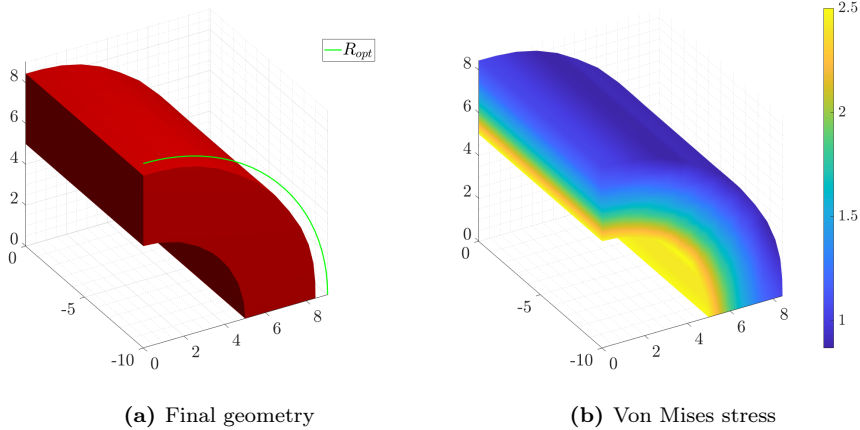


Figure 3.15: Reference problem. Optimal geometry (in red) from the hybrid optimization methodology, providing a cylinder whose external radius is $R = 8.5776$ along with the optimal analytic radius (in green) $R_{opt} = 9.0468$ (a) and the recovered von Mises stress field (b). The results were obtained using meshes of element size $h_{\text{TO}} = h_{\text{SO}} = 0.9563$.

Figure 3.15 shows the results that satisfy the constraint $\max(\sigma_{eq}) \leq S_y$. However, the geometry obtained is far from the analytical optimum. Since the FE numerical results guide the optimization process, improving their quality can enhance the accuracy of the optimal solution. One way to improve the solution is to reduce the element size of the FE analysis mesh. However, if we consider that the main goal of the TO algorithm is to determine the preform of the solution, i.e., a definition of its topology, the TO algorithm would not require the use of fine discretizations. We will therefore focus on improving the solution quality considering morerefined meshes in the shape optimization step, which will ultimately describe the geometry.

The optimal solution depicted in Figure 3.16 was computed using an element size of $h_{\text{TO}} = 0.9563$ for the topology optimization algorithm and an element size of $h_{\text{SO}} = 0.2391$ for the shape optimization.

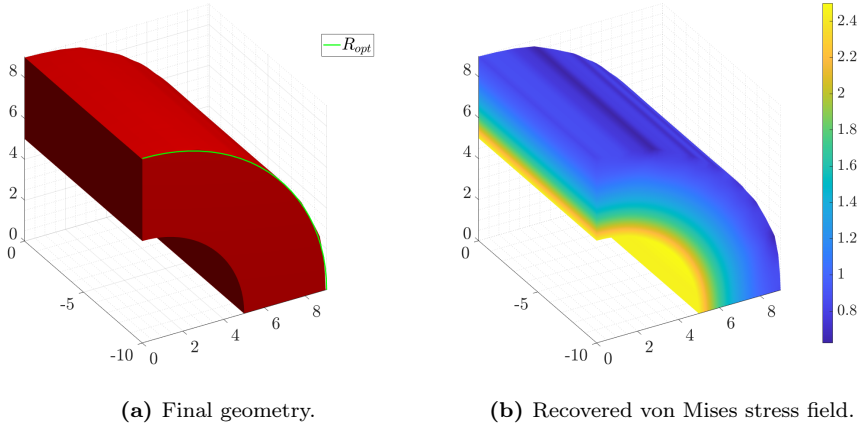


Figure 3.16: Reference problem. Results from the hybrid optimization methodology applied to the reference problem with the optimal analytic radius $R_{opt} = 9.0468$, giving a cylinder whose external radius is $R = 9.0477$ (a) and Von Mises stresses (b). The results were obtained using meshes of element size $h_{\mathbb{T}\mathbb{O}} = 0.9563$ and $h_{\mathbb{S}\mathbb{O}} = 0.2391$.

As in the previous analysis, the constraint $\max(\sigma_{eq}) \leq S_y$ is satisfied. However, in this case, the optimal radius we obtained is significantly closer to the optimal analytic solution.

The previous strategy is effective when the database has no topological changes, which is not always the case when collecting snapshots. The LLE algorithm’s linear interpolation limits the variability allowed in the geometry represented by the snapshots. The interpolation between two snapshots with notable geometrical differences often results in non-physical components or the emergence of artifacts. This issue is due to the metric used to classify the geometries and to evaluate the distance between them. To generalize the methodology, three modifications are required:

1. A suitable metric to assess the similarity between snapshots.
2. An effective strategy for interpolating between geometrical objects.
3. An auxiliary method to classify each individual based on its topology.

The previous points will be discussed in detail in the following section.

3.2. Knowledge-driven design generation

This section addresses the limitations identified in the hybrid optimization strategy. The aim of this new methodology is to extract knowledge from a database and utilize it in various applications, including structural optimization. Therefore, this approach extends the previous concept into a numerical reverse engineering framework that relies on object interpolation techniques. This section outlines the diverse technologies required to achieve this goal and examines their respective impact on the resulting outcomes, as well as how they address the aforementioned limitations.

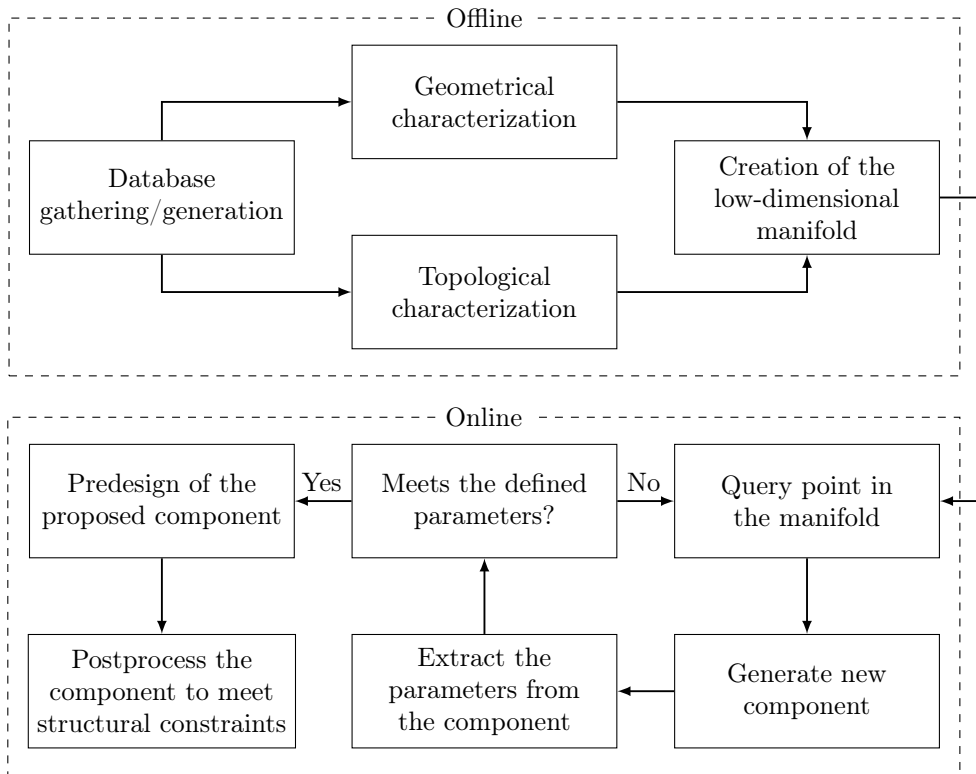


Figure 3.17: Simplified workflow of the methodology proposed.

Figure 3.17 represents the main steps of the methodology presented. In summary, the main goal of this work is to define an interpolation procedure between existing components living in a common manifold. The procedure has an offline and an online phase. The offline phase refers to gathering the dataset and the subsequent treatment that generates the reduced manifold, while the online phase involves the navigation

within the manifold and the creation of new components through the interpolation scheme.

3.2.1. Benchmark Problem

This section demonstrates the application of the previous methodology to an industrial example that emulates a car’s bumper. Due to the unavailability of actual data, we generate an artificial database using the aforementioned hybrid optimization technique. The database simulates the work of manufacturers engaged in designing car bumpers. The example aims to replicate actual designs of a car’s bumper, taking into account a simplified 2D domain (Figure 3.18).

The design domain of the problem is characterized by variables h_1 , h_2 , and X . The Dirichlet boundary conditions are defined by the variables w and W , which specify the position where all displacements are restricted. Additionally, the variable P determines the value of the applied pressure. For all bumpers, we set P to achieve the same resulting force applied to each bumper. This example demonstrates how the proposed strategy performs with complex domains and how it addresses the unusual issue of data scarcity.

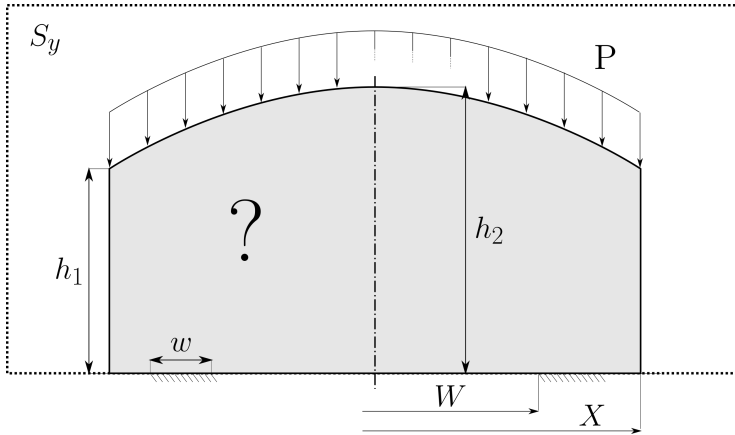


Figure 3.18: Parametrization of the variables that define the design domain and the boundary conditions of the hybrid optimisation algorithm.

Figure 3.19 presents a representative sample of 9 individuals from a database of 83 individuals, each discretized by 10201 nodes. Each individual is illustrated in the Figure with a procedure explained in the following section. While bumpers in the original dataset exhibit varying topologies, we disregard those of little importance and restrict the final database, as illustrated in Figure 3.19, to bumpers with either 2

holes or none, given the limited number of bumpers with more than 2 holes obtained during database creation.

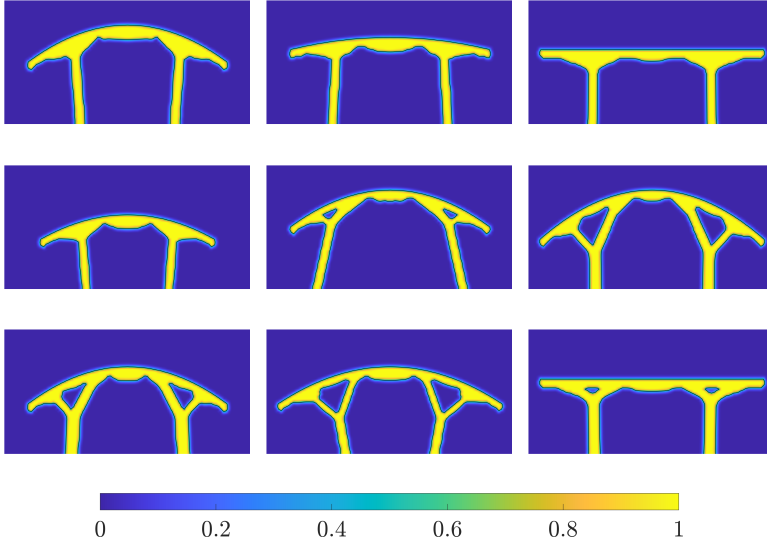


Figure 3.19: Representative sampling of the dataset.

3.2.2. Methodology

This section aims to provide a brief explanation of the various components that make up the proposed strategy, as illustrated in Figure 3.17.

3.2.2.1. Geometrical characterization

Figure 3.20a displays a component resulting from the hybrid optimization methodology. It depicts the SDF, with the boundary defined by its zero value. However, to use the OT tools correctly, the geometrical objects used as inputs need to be described by a probabilistic function. In our study, we convert the SDF into a probabilistic function that takes values between 0 and 1, where the boundary is described using the mid-value, 0.5. The probabilistic function's value shows the probability of a point belonging to the geometry's interior, which is straightforward when the SDF is available. Figure 3.20b displays the resulting function that describes the geometry of the component after its transformation.

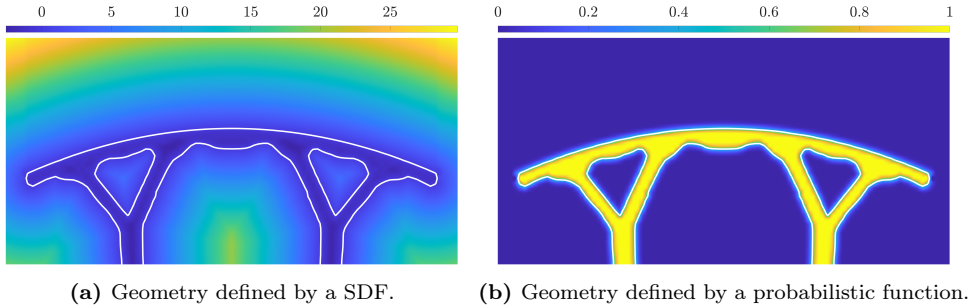


Figure 3.20: Conversion of the SDF (a) into a probabilistic distribution (b).

3.2.2.2. Topological characterization

We utilize TDA techniques to characterize the topology of each individual component, using their persistent homology described by the persistence image.

For example, Figure 3.20b shows the bumper with two holes that we will use to illustrate our topological characterization. In this particular example, as seen in Figure 3.21a, the persistent homology seems to capture only one of the two holes, possibly indicating that they are overlapped in the representation since their birth and lifetime are the same because of the symmetry of the problem. This overlapping may cause issues in the clustering task; thus, we consider a different coordinate system to represent the persistent homology.

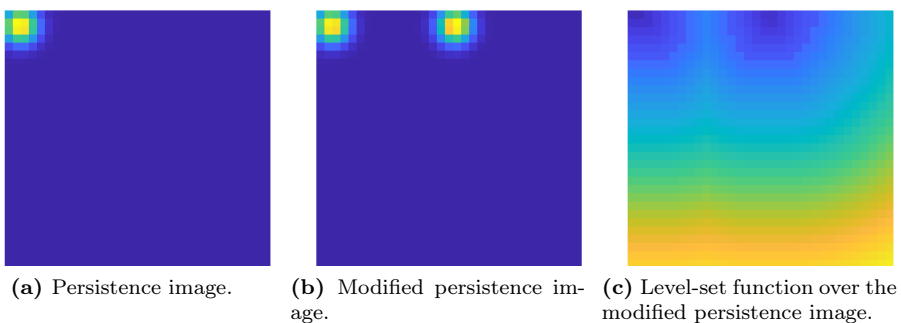


Figure 3.21: Persistent homology of the car's bumper in Figure 3.20 considering the repeatability of each persistent feature.

To achieve that, we replace the x -axis of the lifetime diagram, previously representing the birth, with the repeatability coordinate. This approach provides the

corresponding persistence image in Figure 3.21b, where two holes are now represented. As most of the image domain has a value of 0, this image may be converted into a function over the whole domain, for instance, employing the level-set method (see Figure 3.21c).

3.2.2.3. Modifications in LLE to consider geometry and topology

We employ the LLE algorithm to project individuals into a low-dimensional manifold, which allows for easy visualization and manipulation. Since the components are described using a set of shape descriptors, we need to make some modifications to the standard LLE implementation. Our modification involves incorporating the persistence image (\mathbf{T}_i) of each individual as a topological descriptor, in addition to its geometrical description defined by its SDF (\mathbf{X}_i), into the ML stage.

Up to this point, we have solely utilized the geometric representation of the components, specifically the SDF, to input data into the LLE algorithm. However, we suggest integrating both geometrical and topological data by employing a weighted linear combination of the distances derived from each shape descriptor, where θ represents the weighting factor. This approach provides a more comprehensive representation of an individual's attributes in the low-dimensional manifold. Mathematically, the combination can be expressed as follows:

$$d_{ij}^2 = \frac{\theta}{\sum_i \sum_j \|\mathbf{X}_i - \mathbf{X}_j\|^2} \cdot \|\mathbf{X}_i - \mathbf{X}_j\|^2 + \frac{(1 - \theta)}{\sum_i \sum_j \|\mathbf{T}_i - \mathbf{T}_j\|^2} \cdot \|\mathbf{T}_i - \mathbf{T}_j\|^2 \quad (3.9)$$

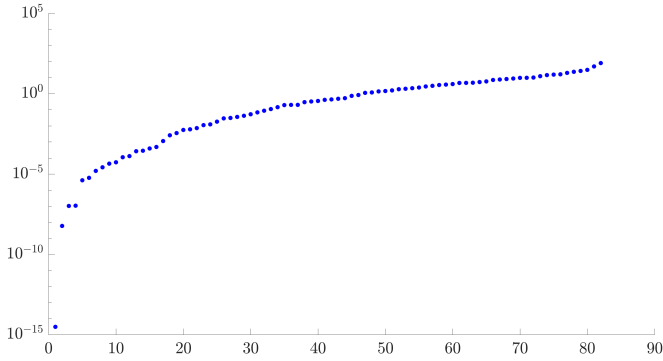
We propose a modification to the LLE algorithm by incorporating topological information. To achieve this, we modify (2.12), resulting in:

$$\varepsilon(\mathbf{w}) = \sum_i \left[\frac{\theta}{\sum_i \sum_j \|\mathbf{X}_i - \mathbf{X}_j\|^2} \cdot \|\mathbf{X}_i - \sum_j w_{ij} \mathbf{X}_j\|^2 \right] + \sum_i \left[\frac{(1 - \theta)}{\sum_i \sum_j \|\mathbf{T}_i - \mathbf{T}_j\|^2} \cdot \|\mathbf{T}_i - \sum_j w_{ij} \mathbf{T}_j\|^2 \right], \quad (3.10)$$

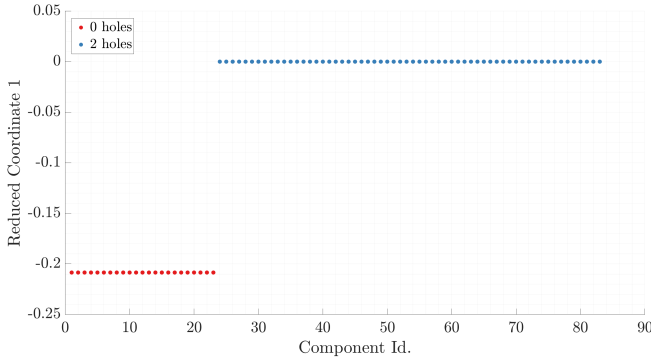
where \mathbf{X}_i is the level-set representation of the geometry, i.e., the SDF and \mathbf{T}_i is the corresponding persistence image. The optimal weight vector \mathbf{w} should consider a combination of both geometry and topology similarities.

Influence of the weighting factor θ

After processing the database, each component has two shape descriptors: a geometrical descriptor defined as a distance function, and a topological descriptor described with the persistence image. The next step in our proposed strategy is to obtain the reduced manifold containing the projection of each individual. To accomplish this, we use the modified version of the LLE algorithm that incorporates both geometrical and topological information and evaluates local vicinities using the Euclidean distance, as shown in equation (3.9). We set the weighting factor to $\theta = 0.5$ and the vicinity to 9 neighbors.



(a) Eigenvalue distribution.

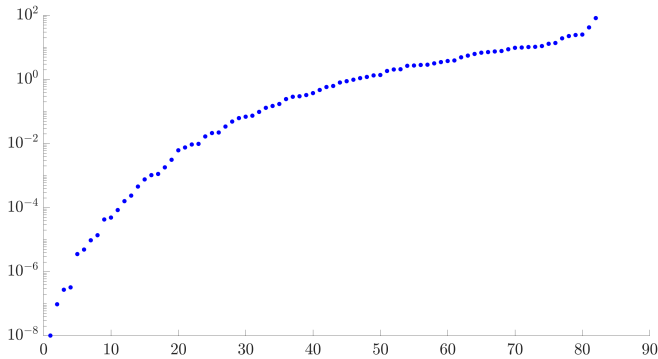


(b) First coordinate of the reduced latent space.

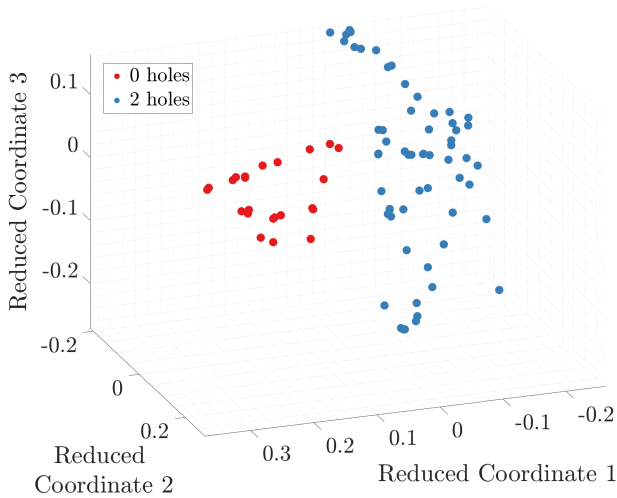
Figure 3.22: Resulting eigenvalue distribution (a) and reduced coordinates (b) employing the LLE technique with the original data plus the persistence images.

Figure 3.22a shows the eigenvalue distribution, where the smallest eigenvalue is significantly separated from the rest, indicating that there is one dominant dimension

in the reduced manifold. This result is unexpected, as it is difficult to represent all the geometrical and topological details we described earlier with just one dimension. Figure 3.22b depicts the components' representation in the reduced manifold, which suggests that only the topology is inferred, while the geometrical descriptor is not adequately represented.



(a) Eigenvalue distribution.



(b) Three first coordinates of the reduced latent space.

Figure 3.23: Resulting eigenvalue distribution (a) and reduced coordinates (b) by using the LLE technique with the original data plus the persistence images.

To address the previous issue, we increased the weighting factor to enhance the geometrical descriptor's contribution. Specifically, we set the value of the weighting factor to $\theta = 0.75$. As shown in Figure 3.23a, this led to a more meaningful

distribution of eigenvalues, with more dimensions characterizing the database. We selected the first three dimensions for representation purposes, as shown in Figure 3.23b. These results highlight the importance of selecting an appropriate value for θ . In practice, the user should experiment with several configurations of hyperparameters, such as θ and the number of neighbors k , until a desired criterion is met in the reduced space.

3.2.2.4. Optimal transport-based interpolation to recover dimensionality

One notable feature of the LLE is its ability to define an individual based on the linear interpolation of its neighbors in the vicinity. However, due to the limited data available, this interpolation scheme is not suitable when using the original LLE technique. To address this issue, we propose an OT approach for object interpolation. To test the feasibility of this methodology in producing components with physical sense and align with the nature of the database, we remove an individual from the database and attempt to recover it using the inverse mapping of the LLE. Figure 3.24 shows one such recovered individual.

We represent the original geometry to be recovered and the results obtained through both linear interpolation and the proposed strategy, which computes the barycenter problem considering the Wasserstein distances, as in 2.16. In these figures, some individuals are highlighted: the reference bumpers to be recovered, removed from the database, are highlighted with a black contour, while the neighbors used to recover the reference bumper are highlighted with a green contour.

Upon analyzing the recovered components, we conclude that the interpolation based on OT techniques provides components with a physical sense, which are quite similar to the reference component and preserve the features in the database. In contrast, linear-based interpolation schemes seem to produce bumpers with artifacts and loss of features. These results suggest that OT-based interpolation is a more effective approach for producing components that will enable successful numerical simulation.

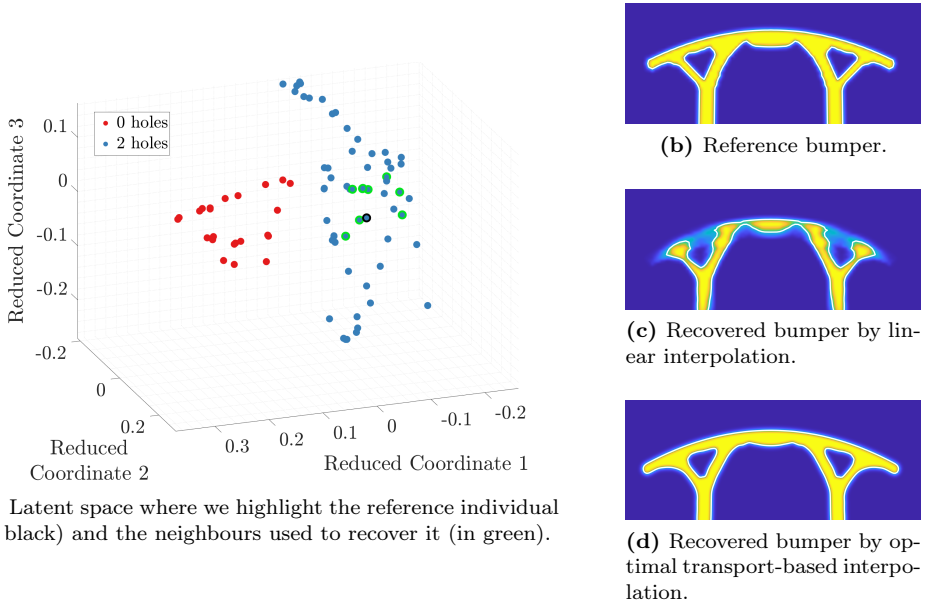


Figure 3.24: Recovery of a bumper of the cluster with 2 holes removed from the database.

We present a quantitative analysis of the differences between the recovered bumpers and the reference bumper, in addition to the qualitative comparison shown in Figure 3.24. Since the bumper component must satisfy certain structural requirements, we find it interesting to measure the error metric based on its structural behavior. We conduct a modal analysis on each recovered component and compare their first natural frequencies, excluding those associated with the rigid solid movement. We use the following equation to measure the error:

$$Error_i = 100 \cdot \left| \frac{\hat{\omega}_i - \omega_i}{\omega_i} \right|, \quad (3.11)$$

where $\hat{\omega}_i$ and ω_i correspond to the i th natural frequency of the recovered bumper and the reference bumper, respectively.

Figure 3.25 shows that the bumper obtained using the optimal transport-based interpolation exhibits lower error levels for the first 10 natural frequencies. This result is significant since it confirms that the proposed method is capable of generating high-quality reconstructions with minimal errors.

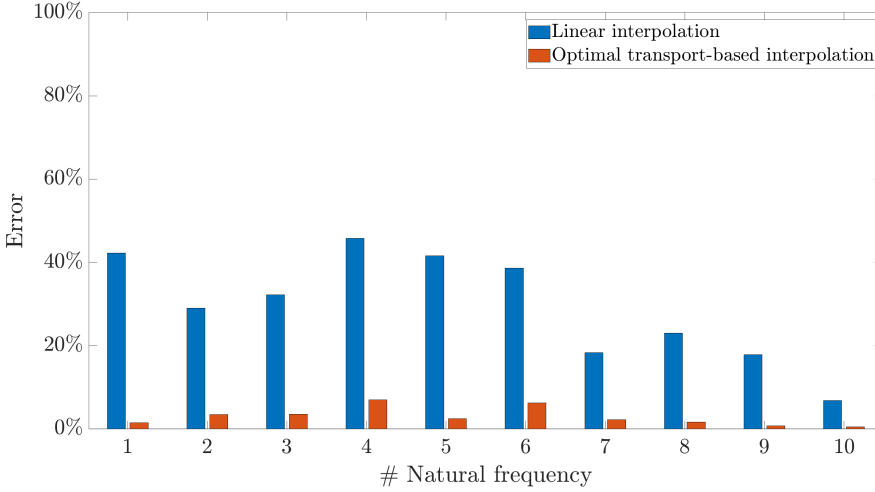


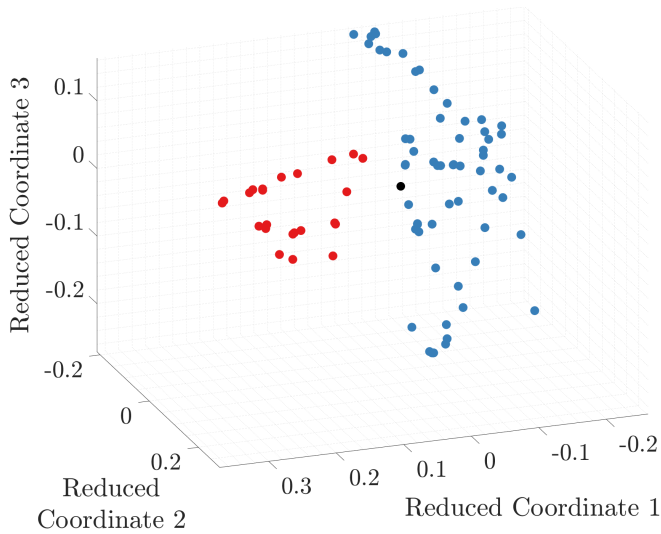
Figure 3.25: Error measure of each natural frequency for the reconstruction employing the linear interpolation (blue) and the optimal transport-based interpolation (orange).

3.2.2.5. Methodology to propose suitable designs

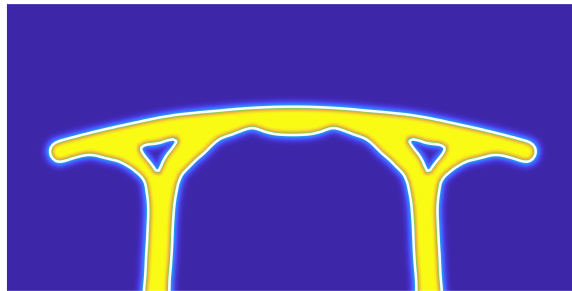
The example above demonstrates the capability of this methodology to accurately capture the high-dimensionality of the data. By representing the high-dimensional manifold of the data, we can extend this capability to generate components that may not exist in the original database. These generated components are based on the current individuals and their geometrical representations are obtained by projecting points from the low-dimensional manifold to the high-dimensional manifold. This is done considering the interpolation scheme in the high-dimensional manifold using the OT with the weights proposed in the low-dimensional manifold.

To create a new design, the analyst would define a set of geometric constraints that the design to be created must satisfy. However, since the relationship between the coordinates of the reduced space and the geometric characteristics in the physical space is unknown, it will be necessary to navigate the low dimensional manifold to find the combination of values of the dimensions of the reduced space that provides a design that meets with the geometric constraints defined by the analyst. This navigation will be guided by an optimization algorithm. In particular, this example uses genetic algorithms as the gradient information is not directly available. Figure 3.26 illustrates the component provided by the algorithm for the following user-defined parameters: $X = 84.91$, $W = 43.20$, $h_1 = 25.00$, $h_2 = 32.62$ and $w = 4.43$, as shown in Figure 3.18. Additionally, the component is required to have two holes. These parameters could be those in the construction of the initial database or any parameters that can

be evaluated from the reconstructed geometries. Additionally, this Figure displays the coordinates of the proposed component within the low-dimensional manifold.



(a) Latent space where we highlight the corresponding coordinates of the proposed component (in black).



(b) Proposed component that meets the parameters criteria.

Figure 3.26: Example of navigation within the low-dimensional manifold to find a given set of parameters.

The proposed component is a preliminary design based on assumed geometrical parameters. Its final form must satisfy a set of structural criteria. An analyst can modify the component’s geometry iteratively until these criteria are met. Alternatively, an algorithmic approach can be employed to fulfill the criteria. Figure 3.27 illustrates the resulting component obtained through our hybrid optimization methodology.

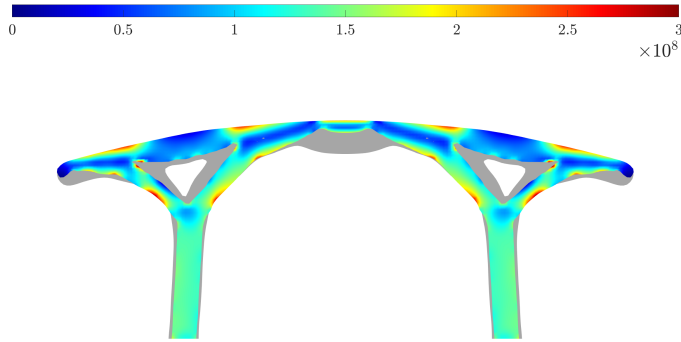


Figure 3.27: Optimal component provided by the hybrid optimization methodology with its corresponding von Mises stress field. The original predesign is represented in gray.

To execute this algorithm, material properties need to be assigned to the geometrical domain. We took $E = 70$ GPa, $\nu = 0.33$, and $S_y = 300$ MPa. Regarding the boundary conditions, a pressure P was applied, generating a resulting force of 1×10^9 N. The optimization algorithm aims to find the component with the minimum volume/mass while ensuring that the maximum von Mises stress remains below the yield limit S_y .

Chapter 4

Closure

4.1. Summary

This thesis presents a set of advances for 3D structural optimization using the *cgFEM*. Several contributions were made within this work, including strategies to improve the quality and geometrical definition of the solution in TO algorithms through mesh refinement methods, an interface to join topology and shape optimization and a strategy to rapidly generate predesigns for certain applications. These contributions are detailed as follows:

- **Efficient framework for topology optimization based on *cgFEM*.** It has been shown that *cgFEM* provides an efficient framework for TO. Thanks to the use of uniform shape elements the computational cost of the integration is reduced. Also, the Cartesian structure of the meshes enable the fast filtering of the sensitivities.
- **Improvement of the solution provided by TO algorithms.** The voxel-type integration technique enables sharper solutions without increasing computational cost. Mesh refinement strategies improve the boundary definition through density-based refinements while the error of the discretization is reduced through error-based refinements.
- **Reduction of human intervention in structural design.** The hybrid optimization methodology, first, employs the TO algorithm to explore the space of topologies. Then, with the ML technique, an automatic parametrization of the

boundary is obtained. Finally, these parameters are tuned by SO algorithms to fulfill the structural constraints.

- **Development of a generative design tool that preserves the existing knowledge.** Taking ideas from the hybrid optimization methodology, we used ML tools to develop a new methodology to create low-dimensional manifolds from available databases of components. The metric employed to create the manifolds considered not only geometrical information but also topological information. Then, we established a method to navigate within this manifold, using OT tools, to generate new components coherent with the previously existing designs of the database.

Bibliography

- [1] M. P. Bendsøe, “Optimal shape design as a material distribution problem,” *Structural Optimization*, vol. 1, pp. 193–202, dec 1989.
- [2] M. Zhou and G. I. Rozvany, “The COC algorithm, Part II: Topological, geometrical and generalized shape optimization,” *Computer Methods in Applied Mechanics and Engineering*, vol. 89, pp. 309–336, aug 1991.
- [3] H. P. Mlejnek, “Some aspects of the genesis of structures,” *Structural Optimization*, vol. 5, pp. 64–69, mar 1992.
- [4] M. Y. Wang, X. Wang, and D. Guo, “A level set method for structural topology optimization,” *Computer Methods in Applied Mechanics and Engineering*, vol. 192, no. 1-2, pp. 227–246, 2003.
- [5] M. Y. Wang and X. Wang, “"Color" level sets: A multi-phase method for structural topology optimization with multiple materials,” *Computer Methods in Applied Mechanics and Engineering*, vol. 193, no. 6-8, pp. 469–496, 2004.
- [6] L. Shu, M. Yu Wang, and Z. Ma, “Level set based topology optimization of vibrating structures for coupled acoustic-structural dynamics,” *Computers and Structures*, vol. 132, pp. 34–42, 2014.
- [7] J. J. Ródenas, G. Bueda, J. Albelda, and E. Oñate, “On the need for the use of error-controlled finite element analyses in structural shape optimization processes,” *International Journal for Numerical Methods in Engineering*, vol. 87, pp. 1105–1126, sep 2011.
- [8] J. Parvizian, A. Düster, and E. Rank, “Finite cell method : hh- and p-extension for embedded domain problems in solid mechanics,” *Computational Mechanics*, vol. 41, pp. 121–133, sep 2007.

- [9] A. Düster, J. Parvizian, Z. Yang, and E. Rank, “The finite cell method for three-dimensional problems of solid mechanics,” *Computer Methods in Applied Mechanics and Engineering*, vol. 197, pp. 3768–3782, aug 2008.
- [10] J. Parvizian, A. Düster, and E. Rank, “Topology optimization using the finite cell method,” *Optimization and Engineering*, vol. 13, pp. 57–78, mar 2012.
- [11] E. Burman, S. Claus, P. Hansbo, M. G. Larson, and A. Massing, “CutFEM: Discretizing geometry and partial differential equations,” *International Journal for Numerical Methods in Engineering*, vol. 104, pp. 472–501, nov 2015.
- [12] E. Nadal, J. J. Ródenas, J. Albelda, M. Tur, J. E. Tarancón, and F. J. Fuenmayor, “Efficient Finite Element Methodology based on Cartesian grids: Application to structural shape optimization,” *Abstract and Applied Analysis*, vol. 2013, pp. 1–19, apr 2013.
- [13] E. Nadal, “Cartesian grid FEM (cgFEM): High performance h-adaptive FE analysis with efficient error control. Application to structural shape optimization,” p. 312, 2014.
- [14] P. Ladeveze and D. Leguillon, “Error Estimate Procedure in the Finite Element Method and Applications,” *SIAM Journal on Numerical Analysis*, vol. 20, no. 3, pp. 485–509, 1983.
- [15] P. Díez, J. J. Ródenas, and O. C. Zienkiewicz, “Equilibrated patch recovery error estimates: Simple and accurate upper bounds of the error,” *International Journal for Numerical Methods in Engineering*, vol. 69, pp. 2075–2098, mar 2007.
- [16] O. A. González-Estrada, E. Nadal, J. J. Ródenas, P. Kerfriden, S. P. Bordas, and F. J. Fuenmayor, “Mesh adaptivity driven by goal-oriented locally equilibrated superconvergent patch recovery,” *Computational Mechanics*, vol. 53, pp. 957–976, may 2014.
- [17] T. Gerasimov, E. Stein, and P. Wriggers, “Constant-free explicit error estimator with sharp upper error bound property for adaptive FE analysis in elasticity and fracture,” *International Journal for Numerical Methods in Engineering*, vol. 101, pp. 79–126, jan 2015.
- [18] J. J. Ródenas, J. Albelda, M. Tur, and F. Fuenmayor, “A hierarchical h adaptivity methodology based on element subdivision,” *Revista UIS Ingenierías*, vol. 16, pp. 263–280, sep 2017.
- [19] M. Papadrakakis and B. H. Topping, *Innovative computational methods for structural mechanics*. Saxe-Coburg Publications, 1999.
- [20] P. S. Tang and K. H. Chang, “Integration of topology and shape optimization for design of structural components,” *Structural and Multidisciplinary Optimization*, vol. 22, no. 1, pp. 65–82, 2001.

- [21] G. W. Jang, K. J. Kim, and Y. Y. Kim, “Integrated topology and shape optimization software for compliant MEMS mechanism design,” *Advances in Engineering Software*, vol. 39, no. 1, pp. 1–14, 2008.
- [22] A. R. Yildiz, N. Öztürk, N. Kaya, and F. Öztürk, “Integrated optimal topology design and shape optimization using neural networks,” *Structural and Multidisciplinary Optimization*, vol. 25, no. 4, pp. 251–260, 2003.
- [23] M. Bremicker, M. Chirehdast, N. Kikuchi, and P. Y. Papalambros, “Integrated topology and shape optimization in structural design,” *Mechanics of Structures and Machines*, vol. 19, no. 4, pp. 551–587, 1991.
- [24] G. A. Méndez Algarra and A. Tovar Pérez, “Integrating topology and shape optimization: a way to reduce weight in structural ship design,” *Ciencia y tecnología de buques*, vol. 3, pp. 83–92, 1 1.
- [25] M. P. Bendsøe and H. C. Rodrigues, “Integrated topology and boundary shape optimization of 2-D solids,” *Computer Methods in Applied Mechanics and Engineering*, vol. 87, no. 1, pp. 15–34, 1991.
- [26] M. Zhou, N. Pagaldipti, H. L. Thomas, and Y. K. Shyy, “An integrated approach to topology, sizing, and shape optimization,” *Structural and Multidisciplinary Optimization*, vol. 26, no. 5, pp. 308–317, 2004.
- [27] A. N. Christiansen, J. A. Bærentzen, M. Nobel-Jørgensen, N. Aage, and O. Sigmund, “Combined shape and topology optimization of 3D structures,” *Computers and Graphics (Pergamon)*, vol. 46, pp. 25–35, 2015.
- [28] T. T. Nguyen, J. A. Bærentzen, O. Sigmund, and N. Aage, “Efficient hybrid topology and shape optimization combining implicit and explicit design representations,” *Structural and Multidisciplinary Optimization*, vol. 62, no. 3, pp. 1061–1069, 2020.
- [29] L. Jiang, S. Chen, and X. Jiao, “Parametric shape and topology optimization: A new level set approach based on cardinal basis functions,” *International Journal for Numerical Methods in Engineering*, vol. 114, no. 1, pp. 66–87, 2018.
- [30] N. Ferro, S. Micheletti, and S. Perotto, “An optimization algorithm for automatic structural design,” *Computer Methods in Applied Mechanics and Engineering*, vol. 372, p. 113335, 2020.
- [31] I. T. Jolliffe, “Principal Component Analysis, Second Edition,” *Springer Series in Statistics*, vol. 98, p. 487, 2002.
- [32] S. T. Roweis and L. K. Saul, “Nonlinear dimensionality reduction by locally linear embedding,” *Science*, vol. 290, no. 5500, pp. 2323–2326, 2000.

- [33] G. Carlsson, "Topology and data," *Bulletin of the American Mathematical Society*, vol. 46, no. 2, pp. 255–308, 2009.
- [34] L. Wasserman, "Topological Data Analysis," *Annual Review of Statistics and Its Application*, vol. 5, pp. 501–532, 2018.
- [35] F. L. Hitchcock, "The Distribution of a Product from Several Sources to Numerous Localities," *Journal of Mathematics and Physics*, vol. 20, no. 1-4, pp. 224–230, 1941.
- [36] L. Kantorovitch, "On the Translocation of Masses," *Management Science*, vol. 5, no. 1, pp. 1–4, 1958.
- [37] C. Villani, *Topics in optimal transportation*. 2003.
- [38] J. Solomon, F. De Goes, G. Peyré, M. Cuturi, A. Butscher, A. Nguyen, T. Du, and L. Guibas, "Convolutional Wasserstein distances: Efficient optimal transportation on geometric domains," in *ACM Transactions on Graphics*, vol. 34, pp. 1–11, Association for Computing Machinery, 2015.
- [39] Y. M. Xie and G. P. Steven, "A simple evolutionary procedure for structural optimization," *Computers and Structures*, vol. 49, pp. 885–896, dec 1993.
- [40] P. Tanskanen, "The evolutionary structural optimization method: Theoretical aspects," *Computer Methods in Applied Mechanics and Engineering*, vol. 191, pp. 5485–5498, nov 2002.
- [41] D. J. Munk, G. A. Vio, and G. P. Steven, "Topology and shape optimization methods using evolutionary algorithms: a review," *Structural and Multidisciplinary Optimization*, vol. 52, pp. 613–631, sep 2015.
- [42] P. A. Vikhar, "Evolutionary algorithms: A critical review and its future prospects," in *2016 International Conference on Global Trends in Signal Processing, Information Computing and Communication (ICGTSPICCC)*, pp. 261–265, IEEE, dec 2016.
- [43] M. P. Bendsøe and N. Kikuchi, "Generating optimal topologies in structural design using a homogenization method," *Computer Methods in Applied Mechanics and Engineering*, vol. 71, pp. 197–224, nov 1988.
- [44] M. Y. Wang, X. Wang, and D. Guo, "A level set method for structural topology optimization," *Computer Methods in Applied Mechanics and Engineering*, vol. 192, pp. 227–246, jan 2003.
- [45] M. Y. Wang and X. Wang, "'Color' level sets: A multi-phase method for structural topology optimization with multiple materials," *Computer Methods in Applied Mechanics and Engineering*, vol. 193, pp. 469–496, feb 2004.

- [46] G. Allaire, F. De Gournay, F. Jouve, and A.-M. Toader, “Structural optimization using topological and shape sensitivity via a level set method,” tech. rep., 2005.
- [47] S. Amstutz and H. Andrä, “A new algorithm for topology optimization using a level-set method,” *Journal of Computational Physics*, vol. 216, pp. 573–588, aug 2006.
- [48] T. Yamada, K. Izui, S. Nishiwaki, and A. Takezawa, “A topology optimization method based on the level set method incorporating a fictitious interface energy,” *Computer Methods in Applied Mechanics and Engineering*, vol. 199, pp. 2876–2891, nov 2010.
- [49] L. Dedè, M. J. Borden, and T. J. Hughes, “Isogeometric Analysis for Topology Optimization with a Phase Field Model,” *Archives of Computational Methods in Engineering*, vol. 19, pp. 427–465, sep 2012.
- [50] A. Ferrer, “SIMP-ALL : a generalized SIMP method based on the topological derivative concept,” *International Journal for Numerical Methods in Engineering*, p. nme.6140, jul 2019.
- [51] O. Sigmund, “A 99 line topology optimization code written in matlab,” *Structural and Multidisciplinary Optimization*, vol. 21, pp. 120–127, apr 2001.
- [52] M. P. Bendsøe and O. Sigmund, “Material interpolation schemes in topology optimization,” *Archive of Applied Mechanics*, vol. 69, no. 9-10, pp. 635–654, 1999.
- [53] O. Sigmund and J. Petersson, “Numerical instabilities in topology optimization: A survey on procedures dealing with checkerboards, mesh-dependencies and local minima,” *Structural Optimization*, vol. 16, pp. 68–75, aug 1998.
- [54] B. Bourdin, “Filters in topology optimization,” *International Journal for Numerical Methods in Engineering*, vol. 50, no. 9, pp. 2143–2158, 2001.
- [55] B. S. Lazarov and O. Sigmund, “Filters in topology optimization based on Helmholtz-type differential equations,” *International Journal for Numerical Methods in Engineering*, vol. 86, pp. 765–781, may 2011.
- [56] K. Svanberg, “The method of moving asymptotes—a new method for structural optimization,” *International Journal for Numerical Methods in Engineering*, vol. 24, pp. 359–373, feb 1987.
- [57] C. Zhang and R. Ordóñez, “Numerical optimization,” in *Advances in Industrial Control*, no. 9781447122234, pp. 31–45, Springer, 2012.
- [58] O. C. Zienkiewicz and J. Z. Zhu, “The superconvergent patch recovery (SPR) and adaptive finite element refinement,” *Computer Methods in Applied Mechanics and Engineering*, vol. 101, pp. 207–224, dec 1992.

- [59] J. J. Ródenas, M. Tur, F. J. Fuenmayor, and A. Vercher, “Improvement of the superconvergent patch recovery technique by the use of constraint equations: The SPR-C technique,” *International Journal for Numerical Methods in Engineering*, vol. 70, pp. 705–727, may 2007.
- [60] M. Bruggi, “On an alternative approach to stress constraints relaxation in topology optimization,” *Structural and Multidisciplinary Optimization*, vol. 36, pp. 125–141, aug 2008.
- [61] C. Le, J. Norato, T. Bruns, C. Ha, and D. Tortorelli, “Stress-based topology optimization for continua,” *Structural and Multidisciplinary Optimization*, vol. 41, pp. 605–620, apr 2010.
- [62] L. Giovannelli, *Direct creation of patient-specific Finite Element models from medical images and preoperative prosthetic implant simulation using h-adaptive Cartesian grids*. PhD thesis, Universitat Politècnica de València, Valencia (Spain), nov 2018.
- [63] D. Schillinger and M. Ruess, “The Finite Cell Method: A Review in the Context of Higher-Order Structural Analysis of CAD and Image-Based Geometric Models,” *Archives of Computational Methods in Engineering*, vol. 22, pp. 391–455, jul 2015.
- [64] E. Burman, “La pénalisation fantôme,” *Comptes Rendus Mathématique*, vol. 348, pp. 1217–1220, nov 2010.
- [65] M. Tur, J. Albelda, O. Marco, and J. J. Ródenas, “Stabilized method of imposing Dirichlet boundary conditions using a recovered stress field,” *Computer Methods in Applied Mechanics and Engineering*, vol. 296, pp. 352–375, nov 2015.
- [66] M. Dauge, A. Düster, and E. Rank, “Theoretical and Numerical Investigation of the Finite Cell Method,” *Journal of Scientific Computing*, vol. 65, pp. 1039–1064, mar 2015.
- [67] C. V. Verhoosel, G. J. van Zwieten, B. van Rietbergen, and R. de Borst, “Image-based goal-oriented adaptive isogeometric analysis with application to the micro-mechanical modeling of trabecular bone,” *Computer Methods in Applied Mechanics and Engineering*, vol. 284, pp. 138–164, feb 2015.
- [68] D. Elfverson, M. G. Larson, and K. Larsson, “CutIGA with basis function removal,” *Advanced Modeling and Simulation in Engineering Sciences*, vol. 5, dec 2018.
- [69] J. M. Navarro-Jiménez, H. Navarro-García, M. Tur, and J. J. Ródenas, “Superconvergent patch recovery with constraints for three-dimensional contact problems within the Cartesian grid Finite Element Method,” *International Journal for Numerical Methods in Engineering*, p. nme.6266, nov 2019.

- [70] J. F. Abel and M. S. Shephard, “An algorithm for multipoint constraints in finite element analysis,” *International Journal for Numerical Methods in Engineering*, vol. 14, pp. 464–467, jan 1979.
- [71] R. Sevilla, S. Fernández-Méndez, and A. Huerta, “NURBS-enhanced finite element method (NEFEM),” *International Journal for Numerical Methods in Engineering*, vol. 76, pp. 56–83, oct 2008.
- [72] O. Marco, R. Sevilla, Y. Zhang, J. J. Ródenas, and M. Tur, “Exact 3D boundary representation in finite element analysis based on Cartesian grids independent of the geometry,” *International Journal for Numerical Methods in Engineering*, vol. 103, no. 6, pp. 445–468, 2015.
- [73] D. P. Bertsekas, *Constrained Optimization and Lagrange Multiplier Methods*. 1982.
- [74] E. Burman and P. Hansbo, “Fictitious domain finite element methods using cut elements: II. A stabilized Nitsche method,” in *Applied Numerical Mathematics*, vol. 62, pp. 328–341, apr 2012.
- [75] D. González, E. Cueto, and F. Chinesta, “Computational Patient Avatars for Surgery Planning,” *Annals of Biomedical Engineering*, vol. 44, no. 1, pp. 35–45, 2016.
- [76] A. Zomorodian and G. Carlsson, “Computing persistent homology,” *Discrete and Computational Geometry*, vol. 33, no. 2, pp. 249–274, 2005.
- [77] H. Adams, T. Emerson, M. Kirby, R. Neville, C. Peterson, P. Shipman, S. Chepushtanova, E. Hanson, F. Motta, and L. Ziegelmeier, “Persistence images: A stable vector representation of persistent homology,” *Journal of Machine Learning Research*, vol. 18, pp. 1–35, 2017.
- [78] J. E. Shigley, C. R. Mischke, and R. G. Budynas, *Shigley’s mechanical engineering design - 9th Ed.* PhD thesis, 2002.
- [79] C. R. Dohrmann, M. W. Heinstein, J. Jung, S. W. Key, and W. R. Witkowski, “Node-based uniform strain elements for three-node triangular and four-node tetrahedral meshes,” *International Journal for Numerical Methods in Engineering*, vol. 47, pp. 1549–1568, mar 2000.
- [80] L. Giovannelli, J. J. Ródenas, J. M. Navarro-Jiménez, and M. Tur, “Direct medical image-based Finite Element modelling for patient-specific simulation of future implants,” *Finite Elements in Analysis and Design*, vol. 136, pp. 37–57, nov 2017.
- [81] H. Wille, E. Rank, and Z. Yosibash, “Prediction of the mechanical response of the femur with uncertain elastic properties,” *Journal of Biomechanics*, vol. 45, pp. 1140–1148, apr 2012.

- [82] M. A. Salazar de Troya and D. A. Tortorelli, “Adaptive mesh refinement in stress-constrained topology optimization,” *Structural and Multidisciplinary Optimization*, vol. 58, pp. 2369–2386, dec 2018.
- [83] O. C. Zienkiewicz and J. Z. Zhu, “Adaptivity and mesh generation,” *International Journal for Numerical Methods in Engineering*, vol. 32, pp. 783–810, sep 1991.
- [84] W. E. Lorensen and H. E. Cline, “Marching Cubes: A high resolution 3D surface construction algorithm.,” *Computer Graphics (ACM)*, vol. 21, no. 4, pp. 163–169, 1987.
- [85] S. T. Roweis and L. K. Saul, “Nonlinear Dimensionality Reduction by Locally Linear Embedding,” *Science*, vol. 290, pp. 2323–2326.

Part II

Articles

PAPER A

Improvement in 3D Topology Optimization with h -adaptive refinement using the Cartesian Grid Finite Element Method (*cg*FEM)

D. Muñoz, J. Albelda, J.J. Ródenas and E. Nadal

International Journal for Numerical Methods in Engineering

Volume 123, Issue 13, 2022

DOI: 10.1002/nme.6652

Abstract

The growing number of scientific publications on Topology Optimization (TO) shows the great interest that this technique has generated in recent years. Among the different methodologies for TO, this paper focuses on the well known Solid Isotropic Material Penalization (SIMP) method [1], broadly used because of its simple formulation and efficiency. Even so, the SIMP method has certain drawbacks, namely: lack of precision in definition of the edges of the optimized geometry and final results strongly influenced by the discretization used for the finite element (FE) analyses. In this paper we propose a combination of techniques to limit the effect of these drawbacks and, thus, to improve the behavior of TO. All these techniques are based on the use of the Cartesian grid finite element method (cgFEM) [2], an immersed boundary method whose Cartesian grid structure and hierarchical data structure makes it specially appropriate for TO. All the proposed techniques are framed under the concept of mesh refinement. First, we propose the use of two meshes, the FE analysis mesh and a finer mesh for integration and evaluation of sensitivities, to improve the resolution of the final solution at a marginal computational cost. Then we propose two h -adaptive mesh refinement strategies [3]. The first one will tend to refine the elements having intermediate density values and will have the effect of sharpening the definition of the edges of the optimized geometry. We will clearly show that if the accuracy of the FE analyses is not taken into account, stress constrained TO will generate solutions that, once manufactured, will not satisfy the constraints. Hence, we also propose an h -refinement strategy based on the estimation of the discretization error in energy norm.

Key words

Topology Optimization; Mesh Refinement; h -adaptivity; cgFEM

Contents

1	Introduction	79
2	Cartesian Grid Finite Element Method	81
3	Topology Optimization in <i>cgFEM</i>	85
3.1	The SIMP method	85
3.2	<i>cgFEM</i> implementation	87
3.3	Stress constraints and accuracy	88
4	Improvement Strategies	90
4.1	Reference problem	90
4.1.1	Solution with a reference implementation of the SIMP method in <i>cgFEM</i>	92
4.2	Voxel integration approach for higher geometrical definition	94
4.3	Adaptive mesh refinement	99
4.3.1	Adaptive virtual filtering	100
4.3.2	Density-based refinement	103
4.3.3	Error-based refinement	106
4.3.4	Numerical performance	107
5	Numerical examples	112
5.1	Hook	112
5.2	Dental implant	115
6	Conclusions	117
	Acknowledgements	118
	References	118

1. Introduction

In structural optimization problems, the optimization algorithms must find the values of a set of parameters that minimize an objective function (usually the mass or the compliance) subjected to the satisfaction of certain constraints (expressed, for example, in terms of stresses). In practice, it is common to use the Finite Element Method (FEM) to evaluate both, the objective function and the constraints.

In the structural optimization field, we can find the shape optimization algorithms. These algorithms consider that the boundary of the design space is defined by the design variables. Hence, no topological change is allowed. We would call shape optimization algorithms to those based on the shape derivatives [4] to update the design variables. If the boundary of the geometry is previously parametrized by an analyst, we would call it parametrized shape optimization. Both algorithms suffer from the impossibility of modifying the topology of the design space, although this issue may be mitigated by the use of topological derivatives [5]. However, there also exist topology optimization approaches to deal with structural optimization [6]. These techniques look for the optimal material distribution within a physical design space. Whereas shape optimization is a boundary optimization problem defined in many cases by a relatively small set of parameters that define the boundary, topology optimization is a domain optimization problem defined by a large set of parameters that depends on the number of elements used to discretize the design space.

Topology optimization has become widely popular thanks to the regularization techniques developed by Bendsoe and Kikuchi [7]. One of the most acclaimed approaches is the Solid Isotropic Material Penalization (SIMP) [1, 8, 9], where the regularization is carried through a penalization of the density interpolation function. Although the SIMP method is the technique used in this work, other approaches are also possible, like those that maintain the discrete definition (0-1 values) of the material layout problem [10–13]. Also Level-Set-based optimization [14–18] processes are common, but need for special tools to generate additional holes to those considered in the initial guess. More recently, a Phase-Field-based topology optimization [19] implementation has been developed, but C^1 continuity is required.

The SIMP method generates a grey scale colour code to represent the quantity of material at each element, yielding images with irregular shapes not directly suitable for manufacturing [20]. There exist some approaches to improve the definition of the boundary. Among others, we emphasize the works in [21], based on projection methods, and [22], where the mesh is refined along the boundary defined by the topology optimization algorithm, i.e. along the regions where intermediate density values have been obtained.

On the other hand, the quality of the finite element (FE) results strongly depends on the mesh used for the analysis. Also, the behaviour of the optimization techniques is strongly influenced by the accuracy of the FE results that drive the iterative optimization process. In the context of structural shape optimization [23] showed the need to control the discretization error of the FE analyses as inaccurate FE solutions will lead to non optimal solutions that, in many cases do not even satisfy the constraints. Obviously, topology optimization driven by FE analyses is also prone to experiencing such problems. Algorithms that consider h -adaptive mesh refinement based on the estimated quality of the FE solution are well-established techniques [24–28] that improve the quality of the solution (evaluated by error estimation techniques) refining the meshes in the regions where the FE solution is less accurate. Mesh optimality criterion (like minimization of the number of elements in the new mesh to obtain a prescribed error level, or equi-distribution of the error in the elements of the new mesh [29]) can be used in h -refinement processes to create computationally efficient meshes to improve the performance of FE analyses.

Reference [23] showed that the use of insufficiently refined meshes in structural shape optimization processes could easily lead to final designs that, once built, will not satisfy the constraints because these constraints were not accurately evaluated. Hence, this reference recommends the use of h -adaptive mesh refinement strategies in structural shape optimization problems. Topology optimization also relies on FE analyses; therefore its output will be influenced by the meshes used for the analyses. As previously mentioned, mesh refinement strategies based on the greyscale levels have been used in the literature about topology optimization [22] to improve the boundary definition. Despite of the importance of the use of mesh refinements strategies in optimization processes, to our knowledge, there is only one reference in the bibliography where mesh refinement guided by error estimation techniques has been taken under consideration [30]. In this reference, the authors use a residual based error estimator to guide the refinement process.

The accuracy of the FE analyses is a relevant factor in topology optimization processes but, as these are iterative processes, the computational efficiency of the FE solvers used is critical. The use of meshes where all the elements have the same shape helps to improve the performance of the FE solver used for topology optimization because, in these cases, it is only necessary to evaluate the original stiffness matrix for one of the elements. Then, the stiffness matrix of any other element is simply obtained scaling this original matrix if the element has a different size. In fact, in many of the numerical examples shown in the literature about topology optimization, the domain used for the optimization is a rectangle (in 2D problems) or a cuboid (in 3D problems), as these shapes can be easily meshed with Cartesian elements. However, practical applications cannot be restricted to this kind of domains. If standard boundary-conforming FE meshes are used, it will not be possible to ensure that all the elements have the same shape. In the Fictitious Domain Methods (FDM), like the Finite Cell Method (FCM) [31–33], the CutFEM [34] or the cartesian grid finite

element method (*cgFEM*) [2, 35], the FE mesh is not necessarily conforming to the geometry. As FCM and *cgFEM* are both based on the use of Cartesian grids, these methods represent an alternative to solve this issue. Biomechanical simulations are very relevant applications of the finite element method. Given the Cartesian structure used to define medical images, the *cgFEM*, developed in our research group, was adapted to automatically create patient-specific FE models, specially of bone structures, directly from images, eliminating the need to segment the different tissues. We combined this characteristic of *cgFEM* with its ability to create FE models from CAD models to define a basic methodology to run patient-specific implant simulations considering complete bone-implant osseointegration [36]. A contact formulation was also developed for the *cgFEM* framework [37] that allowed us to define a methodology to run bone-implant simulations considering frictional contact conditions [38]. This methodology opens the possibility to run realistic patient-specific implant optimizations, including, not only, shape optimization, but also, topology optimization that has motivated the elaboration of this paper.

In this paper we will propose a combination of techniques developed within the framework of *cgFEM* to enhance the performance of SIMP-based topology optimization algorithms in terms of: a) accuracy of FE results to improve the reliability of the solution, b) boundary definition accuracy to improve suitability for the manufacture of the final result and c) computer efficiency to control the computational cost of the topology optimization process.

The paper is organized as follows. The computational efficiency of the techniques proposed on this paper relies on the characteristics of *cgFEM*; hence, we will first describe the most relevant features of *cgFEM* in Section 2. Section 3 will show how the SIMP method can be adapted to solve Topology Optimization problems using *cgFEM*. Later, in Section 4, we will describe the different improvement techniques proposed in this paper: the voxel-integration technique, the adaptive filtering and the density-based and error-based mesh refinement strategies. In this section we defined an optimization problem with analytical solution to show the performance of the proposed improvement techniques, whereas Section 5 we will use more complex numerical examples to show this performance. To conclude, Section 6 will summarize the main conclusions of this paper.

2. Cartesian Grid Finite Element Method

The use of FDM has gained popularity in the computational mechanics community because the geometry-mesh independence enormously reduces the meshing burden (see for instance [2, 31, 34]), even converting the meshing process in most cases

into a trivial process. Additionally, some of the FDM implementations have been successfully adapted to problems where the object to be analyzed is described by an image, including medical images. The Finite Cell Method [31–33] and the Cartesian grid Finite Element Method (*cgFEM*) [2, 35] have demonstrated their capabilities to deal with these problems [39, 40].

The basic idea of FDM is to extend the structural analysis problem to an easy-to-mesh fictitious domain that encloses the physical domain with its complex boundaries. The attractive advantages of this kind of methods, like the simplification of the meshing process and the possibility to define a data structure to reuse calculations, come together with some issues that must be considered. The computational cost with these techniques moves from the expensive meshing algorithm towards the need for:

- a) **More complex numerical integration schemes for the elements cut by the boundary** so that only the part of the element lying into the physical domain is considered in the evaluation of volume integrals; and
- b) **The use of special formulations to impose the boundary conditions** [41–46]. The standard FEM techniques to impose boundary conditions assume that the boundary of the domain is represented by element sides described by nodes placed on the boundary. Hence, these techniques are not valid for FDM as, in general, the boundaries will cut the elements and there will be no nodes on the boundaries. The case of Neumann boundary conditions is simply solved considering that the integration of the surface is deemed inside the element as, in general, it will not coincide with any element face. The case of Dirichlet boundary conditions is more complex than the previous one. To deal with it, a common approach is to impose the essential boundary conditions in a weak form by using the Lagrange multipliers technique [47]. However, the choice of an appropriate Lagrange multiplier space is not trivial. A wrong choice could produce oscillations in the Lagrange multipliers field and thus in the FE solution. Hence, stabilization techniques are needed, being an adaption of the Nitsche’s method one of the most popular ways of stabilization [48].

As indicated in Section 1, in this contribution we consider *cgFEM*, developed by our research group. In *cgFEM* the embedding domain is a cuboid (or a rectangle in the 2D case) that is meshed with elements of different levels. In the *Level-0* mesh, the cuboid is meshed with one single element. Using mesh splitting, this element is divided into 8 new Cartesian elements that will form the *Level-1* mesh. This splitting process is recursively applied to create meshes (hierarchically related) of higher refinement levels. Then, elements of different levels of this set of meshes are used to create the mesh for the FE analysis, where multi-point constraints are used to impose C^0 displacements continuity between adjacent elements of different refinement levels. Figure 1a represents an example of physical domain, Ω_{Phys} , with a sufficiently smooth boundary Γ , embedded into the embedding domain Ω_{Fic} . The boundary Γ of Ω_{Phys} can be divided into two non-overlapping parts, Γ_D and Γ_N , where the Dirichlet

and Neumann conditions are respectively imposed. Figure 1b, shows the embedding domain Ω_{Fic} , discretized with Cartesian elements. The following expression relates the different domains:

$$\Omega_{Phys} \subseteq \Omega_{Fic} = \bigcup_{e=1}^{n_e} \Omega^e \quad (1)$$

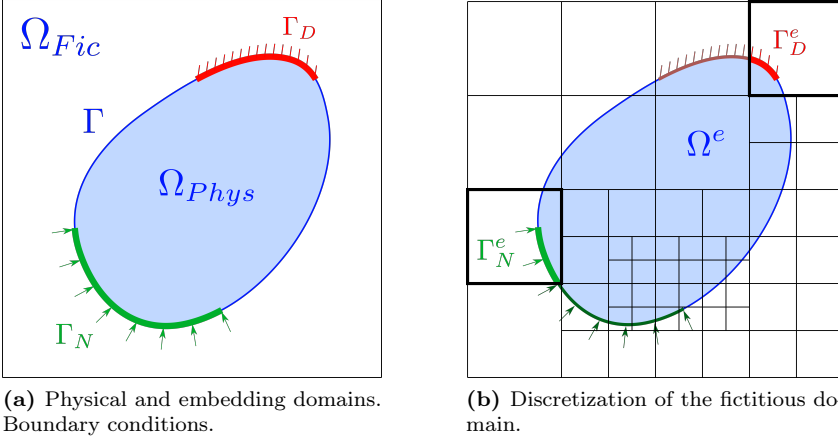
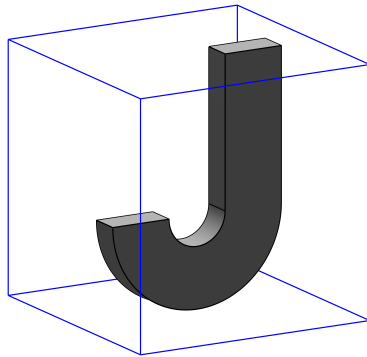


Figure 1: Cartesian grid finite element method (*cgFEM*). Representation of the physical domain and the discretization of the fictitious domain.

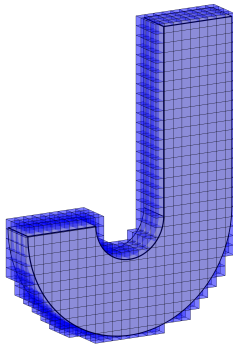
Figure 2 shows a 3D example analyzed with *cgFEM* that is used here to summarize the main characteristics of this methodology:

- *cgFEM* is an efficient FE analysis technique as it considers a Cartesian discretization of the embedding domain (see Figure 2a) and a Cartesian hierarchical data structure [2] that manages the hierarchical relations between the different refinement levels. This allows *cgFEM* to easily: share information between elements of the same or different refinement levels, project information between meshes, use domain decompositions and multi-grid techniques, etc.
- The analysis mesh used by *cgFEM* to model the physical domain Ω_{Phys} can consider elements of different refinement levels. These elements include elements fully placed into Ω_{Phys} and elements cut by its boundary Γ . Elements fully outside of Ω_{Phys} are not considered in the analysis mesh (see Figure 2b).
- *cgFEM* uses a specifically designed integration mesh (Figure 2c) [49], based on the NEFEM integration approach [50] that allows to consider the exact boundary representation given by, for instance, NURBS or T-Splines.

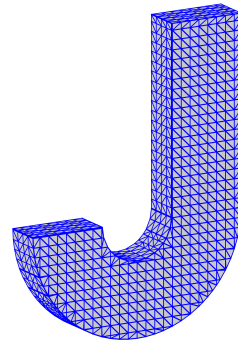
- *cgFEM* considers mesh refinement procedures based on the complexity of the geometry and on the Zienkiewicz and Zhu error estimator, using accurate solution recovery techniques efficiently adapted to *cgFEM*.
- To impose Dirichlet and Neumann boundary conditions *cgFEM* uses stabilization procedures for the Lagrange multipliers space and for the FE space, where the stabilization terms are obtained from accurate recovered fields, also used for error estimation. We refer the interested reader to [42, 51] and [46] for full details about the techniques used by *cgFEM* to impose Dirichlet and Neumann boundary conditions and the stabilization techniques considered in *cgFEM*.



(a) Physical domain Ω_{Phys} (hook) embedded in the fictitious domain Ω_{Fic} (cube).



(b) Discretization of the fictitious domain: analysis mesh.



(c) Integration Mesh.

Figure 2: *cgFEM*. Different domains involved in a finite element analysis.

3. Topology Optimization in *cgFEM*

3.1. The SIMP method

In structural topology optimization we compute the optimal material distribution ρ in a given design domain Ω . In the context of *cgFEM* Ω will be the physical domain Ω_{Phys} previously mentioned. When the topology optimization problem is solved using the SIMP method, introduced in [1, 8, 9], the standard optimization problem consists in minimizing the compliance c subject to certain constraints concerning the amount of material to be used, expressed as a volume fraction of the total volume of the design space. In order to solve the standard optimization problem, in the SIMP method the relative density ρ is considered as a continuous variable, rather than a discrete (0-1 values) variable. In order to enforce as much as possible the segregation of material and void, the method uses a penalization parameter p to penalize intermediate density values of ρ . Thus, a typical topology optimization problem that considers the SIMP method may be presented as,

$$(\text{TO}(v_f)) = \left\{ \begin{array}{ll} \min_{\rho, \mathbf{u}} : & c(\rho; \mathbf{u}) = \frac{1}{2} \int_{\Omega} \boldsymbol{\varepsilon}(\mathbf{u}) \mathbf{D}(\rho) \boldsymbol{\varepsilon}(\mathbf{u}) d\Omega \quad (2a) \\ & \text{with } \mathbf{D}(\rho) = \rho^p \mathbf{D}_0 \quad (2b) \\ \text{subject to:} & V(\rho) = \int_{\Omega} \rho d\Omega = \bar{V}_e \sum \rho_e = v_f V_0 \quad (2c) \\ & a(\mathbf{u}, \boldsymbol{\nu}; \rho) = l(\boldsymbol{\nu}) \text{ where,} \quad (2d) \\ & a(\mathbf{u}, \boldsymbol{\nu}; \rho) = \int_{\Omega} \boldsymbol{\varepsilon}(\mathbf{u}) \mathbf{D}(\rho) \boldsymbol{\varepsilon}(\boldsymbol{\nu}) d\Omega \quad (2e) \\ & l(\boldsymbol{\nu}) = \int_{\Omega} \mathbf{b}^T \boldsymbol{\nu} d\Omega + \int_{\Gamma_N} \mathbf{t}^T \boldsymbol{\nu} d\Gamma_N \quad (2f) \\ & 0 \leq \rho_{min} \leq \rho \leq 1, \quad (2g) \end{array} \right.$$

where $\boldsymbol{\varepsilon}$ is the strain field, \mathbf{u} is the displacement field and $\boldsymbol{\nu}$ is the virtual displacement field. \mathbf{D} is the matrix of the Hook's law that relates strains $\boldsymbol{\varepsilon}$ and stresses $\boldsymbol{\sigma}$. Note that the relation between \mathbf{D} and \mathbf{D}_0 proposed by the SIMP method is $\mathbf{D}(\rho) = \rho^p \mathbf{D}_0$, being \mathbf{D}_0 the matrix of the Hook's law for the fully dense material. When $p > 1$, intermediate densities in elements are penalized because they contribute with little stiffness in terms of its volume fraction. For isotropic materials and non-negative v values, the penalization parameter $p = 3$ provides intermediate materials in between

the H-S bound, this is, with physical meaning [52]. Additionally, v_f is a prescribed volume fraction and V_0 is the total volume of the design domain. As all elements have the same size and shape, the volume $V(\rho)$ is evaluated as the volume of the reference element \bar{V}_e multiplied by the sum of the relative densities of the elements, $\sum \rho_e$. Finally, additional side-constraints are added to ρ such that its maximum value is the unity (fully dense material) while its lower bound is commonly set to 10^{-3} to avoid ill-conditioning issues in the elasticity problem [53].

An additional consideration about the parameter p is that it can influence the convergence of the optimization algorithm. This is why a continuation strategy is commonly used to avoid local minima issues. Therefore, the SIMP method proposes to start with a value of $p = 1$ that slowly increases up to a value $p = 3$ [54] with the convergence of the optimization process.

In order to update the layout of material distribution, the sensitivities of the compliance are needed. In [53] a low-pass filter is applied to the sensitivities to avoid numerical instabilities [55, 56] such as the checkerboard pattern. The filtering is evaluated as:

$$\widehat{\frac{\partial c}{\partial \rho_e}} = \frac{1}{\rho_e \sum_{k=1}^N \widehat{H}_k} \sum_{k=1}^N \widehat{H}_k \rho_k \frac{\partial c}{\partial \rho_k}, \quad (3)$$

with \widehat{H}_k defined as:

$$\begin{aligned} \widehat{H}_k &= r_{min} - dist(e, k), \\ &\{k \in N \mid dist(e, k) \leq r_{min}\}, \\ &e = 1, 2, \dots, N, \end{aligned} \quad (4)$$

where e is the element to be filtered and k are each of the neighbors of element e . Neighbors N are defined as those elements located at a distance less or equal to r_{min} , commonly known as size of the filter. The choice of this filtering technique among others is due to simplicity. Other approaches need the resolution of a differential equation, like those based on the Helmholtz equation [57].

The topology optimization algorithm uses the filtered sensitivities to obtain the new material distribution ρ . In [53], the Optimality Criteria (OC) algorithm is used, whereas exist some alternatives like the Method of Moving Asymptotes (MMA) [58] and the Sequential Quadratic Programming (SQP) [59]. The iterative procedure is repeated until a convergence criterion is accomplished. We describe the structure of the SIMP method for solving the $\mathbb{T}\mathbb{O}$ problem in *Algorithm 1*, where we use the OC algorithm [53] as the updating scheme f ,

Algorithm 1: $\mathbb{T}\mathbb{O}(v_f)$. Compliance minimization algorithm

```

Define  $v_f$ 
Initialize counter:  $i = 0$ 
Initialize relative density at each element  $e$ :  $\rho_{e_i} = v_f$ 
Repeat = 1
while Repeat = 1 do
  Run FE analysis
  Obtain compliance,  $c_i$ , and sensitivities ,  $\partial c_i / \partial \rho_{e_i}$ 
  Filter sensitivities
  Update relative density field:  $\rho_{e_{i+1}} = f(\rho_{e_i}, \partial c_i / \partial \rho_{e_i})$ 
  if  $\|\rho_{e_{i+1}} - \rho_{e_i}\|_\infty \leq \textit{tolerance}$  then
    | Repeat = 0
  end
   $i = i + 1$ 
end

```

3.2. *cgFEM* implementation

We propose the use of *cgFEM*, hence, the topology optimization algorithm must be adapted to the *cgFEM* framework. In the version of the SIMP method presented in [53] all the elements in the mesh had the same shape and size. Hence, the first two features of *cgFEM* that we must consider when implementing the SIMP method in *cgFEM* are that: a) elements of different sizes (i.e. elements from different levels) are used to create the analysis mesh; and b) only the part of the element within the physical domain must be considered in the elements cut by the boundary. Thus, the volume of the domain once discretized must be evaluated as the contribution of the volume of each element e within the physical domain:

$$V(\rho) = \sum_e V_e \rho_e, \quad (5)$$

The volume sensitivities must be evaluated in order to satisfy the volume constraint when updating the material distribution ρ . Note that this was unnecessary in the implementation of the SIMP method in [53] since all elements had the same size. The volume sensitivities are evaluated as:

$$\frac{\partial V(\rho)}{\partial \rho_e} = V_e, \quad (6)$$

Additionally, the expression that computes the filtered sensitivities (3) must be modified in order to take into account the volume of each element V_e as follows:

$$\frac{\widetilde{\partial c}}{\partial \rho_e} = \frac{1}{\rho_e \sum_{f=1}^N \widehat{H}_f V_f} \sum_{f=1}^N \widehat{H}_f \rho_f V_f \frac{\partial c}{\partial \rho_f}, \quad (7)$$

To adapt the features shown above, the topology optimization formulation must be modified. First, the equation (2c) should be replaced by equation (5), considering that each element has different volume V_e either because the mesh is h -adapted or because the element is cut by the domain's boundary. And second, a stabilized Lagrange multipliers formulation is used to impose boundary conditions in elements cut by the Dirichlet boundary. As a result, equation (2d) is replaced by the following equation,

$$a(\mathbf{u}, \boldsymbol{\nu}) + \frac{k}{h} \int_{\Gamma_D} \mathbf{u} \cdot \boldsymbol{\nu} d\Gamma = l(\boldsymbol{\nu}) + \frac{k}{h} \int_{\Gamma_D} \mathbf{g} \cdot \boldsymbol{\nu} d\Gamma + \int_{\Gamma_D} \mathbf{T}(\bar{\mathbf{u}}) \cdot \boldsymbol{\nu} d\Gamma \quad (8)$$

A detailed description of the derivation of this equation and the description of its behavior, out of the scope of this paper, can be found in Reference [42]. The most relevant feature of the proposed stabilized Lagrange multipliers formulation is that the stabilization term \mathbf{T} is evaluated as a recovered [60,61] traction field. As this traction field depends on the FE solution, an iterative process, i.e. Richardson iterations, are used to solve (8). In any case, this is just a technical issue since the stabilization terms are not affected by ρ and do not play any role in the TO procedure.

3.3. Stress constraints and accuracy

Stress constraints are quite common in structural mechanics. In FE based structural optimization with stress constraints, the behavior of the optimization technique is strongly influenced by the accuracy of the stresses evaluated with the FEM that drive the iterative optimization process. In the context of structural shape optimization, [23] showed that inaccurate FE solutions will lead to non optimal solutions that do not even satisfy the constraints.

Although the discretization error is inherent to the FEM, to the authors' knowledge, its effect on the outcome of the topology optimization process with structural constraints, has not been yet analyzed in the literature. In this work, we will analyse this effect in the case of topology optimization processes with stress constraints. The original SIMP method (*Algorithm 1*) does not directly considers this kind of constraints as it is based on a volume constraint. Reference [62] presents a topology optimization algorithm where the volume constraint of the SIMP method is substituted by a maximum stress-measure constraint, such as the KS functions [63]. As the effect of the FE discretization will be present regardless of the method considered

to impose the satisfaction of the stress constraints, for the sake of simplicity, we implement a very basic, not necessarily efficient, modification of the SIMP method to impose this kind of constraints, whose behaviour has been checked for the examples presented in this paper. Thus, in this work, we considered a volume minimization problem with stress constraints that considers an internal topology optimization loop based on the SIMP method. Hence, the standard SIMP method described in *Algorithm 1*, is embedded in a volume optimization as follows:

$$(\text{TO}_\sigma(S_y)) = \begin{cases} \min_{v_f} : & \text{TO}(v_f) & (9a) \\ \text{subjected to:} & \sigma_{vm}^* \leq S_y & (9b) \end{cases}$$

where S_y is the yield limit of the material and σ_{vm}^* is the recovered von Mises stress field evaluated from σ^* , the so called recovered stress field, more accurate than the stress field σ^h provided by the FEM.

The recovered fields are also called smoothed fields, as, in general terms, the stress recovery procedures take the discontinuous FE stress solution and post-process it to obtain a continuous smoother solution. There are different procedures to obtain σ^* . Because of their accuracy, the most commonly used techniques are the Superconvergent Patch Recovery (SPR) technique (also proposed by Zienkiewicz and Zhu [60]) and enhanced versions of this technique, like the SPR-C technique [61]. The basic idea of the SPR technique consists in defining a patch Ω_{pi} with the elements that share a vertex node i and to evaluate each component of the recovered stress field σ_{pi}^* in Ω_{pi} using least squares fitting to fit a polynomial (of the degree of the displacements) to the values of each component of σ^h evaluated at the Gauss points of the elements in Ω_{pi} .

The use of the density field ρ in topology optimization implies, a particular definition of the stress field to keep consistency with the expression of the strain energy (compliance) in (2a). We can rewrite equation (2a) as:

$$\sigma_e^{h\rho} = \mathbf{D}(\rho_e)\varepsilon_e^h = \rho_e^p \mathbf{D}_0 \varepsilon_e^h = \rho_e^p \sigma_e^{h_0} \quad (10)$$

where $\sigma_e^{h_0} = \mathbf{D}_0 \varepsilon_e^h$ would represent the original FE stress field at the element, before considering the density correction. The penalization parameter p in (10) is consistent with the equation (2b) [64, 65].

Given equation (10), for the evaluation of the recovered stress field we propose to smooth the original stress field at elements, σ^{h_0} , and then to modify the resulting recovered stress field using the density correction.

There exist many possibilities to address the problem in (9), such MMA or SQP, which are gradient-based algorithms and need for a regularization of (9b), like KS

functions. However, the analysis of these techniques is out of the scope of this contribution. This structure is presented in *Algorithm 2*. For sake of simplicity, the updating scheme, g in *Algorithm 2*, used in this work consists on generating a quadratic polynomial surrogate model, from which the next volume fraction v_f^{i+1} is obtained as the volume fraction that produces $\max(\sigma_{vm})$ equal the yielding stress limit S_y . The quadratic polynomial surrogate model is obtained by a curve fitting procedure over the vectors $\overline{v_f}$ and $\overline{\max(\sigma_{vm}^*)}$, that include the last results of the iterative process.

Algorithm 2: $\mathbb{T}\mathbb{O}_\sigma(S_y)$. Volume Minimization problem with stress constraint

```

Set  $S_y$ 
Initialize counter:  $i = 0$ 
Initialize volume fraction  $v_f^i$ 
while Repeat = 1 do
     $i = i + 1$ 
    Run Algorithm 1  $\mathbb{T}\mathbb{O}(v_f^i)$ 
    Obtain the Stresses of the optimal layout distribution
    Evaluate the maximum Von Mises Stress:  $\max(\sigma_{vm}^{*i})$ 
    if  $\max(\sigma_{vm}^{*i}) \leq S_y$  then
        | Repeat = 0
    end
    Update the volume fraction:  $v_f^{i+1} = g(\overline{v_f}, \overline{\max(\sigma_{vm}^*)}, S_y)$ 
end

```

4. Improvement Strategies

In this section we propose a set of methodologies based on the use of *cgFEM* to improve topology optimization algorithms. However, before describing the methodologies, we will first introduce an optimization example with analytical solution that will be used to create a reference solution and, then, to explain the proposed improvement strategies.

4.1. Reference problem

The reference problem used to describe the proposed methodologies is defined in Figure 3 and corresponds to a constant hollowed cross sectional area beam, with two perpendicular planes of symmetry ($x = 0$ and $z = 0$), under plain strain conditions, subjected to a pressure P on the internal cylindrical surface.

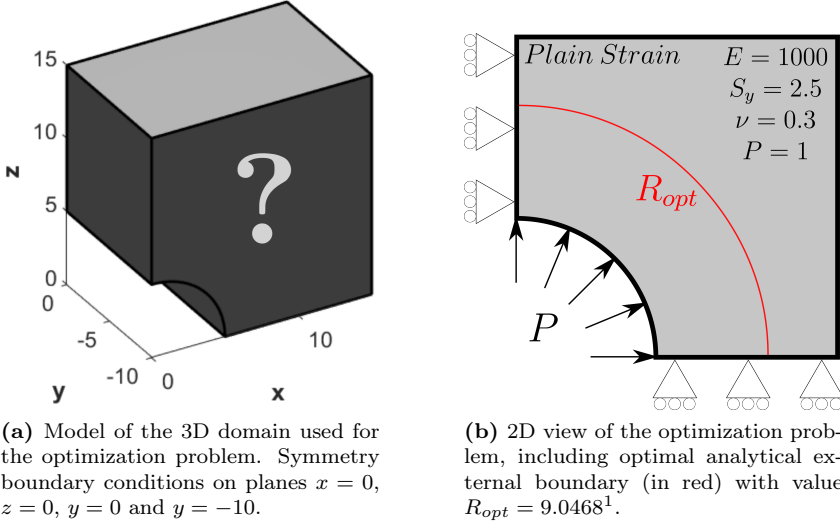


Figure 3: Reference problem.

The objective of the optimization problem is to minimize the amount of material while satisfying $\sigma_{vm} \leq S_y$. It is known that the optimal shape will also correspond to a circular external shape, i.e., the optimal shape will take the form of a thick-walled cylinder. The following equations are the analytical solutions for displacements (11) and stresses (12) of thick-walled cylinders subjected to internal pressure [66]:

$$\mathbf{u} = \begin{Bmatrix} u_R \cos(\theta) \\ 0 \\ u_R \sin(\theta) \end{Bmatrix} \quad u_R = \frac{P(1+\nu)}{E(\kappa^2-1)} \left[(1-2\nu)r + \frac{r_{ext}^2}{r} \right] \quad (11)$$

$$\boldsymbol{\sigma} = \begin{Bmatrix} \sigma_R \cos^2(\theta) + \sigma_H \sin^2(\theta) \\ \nu(\sigma_x + \sigma_z) \\ \sigma_R \sin^2(\theta) + \sigma_H \cos^2(\theta) \\ 0 \\ 0 \\ (\sigma_R - \sigma_H) \sin(\theta) \cos(\theta) \end{Bmatrix} \quad \begin{aligned} \sigma_R &= \frac{P}{\kappa^2-1} \left[1 - \left(\frac{r_{ext}}{r} \right)^2 \right] \\ \sigma_H &= \frac{P}{\kappa^2-1} \left[1 + \left(\frac{r_{ext}}{r} \right)^2 \right] \end{aligned} \quad (12)$$

where $r = \sqrt{x^2 + z^2}$ is the radius of the point, r_{ext} and r_{int} are the external and internal radii, $\kappa = r_{ext}/r_{int}$, $\theta = \arctan(z, x)$, P is the internal pressure, E is the Young Modulus and ν is the Poisson's ratio.

¹Value truncated to 4 decimal places.

The maximum von Mises stress in the cylinder can be evaluated, considering the exact solution in stresses, as a function of the external radius. Therefore, it is possible to find the value of the minimum external radius that satisfies $\sigma_{vm} \leq S_y$. For the data shown in Figure 3, this radius is $R_{opt} = 9.0468$, represented in Figure 3b, that leads to an optimum volume of $V_{opt} = 446.4545$. Taking into account the dimensions of the design space shown in Figure 3 this corresponds to a volume fraction $V/V_0 = 0.2174$.

4.1.1. Solution with a reference implementation of the SIMP method in cgFEM

The reference problem can be solved using topology optimization. Let us assume that we use the iterative process (*Algorithm 2*) described in Section 3 to solve it, considering uniform element size $h_{ref} = 0.9563$, filtering radius $r_0 = 1.5 \times h_{ref} = 1.4345$ and penalization parameter $p = 3$. The evolution of the optimization algorithm is shown in Figure 4 while Figure 5 shows 3D and 2D views of the solution obtained. This solution will be considered as the Reference Solution.

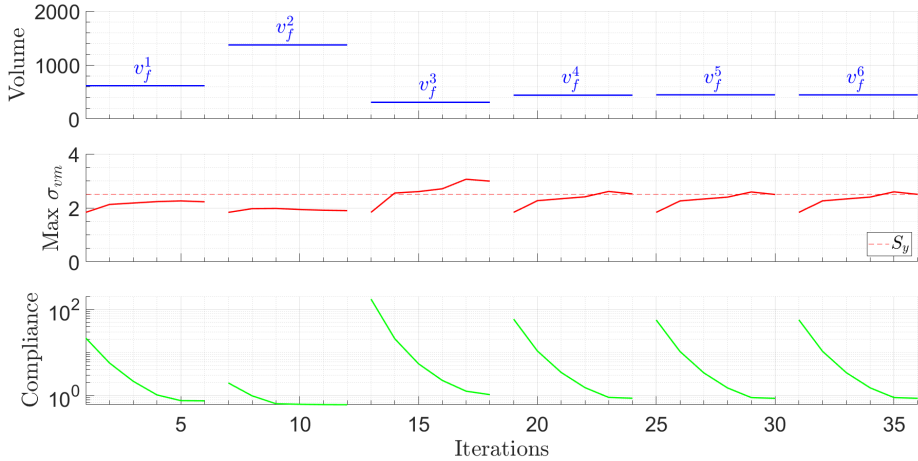


Figure 4: Reference Problem: Convergence curves of volume (Top), maximum von Mises stress (Middle) and compliance (Bottom).

Figure 5 shows that the topology optimization process provides a cylinder-like solution, similar to the optimal analytical solution. Figure 5.b) includes the optimal analytical radius R_{opt} together with the iso-contours of relative densities $\rho = 0.01$, $\rho = 0.5$ and $\rho = 0.99$. To obtain these iso-contours we smoothed the discontinuous original solution of the topology optimization process, given by a constant value of ρ at each element, simply using nodal averaging [67]. These iso-contours show a first problem associated to the solution: the solution obtained does not provide a clearly

defined representation of the edges but a diffuse representation given by intermediate values of ρ along a region whose thickness is approximately equal to twice the filtering radius $2 \times r_0$.

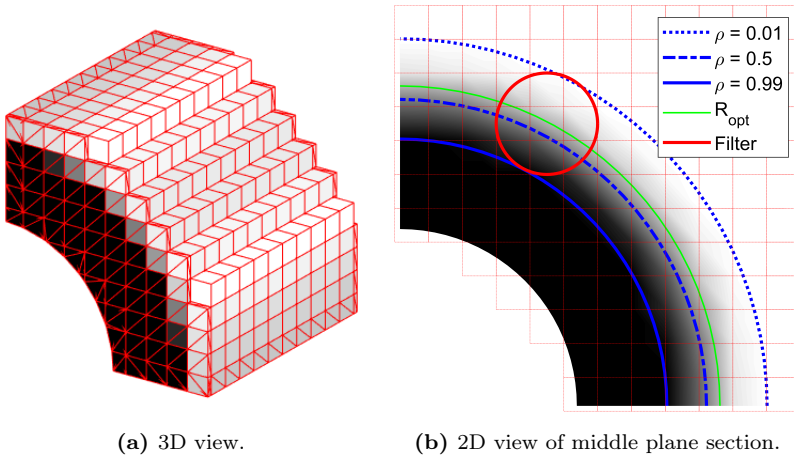


Figure 5: Reference Solution of the reference optimization problem. Elements with relative density $\rho \leq 0.01$ have not been represented in (a). The 2D view in (b) includes the optimal analytical radius R_{opt} and the iso-contours $\rho = 0.01$, $\rho = 0.5$ and $\rho = 0.99$ and an example of the area covered by the filter radius.

If we want to manufacture a component from the solution shown in Figure 5, it would be reasonable to create a hollowed cylinder. The external radius of the cylinder could be defined as a function of a threshold value of relative density ρ selected by the user. Let \bar{R}_ρ be this radius, defined as the mean value of external radius evaluated from the iso-contour of a relative density ρ arbitrarily selected by the user. As the object to be manufactured would be a thick-walled cylinder subjected to an internal pressure, it is possible to use the exact solution in (11) and (12) to evaluate the exact maximum value of the von Mises stress $\hat{\sigma}_{vm}(\rho)$ that would appear in the object. Table 1 shows the values of \bar{R}_ρ and $\hat{\sigma}_{vm}(\rho)$ that would be obtained for 3 different values of ρ and the relative errors of these magnitudes $e(R)$ and $e(\hat{\sigma}_{vm})$, with respect to the optimal analytical solution of this problem.

Table 1 shows a second problem associated to the solution: the blurred representation of the boundary can lead to the selection of an external radius significantly different to R_{opt} . In particular, selecting an external radius smaller than R_{opt} would produce a component that would not satisfy the stress constrain $\sigma_{vm} \leq S_y$, i.e., a component that would fail.

Threshold	\bar{R}_ρ	$e(R)$	$\hat{\sigma}_{vm}(\rho)$	$e(\hat{\sigma}_{vm})$
$\rho = 0.01$	10.3804	14.7408%	2.2586	-9.6579%
$\rho = 0.5$	8.6663	-4.2057%	2.6039	4.1570%
$\rho = 0.99$	7.5457	-16.5922%	3.1037	24.1470%

Table 1: Reference Problem. Comparison between the solution obtained and the analytical solution, including the relative error measured as $e(R) = 100 \frac{\bar{R}_\rho - R_{opt}}{R_{opt}}$ and $e(\sigma_{vm}) = 100 \frac{\hat{\sigma}_{vm}(\rho) - S_y}{S_y}$.

In Figure 6 we represent the evolution of the density along an axis corresponding the $\theta = \frac{\pi}{4}$ angle of the cylinder in polar coordinates, where the diffuse zone starts from $r \approx 7.2$.

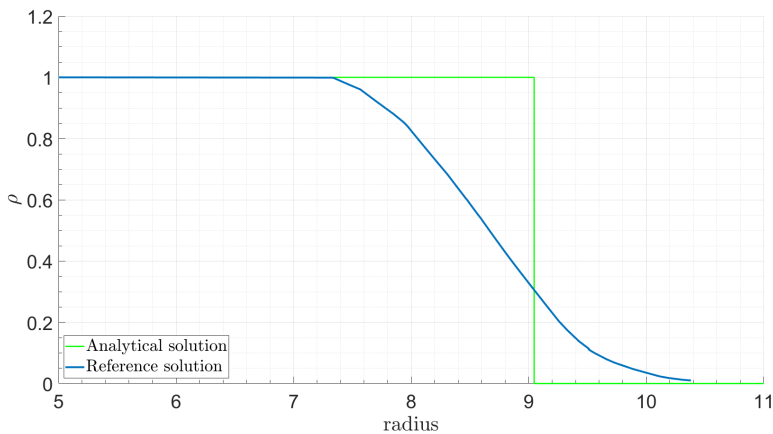


Figure 6: Reference Problem. Density evolution along radius $\theta = \frac{\pi}{4}$ compared with analytical solution.

4.2. Voxel integration approach for higher geometrical definition

As indicated in the introduction of this paper, one of the applications of *cgFEM* is the automatic creation of FE meshes from medical images [36] in which the information is also stored using a Cartesian format. *cgFEM* is especially useful to create FE models to represent bone tissues. The basic idea consist in placing a Cartesian grid (either uniform or *h*-adapted) over the image. The voxels into each element will

be coupled to the element and considered as integration subdomains, with integration points associated to each voxel, see Figure 7. It is possible to find relations between the values used to represent the medical image and material properties. For example, it is possible to find relations between Young's modulus and Hounsfield values used to represent bone structures [36, 68]. Considering these relations during the numerical integration stage of the stiffness matrix of each element will lead to homogenized stiffness matrices where the different voxel values (and their associated material properties) have been taken into account. Therefore, in this modelling technique we can consider that there are two meshes:

- a) The analysis mesh used for the FE analysis, and
- b) The integration mesh, finer than the analysis mesh, defined by voxels, that represents the distribution of material into the model with a resolution higher than the analysis mesh.

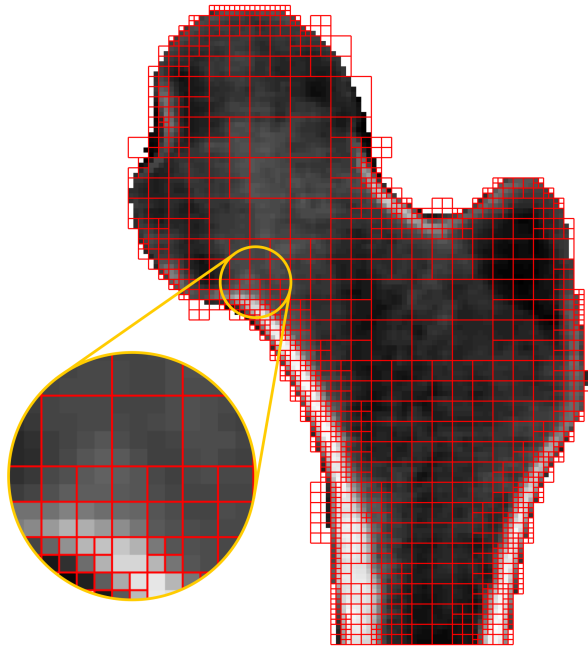


Figure 7: FE model of medical image generated with *cgFEM*.

We have adapted this idea to the topology optimization framework. We propose to use an analysis mesh for the FE analyses and a finer mesh, the integration mesh, obtained by subdivision of the elements not cut by the boundary into 2^3 integration subdomains (equivalent to the voxels considered for FE analysis from medical images)

that will be used to provide a finer topological representation of the material distribution. Note that this approach, called *voxel-type integration*, can be considered similar to the multiresolution (MOPT) design representation approach first proposed in [69] and later used in [70]. Figure 8 compares the standard approach and the proposed voxel-type integration approach in a mesh with elements of different sizes.

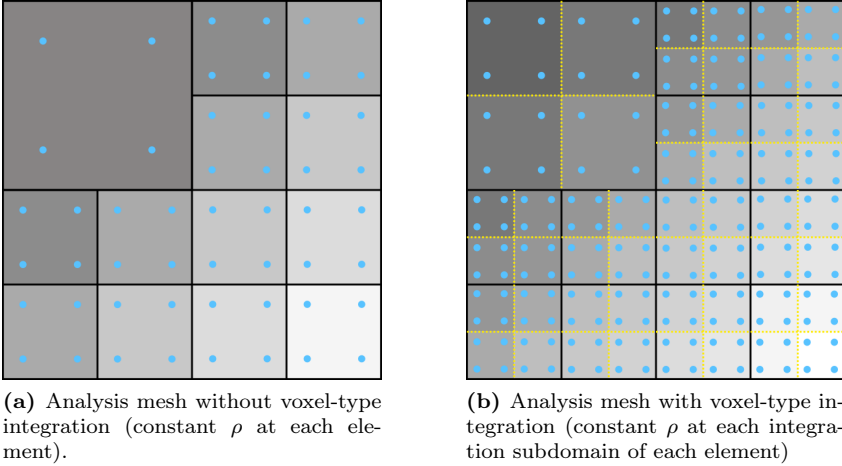


Figure 8: Standard vs. Voxel Integration Mesh: representation of ρ and distribution of Gauss Points (in blue).

With the voxel-type integration approach, volume integrals at each element will be evaluated as:

$$\int_{\Omega_e} f(x, y, z) d\Omega_e = \sum_i^{NS} \int_{\Omega_i} f(x, y, z) d\Omega_i \quad (13)$$

where $f(x, y, z)$ is the function to be integrated, Ω_e is the domain of the element, NS stands for the number of integration subdomains in each element and Ω_i is the i th integration subdomain. The integral in (13) is numerically evaluated as:

$$\int_{\Omega_e} f(x, y, z) d\Omega_e = \sum_i^{NS} \sum_j^{GP} f(\xi, \eta, \tau) |J_{\Omega_i \rightarrow \widetilde{\Omega}_i}| H_j \quad (14)$$

where the domains Ω_i and $\widetilde{\Omega}_i$ are shown in Figure 9 in a 2D view, GP stands for the number of Gauss Points used in each integration subdomain, $|J|$ is the Jacobian of the transformations of coordinates and H are the weights of each Gauss Point.

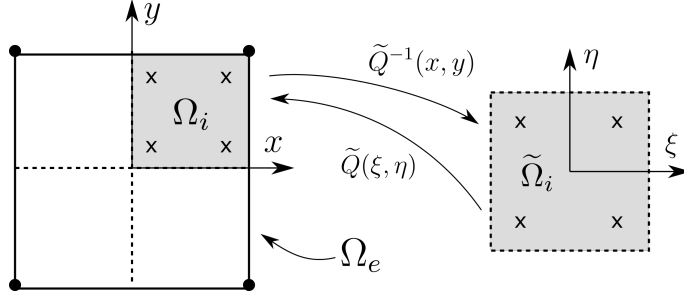


Figure 9: Voxel Integration Mesh. Spaces used for integration.

Note that in the proposed voxel-type integration approach, the design variables are not associated to the elements, instead, they are associated to the integration subdomains into the elements. Hence, the sensitivities of the compliance must be computed at the level of the integration subdomains (voxels) and the filter radius must be related also to the size of the integration subdomains. The structure of the SIMP method *Algorithm 1* considering the voxel-integration approach is stated in the *Algorithm 3*.

Algorithm 3: $\mathbb{T}\mathbb{O}_V(v_f)$. Compliance minimization algorithm with voxel-integration approach.

Define v_f

Initialize counter: $i = 0$

Initialize relative density at each element e : $\rho_{e_i} = v_f$

Subdivide the elements of analysis mesh into voxels v .

Repeat = 1

while *Repeat* = 1 **do**

 Run FE calculations on analysis mesh

 Project the results to the voxel mesh

 Obtain compliance, c_i , and sensitivities, $\partial c_i / \partial \rho_{v_i}$ at voxels

 Filter sensitivities at voxels

 Update relative density field: $\rho_{v_{i+1}} = f(\rho_{v_i}, \partial c_i / \partial \rho_{v_i})$ at voxels

if $\|\rho_{v_{i+1}} - \rho_{v_i}\| \leq \textit{tolerance}$ **then**

 | *Repeat* = 0

else

 | Project relative density field to analysis mesh

end

$i = i + 1$

end

We ran numerical analyses on the reference problem to test the performance of the proposed voxel-integration technique. In the analyses, to simplify the comparisons

with the optimal analytical solution, we used the SIMP method algorithm without considering iterations on the volume fraction, which was prescribed equal to the volume fraction of the optimal analytical solution, i.e. $V/V_0 = 0.2174$. Figure 10 and Table 2 compare three kinds of results: the reference results (Figure 10.a) shown in Section 4.1.1, the results obtained following the proposed voxel-type integration approach (Figure 10.b) and the reference results that would be obtained with one order finer mesh (Figure 10.c). The results show that whereas the total execution time of the voxel-type integration approach is barely higher than that of the reference solution, the boundary definition considerably improves, reaching the accuracy that would be obtained with finer meshes. Thus, the proposed technique allows us to obtain a boundary definition of a quality corresponding to a mesh of elements of size $h/2$ at a computational cost only slightly higher than that of a mesh of elements of size h . These results are also shown in Figure 11 where we compare the evolution of the density in the reference problem for these three cases with the exact analytical solution along an axis corresponding to a $\theta = \frac{\pi}{4}$ angle.

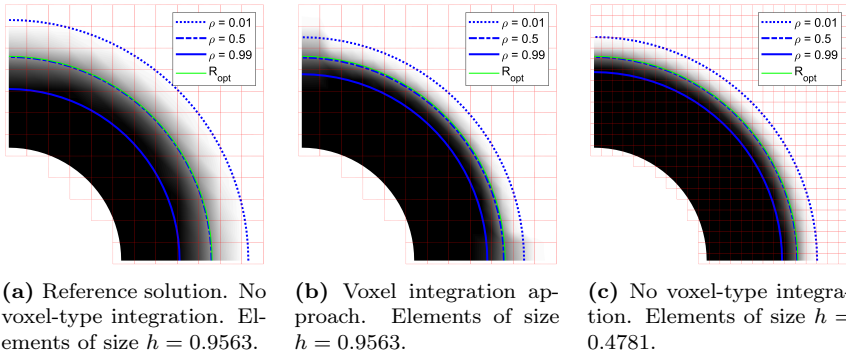


Figure 10: Effect of voxel-type integration.

	Coarse Mesh				Fine Mesh	
	No voxel-integration		Voxel-integration		No voxel-integration	
Threshold	\bar{R}_ρ	$e(R)$	\bar{R}_ρ	$e(R)$	\bar{R}_ρ	$e(R)$
$\rho = 0.01$	10.6583	17.8136%	9.8911	9.3332%	9.9026	9.4596%
$\rho = 0.5$	9.0221	-0.2731%	8.9931	-0.5936%	9.0211	-0.2840%
$\rho = 0.99$	7.5988	-16.0059%	8.2537	-8.7662%	8.3473	-7.7321%

Table 2: Results obtained for the Reference problem with a coarse mesh, a coarse mesh with the voxel-integration technique and a fine mesh.

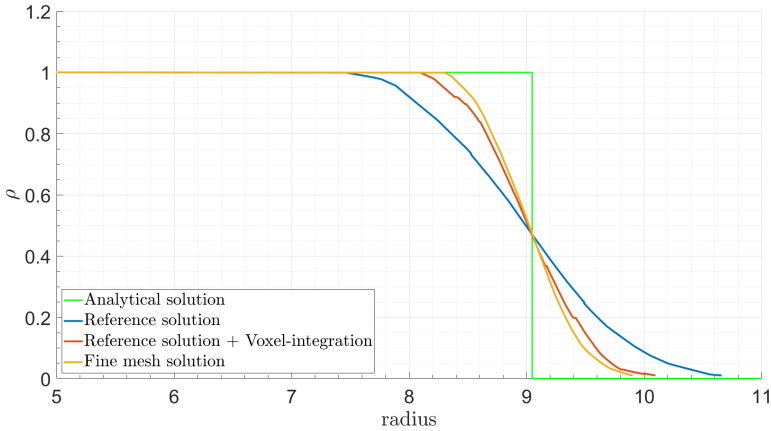


Figure 11: Reference Problem. Density evolution along radius for angle $\theta = \frac{\pi}{4}$ showing the effect for the voxel integration approach.

4.3. Adaptive mesh refinement

The accuracy of the edge definition depends on the size of the element used for the topology optimization process and the size of the filter used (i.e. smaller elements and/or smaller radius produce sharper geometries). However, the complexity of the topology obtained also depends on these two quantities (smaller elements and/or smaller radius will produce more complex geometries). We propose to use h -adapted meshing techniques (more efficient than uniform meshes) to decouple these two effects to be able to obtain sharp edge representation of controlled topological complexity of the solution together with the following two mesh refinement strategies to improve boundary sharpness and accuracy of the solution:

- a) Density-based refinement, where the mesh is refined in regions with intermediate values of relative density, and
- b) Error-based refinement, where the mesh is refined in regions where the estimated discretization error is higher.

In both cases the mesh is refined using element splitting (each parent Cartesian brick element of size h will be subdivided into 8 children Cartesian elements of size $h/2$). Multi-point constraints are used to enforce C^0 continuity of the displacement field between adjacent elements of different refinement levels [71].

4.3.1. Adaptive virtual filtering

Filtering techniques are commonly used in topology optimization to avoid checkerboard patterns. As mentioned in Section 4.1.1, the size of the region of intermediate densities is approximately equal to the double of the size of the filtering radius r_f . Taking this into account, we propose to use an adaptive filter size strategy where the filter radius at each element is proportional to the element size (being the proportionality constant defined by the analyst), thus allowing for different filter sizes in the same mesh. This strategy will be useful both, to limit the minimum size of the features that define the solution and to improve its boundary definition. This adaptive filter strategy is described by Algorithm 4:

Algorithm 4: $\mathbb{T}\mathbb{O}_{V,AFS}(v_f)$. Adaptive Filter Strategy

```

Define volume fraction  $v_f$ .
Create initial analysis mesh with elements of uniform size  $h = H_0$ .
Subdivide elements of analysis mesh into "voxels" of uniform size  $h^v = H_0^v$ .
Define initial filtering radius  $r_f^0$ .
Define filter size ratio  $C_r = \frac{r_f^0}{H_0^v}$ .
Initialize relative density at each element  $e$ :  $\rho_{e_i} = v_f$ .
Assign each voxel  $v$  the density of its parent element  $\rho_{e_i}$ .
Refine = 1
while Refine = 1 do
    Define filter radius  $r_f^v$  of each voxel  $v$  of size  $h^v$  as  $r_f^v = C_r h^v$ .
    Run Algorithm 3  $\mathbb{T}\mathbb{O}_V(v_f)$  using a relaxed stopping criterion.
    Find the set  $S_R$  of elements of the analysis mesh to be refined, as
    indicated by the density- and/or the error-based refinement strategies.
    if  $S_R \neq \emptyset$  then
        Split elements in  $S_R$ .
        Project  $\rho_e$  of original elements to their children elements.
        Discard children elements fully lying outside the design space.
        Subdivide resulting elements into voxels  $v$  and assign its density.
    else
        Refine = 0
    end
end

```

From now on, Algorithm 2 $\mathbb{T}\mathbb{O}_\sigma(S_y)$ will call Algorithm 4 $\mathbb{T}\mathbb{O}_{V,AFS}(v_f)$, as inner topology optimization algorithm, instead of Algorithm 1 $\mathbb{T}\mathbb{O}(v_f)$. Strict convergence criterion are not necessary in the proposed strategy because the general characteristics of the solution are already defined after the initial iterations of the SIMP method algorithm. Hence we use a relaxed stopping criterion to alleviate the computational burden. We propose, the computation of the relative variation of the objective func-

tion (the compliance in the SIMP method), evaluated as:

$$\frac{c_{i-1} - c_i}{c_{i-1}} \times 100 \leq SC \quad (15)$$

where c represents the compliance, i stands for the iteration number and SC is the stopping criteria value defined by the user, in our case we have selected $SC = 0.01\%$.

Figure 12 shows the results of different topology optimization strategies used to solve a cantilever beam clamped on the left hand-side of the domain with a distributed tangential load applied on the central part of the boundary located at the right hand-side of the domain and solved with a 2D implementation of the proposed methodology. These results will be used to explain how does the adaptive filter strategy work.

Figure 12a shows the result obtained with a coarse mesh of elements of uniform size $H_a = 1$ and a filter radius set to $r_a = 1.5H_a = 1.5$. The figure shows that the internal boundaries of the solution are diffusely defined and that the minimum thickness of the bars is about $3H_a = 2r_a$.

Figure 12b shows the result obtained with a finer mesh of elements of uniform size $H_b = 0.25H_a = 0.25$, and a filter radius $r_b = r_a = 1.5$. Because of the smaller element size, the density distribution is smoother; however, the internal boundaries of the solution are, again, not clearly defined and the minimum thickness of the bars is similar to that of the previous case.

Figure 12c shows the results considering the mesh size used in the previous case, i.e. $H_c = H_b = 0.25H_a = 0.25$. However, in this case, we used a filter radius $r_c = 1.5H_c = 0.375$. As shown, the thickness of the diffuse internal boundaries that define the solution is smaller than in the previous cases, but, the minimum thickness of its features is smaller than in the previous cases, thus leading to a more complex and difficult to manufacture design.

Figure 12d shows the result of the proposed strategy, in which three mesh refinement levels have been used with sizes $H_a = 1$, $H_b = 0.5H_a = 0.5$ and $H_c = 0.25H_a = 0.25$ and corresponding filter radii $r_a = 1.5H_a = 1.5$, $r_b = 0.5r_a = 0.75H_a = 0.75$ and $r_c = 0.25r_a = 1.5H_c = 0.375$. It can be observed that there is a better definition of the internal boundaries, because smaller filter radii are used along these regions as a consequence of using smaller elements. It can also be observed that the use of the biggest filter radius in the initial mesh has the effect of defining the overall features of the solution that will be kept during the process. Hence, with this strategy the filter radius considered in the coarsest mesh is used to limit the minimum size of the features that define the solution. This will help to control the overall complexity of the solution and to facilitate its manufacture. Then, the subsequent meshes are used to sharpen the definition of the boundaries that define the solution, thus limiting the mesh-dependency of the solution.

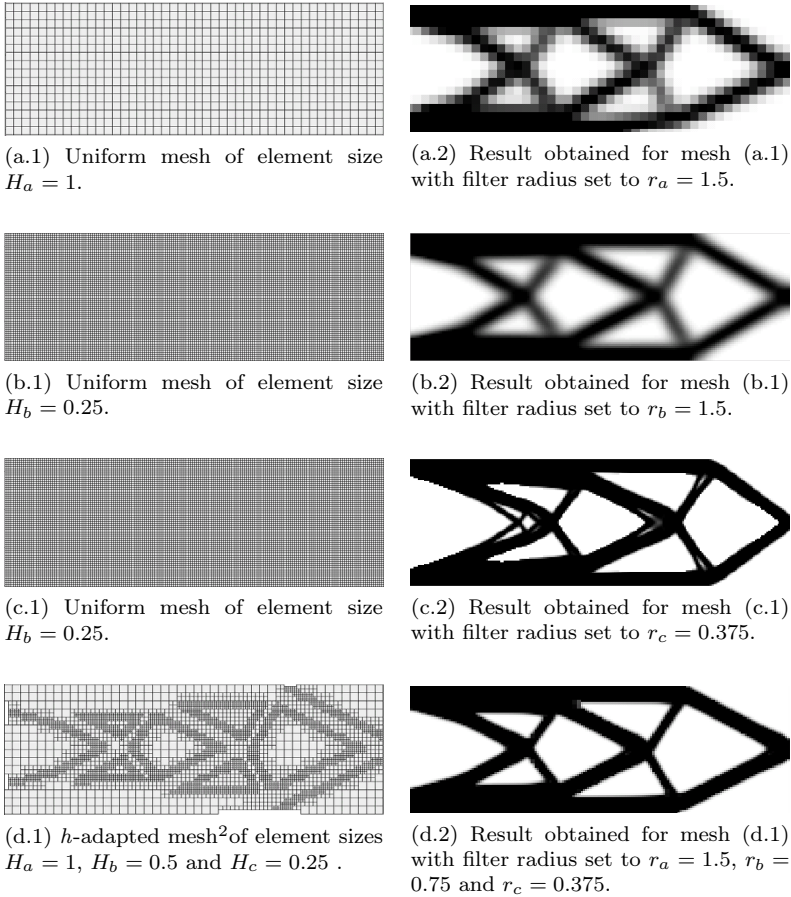


Figure 12: Filtering Technique. Optimal solution of the "Cantilever" problem considering different types of discretizations.

The use of the filtering techniques in an h -adapted mesh involves a considerable computational cost in standard FE implementations since the surrounding elements falling into the filtering radius must be localized at each iteration step. This is even accentuated when a set of voxels are considered into an element to increase the accuracy of the representation. The Cartesian structure of the $cgFEM$ meshes is useful to reduce this computational cost. We propose the use of a virtual filtering technique, described in *Algorithm 5*, based in the hierarchical structure of the Cartesian grid.

²Note that children elements fully outside the design space are removed from the mesh when their parent elements cut by the boundary are refined.

Algorithm 5: Virtual Filter Creation

```

Define initial filtering radius  $r_f^0$ .
Define mesh of elements of uniform size  $H_0$ .
Define filter size ratio  $C_r = r_f^0/H_0$ .
 $N_e$  =Number of elements
for  $e \leftarrow 1$  to  $N_e$  do
    Get size of element  $e$ :  $h_e$ 
    Compute filter radius for element  $e$ :  $r_f^e = h_e C_r$ 
    Use Cartesian structure to select  $K =$  set of elements whose center is
        within a cube of size  $2r_f^e$  centered in  $e$ .
    Subdivide the  $K$  elements into  $K_v$  voxels.
     $N_v$  =Number of voxels
    for  $v \leftarrow 1$  to  $N_v$  do
        Get filter size of  $v$ :  $r_f^v = h_v C_r$ 
        Assess distance between  $v$  and each voxel  $k_v$  in  $K_v$ 
    end
end
Assemble filter matrix  $H_f$ .

```

4.3.2. Density-based refinement

The first refinement criterion considered in this work consists in refining the elements whose relative density ρ takes intermediate values i.e. elements where $1 > \rho > \rho_{min}$.

Let us consider the well-known "MBB-Beam" problem to illustrate the procedure. To reduce computational cost only half of the beam has been modelled, considering the symmetry of the problem. Figure 13 shows the evolution of the process and a total of 3 refinement steps. For each of them, the figure represents the mesh used and the solution provided by the topology optimization algorithm, clearly showing how the solution evolves toward sharper representations of the edges.

Figure 14 shows the evolution of the compliance along the process. The graph shows that after the convergence criterion has been met for each mesh, the mesh refinement leads to further reduction of the compliance.

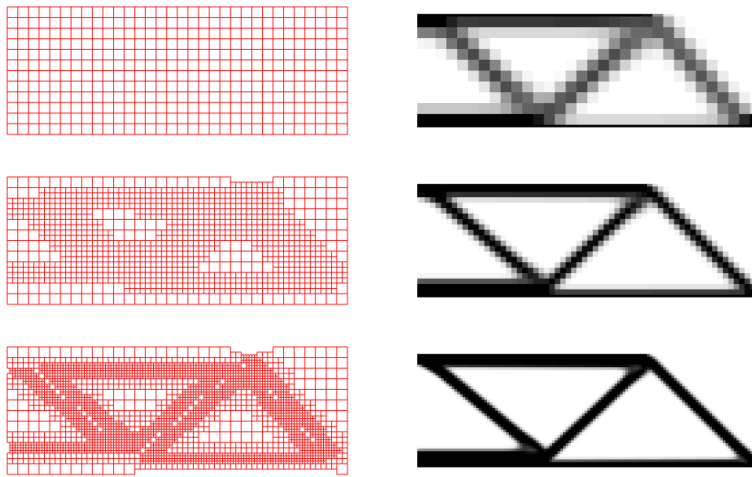


Figure 13: Detailed example of Density-based refinement.

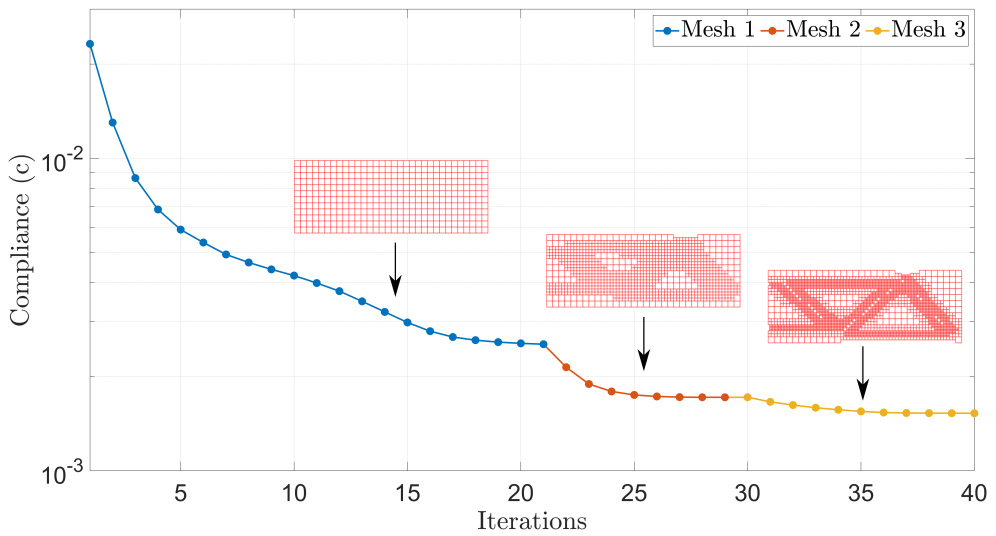


Figure 14: Density-based refinement. Evolution of the compliance along the density-based refinement process.

The effects of the proposed density-based refinement procedure were evaluated on the reference problem and shown in Figure 15. The figure compares the results provided by the SIMP method with a coarse mesh with the result obtained through the refinement process. As in the case of Figure 10, we did not consider iterations

on the volume fraction and prescribed its value to that of the optimal solution, i.e. $V/V_0 = 0.2174$. The figure shows how the thickness of the diffuse region that defines the edge of the solution decreases, leading to a more accurate representation of the boundary. Table 3 numerically compares the solutions obtained with the analytical solution. A graphical representation of this information is also shown in Figure 16.

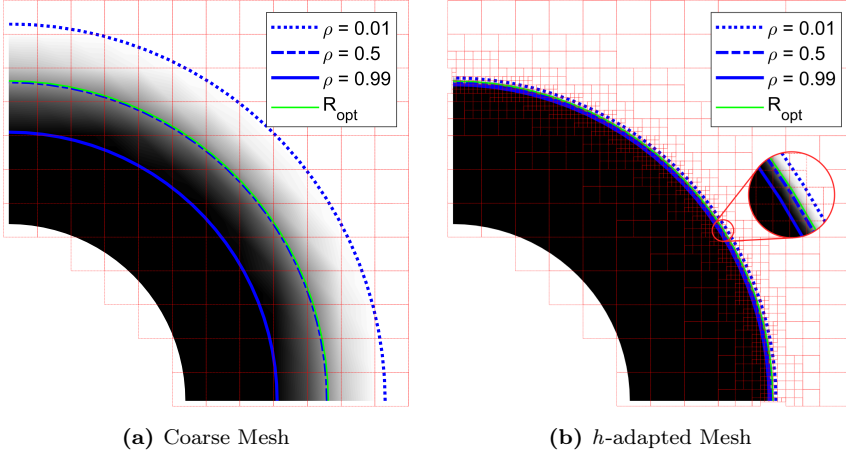


Figure 15: Density based refinement. Comparison of the material distribution obtained with a) a coarse mesh and b) an h -adapted mesh.

Threshold	Coarse Mesh		h -adapted Mesh	
	\bar{R}_ρ	$e(R)$	\bar{R}_ρ	$e(R)$
$\rho = 0.01$	10.6583	17.8136%	9.1336	0.9601%
$\rho = 0.5$	9.0221	-0.2731%	9.0273	-0.2149%
$\rho = 0.99$	7.5988	-16.0059%	8.9410	-1.1697%

Table 3: Reference Problem: Effect of density-based refinement. Comparison with reference solution.

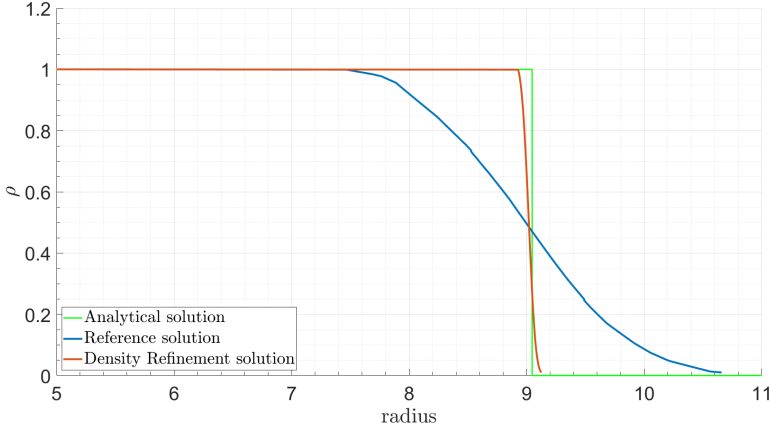


Figure 16: Reference Problem. Density evolution along radius $\theta = \frac{\pi}{4}$, comparing the reference solution with the solution obtained with density-based refinement. Volume fraction v_f set to optimal value.

4.3.3. Error-based refinement

The second refinement criterion considered in this work is to h -adapt the mesh as a function of the accuracy of the numerical solution, evaluated in terms of the estimation of the discretization error in energy norm. Increasing the accuracy of the FE results is specially relevant for the volume minimization problems with stress constrains since non accurate stress evaluations would lead to non-optimal solutions. However, the use of error estimation techniques to improve the behaviour of topology optimization algorithms is scarce. In previous publications where the accuracy of the solution was considered as a mesh refinement criterion in topology optimization, the authors used residual-based error estimators [30]. In our case, we propose to estimate the discretization error in energy norm following the idea proposed by Zienkiewicz and Zhu [3], who estimated the error in energy norm using the following equation:

$$\|\mathbf{e}^*\| = \sqrt{\int_{\Omega} (\boldsymbol{\sigma}^* - \boldsymbol{\sigma}^h) \mathbf{D}^{-1} (\boldsymbol{\sigma}^* - \boldsymbol{\sigma}^h) d\Omega} \quad (16)$$

where Ω is the domain of integration, that can be restricted to the domain Ω_e of a single element to obtain the estimate at the element level. The accuracy of (16) depends on the accuracy of the $\boldsymbol{\sigma}^*$ field. We propose the use of the following expression, consistent with (2a), to evaluate an error indicator ζ_e of the discretization error at element level for this kind of problems:

$$\zeta_e = \sqrt{\int_{\Omega_e} \rho_e^p (\boldsymbol{\sigma}_e^* - \boldsymbol{\sigma}_e^{h_0}) \mathbf{D}_0^{-1} (\boldsymbol{\sigma}_e^* - \boldsymbol{\sigma}_e^{h_0}) d\Omega_e} \quad (17)$$

In Reference [30] the authors indicated that recovery-based error estimators are not effective along material interfaces. Therefore, the authors of this reference advised against the use of recovery-based error estimation in topology optimization because it would produce unnecessary overrefinement along the material/no-material interface. However, we are not considering a binary representation of the material but its regularized representation through the relative density ρ . In fact, in (17), elements with intermediate ρ values usually result in low ζ_e values because of the penalization induced by the term ρ_e^p . Hence, the mesh optimality criterion used for mesh refinement will tend not to refine these elements, concentrating the mesh refinement mainly in fully dense elements ($\rho = 1$) with high stress gradients.

As the error-based refinement will not produce refinement in elements with intermediate values of ρ , it will not help to improve the boundary representation. Therefore we propose the combined use of the error-based refinement and the density-based refinement, each of them having a different role: while the objective of the error-based refinement will be to increase the accuracy of the FE results, the objective of the density-based refinement will be to improve the boundary representation.

4.3.4. Numerical performance

We ran the volume optimization with stress constraints on the reference problem to test the effect of the different refinement criteria. The results are shown in Figure 17. This figure compares the optimal analytical solution with the results obtained through the use of the improvements proposed in this paper. The reference result, obtained with elements of uniform size and none of the proposed improvements, is shown in Figure 17a (already shown if Figure 5b). As previously indicated, the most relevant characteristic of this solution is the diffuse representation of the external surface of the solution. Considering the isocontour $\rho = 0.5$ since, in this case, the control on the solution quality (error estimation) is not activated, the maximum stress value is underestimated, yielding to wrong reduction of the amount of material needed.

Figure 17b shows that the use of the proposed Voxel Integration approach in the elements fully located into the domain, that only represents a small increment of the computational cost, reduces the thickness of the diffuse representation of the external boundary; hence, this technique has been used in the remaining cases. Figure 17b and 17c also shows that by using the voxel integration and density-based refinement, even if the accuracy of the boundary is increased, the material quantity remains underestimated considering the isocontour $\rho = 0.5$.

Figure 17d shows the result of considering the error based refinement prescribing a 5% error level, that reduces the element size in the region of the internal radius increasing the accuracy of the maximum von Misses FE stress that drives the optimization loop with stress constrains. As a consequence of this, the amount of material

used increases, getting closer to the analytical solution.

Finally Figure 17e displays the result obtained when considering the proposed Voxel Integration approach together with the proposed density-based and error-based refinement strategies. This result shows that the synergistic effect of these techniques leads to a sharp definition of the external boundary with a radius close to the optimal analytical value.

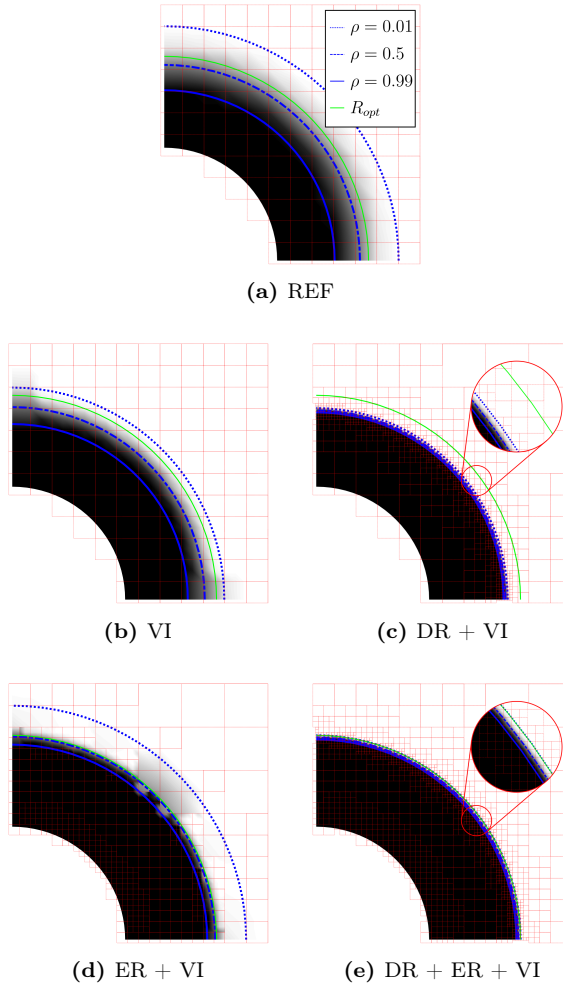


Figure 17: Reference Problem: Effect of the proposed improvement strategies on the final result of the topology optimization process. The acronyms stand for: Reference solution (REF), Voxel-type Integration (VI), Density-based Refinement (DR), and Error-based Refinement (ER).

Figure 18 compares the density distribution along an angle $\theta = \frac{\pi}{4}$ obtained using the proposed techniques with the analytical solution while Figure 19 compares the von Mises stress. As observed, when error-based refinement is used a more accurate von Mises stress distribution is obtained, that leads to better representation of the external radius. Obviously, the underestimations / overestimations of the optimal external radius will lead to maximum von Mises stresses over / below S_y , represented in Figure 20. These figures show that although the use of the voxel-type integration reduces the size of the region with intermediate values of ρ , the most significant improvement on the sharp definition of the boundary is obtained through the use of the density-based mesh refinement. This improvement on the sharp definition of the boundary does not necessarily come together with the accurate placement of the boundary, that requires the use of the error-based refinement.

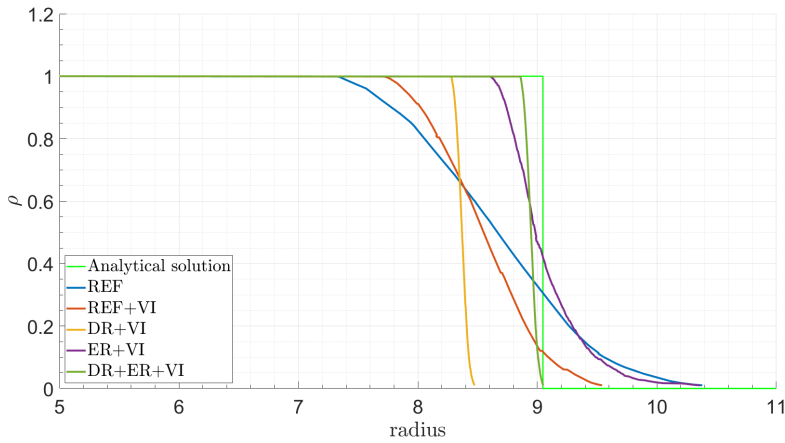


Figure 18: Reference Problem: Effect of the proposed improvement strategies on the radius. Acronyms stand for: Reference solution (REF), Voxel-type Integration (VI), Density-based Refinement (DR), and Error-based Refinement (ER).

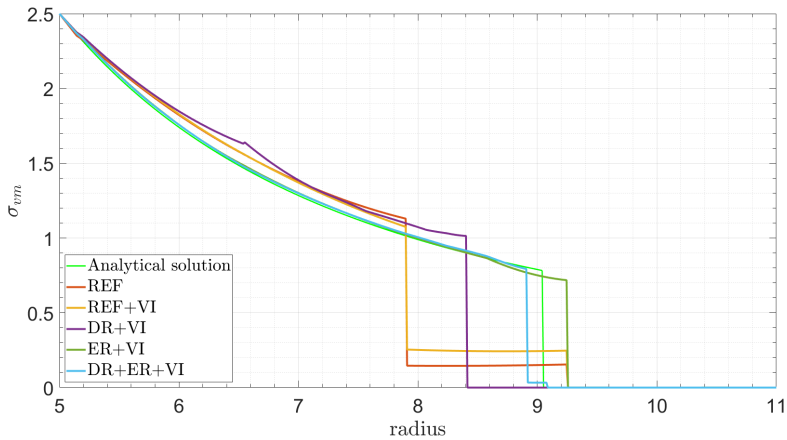


Figure 19: Reference Problem: Effect of the proposed improvement strategies on the von Mises stress value along a $\theta = \pi/4$ angle. Acronyms stand for: Reference solution (REF), Voxel-type Integration (VI), Density-based Refinement (DR), and Error-based Refinement (ER).

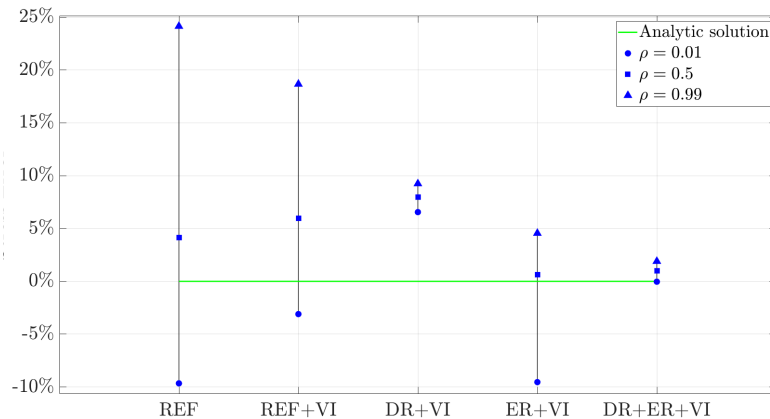
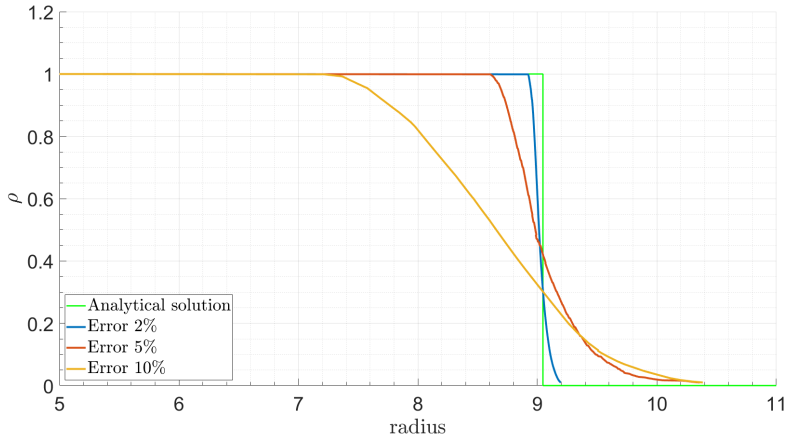


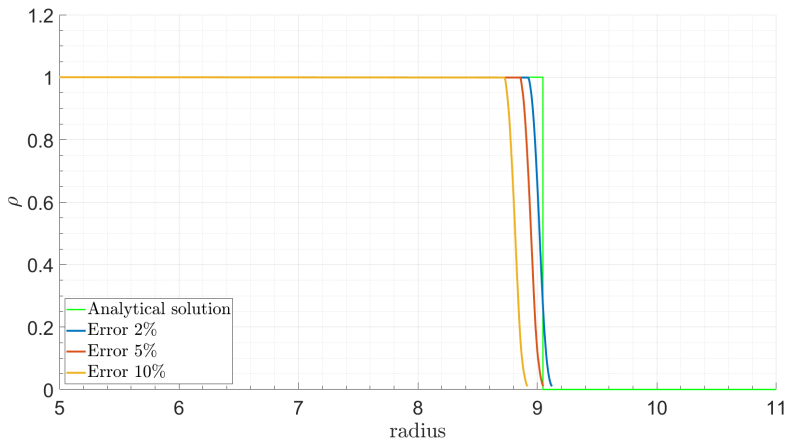
Figure 20: Reference Problem: Effect of the proposed improvement strategies on the maximum von Mises stress value. Reference solution (REF), Voxel-type Integration (VI), Density-based Refinement (DR), and Error-based Refinement (ER).

In order to analyse the influence of the prescribed error level, we run the topology optimization process with 3 different values (10%, 5% and 2%) of the prescribed relative value of the indicator of the relative discretization error in energy norm.

Figure 21 shows how the value of the external radius is affected by the prescribed error of the FE analyses in two different cases, when the error-based refinement is considered (Figure 21.a) and when the density-based refinement is also considered (Figure 21.b). The graphs shows that the results converge to the optimal analytical solution when the accuracy of the FE analyses is increased, showing also the need of using the density-based refinement to obtain a sharper boundary representation.



(a) Effect of error-based refinement



(b) Effect of error + density based refinement.

Figure 21: Reference Problem: Effect of prescribed error in energy norm on the external radius of the solution.

5. Numerical examples

We used the academic problem in the Section 4 to show the performance of the proposed techniques. In this Section we have applied these techniques on a more complex examples.

5.1. Hook

The first example corresponds to a hook as displayed in Figure 22. The vertical displacements of the top surface are constrained. Rigid body motion is avoided using appropriate constraints on this surface. A pressure $P=1$ is imposed in the inner cylindrical surface. The material properties considered in this problem are: Young's Modulus $E = 1000$, Poisson ratio $\nu = 0.3$ and yield limit $S_y = 2$. We used *Algorithm 2* $\mathbb{T}\mathbb{O}_\sigma(S_y)$ to minimize the mass of the hook satisfying $\hat{\sigma}_{vm} \leq S_y$, considering the voxel-integration approach, the density-based refinement strategy and the error-based refinement strategy.

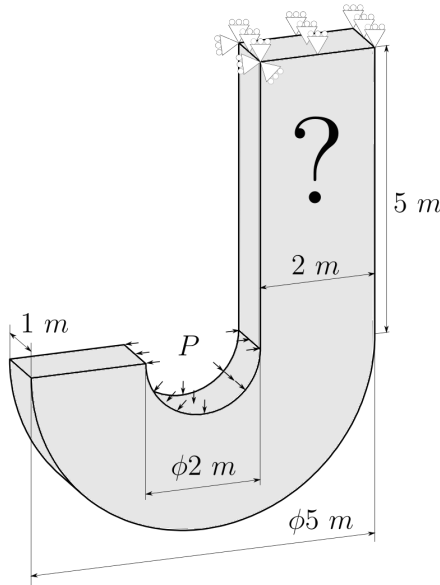


Figure 22: Design domain of the hook problem with dimensions and boundary conditions.

The analysis has been carried out considering a initial mesh with elements of uniform size $H_1 = 0.2550$ and a filter radius set to $r_1 = 1.5H_1 = 0.3825$. In the h-

adaptive analyses we used up to 2 further mesh refinement levels obtained by element splitting, leading to elements of size $H_2 = 0.5H_1 = 0.1275$ and $H_3 = 0.25H_1 = 0.0637$. As the adaptive filtering technique (Section 4.3.1) is considered, the filter sizes for these element sizes are: $r_2 = 0.5r_1 = 0.1913$ and $r_3 = 0.25r_1 = 0.0956$. The refinement criterion considers both, the density-based and the error-based strategies. The prescribed estimated error in energy nor of the FE solution was set to 7.5%. The topology of the solution obtained, together with the h -adapted mesh used is shown in Figure 23.

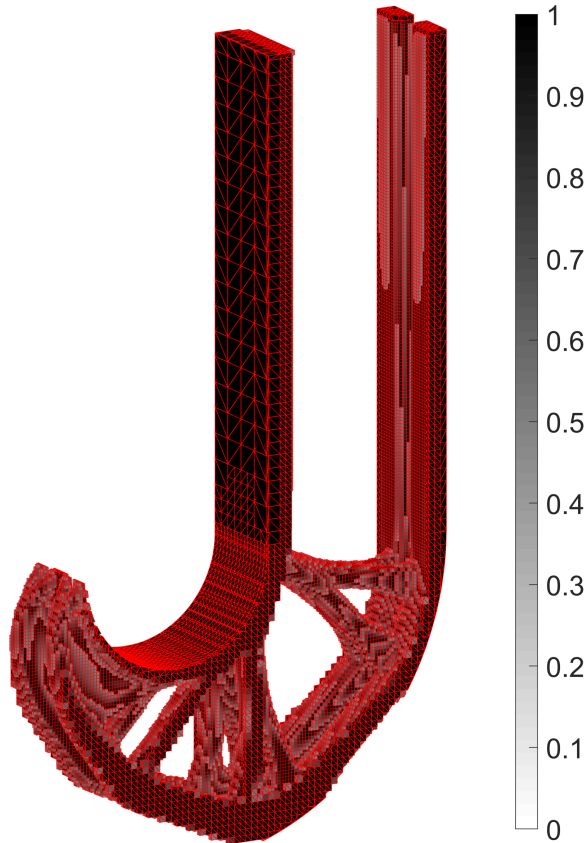
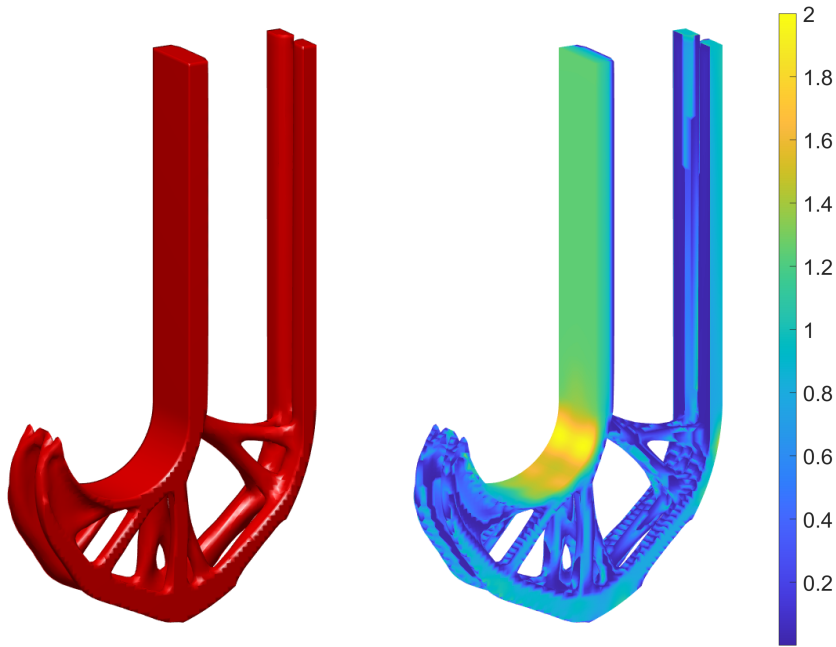


Figure 23: Hook problem: Results obtained with the refinement techniques proposed in this paper (the elements whose density is $\rho < 0.5$ are not shown).

A pictorial representation of this solution together with the Von Mises stress distribution is shown in Figure 24.



(a) Representation of the optimal solution.

(b) Penalized recovered Von Mises stresses.

Figure 24: Hook problem: Results obtained with the strategies proposed in this work.

In order to analyze the quality of the solution obtained with the techniques proposed in this paper, we solved the same problem with a fixed size coarse. The result, including the von Mises stress distribution, is shown on Figure 25a, where the only elements represented are those with $\rho \geq 0.5$. Figure 25a shows that the stress constraint is satisfied. However, if we refine the mesh around the inner cylindrical surface, project the material distribution obtained with the coarse mesh on this new mesh and run the FE analysis we will obtain a different stress distribution. This new stress distribution, obtained with a mesh finer than in the previous case and, thus, more accurate, is shown in Figure 25b. This figure shows von Mises stresses undoubtedly above the maximum allowable limit on the inner cylindrical surface stress (grey color is used for $\sigma_{vm} > S_y$), clearly showing the need to use the error-based refinement strategy. Figure 25, where the only elements represented are those with $\rho \geq 0.5$, also clearly shows the staircase (jagged boundary) effect produced by the coarse elements, much more noticeable than in the case of Figure 23, that shows a better boundary definition, clearly showing the need to use the density refinement strategy.

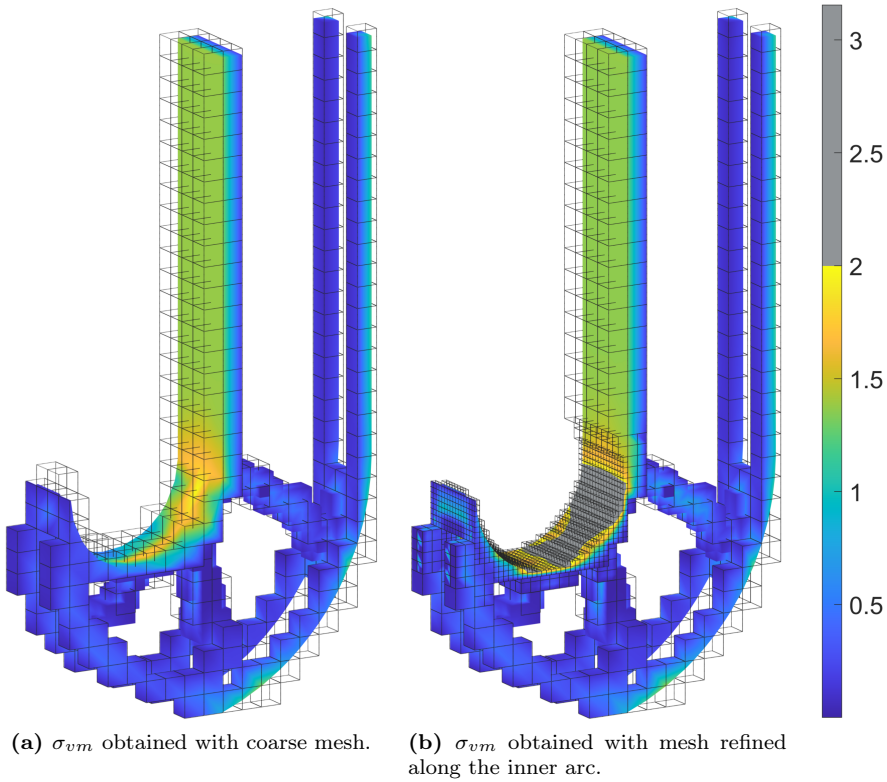


Figure 25: Hook problem: Results obtained with coarse mesh (the elements whose density is $\rho < 0.5$ have not been represented), the mesh is shown as well.

5.2. Dental implant

As indicated in the introduction, *cgFEM* can be used to run patient-specific simulations considering bone-implant frictional contact conditions. A detailed description of the methodologies involved, out of the scope of this paper, can be found in [37–39, 46, 72]. Hence, in this example, we used this simulation techniques to test the behaviour of the methodologies proposed in this paper in implant optimization. In particular, this second numerical example corresponds to a dental implant in a mandible, as show in Figure 26. In this example, we considered Dirichlet constraints applied on the bone and a constant pressure ($P = 2$) on the upper surface of the implant. Finally, a bone-implant contact interaction was defined. The Young’s Modulus of the prosthesis is $E = 1000$, with a Poisson ratio $\nu = 0.3$. The elastic properties of the image are based on its Hounsfield scale as described in [73]. In this case, we use the *Algorithm 1* to minimize the compliance subject to a volume constrain, in this

case $v_f = 0.5$. The analysis was addressed considering a initial mesh with uniform size $H_1 =$ and a filter radius set to $r_1 = 1.75H_1$. We consider one further mesh refinement with the parameters of element size as $H_2 = 0.5H_1 =$ and a filter of $r_2 = 0.5r_1 =$. The mesh refinement strategy selected in this analysis is based on the density information. Furthermore, a subdivision in the analysis mesh is considered to conform the voxel integration mesh, and improve the geometry resolution. This information is all referred to the mesh of the prosthesis. Regarding the mesh of the medical image, we consider a initial refinement based on the Hounsfield scale, to properly represent the elastic properties assigned to each element.

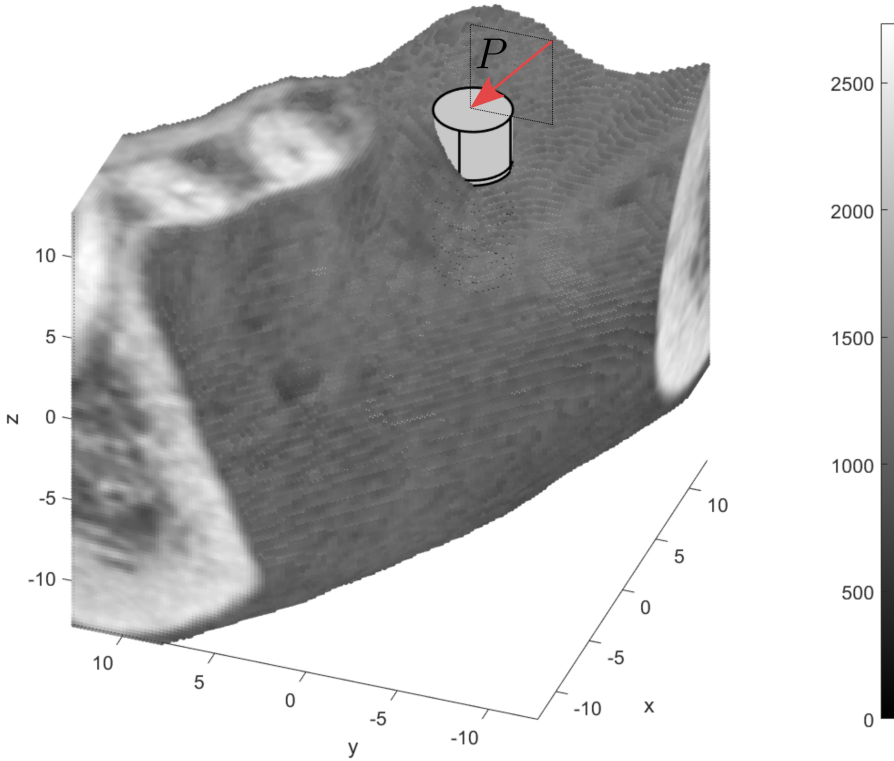
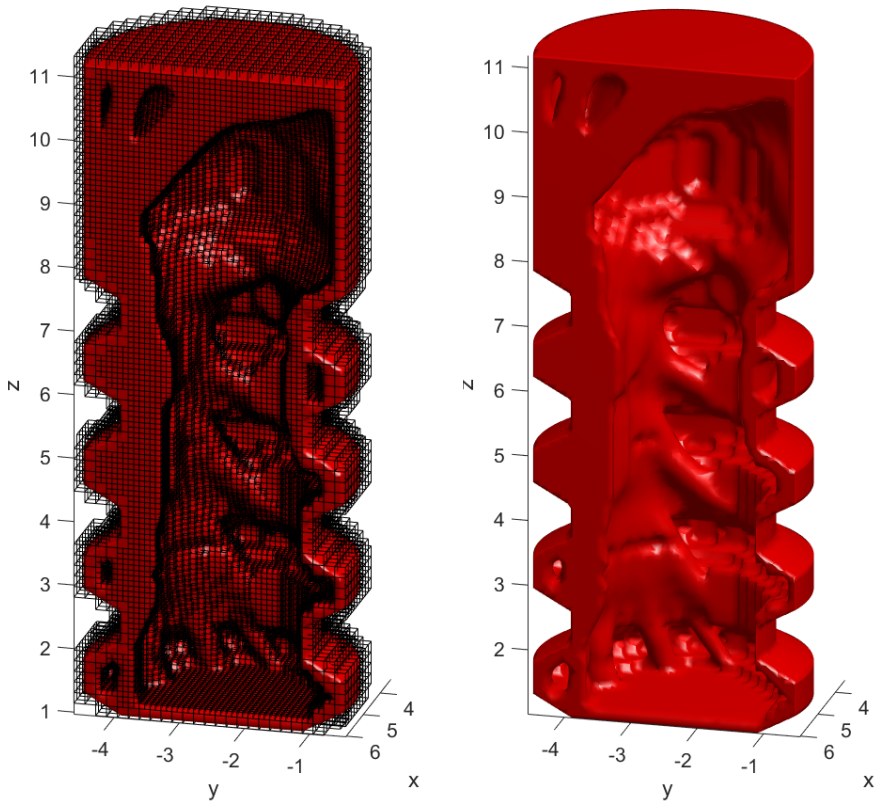


Figure 26: Portion of mandible with prosthesis. The colorbar represents the value in the Hounsfield scale for the mandible.

The results obtained, considering a fully dense layer of elements on the implant surface are show in Figure 27.



(a) Topology optimization result and mesh. (b) Representation of the topology optimization result.

Figure 27: Dental implant optimization (section).

6. Conclusions

We would like to conclude with the most relevant conclusions of this paper:

- *cgFEM* represents an appropriate framework for topology optimization as it allows to consider any arbitrary domain taking advantage of the computational efficiency provided by the Cartesian mesh structure and the hierarchical data structure.
- The voxel-type integration technique is an efficient method to achieve sharper geometries without increasing the computational cost of the FE calculations .

- The use of the adaptive filter allows to create optimal material distributions with geometric complexity control, where the size of the geometrical details is essentially defined by the size of the filter radius specified for the elements of the coarsest mesh, but allowing for a sharp definition of the boundary of the final solution. This is a relevant property that allow us to tune the topology optimization process as a function of the resolution of the fabrication process to be used. This achievement is highly related to the manufacturing point of view, where the simplicity of a given component is translated in a reduction of the final cost, in raw material and manufacturing processes.
- The mesh refinement procedure has impact on two aspects of the obtained optimal geometry. In the first place, the density-based refinement allows us to obtain geometrical definitions of the boundaries. In the second place, the error-based refinement provides solutions with discretization error control, through the accuracy for the FE analyses prescribed by the analyst. This implies a more accurate evaluation of the constraints evaluated by means of the FEM, as required to appropriately drive the TO process. Hence, by coupling this two approaches, the optimal material distribution obtained is more accurate and alike to the real manufacturing component.

Acknowledgements

The authors gratefully acknowledge the financial support of Conselleria d'Educació, Investigació, Cultura i Esport (Generalitat Valenciana, project Prometeo/2016/007), Ministerio de Economía, Industria y Competitividad (project DPI2017-89816-R) and Ministerio de Educación (FPU16/07121).

References

- [1] M. P. Bendsøe, "Optimal shape design as a material distribution problem," *Structural Optimization*, vol. 1, pp. 193–202, dec 1989.
- [2] E. Nadal, J. J. Ródenas, J. Albelda, M. Tur, J. E. Tarancón, and F. J. Fuenmayor, "Efficient Finite Element Methodology based on Cartesian grids: Application to structural shape optimization," *Abstract and Applied Analysis*, vol. 2013, pp. 1–19, apr 2013.

-
- [3] O. C. Zienkiewicz and J. Z. Zhu, "Adaptivity and mesh generation," *International Journal for Numerical Methods in Engineering*, vol. 32, pp. 783–810, sep 1991.
- [4] J. Sokolowski and J. P. Zolésio, "Introduction to Shape Optimization: Shape Sensitivity Analysis," vol. 16, p. 250, 1992.
- [5] A. A. Novotny and J. Sokołowski, "Topological derivatives in shape optimization," *Interaction of Mechanics and Mathematics*, pp. 1–427, 2013.
- [6] M. P. Bendsøe and O. Sigmund, *Topology optimization: theory, methods, and applications*, vol. 2nd Editio. 2003.
- [7] M. P. Bendsøe and N. Kikuchi, "Generating optimal topologies in structural design using a homogenization method," *Computer Methods in Applied Mechanics and Engineering*, vol. 71, pp. 197–224, nov 1988.
- [8] M. Zhou and G. I. Rozvany, "The COC algorithm, Part II: Topological, geometrical and generalized shape optimization," *Computer Methods in Applied Mechanics and Engineering*, vol. 89, pp. 309–336, aug 1991.
- [9] H. P. Mlejnek, "Some aspects of the genesis of structures," *Structural Optimization*, vol. 5, pp. 64–69, mar 1992.
- [10] Y. M. Xie and G. P. Steven, "A simple evolutionary procedure for structural optimization," *Computers and Structures*, vol. 49, pp. 885–896, dec 1993.
- [11] P. Tanskanen, "The evolutionary structural optimization method: Theoretical aspects," *Computer Methods in Applied Mechanics and Engineering*, vol. 191, pp. 5485–5498, nov 2002.
- [12] D. J. Munk, G. A. Vio, and G. P. Steven, "Topology and shape optimization methods using evolutionary algorithms: a review," *Structural and Multidisciplinary Optimization*, vol. 52, pp. 613–631, sep 2015.
- [13] P. A. Vikhar, "Evolutionary algorithms: A critical review and its future prospects," in *2016 International Conference on Global Trends in Signal Processing, Information Computing and Communication (ICGTSPICC)*, pp. 261–265, IEEE, dec 2016.
- [14] M. Y. Wang, X. Wang, and D. Guo, "A level set method for structural topology optimization," *Computer Methods in Applied Mechanics and Engineering*, vol. 192, pp. 227–246, jan 2003.
- [15] M. Y. Wang and X. Wang, "Color" level sets: A multi-phase method for structural topology optimization with multiple materials," *Computer Methods in Applied Mechanics and Engineering*, vol. 193, pp. 469–496, feb 2004.
- [16] G. Allaire, F. De Gournay, F. Jouve, and A.-M. Toader, "Structural optimization using topological and shape sensitivity via a level set method," tech. rep., 2005.

- [17] S. Amstutz and H. Andrä, “A new algorithm for topology optimization using a level-set method,” *Journal of Computational Physics*, vol. 216, pp. 573–588, aug 2006.
- [18] T. Yamada, K. Izui, S. Nishiwaki, and A. Takezawa, “A topology optimization method based on the level set method incorporating a fictitious interface energy,” *Computer Methods in Applied Mechanics and Engineering*, vol. 199, pp. 2876–2891, nov 2010.
- [19] L. Dedè, M. J. Borden, and T. J. Hughes, “Isogeometric Analysis for Topology Optimization with a Phase Field Model,” *Archives of Computational Methods in Engineering*, vol. 19, pp. 427–465, sep 2012.
- [20] G. Yi and N. H. Kim, “Identifying boundaries of topology optimization results using basic parametric features,” *Structural and Multidisciplinary Optimization*, vol. 55, pp. 1641–1654, may 2017.
- [21] F. Wang, B. S. Lazarov, and O. Sigmund, “On projection methods, convergence and robust formulations in topology optimization,” *Structural and Multidisciplinary Optimization*, vol. 43, pp. 767–784, jun 2011.
- [22] S. Wang, E. de Sturler, and G. H. Paulino, “Dynamic Adaptive Mesh Refinement for Topology Optimization,” 2010.
- [23] J. J. Ródenas, G. Bugada, J. Albelda, and E. Oñate, “On the need for the use of error-controlled finite element analyses in structural shape optimization processes,” *International Journal for Numerical Methods in Engineering*, vol. 87, pp. 1105–1126, sep 2011.
- [24] P. Ladeveze and D. Leguillon, “Error Estimate Procedure in the Finite Element Method and Applications,” *SIAM Journal on Numerical Analysis*, vol. 20, no. 3, pp. 485–509, 1983.
- [25] P. Díez, J. J. Ródenas, and O. C. Zienkiewicz, “Equilibrated patch recovery error estimates: Simple and accurate upper bounds of the error,” *International Journal for Numerical Methods in Engineering*, vol. 69, pp. 2075–2098, mar 2007.
- [26] O. A. González-Estrada, E. Nadal, J. J. Ródenas, P. Kerfriden, S. P. Bordas, and F. J. Fuenmayor, “Mesh adaptivity driven by goal-oriented locally equilibrated superconvergent patch recovery,” *Computational Mechanics*, vol. 53, pp. 957–976, may 2014.
- [27] T. Gerasimov, E. Stein, and P. Wriggers, “Constant-free explicit error estimator with sharp upper error bound property for adaptive FE analysis in elasticity and fracture,” *International Journal for Numerical Methods in Engineering*, vol. 101, pp. 79–126, jan 2015.

-
- [28] J. J. Ródenas, J. Albelda, M. Tur, and F. Fuenmayor, “A hierarchical h adaptivity methodology based on element subdivision,” *Revista UIS Ingenierías*, vol. 16, pp. 263–280, sep 2017.
- [29] F. J. Fuenmayor and J. L. Oliver, “Criteria to achieve nearly optimal meshes in the h-adaptive finite element method,” *International Journal for Numerical Methods in Engineering*, vol. 39, pp. 4039–4061, dec 1996.
- [30] M. A. Salazar de Troya and D. A. Tortorelli, “Adaptive mesh refinement in stress-constrained topology optimization,” *Structural and Multidisciplinary Optimization*, vol. 58, pp. 2369–2386, dec 2018.
- [31] J. Parvizian, A. Düster, and E. Rank, “Finite cell method : hh- and p-extension for embedded domain problems in solid mechanics,” *Computational Mechanics*, vol. 41, pp. 121–133, sep 2007.
- [32] A. Düster, J. Parvizian, Z. Yang, and E. Rank, “The finite cell method for three-dimensional problems of solid mechanics,” *Computer Methods in Applied Mechanics and Engineering*, vol. 197, pp. 3768–3782, aug 2008.
- [33] J. Parvizian, A. Düster, and E. Rank, “Topology optimization using the finite cell method,” *Optimization and Engineering*, vol. 13, pp. 57–78, mar 2012.
- [34] E. Burman, S. Claus, P. Hansbo, M. G. Larson, and A. Massing, “CutFEM: Discretizing geometry and partial differential equations,” *International Journal for Numerical Methods in Engineering*, vol. 104, pp. 472–501, nov 2015.
- [35] E. Nadal, “Cartesian grid FEM (cgFEM): High performance h-adaptive FE analysis with efficient error control. Application to structural shape optimization,” p. 312, 2014.
- [36] L. Giovannelli, J. J. Ródenas, J. M. Navarro-Jiménez, and M. Tur, “Direct medical image-based Finite Element modelling for patient-specific simulation of future implants,” *Finite Elements in Analysis and Design*, vol. 136, pp. 37–57, nov 2017.
- [37] J. M. Navarro-Jiménez, M. Tur, J. Albelda, and J. J. Ródenas, “Large deformation frictional contact analysis with immersed boundary method,” *Computational Mechanics*, vol. 62, pp. 853–870, oct 2018.
- [38] J. M. Navarro Jiménez, *Contact problem modelling using the Cartesian grid Finite Element Method*. PhD thesis, Universitat Politècnica de València, Valencia (Spain), jun 2019.
- [39] L. Giovannelli, *Direct creation of patient-specific Finite Element models from medical images and preoperative prosthetic implant simulation using h-adaptive Cartesian grids*. PhD thesis, Universitat Politècnica de València, Valencia (Spain), nov 2018.

- [40] D. Schillinger and M. Ruess, “The Finite Cell Method: A Review in the Context of Higher-Order Structural Analysis of CAD and Image-Based Geometric Models,” *Archives of Computational Methods in Engineering*, vol. 22, pp. 391–455, jul 2015.
- [41] E. Burman, “La pénalisation fantôme,” *Comptes Rendus Mathématique*, vol. 348, pp. 1217–1220, nov 2010.
- [42] M. Tur, J. Albelda, O. Marco, and J. J. Ródenas, “Stabilized method of imposing Dirichlet boundary conditions using a recovered stress field,” *Computer Methods in Applied Mechanics and Engineering*, vol. 296, pp. 352–375, nov 2015.
- [43] M. Dauge, A. Düster, and E. Rank, “Theoretical and Numerical Investigation of the Finite Cell Method,” *Journal of Scientific Computing*, vol. 65, pp. 1039–1064, mar 2015.
- [44] C. V. Verhoosel, G. J. van Zwieten, B. van Rietbergen, and R. de Borst, “Image-based goal-oriented adaptive isogeometric analysis with application to the micro-mechanical modeling of trabecular bone,” *Computer Methods in Applied Mechanics and Engineering*, vol. 284, pp. 138–164, feb 2015.
- [45] D. Elfverson, M. G. Larson, and K. Larsson, “CutIGA with basis function removal,” *Advanced Modeling and Simulation in Engineering Sciences*, vol. 5, dec 2018.
- [46] J. M. Navarro-Jiménez, H. Navarro-García, M. Tur, and J. J. Ródenas, “Super-convergent patch recovery with constraints for three-dimensional contact problems within the Cartesian grid Finite Element Method,” *International Journal for Numerical Methods in Engineering*, p. nme.6266, nov 2019.
- [47] D. P. Bertsekas, *Constrained Optimization and Lagrange Multiplier Methods*. 1982.
- [48] E. Burman and P. Hansbo, “Fictitious domain finite element methods using cut elements: II. A stabilized Nitsche method,” in *Applied Numerical Mathematics*, vol. 62, pp. 328–341, apr 2012.
- [49] O. Marco, R. Sevilla, Y. Zhang, J. J. Ródenas, and M. Tur, “Exact 3D boundary representation in finite element analysis based on Cartesian grids independent of the geometry,” *International Journal for Numerical Methods in Engineering*, vol. 103, pp. 445–468, aug 2015.
- [50] R. Sevilla, S. Fernández-Méndez, and A. Huerta, “NURBS-enhanced finite element method (NEFEM),” *International Journal for Numerical Methods in Engineering*, vol. 76, pp. 56–83, oct 2008.

-
- [51] M. Tur, J. Albelda, E. Nadal, and J. J. Ródenas, “Imposing Dirichlet boundary conditions in hierarchical Cartesian meshes by means of stabilized Lagrange multipliers,” *International Journal for Numerical Methods in Engineering*, vol. 98, pp. 399–417, may 2014.
- [52] A. Ferrer, “SIMP-ALL : a generalized SIMP method based on the topological derivative concept,” *International Journal for Numerical Methods in Engineering*, p. nme.6140, jul 2019.
- [53] O. Sigmund, “A 99 line topology optimization code written in matlab,” *Structural and Multidisciplinary Optimization*, vol. 21, pp. 120–127, apr 2001.
- [54] M. P. Bendsøe and O. Sigmund, “Material interpolation schemes in topology optimization,” *Archive of Applied Mechanics*, vol. 69, no. 9-10, pp. 635–654, 1999.
- [55] O. Sigmund and J. Petersson, “Numerical instabilities in topology optimization: A survey on procedures dealing with checkerboards, mesh-dependencies and local minima,” *Structural Optimization*, vol. 16, pp. 68–75, aug 1998.
- [56] B. Bourdin, “Filters in topology optimization,” *International Journal for Numerical Methods in Engineering*, vol. 50, no. 9, pp. 2143–2158, 2001.
- [57] B. S. Lazarov and O. Sigmund, “Filters in topology optimization based on Helmholtz-type differential equations,” *International Journal for Numerical Methods in Engineering*, vol. 86, pp. 765–781, may 2011.
- [58] K. Svanberg, “The method of moving asymptotes—a new method for structural optimization,” *International Journal for Numerical Methods in Engineering*, vol. 24, pp. 359–373, feb 1987.
- [59] C. Zhang and R. Ordóñez, “Numerical optimization,” in *Advances in Industrial Control*, no. 9781447122234, pp. 31–45, Springer, 2012.
- [60] O. C. Zienkiewicz and J. Z. Zhu, “The superconvergent patch recovery (SPR) and adaptive finite element refinement,” *Computer Methods in Applied Mechanics and Engineering*, vol. 101, pp. 207–224, dec 1992.
- [61] J. J. Ródenas, M. Tur, F. J. Fuenmayor, and A. Vercher, “Improvement of the superconvergent patch recovery technique by the use of constraint equations: The SPR-C technique,” *International Journal for Numerical Methods in Engineering*, vol. 70, pp. 705–727, may 2007.
- [62] D. Yang, H. Liu, W. Zhang, and S. Li, “Stress-constrained topology optimization based on maximum stress measures,” *Computers and Structures*, vol. 198, pp. 23–39, mar 2018.

- [63] K. J. Chang, “Optimality criteria methods using K-S functions,” *Structural Optimization*, vol. 4, pp. 213–217, sep 1992.
- [64] M. Bruggi, “On an alternative approach to stress constraints relaxation in topology optimization,” *Structural and Multidisciplinary Optimization*, vol. 36, pp. 125–141, aug 2008.
- [65] C. Le, J. Norato, T. Bruns, C. Ha, and D. Tortorelli, “Stress-based topology optimization for continua,” *Structural and Multidisciplinary Optimization*, vol. 41, pp. 605–620, apr 2010.
- [66] J. E. Shigley, C. R. Mischke, and R. G. Budynas, *Shigley’s mechanical engineering design - 9th Ed.* PhD thesis, 2002.
- [67] C. R. Dohrmann, M. W. Heinstein, J. Jung, S. W. Key, and W. R. Witkowski, “Node-based uniform strain elements for three-node triangular and four-node tetrahedral meshes,” *International Journal for Numerical Methods in Engineering*, vol. 47, pp. 1549–1568, mar 2000.
- [68] H. Wille, E. Rank, and Z. Yosibash, “Prediction of the mechanical response of the femur with uncertain elastic properties,” *Journal of Biomechanics*, vol. 45, pp. 1140–1148, apr 2012.
- [69] T. H. Nguyen, G. H. Paulino, J. Song, and C. H. Le, “A computational paradigm for multiresolution topology optimization (MTOPT),” *Structural and Multidisciplinary Optimization*, vol. 41, pp. 525–539, apr 2010.
- [70] N. Aage, M. Nobel-Jørgensen, C. S. Andreasen, and O. Sigmund, “Interactive topology optimization on hand-held devices,” *Structural and Multidisciplinary Optimization*, vol. 47, pp. 1–6, jan 2013.
- [71] J. F. Abel and M. S. Shephard, “An algorithm for multipoint constraints in finite element analysis,” *International Journal for Numerical Methods in Engineering*, vol. 14, pp. 464–467, jan 1979.
- [72] J. M. Navarro-Jiménez, M. Tur, F. J. Fuenmayor, and J. J. Ródenas, “On the effect of the contact surface definition in the Cartesian grid finite element method,” *Advanced Modeling and Simulation in Engineering Sciences*, vol. 5, pp. 1–19, dec 2018.
- [73] C. Hellmich, C. Kober, and B. Erdmann, “Micromechanics-based conversion of CT data into anisotropic elasticity tensors, applied to FE simulations of a mandible,” *Annals of Biomedical Engineering*, vol. 36, pp. 108–122, jan 2008.

PAPER B

Allying topology and shape optimization through machine learning algorithms

D. Muñoz, E. Nadal, J. Albelda, F. Chinesta and J.J. Ródenas

Finite Elements in Analysis and Design

Volume 204, 2022

DOI: [10.1016/j.finel.2021.103719](https://doi.org/10.1016/j.finel.2021.103719)

Abstract

Structural optimization is part of the mechanical engineering field and, in most cases, tries to minimize the overall weight of a given design domain, subjected to functionality constraints given in terms of stresses or displacements. The most relevant techniques are topology and shape optimization. Topology optimization provides the optimal material distribution layout into a given, static, design domain. On the other hand, shape optimization provides the optimal combination of the parameters that define the required parametrization of the domain's boundary. Both techniques have strengths and weaknesses, thus a hybrid optimization approach that combines the former techniques will define a more general structural optimization framework that will take advantage of their synergistic combination. The difficulty arises when communicating both techniques for which, in this paper, we propose a machine learning-based methodology.

Key words

Topology Optimization; Mesh Refinement; h -adaptivity; $cgFEM$; Shape Optimization; Hybrid Optimization; Machine Learning; Dimensionality Reduction; Locally Linear Embedding

Contents

1	Introduction	131
2	Methodologies	133
3	Reference Benchmark Problem	134
4	Hybrid Optimization	136
4.1	Manifold Learning. Parametrization	137
4.2	Generation of new geometries	142
4.3	Shape Optimization	143
5	Numerical Examples	147
5.1	MBB Problem	148
5.2	Hook Problem	153
6	Conclusion	156
A	Appendices	157
A.1	Appendix: Topology Optimization	157
A.2	Appendix: Shape Optimization	161
A.3	Appendix: Manifold Learning	162
A.4	Appendix: Cartesian grid Finite Element Method (<i>cgFEM</i>)	163
	Acknowledgements	166
	References	166

1. Introduction

Optimization is the mathematical discipline that tries to find the best element of a given set. The search is driven by the performance of each element, measured through a predefined loss function. Optimization techniques are extensively used in fields such as science, engineering or economics. We will focus on the engineering field, specially on structural optimization.

Structural optimization is a crucial tool in the design process of mechanical components, since it is able to generate the optimal design domain according to a set of applied loads. The optimal design must minimize or maximize an objective function while satisfying a set of constraints. The most common pairs of objective function and constraints found in the structural optimization field are: the minimization of the mass/volume while satisfying a yielding stress constraint and the maximization of the stiffness while satisfying a volume fraction constraint. There exist different approaches to solve the structural optimization problems. Among them, we will focus on the most common ones, namely, topology and shape optimization techniques.

Topology optimization algorithms allow to modify the topology of the material in the design space at the expense of a large amount of design variables, such as the relative density of each element with the SIMP method [1–3], the distance of each node to the implicit boundary with the Level-Set approaches [4–6] or the Phase Field for topology optimization [7–9]. The current work is based on the SIMP method that provides an optimal material distribution layout over the design domain defined by a blurred boundary which is not directly suitable for manufacturing. A review of the SIMP method can be found in *Appendix A.1*. On the other hand, shape optimization techniques, use a CAD representation of the boundary of the geometry to compute the objective function and constraints. This CAD representation may be defined using many types of geometrical entities (splines, NURBS, etc.). In our case, the boundary will be represented using the STL format, i.e., a triangular tessellation of the geometric boundary. Thus, the optimal geometry provided is directly suitable for manufacturing. In this work, we consider the parameterized shape optimization algorithm which needs a user-defined parameterized boundary of fixed topology that does not allow to explore new topologies. The main benefit of using shape optimization techniques is the accuracy and smoothness of the boundary definition. This benefit is even greater if we take into account that the number of design variables necessary to parameterize the boundary of the geometry is usually low, this allowing the exploration of the design space with a huge variety of optimization algorithms. A description of the shape optimization problem considering geometrical parameters can be found in the *Appendix A.2*.

Given the characteristics of these two types of optimization techniques, it would be desirable to develop a hybrid approach that harnesses the strengths and discards the weaknesses of the topology and shape optimization techniques when used separately.

This hybrid algorithm could be defined by the following steps:

1. **Topology optimization.** This step should provide a preform with topological characteristics defined in terms of an optimal material distribution layout, consider the design domain defined by the analyst.
2. **Interface.** This step should communicate both topology and shape optimization algorithms. This interface should generate the parametric geometrical model (defined by design variables) required by the shape optimization algorithm from the results of the topology optimization process.
3. **Shape optimization.** The shape optimization algorithm should then use this model and will find the optimal combination of its parameters that minimize a given objective function while satisfying the prescribed constraints. The final results of this step should be a CAD-like representation of the optimal geometry directly suitable for manufacturing.

The main issue that we face when implementing such a hybrid algorithm is the development of step 2, the interface step, that allies both topology and shape optimization algorithms. Below are, to the authors' knowledge, the main contribution to this topic that can be found in the bibliography. Reference [10] manually parametrized the result of the topology optimization solution, and used it in the parametrized shape optimization algorithm. In the approach described in [11,12], the authors parametrize the optimal material distribution of a 2D design domain by means of curve fitting algorithms. The parameters that define those curves are then modified by the shape optimization algorithm to find the optimal geometry. Also, we would like to highlight the work in [13] where the use of Artificial Neural Networks allow to find the set of simple entities that reproduce the material distribution provided by the topology optimization algorithm. Additionally, alternative approaches are found in the literature. For instance, in [14] the authors use an edge detection technique to identify the structural elements provided by the topology optimization algorithm. In ref. [15] the authors use an edge detection technique, the Canny algorithm, and manually create a B-spline representation of the model. In [16] the authors manually create the mesh for the shape optimization algorithm by means of the material distribution layout indicated by the topology optimization algorithm. Also, in [17] the authors simultaneously evaluate both optimization algorithms; in this case the shape is modified considering the variation of the nodal coordinates of the mesh by means of weights, acting as design variables, and predefined perturbation vectors. In [18,19], the authors create a two-stage algorithm where the overall geometric definition is achieved in the topology optimization step. Then the result is represented with Deformable Simplicial Complex entities whose vertices' positions can be modified by the shape

optimization algorithm. Also, [20] presented a new level-set algorithm that allows to reduce the dimension of the functional by means of the Radial Basis Functions. Finally, we highlight the interesting work developed in [21] where the authors propose to first use a shape optimization algorithm to define the design domain and then to use a topology optimization algorithm to find the optimal material distribution.

In our work, we propose the use of a machine learning technique to infer the geometrical characterization defined by a set of parameters. Specifically, we use a Manifold Learning (ML) algorithm, a subfield of the machine learning techniques. These algorithms will automatically create a parametric model, defined as a combination of geometrical modes that explicitly characterizes the implicit boundary given by the material distribution provided by the topology optimization algorithm. The extracted geometrical features may take the form of simple geometrical entities, such as radius or thickness but, in general, the extracted geometrical features will be more complex. In any case, the ML tool will be able to identify the geometrical modes, providing a parametric geometrical representation. We will then be able to use this parametric characterization to generate new geometries by modifying the value of the parameters, either manually or guided by an external algorithm. In our case, we will introduce these parameters as the design variables used by a shape optimization algorithm.

The paper is organized as follows. The implementation of the hybrid optimization algorithm relies on a set of technologies or methods, that are presented in *Section 2*. Following, in *Section 3*, we will describe the benchmark analytic problem used to check the functionalities developed. Then, in *Section 4* we will describe the strategy considered to achieve an hybrid optimization framework and how the previously described technologies interact with each other. Later, in *Section 5* we will show the behaviour of the proposed methodology by means of numerical analyses considering the benchmark problem together with the numerical analyses on the well-known MBB beam problem and a hook problem. Finally, in *Section 6*, we will conclude the paper with some final remarks. An *Appendix* is also included, for the sake of completeness, to properly describe some methods and technologies discussed in this work.

2. Methodologies

As proposed in *Section 1*, our goal is to ally topology and shape optimization techniques in order to develop a hybrid optimization framework. To accomplish this objective, we will make use of different methodologies and technologies.

On one hand, we will harness the capabilities of ML techniques to infer information from datasets. The topology optimization technique produces intermediate solutions during the iterative process. After the initial steps of the process, characterized by substantial modification of the solution, i.e., once the final convergence to the solution has started, the intermediate solutions will only undergo minor modifications around the final solution. Then, we propose to consider these solutions obtained from the iterative process as snapshots that will be used by a ML algorithm to infer the characteristics of the geometry provided by the TO technique. We will use the parameters associated to the geometrical modes to generate new geometries, not existing in the original dataset. The generation of the new geometries may be guided through a shape optimization technique, accordingly, obtaining an optimal geometry suitable for manufacturing. In order to achieve this objective, we rely on the ML algorithms. There exist a huge variety of techniques in the ML field, such as the Principal Component Analysis (PCA) [22], which finds the directions of maximum variation in the original dataset. The former algorithm is a linear technique, mainly used some time ago, but currently non-linear techniques have been developed to obtain the inherent structure of the dataset. These techniques can preserve the non-linear behaviour of the initial dataset, such as the Locally Linear Embedding (LLE) [23] (see *Appendix A.3*). In this work we use the LLE to compute the manifold space. As the geometrical modes indicate the directions of the geometry evolution towards the minimization of the fitness function, we will use the parameters associated to the geometrical modes to generate new geometries, not existing in the original dataset.

On the other hand, the main concerns about structural optimization are its efficiency and accuracy. Therefore, we use the *cgFEM* framework to compute the FE calculations. In short, *cgFEM* [24,25] is a Fictitious Domain Method (FDM) [26–28], thus the domain discretization is considered over an easy-to-mesh fictitious domain that embeds the physical domain. In *cgFEM*, this embedding domain is a cube and the mesh is obtained by using a set of Cartesian grids. The inherent hierarchical structure of mesh allows to easily share information between elements or meshes. Thanks to the use of the Cartesian grids, all elements in the mesh are regular hexahedrons. This particular feature decreases drastically the computational effort devoted to integration, as the information of one element may be shared with the rest. *Appendix A.4* conscientiously review the *cgFEM*.

3. Reference Benchmark Problem

The reference problem used to describe the proposed methodologies is defined in Figure 1 where we use a coherent system of units. This problem corresponds to a constant hollowed cross sectional area beam, with 2 perpendicular planes of symmetry

($x = 0$ and $z = 0$), under plain strain conditions, subjected to a pressure P on the internal cylindrical surface.

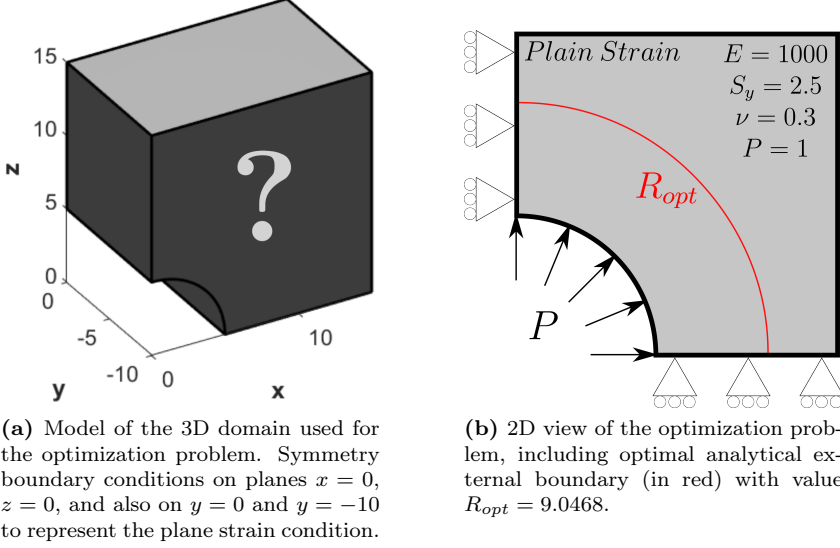


Figure 1: Reference problem.

The objective of the optimization problem is to minimize the amount of material while the maximum von Mises stress value ($\max(\sigma_{vm})$) is equal to the yield limit (S_y). It is known that the optimal shape will also correspond to a circular external shape, i.e., the optimal shape will take the form of a thick-walled cylinder. The following equations are the analytical solutions for displacements (1) and stresses (2) of thick-walled cylinders subjected to internal pressure [29]:

$$\mathbf{u} = \begin{Bmatrix} u_R \cos(\theta) \\ 0 \\ u_R \sin(\theta) \end{Bmatrix} \quad u_R = \frac{P(1+\nu)}{E(\kappa^2-1)} \left[(1-2\nu)r + \frac{r_{ext}^2}{r} \right] \quad (1)$$

$$\boldsymbol{\sigma} = \begin{Bmatrix} \sigma_R \cos^2(\theta) + \sigma_H \sin^2(\theta) \\ \nu(\sigma_x + \sigma_z) \\ \sigma_R \sin^2(\theta) + \sigma_H \cos^2(\theta) \\ 0 \\ 0 \\ (\sigma_R - \sigma_H) \sin(\theta) \cos(\theta) \end{Bmatrix} \quad \begin{aligned} \sigma_R &= \frac{P}{\kappa^2-1} \left[1 - \left(\frac{r_{ext}}{r} \right)^2 \right] \\ \sigma_H &= \frac{P}{\kappa^2-1} \left[1 + \left(\frac{r_{ext}}{r} \right)^2 \right] \end{aligned} \quad (2)$$

where $r = \sqrt{x^2 + z^2}$ is the radius of a point of coordinates (x, y, z) in the domain, r_{ext} and r_{int} are the external and internal radii, $\kappa = r_{ext}/r_{int}$, $\theta = \arctan(z, x)$, E is the Young Modulus and ν is the Poisson's ratio.

The maximum von Mises stress in the cylinder can be evaluated, considering the exact solution in stresses, as a function of the external radius. Therefore, it is possible to find the value of the minimum external radius that satisfies $max(\sigma_{vm}) \leq S_y$. For the data shown in Figure 1, this radius is $R_{opt} = 9.0468$, represented in Figure 1, that leads to an optimum volume $V_{opt} = 446.4545$.

4. Hybrid Optimization

In this section we will describe the details about the strategy that we propose to ally topology and shape optimization techniques and to create a general structural optimization framework. We will describe the procedure developed to automatically extract the geometrical parameters and how we use them. In Figure 2, we show the main steps in the proposed strategy.

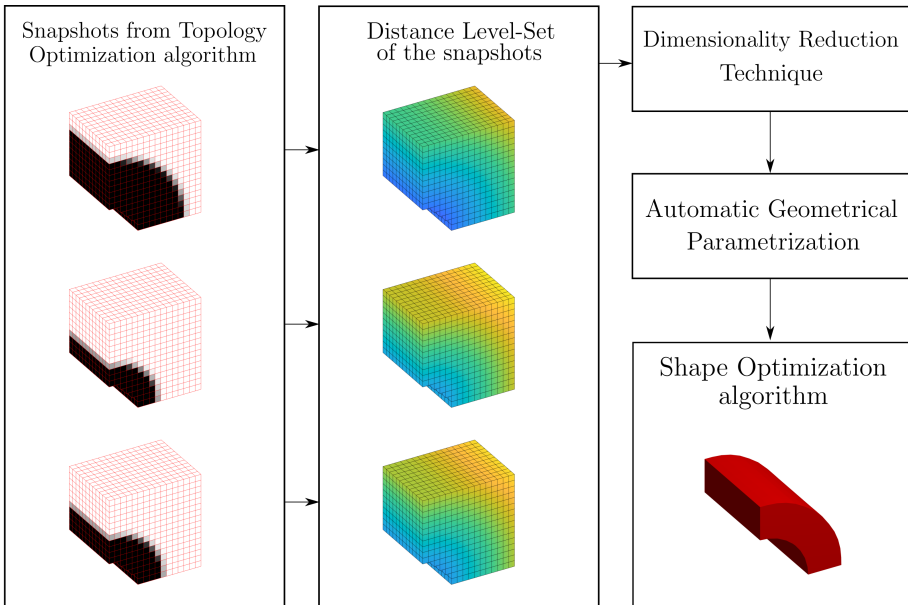


Figure 2: Hybrid optimization workflow.

To summarize, as represented in Figure 2, we postprocessed the material distribution layout provided by the TO algorithm to create a distance level-set. This level-set has the information of the distance between each node to the implicit boundary. Then, the level-set is used to extract the geometrical modes by using a ML tool. This process is based on the procedure presented in [30] where, using a set of \mathbf{X} segmented images of livers, a ML technique, trained to infer the shape of livers provided a parametrized model to represent livers based on just two parameters. Finally, using the reduced parametric geometrical model, the procedure is able to reconstruct a CAD geometry and, thus, to use a standard parametric shape optimization tool to obtain the final geometry, both topologically and structurally optimized.

4.1. Manifold Learning. Parametrization

Topology optimization algorithms provide an optimal material distribution layout of the design domain, i.e. the material/void status of each element considered in the discretization. In our case, based on the SIMP method, the elements also may have intermediate relative densities, representing fictitious material properties. We want to infer the geometry of the solution provided by the TO algorithm, described by a large number of parameters (one relative density per element) and to describe it using a reduced number of parameters. Hence, we will use a ML algorithm to reduce the dimensionality of the solution. The training process of a ML algorithm requires the use of a sufficiently large amount of snapshots, each of them representing the geometry to be inferred. As most optimization techniques, TO is an iterative method, which means that the material distribution information of each iteration will be available. Once the TO process has started to converge, there will only be minor changes in the material distribution, that will be very similar to that of the final solution and, therefore, with the same topology. Hence, these intermediate material distributions of the iterative process will be suitable for the ML tool, that will be able to describe the geometry using a reduced number of parameters, each of them associated to a geometrical mode. The choice of snapshots is arbitrary, as far as all of them maintain the same topology. The strategy followed in this work is to select the last iterations from the topology optimization process, thus mainly ensuring the topology invariance while detecting the evolution of the geometry in these last steps. As each snapshot can have different size, we propose to project the information of each snapshot to a common uniform mesh of elements having the size of the smallest element used in the definition of the snapshots. Thanks to the Cartesian grid and the hierarchical data structure of *cgFEM*, this projection process is costless and straightforward.

In Figure 3a, we show the optimal material distribution layout provided by the TO algorithm for the Benchmark problem. Although, in this example there will be no change in the topology, but it will help us to illustrate the procedure. The element-wise solution directly provided by the TO algorithm, will be first smoothed

using nodal averaging procedure, whose result is show in Figure 3b, to obtain a nodal representation.

As shown in Figure 3b, the field represented over the design domain is quasi-boolean, so the information it provides is very limited. To solve this problem, this information must be postprocessed in order to obtain a much richer information given by the distance of each node to the implicit boundary. As the boundary in the regions with intermediate values of ρ is not explicitly defined, we have to generate an explicit geometrical definition. To do it, we use the Marching Cubes (MC) [31] algorithm that provides a polygonal mesh from the isosurfaces, defined by an isovalue ρ_c , existing in the material distribution with $\rho_c \in [0, 1]$.

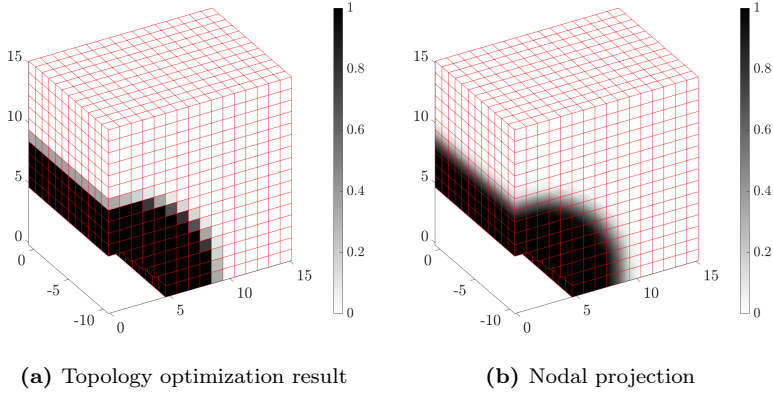


Figure 3: Reference problem. Optimal topology optimization material distribution (a) with its nodal projection equivalent (b).

Figure 4 represents the polygonal mesh obtained from the MC algorithm for different values of v_f for an isovalue $\rho_c = 0.5$ in both cases. The final volume is represented by the isosurface of selected value of ρ_c in the regions with intermediate values of ρ (red surface in Figure 4) and by the regions of the CAD surface that define the design space with $\rho = 1$ (green transparent surfaces in Figure 4).

Once the surface defining the volume has been evaluated, the solutions represented by nodal densities are replaced by the level-set information that represents the distance of each node to the surface. In Figure 5, we represent the distance level-set obtained from the cases represented in Figure 4. With this procedure we transformed the quasi-boolean information of the material distribution into a smooth and monotonous level-set.

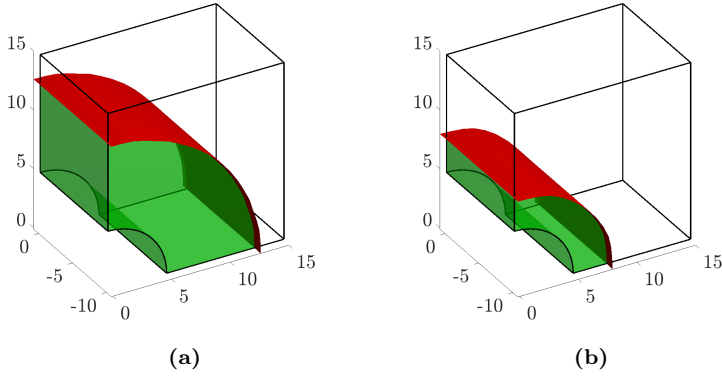


Figure 4: MC polygonal meshes representing the external cylindrical shape of the solution obtained from the material distribution considering an isovalue $\rho_c = 0.5$, for v_f equal to 0.5 (a) and 0.15 (b).

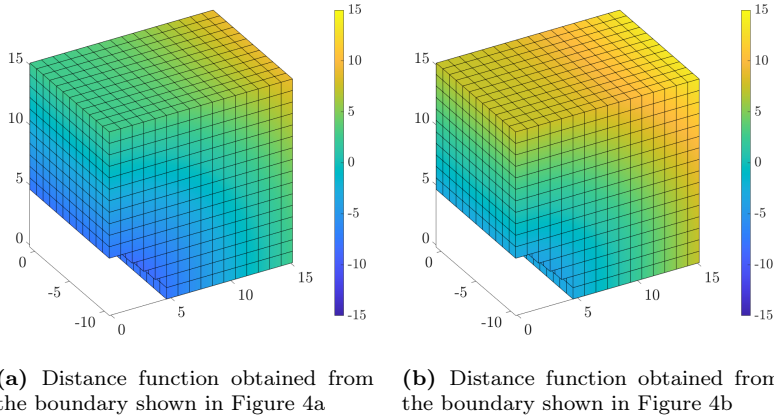


Figure 5: Distance function to the boundary, represented as a value equal to 0, obtained from Figure 4.

In the original algorithm of the SIMP method (see *Algorithm 1* in *Appendix A.1*) the volume fraction is set as a constraint and the compliance is minimized. The algorithm will only provide a limited exploration of the design space as a single value of the volume fraction will be considered. Additionally, as no further constraints are taken into account, the outcome of the algorithm is not fully useful for structural applications where, for example, stress constraints are very common. To ensure de-

sign richness, we have implemented a simple, not fully robust implementation of a TO algorithm, where a heuristic stress scaling technique, not to be compared with a stress constraint, adapts the volume fraction to target a given maximum stress value, for instance the yield limit [32]. It must be taken into account that this simple strategy, not suitable for problems with stress singularities, is not a procedure to impose stress constraints, which would require a consistent treatment of the stress gradients, including a regularization of the stress field [33,34] and a more advanced optimization algorithm. These more advanced algorithms could also be considered, but they are out of the scope of the paper as we simply need a basic exploration of the design space considering appropriate volume fractions. Hence, we propose the use of *Algorithm 2* defined in *Appendix A.1*. *Algorithm 2* consists of two nested loops. The inner loop follows the strategy of the original SIMP method and produces solutions of minimum compliance, subjected to the volume fraction constraints dictated by the outer loop. The main benefit of using this approach within the hybrid optimization framework is that it will automatically increase the richness of the snapshots dataset by extending the exploration of the design space varying the values of the volume fraction that will tend to increase the density of the snapshots around the vicinity of the optimal volume fraction.

We also propose to increase the number of snapshots, by simply repeating the previous strategy. Considering, for each material/void layout different values of ρ_c . The snapshots chosen to train the ML model are arbitrary, but all of them must have the same topology. Once the snapshots have been evaluated as previously described, we will use them as the training dataset for the ML model, specifically for the LLE algorithm, as indicated. LLE algorithm is a ML technique that extracts the embedded manifold structure existing in a high-dimensional space, which in our case is defined by the distance level-set. This embedded manifold or low-dimensional space will be defined by a set of parameters. We will consider that these parameters characterize and describe the geometrical features of our preform. Let \mathbf{X}_i be each of the training high-dimensional points (or snapshots). The LLE hypothesize that any point may be obtained as a linear combination of K neighbours with W_{ij} , $j \in [1, K]$. The number of neighbours K is user-defined and the weights are obtained by minimizing the functional represented in equation (3):

$$e(\mathbf{W}) = \sum_i \|\mathbf{X}_i - \sum_j W_{ij} \mathbf{X}_j\|^2, \quad (3)$$

where W_{ij} are subjected to the constraint $\sum_j W_{ij} = 1$. The LLE entrusts that these weights are invariant to space transformations. Hence, the value of the weights is preserved when changing between spaces. Now, the low-dimensional parameters may be obtained by minimizing the functional in (4):

$$\varphi(\mathbf{Y}) = \sum_i \|\mathbf{Y}_i - \sum_j W_{ij} \mathbf{Y}_j\|^2, \quad (4)$$

where \mathbf{Y}_i represent each of the points projected to the embedded space. The former equation may be represented in the form shown in (5):

$$\varphi(\mathbf{Y}) = \mathbf{Y}^T \mathbf{M} \mathbf{Y}, \quad (5)$$

with,

$$\mathbf{M} = (\mathbf{I} - \mathbf{W})^T (\mathbf{I} - \mathbf{W}). \quad (6)$$

The minimization problem could be considered as an eigenvalue problem, where the eigenvectors represent the low-dimensional points \mathbf{Y} . The dimension of the embedded space may be a user-defined parameter, but it is convenient to study the eigenvalues of \mathbf{M} . As we minimize (5), the target eigenvectors are related to the smallest eigenvalues, as shown in Figure 6, we define the dimensionality as $d = 1$ because the first eigenvalue is far from the following. The detailed mathematical procedure to obtain the low-dimensional embedded space is explained in [35].

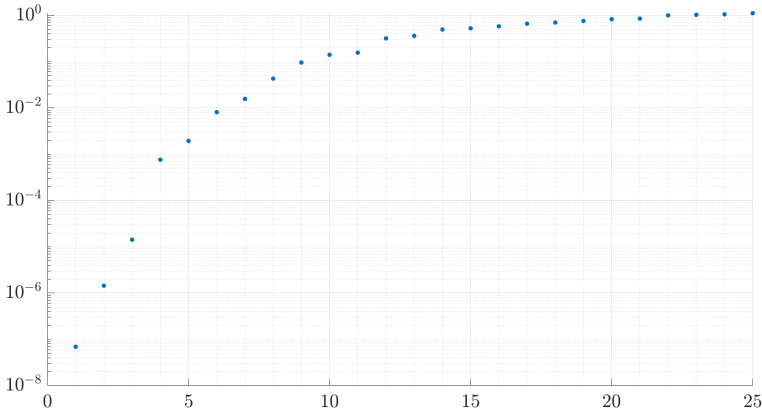


Figure 6: Reference Problem. First 25 eigenvalues of \mathbf{M} (see (6)), in the LLE procedure.

Figure 7 shows the embedded space obtained by this technique applied to the reference problem. The y -axis represents the volume of the final geometry whereas the x -axis represents the extracted low-dimensional parameter. We used $K = 21$ neighbours from a total amount of 101 individuals (snapshots). The colours of the graph in Figure 7 represents the feasibility of the individuals, green points denote structures with maximum stress below the (yield) stress limit while red points have von Mises stresses above the yield limit S_y .

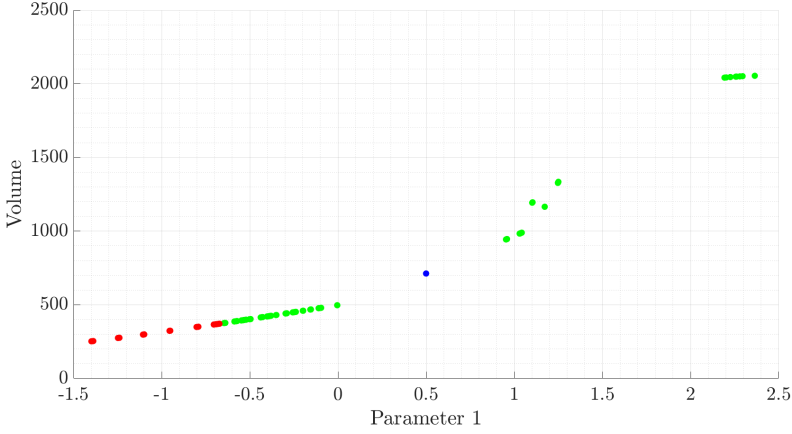


Figure 7: Reference problem. Embedded space¹ for the reference problem considering $K = 21$ neighbours and $d = 1$ parameters. The y-axis represents the volume of each individual, while the colour represents if the maximum stress value is below (green) or above (red) the yield stress limit.

4.2. Generation of new geometries

We have obtained a low-dimensional embedded manifold that defines the geometrical characteristics of the material distribution. Our goal is to use this information to create CAD representations of the geometry. Hence, we define the value of a set of parameters $\hat{\mathbf{Y}}_i$ in the embedded space \mathbf{Y} . This point may be user-defined, however the interesting part of this approach is that it can be automatically defined by an algorithm, e.g. a shape optimization algorithm. We hypothesize that $\hat{\mathbf{Y}}_i$ is a weighted interpolation between a set of \hat{K} neighbours. The value of interpolation weights \hat{W}_{ij} is obtained minimizing the functional,

$$e(\hat{W}) = \sum_i \|\hat{\mathbf{Y}}_i - \sum_j \hat{W}_{ij} \mathbf{Y}_j\|^2 \quad (7)$$

In this case, we assume, as in the LLE technique, that weights \hat{W}_{ij} are invariant to space transformations. As we have computed the neighbours \mathbf{Y}_j , we gather the matching high-dimensional points \mathbf{X}_j . Finally, we apply the following weighted interpolation to compute $\hat{\mathbf{X}}_i$, i.e., a level-set of the new geometry defined in the high-dimensional space:

¹Notice that the design space is not fully represented as it depends on the exploration performed by the topology optimization algorithm.

$$\widehat{\mathbf{X}}_i = \sum_j \widehat{W}_{ij} \mathbf{X}_j \quad (8)$$

In order to show how the geometries are generated, we select a point $\widehat{\mathbf{Y}}_i = 0.5$ that belongs to the embedded space created by \mathbf{Y} . In Figure 7, we show the individual $\widehat{\mathbf{Y}}_i$ (in blue) in its space \mathbf{Y} . This procedure provides as a result a new point located in the high-dimensional space \mathbf{X} , called $\widehat{\mathbf{X}}_i$. The individual $\widehat{\mathbf{X}}_i$ has the distance information of each node to the boundary of the geometry, as represented in Figure 8a. We harness this information to compute the boundaries that define the new geometry, as shown in Figure 8b.

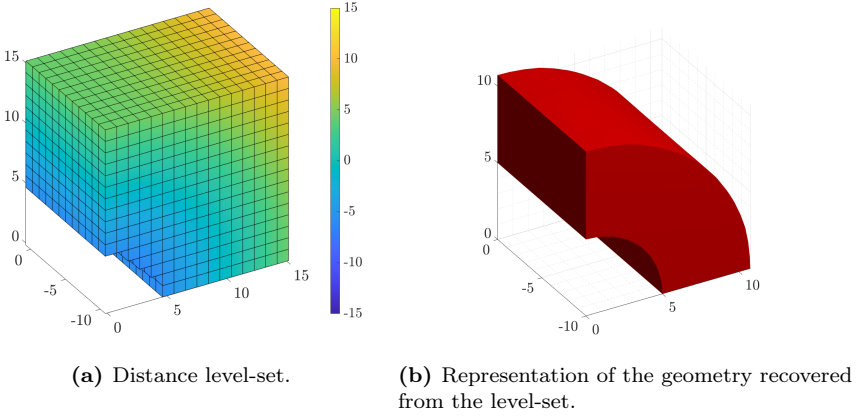


Figure 8: Reference problem. New geometry obtained from the space transformation of $\widehat{\mathbf{Y}}_i$ into $\widehat{\mathbf{X}}_i$.

A clearer understanding of the influence of the geometric modes using this procedure can be obtained through the example shown in *Section 5.1*, where a more complex geometry has been considered.

4.3. Shape Optimization

In previous sections, we have presented a procedure to automatically parametrize the material distribution from the topology optimization and to extract the main geometrical features (Section 4.1). We have also shown how this parametrization is used to generate new geometries (Section 4.2). This strategy has interest in itself, as we are able to generate new geometries not existing in the training set of data. As the purpose of this paper is to ally topology and shape optimization techniques, we propose a final step where the modification of the parameter $\widehat{\mathbf{Y}}_i$ is guided by the

updating scheme of a shape optimization algorithm, the minimization of the volume into the region of feasible design where the maximum von Mises stress value is below the prescribed yield limit.

As we have defined our implicit parametrization of the boundary of the design domain, our shape optimization problem can be expressed with the following equation,

$$(\mathbb{S}\mathbb{O}_\sigma(S_y)) = \begin{cases} \min_{\hat{\mathbf{Y}}} : & \text{Volume}(\hat{\mathbf{Y}}) & (9a) \\ \text{subjected to:} & \max(\sigma_{eq}(\hat{\mathbf{Y}})) = S_{cr} & (9b) \end{cases}$$

where σ_{eq} represents an equivalent stress value and S_{cr} is the limit value of σ_{eq} . For example, the stress value used in this paper is the recovered von Mises stress σ_{vm}^* while the limit value is equal to the yield limit S_y .

Once we have expressed the geometry as a function of a reduced set of design variables, as if we were having a parametrized CAD model, we are able to use a wide range of shape optimization algorithms. In this work, we use, for the numerical examples, the Bayesian optimization algorithm. Additionally, other approaches are available such as Genetic Algorithms or Gradient-based algorithms. Figure 9a shows the optimal geometry of the reference problem, and Figure 9b represents the recovered von Mises stress field. These results are obtained using a mesh of element size $h_{\text{TO}} = h_{\text{SO}} = 0.9563$, for both optimization algorithms.

The results shown in Figure 9 satisfy that the maximum stress value is equal to the stress limit (S_y). However, the optimal geometry is far from the analytical optimum. As the optimization process is guided by the FE numerical results, we need to improve their quality to improve the accuracy of the optimal solution. One strategy to improve the solution is to reduce the element size of the FE analysis mesh. If we consider that the main objective TO algorithm is to obtain the preform of the solution, i.e. a definition of its topology, the TO algorithm does not require the use of fine discretizations, therefore, we focus the solution improvement on the shape optimization step, the step that will finally define the geometry. The optimal solution shown in Figure 10 was computed with an element size of $h_{\text{TO}} = 0.9563$ for the topology optimization algorithm and an element size of $h_{\text{SO}} = 0.2391$ for the shape optimization.

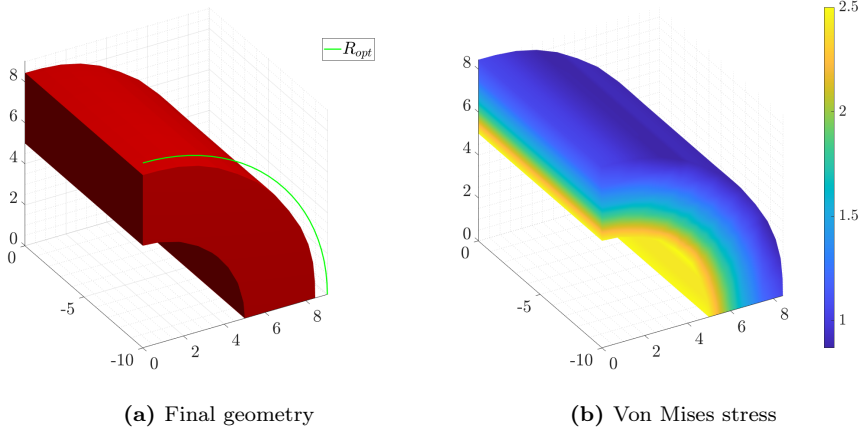


Figure 9: Reference problem. Optimal geometry (in red) from the hybrid optimization algorithm with the optimal analytic radius (in green) $R_{opt} = 9.0468$ (a) and the recovered von Mises stress field (b) The results were obtained using meshes of element size $h_{\mathbb{T}\mathbb{O}} = h_{\mathbb{S}\mathbb{O}} = 0.9563$.

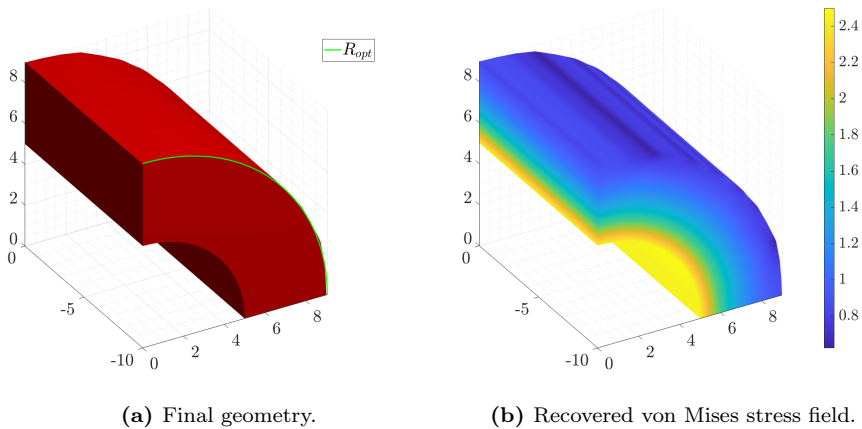


Figure 10: Reference problem. Hybrid optimization result of the reference problem with the optimal analytic radius $R_{opt} = 9.0468$ (a) and Von Mises stresses (b). The results were obtained using meshes of element size $h_{\mathbb{T}\mathbb{O}} = 0.9563$ and $h_{\mathbb{S}\mathbb{O}} = 0.2391$.

As in the previous analysis, the maximum von Mises stress value is equal to the prescribed yield limit, but in this case the optimal radius we get is far closer to

the optimal analytic solution. In order to understand the influence of the mesh in the accuracy and performance, in Table 1 we compare the time consumed in each optimization along with the relative error with the optimal analytic solution. Table 1 includes the analyses whose FE meshes correspond to $h_{\text{TO}} = h_{\text{SO}} = 0.9563$, $h_{\text{TO}} = 0.9563$ with $h_{\text{SO}} = 0.4781$, $h_{\text{TO}} = 0.9563$ with $h_{\text{SO}} = 0.2391$, $h_{\text{TO}} = h_{\text{SO}} = 0.4781$, $h_{\text{TO}} = 0.4781$ with $h_{\text{SO}} = 0.2391$ and $h_{\text{TO}} = h_{\text{SO}} = 0.2391$. Additionally, in Figure 2, we gather the optimal geometry obtained with each of the analysis and compare it with the optimal analytic solution.

	Relative time				$err(R)$ (%)
	$\text{TO}(v_f(S_y))$	MG	$\text{SO}_\sigma(S_y)$	Total	
$h_{\text{TO}} = 0.9563$ $h_{\text{SO}} = 0.9563$	1	1	1	1	-5.1862
$h_{\text{TO}} = 0.9563$ $h_{\text{SO}} = 0.4781$	1	1.333	2.4943	1.5894	-0.0971
$h_{\text{TO}} = 0.9563$ $h_{\text{SO}} = 0.2391$	1	3.9167	14.3239	6.2539	0.0101
$h_{\text{TO}} = 0.4781$ $h_{\text{SO}} = 0.4781$	4.6415	12.2500	3.7898	4.5121	-0.8554
$h_{\text{TO}} = 0.4781$ $h_{\text{SO}} = 0.2391$	4.6415	14.8333	15.3864	9.0861	-0.0043
$h_{\text{TO}} = 0.2391$ $h_{\text{SO}} = 0.2391$	54.4868	187.3333	13.5739	42.1104	-0.0021

Table 1: Reference Problem. Relative time comparison for the different analysis considered. $\text{TO}(v_f(S_y))$ stands for the Topology Optimization process where the v_f scales the von Mises stress to target S_y , MG represents the Model Generation procedure and $\text{SO}_\sigma(S_y)$ refers to the Shape Optimization process defined by (9a) and (9b). The column Total is the accumulated processing time. The last column represents the relative error ($err(R)$) in the radius with respect to the optimal analytical radius for each analysis obtained as $err(R) = \frac{R - R_{opt}}{R_{opt}} \times 100$.

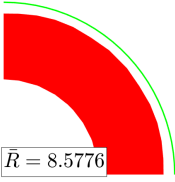
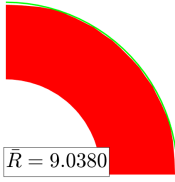
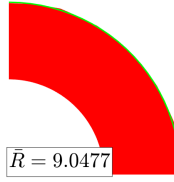
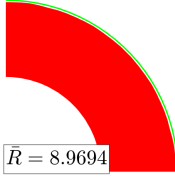
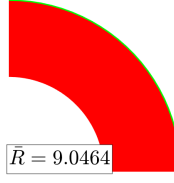
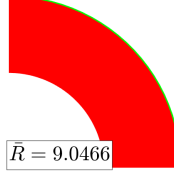
$\text{SO}_\sigma(S_y)$ \ / \ $\text{TO}_\sigma(S_y)$	$h = 0.9563$	$h = 0.4781$	$h = 0.2391$
$h = 0.9563$			
$h = 0.4781$	-		
$h = 0.2391$	-	-	

Table 2: Reference Problem. Comparison of solutions obtained with each analysis. The green curve corresponds to the optimal analytical radius $R_{opt} = 9.0468$.

Tables 1 and 2 show that, for this problem:

- The largest influence on the time taken for the Model Generation (MG) comes from the size of the elements used by the TO process.
- The last column of Table 1 shows that, although smaller values of h_{TO} lead to more accurate results, the main influence on the accuracy comes from the h_{SO} , the size of the elements used for the SO process.

5. Numerical Examples

After having shown the results provided by the proposed hybrid optimization algorithm for the academic reference problem, in this Section, we will use two additional examples. Specifically, we will use the well-known MBB problem and a hook problem.

5.1. MBB Problem

Let us consider the well-known "MBB-Beam" problem to illustrate the proposed procedure. To reduce computational cost only half of the beam has been modelled, considering the symmetry of the problem, as shown in Figure 11. Additionally, in order to consider Plane Strain behaviour, the surface shown in front and its opposite are constrained in its normal direction. Also in Figure 11, we represent the geometrical dimensions of the design space and the boundary conditions. In particular, the beam is bi-supported and subjected to a parabolic pressure P , whose maximum value equals $P_{max} = 1$. As the elastic properties of the material we consider a Young's Modulus $E = 1000$, a Poisson's ratio $\nu = 0.3$ and a yield limit $S_y = 0.3$.

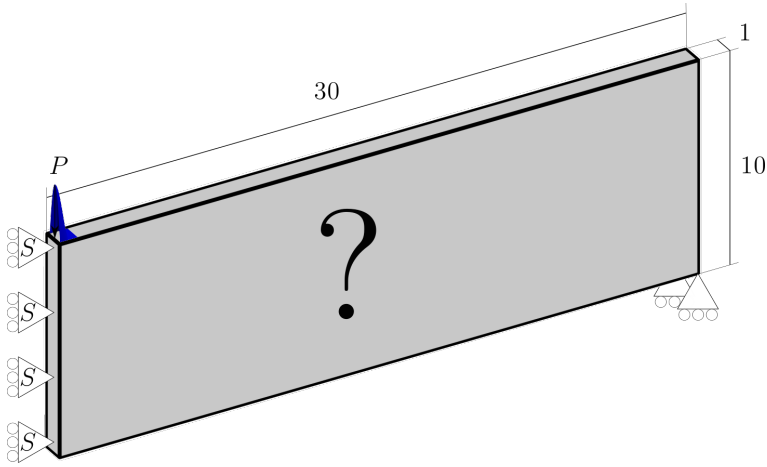


Figure 11: MBB problem.

The first step of the procedure is to run the topology optimization algorithm that will provide the optimal material distribution layout to be used as preform. The analysis was been carried out considering a initial mesh with elements of uniform size $h_{T0} = 0.9563$ and a filter radius set to $r_f = 1.5h_{T0} = 1.4345$. In Figure 12 we show the optimal material distribution provided by the topology optimization algorithms.

From Figure 12, we consider that the preform provided by the topology optimization algorithm lacks of enough boundary definition as the diffuse region (elements with intermediate densities) represents a high percentage of the total design domain. As shown in [32], h -adaptive mesh refinement strategies allow to enhance the boundary resolution and to improve the solution's quality. In *cgFEM* we can consider two refinement strategies, a) a density-based refinement, where elements with intermediate values of relative density are refined to sharpen the boundary definition, and b) a quality-based refinement where the mesh refinement is guided by the estimated

error in energy norm. In this particular case, we harness the density-based refinement strategy to improve the boundary definition, since the shape optimization algorithm will be in charge of the quality of the solution, as explained in Section 4.3. We need to define an acceptable error level to ensure the proper convergence of the *Algorithm 2*. In this example we prescribed a maximum estimated relative error on energy norm $\eta_{max} = 12.5\%$ [32]. With these considerations, we analysed the MBB problem with an initial mesh with elements of uniform size $h_{\mathbb{T}0}^1 = 0.9563$ and a filter radius set to $r_f^1 = 1.5h_{\mathbb{T}0}^1 = 1.4345$ and a second h -adapted mesh with elements of size $h_{\mathbb{T}0}^1$ and $h_{\mathbb{T}0}^2 = 0.4782$ and an adaptive filter radius with lengths of r_f^1 and $r_f^2 = 1.5h_{\mathbb{T}0}^2 = 0.7173$. The resulting material distribution layout is shown in Figure 13, that shows a sharper boundary definition, and a final relative error in energy norm of $\eta = 12.0839\%$.

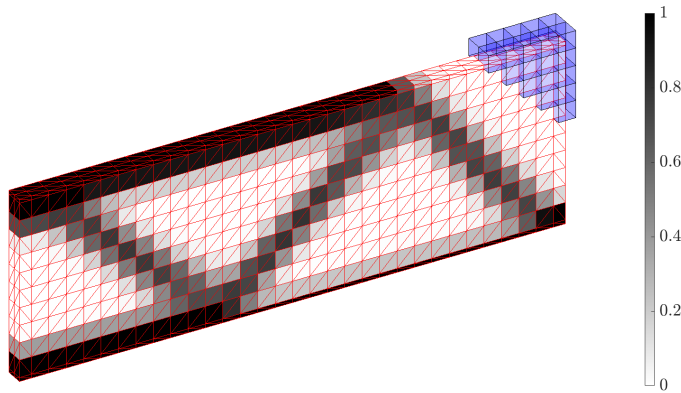


Figure 12: MBB Problem. Optimal material distribution layout from the topology optimization algorithm, obtained with a uniform mesh of non-conforming hexahedra of size $h_{\mathbb{T}0} = 0.9563$, represented on the conforming tetrahedra used as integration subdomains. Some finite elements, in blue, are added in the representation to show the difference between the integration subdomains and elements.

As in the Reference benchmark problem, once the preform is defined by the topology optimization algorithm, we train the reduced model with the material distributions obtained during the topology optimization process. To accomplish this, we use the LLE algorithm with a vicinity $K = 30$ over a total of 140 points (snapshots). Later, we define the number of dimensions of the embedded space taking into account the eigenvalues obtained from the LLE procedure. In this case, we considered $d = 3$ because the first three eigenvalues were isolated from the rest, as shown in Figure 14. Figure 15 represents the resulting embedded space along with several geometries to illustrate the results.

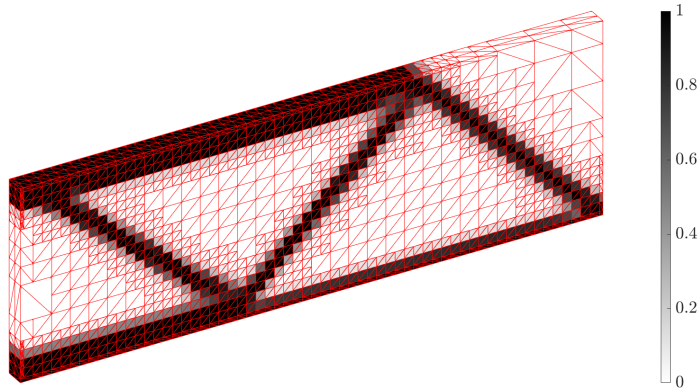


Figure 13: MBB Problem. Optimal material distribution layout from the topology optimization algorithm, obtained with an h -adapted mesh of non-conforming hexahedra of sizes $h_{\text{TO}} = \{0.4782, 0.9563, 1.9126\}$, represented on the conforming tetrahedra used as integration subdomains.²

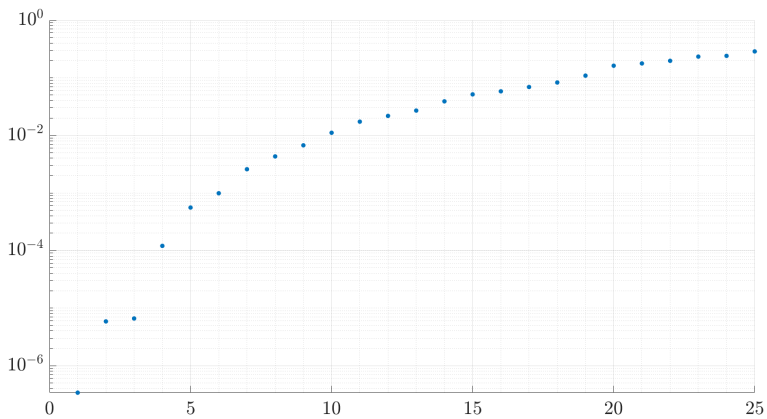


Figure 14: First 25 eigenvalues of the \mathbf{M} (see (6)), belonging to the LLE procedure.

²Note that some elements have been coarsened as they do not influence the overall error.

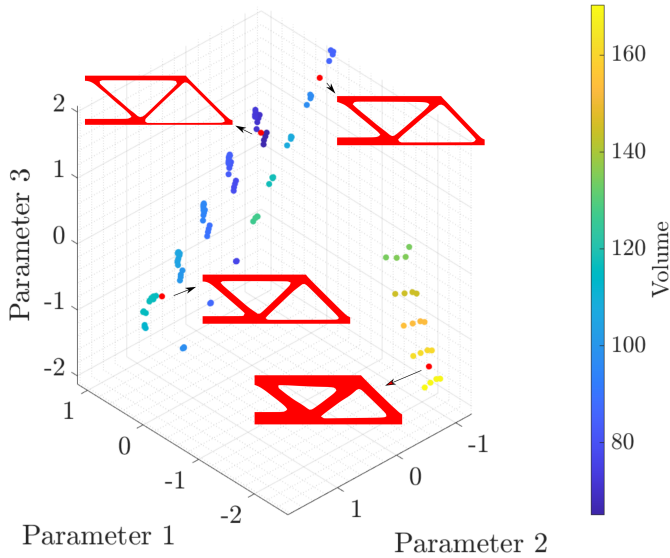


Figure 15: MBB problem. Embedded space for the reference problem considering $K = 30$ neighbours and $d = 3$ parameters. The colours show the volume of each individual. Additionally, some individuals are visualized with its CAD geometry representation.

In Figure 16, we show the reference geometry (obtained with the mean values of the range achieved for each of the three parameters considered) in grey, and the variation of each geometric mode between its lower and upper limit, in red and green colours, respectively. As shown, the variation of the parameters do not only imply the erosion of the structure but also variation of the bars' angles and non-uniform bar sections variations.

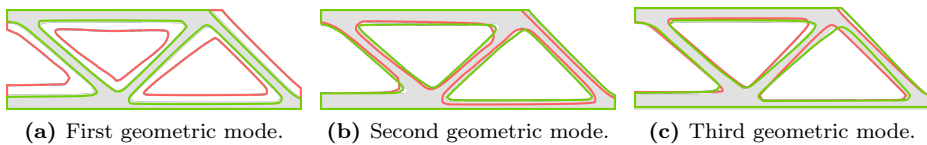


Figure 16: Influence of each geometry mode in the new generated geometries. The reference geometry, obtained from the mean values of the range of each parameter, is represented in grey. We show the variation of each geometric mode by representing their lower and upper values, in red and green colour, respectively.

With the low-dimensional space properly defined, the shape optimization algorithm will use it as a design space. We used a Bayesian algorithm to update the

design variables until the convergence criterion was satisfied. The analysis was carried out with an initial uniform mesh with element size equal $h_{\mathbb{S}0}^1 = 0.4782$. In order to get a solution with a high quality, we use an h -adaptive refinement strategy based on the error, specifically we enforce the maximum estimated relative error to $\eta_{max} = 6\%$. Hence, we allow following h -adapted meshes with elements of size $h_{\mathbb{S}0}^1$ and $h_{\mathbb{S}0}^2 = 0.2391$. The evolution of the optimization process through the Bayesian algorithm is represented in Figure 17. The optimal CAD geometry is shown in Figure 18a, while, in Figure 18b, we display the corresponding recovered von Mises stress field, calculated with a final relative error in energy norm of $\eta = 5.4659\%$.

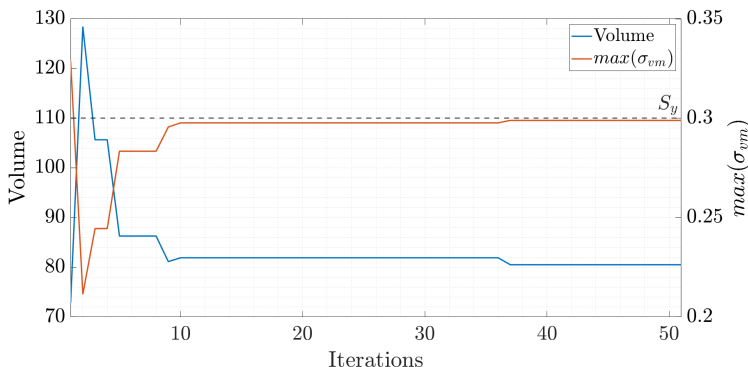


Figure 17: MBB problem. Convergence graph of the Bayesian optimization algorithm.

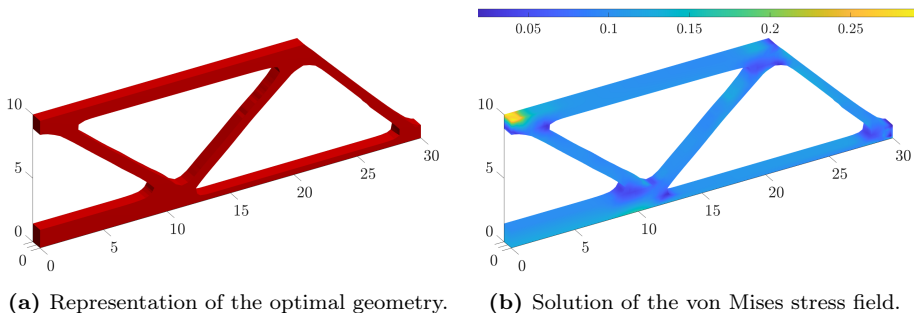


Figure 18: MBB Problem. Hybrid optimization optimal geometry (a) and the corresponding recovered von Mises stress field (b).

As shown in Figure 18a, we obtained a CAD representation of the MBB problem, which is directly suitable for manufacturing. Furthermore, in Figure 18b, we repre-

sented the von Mises stress field whose maximum value is equal to the yield limit $S_y = 0.3$.

5.2. Hook Problem

The second example corresponds to a hook as displayed in Figure 19. The essential boundary conditions are imposed over the green surface, while we consider symmetry on the red surface. Rigid body motion is avoided using appropriate constraints on these surfaces. A parabolic pressure with a maximum value $P = 1$ is imposed in the inner cylindrical surface. The material properties considered in this problem are: Young's Modulus $E = 1000$, Poisson's ratio $\nu = 0.3$ and yield limit $S_y = 3$.

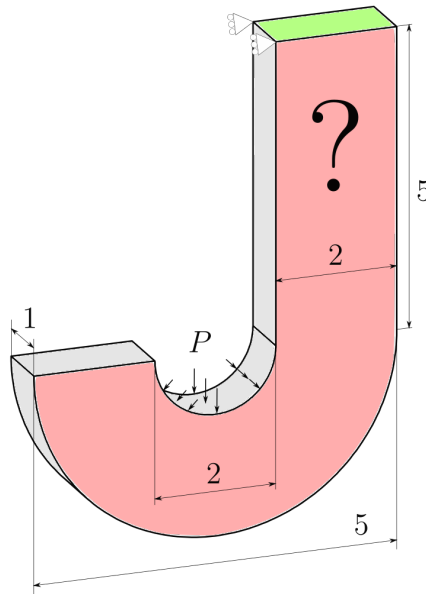


Figure 19: Hook Problem. Problem representation with geometrical dimensions. Essential boundary conditions imposed over the green surface and symmetry on the red surface, also a parabolic pressure with maximum value $P = 1$ is imposed in the inner cylindrical surface.

As in previous examples, the process starts with the topology optimization algorithm. As in the MBB problem, we consider density and error-based h -adaptive refinement with a prescribed maximum estimated relative error in energy norm equal to $\eta_{max} = 7.5\%$. Specifically, we consider an initial mesh with uniform size $h_{\text{T0}}^1 = 0.1275$ and a second h -adapted mesh with elements size h_{T0}^1 and $h_{\text{T0}}^2 = 0.0637$. In Figure

20 we represent the optimal material distribution provided by the TO algorithm, obtained with a final relative error $\eta = 5.9703\%$.

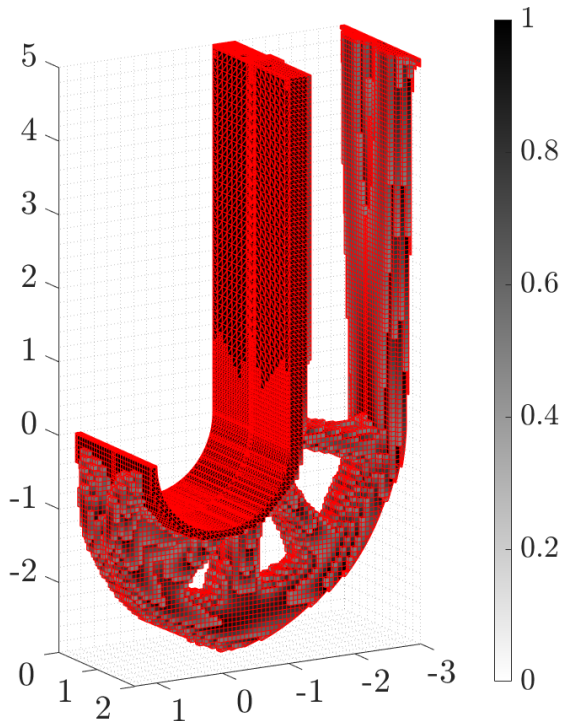


Figure 20: Hook Problem. Optimal material distribution layout obtained from the topology optimization algorithm, represented on the conforming tetrahedra used as integration subdomains. Notice that integration subdomains whose elemental density is $\rho_e < 0.5$ are discarded from the representation.

Once the preform is defined by the topology optimization algorithm, we obtain the embedded manifold. As previously, we use the LLE algorithm, in this particular case, we consider a vicinity of $K = 12$ neighbours over a total of 60 snapshots. Studying the eigenvalues obtained, represented in Figure 21, we consider a dimensionality $d = 2$, as the first two eigenvalues are isolated from the rest.

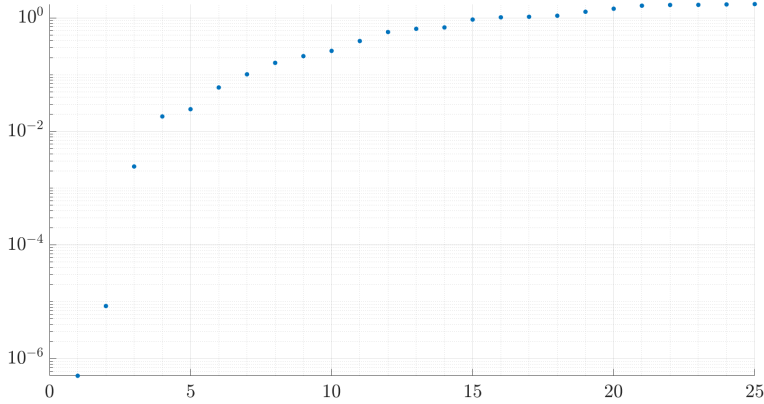


Figure 21: Hook Problem. Eigenvalues of the LLE method that define the quantity of independent geometrical modes.

With the reduced embedded space generated from the LLE algorithm, we run the shape optimization algorithm. The analysis is calculated with an initial uniform mesh of size $h_{\mathbb{S}^0}^1 = 0.0637$ and an h -adapted refinement strategy that allows following meshes with element size $h_{\mathbb{S}^0}^1$ and $h_{\mathbb{S}^0}^2 = 0.03185$, and a prescribed maximum relative error in energy norm $\eta_{max} = 3\%$. For this example, we also use a Bayesian optimization algorithm. The iterative process is represented in Figure 22 and the results we obtained are shown in Figure 23, which are calculated with a final relative error of $\eta = 2.7010\%$.

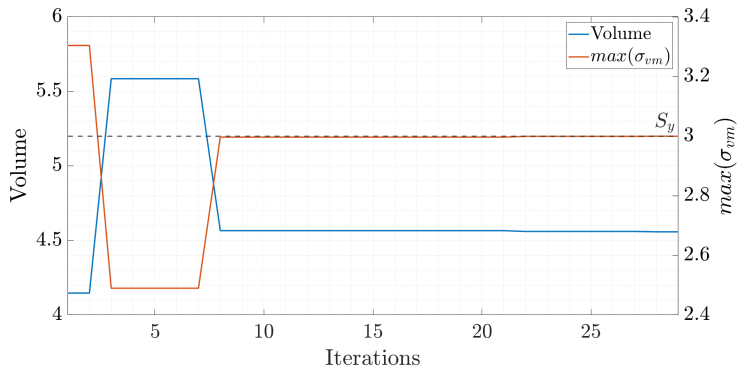
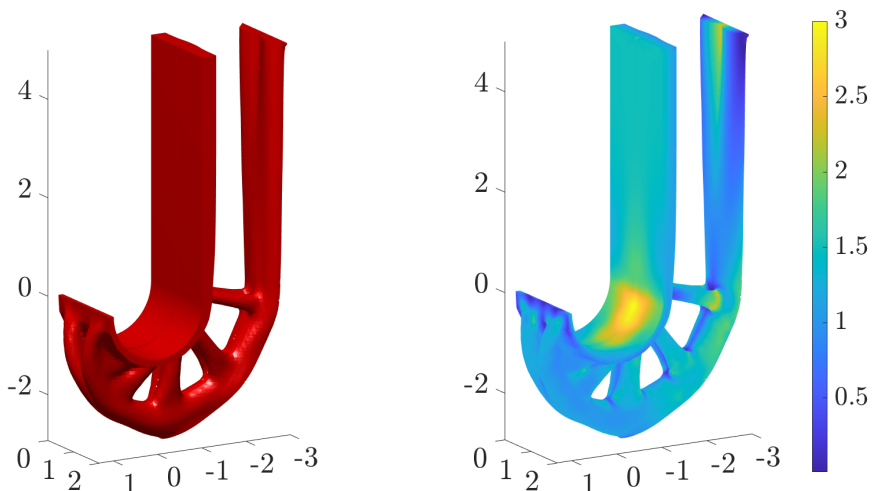


Figure 22: Hook problem. Convergence graph of the Bayesian optimization algorithm.



(a) Representation of the optimal geometry.

(b) Solution of the von Mises stress.

Figure 23: Hook Problem. Representation of the result obtained: optimal geometry (a) and von Mises stress field (b).

6. Conclusion

In order to conclude the current work, we would like to synthesize some final remarks:

- Shape optimization algorithms based on parametrized geometrical representations provide manufacturable solutions but are unable to explore topologies other than the topology described by the prescribed parametrized geometrical model.
- The topology optimization algorithms based on the extensively used SIMP method for structural optimization provide a material distribution that characterizes the topology of the solution. However, this material distribution is not directly suitable for manufacturing.
- In this paper we have proposed a hybrid structural optimization methodology that allies TO and SO algorithms to obtain a synergetic combination of both techniques. This hybrid methodology would represent a more general and powerful structural optimization framework.

- The key aspect of this methodology is the use of a machine learning algorithm to automatically bridge TO and SO algorithm.
- The use of a manifold learning technique, such as the LLE, allowed us to extract the geometrical modes defined by the material distribution information provided by the TO algorithm. In order to correctly use these techniques, the data must be adequately processed. We transform the quasi-boolean material distribution into a richer level-set with the information of the distance of each node to the boundary.
- The existence of a latent embedded space among the material distribution data, allows to extract the geometrical modes that define the solution of the TO algorithm. These modes can then define a parametric geometrical model that will be used to create brand new geometries topologically equivalent to each other.
- The geometry parametrization tool developed in this work may be guided by a user or by an algorithm. In case the tool is managed by a parametrized shape optimization algorithm, this algorithm will consider the embedded space as its design space.

A. Appendices

A.1. Appendix: Topology Optimization

Topology optimization tries to find the optimal material distribution layout over a given physical design domain. As it belongs to the structural optimization field, it handles the minimization of an objective function subjected to the satisfaction of a set of constraints. The topology optimization problem is defined over a design domain, thus it is characterized by a large set of design variables, as any element of the discretization may be material or void. Thanks to the consideration of the fictitious material as a composite behaviour [36] where the elastic properties are defined through a characteristic function, topology optimization has become widely used. The Solid Isotropic Material Penalization (SIMP) method regularizes the material properties as a penalization of the density interpolation function. In addition to the SIMP method, there exist other techniques in the bibliography: strictly based in the 0-1 values of relative density [37–40], level-set based on the nodal values of an implicit function [41–45] and based on the phase-field [46], for instance.

In structural topology optimization we compute the optimal material distribution ρ in a given design domain Ω , which is defined as a continuous variable bounded between 0 (void) and 1 (material). When the structural topology optimization problem is

solved using the SIMP method, introduced in [1–3], usually, the optimization problem consists in minimizing the compliance $c(\rho)$ subject to certain constraints concerning the amount of material. In order to enforce the material/void segregation as much as possible, the method uses a penalization parameter p to penalize intermediate density values. Thus, the SIMP method considers the following optimization problem:

$$(\mathbb{T}\mathbb{O}(v_f)) = \left\{ \begin{array}{ll} \min_{\rho} : & c(\rho) = \frac{1}{2} \int_{\Omega} \boldsymbol{\varepsilon}(\mathbf{u}) \mathbf{D}(\rho) \boldsymbol{\varepsilon}(\mathbf{u}) d\Omega \quad (10a) \\ & \text{with } \mathbf{D}(\rho) = \rho^p \mathbf{D}_0 \quad (10b) \\ \text{subject to:} & V(\rho) = \int_{\Omega} \rho d\Omega = \bar{V}_e \sum \rho_e = v_f V_0 \quad (10c) \\ & a(\mathbf{u}, \mathbf{u}; \rho) = l(\mathbf{u}) \text{ where,} \quad (10d) \\ & a(\mathbf{u}, \boldsymbol{\nu}; \rho) = \int_{\Omega} \boldsymbol{\varepsilon}(\mathbf{u}) \mathbf{D}(\rho) \boldsymbol{\varepsilon}(\boldsymbol{\nu}) d\Omega \quad (10e) \\ & l(\boldsymbol{\nu}) = \int_{\Omega} \mathbf{b}^T \boldsymbol{\nu} d\Omega + \int_{\Gamma_N} \mathbf{t}^T \boldsymbol{\nu} d\Gamma_N \quad (10f) \\ & 0 \leq \rho_{min} \leq \rho \leq 1, \quad (10g) \end{array} \right.$$

considering Voigt’s notation $\boldsymbol{\varepsilon}$ is the strain field and \mathbf{u} is the displacement field. \mathbf{D} is the matrix of the Hooke’s law that relates strains $\boldsymbol{\varepsilon}$ and stresses $\boldsymbol{\sigma}$. As shown in the equation, in the SIMP \mathbf{D} is defined as a function of \mathbf{D}_0 (the matrix of the Hooke’s law for the fully dense material), the density field ρ and the penalization parameter p . Additionally, v_f is a prescribed volume fraction and V_0 is the total volume of the design domain. Finally, an additional side-constraint is added on ρ .

In *Algorithm 1*, we show the structure of the SIMP method with the compliance c as a objective function and the volume fraction as constraint. Additionally, we remark the need of a filtering technique to avoid numerical instabilities, in this case sensitivities filtering. Finally, the use of an updating scheme f to obtain a new set of design variables ρ_{i+1} , such as the Optimality Criteria (OC) [47], is also required.

For the sake of simplicity, we implemented a very basic, not necessarily efficient algorithm (*Algorithm 2*) that performs a heuristic stress scaling procedure [32], whose behaviour has been checked for the examples presented in this paper. The proposed algorithm allows us to explore different volume fraction following a simple stress scaling procedure where the volume fraction is adapted to target a predefined maximum stress value. In particular, the objective of the implemented algorithm is to find the value of volume fraction that would produce a solution whose maximum von Mises stress targets the value of a critical stress, $max(\sigma_{eq}^*) \equiv S_{crit}$. To accomplish this objective, we define two nested loops, the outer loop will drive the selection of the value

Algorithm 1: $\mathbb{T}\mathbb{O}(v_f)$. Compliance minimization algorithm

```

Define  $v_f$ 
Initialize counter:  $i = 0$ 
Initialize relative density at each element  $e$ :  $\rho_{e_i} = v_f$ 
Repeat = 1
while Repeat = 1 do
    Run FE analysis
    Obtain compliance,  $c_i$ , and sensitivities ,  $\partial c_i / \partial \rho_{e_i}$ 
    Filter sensitivities
    Update relative density field:  $\rho_{e_{i+1}} = f(\rho_{e_i}, \partial c_i / \partial \rho_{e_i})$ 
    if  $\|\rho_{e_{i+1}} - \rho_{e_i}\|_\infty \leq tolerance$  then
        | Repeat = 0
    end
     $i = i + 1$ 
end

```

of the volume fraction and evaluate if the prescribed level of stress is achieved. Meanwhile, the inner loop will follow the strategy proposed in the original SIMP method, that minimizes the compliance of the component subjected to a volume fraction constraint, whose value has been defined in the outer loop. As our procedure is based on the original SIMP method, we will only consider minimum compliance solutions. The algorithm described above, may be formulated as follows, where we indicate that the problem is subjected to the calculation of the algorithm that describes the SIMP method (*Algorithm 1*),

$$(\mathbb{T}\mathbb{O}(v_f(S_y))) = \begin{cases} \text{find:} & v_f & (11a) \\ \text{subjected to:} & \max(\sigma_{eq}^*) \equiv S_{crit} & (11b) \\ & \mathbb{T}\mathbb{O}(v_f) & (11c) \end{cases}$$

where S_{crit} is the limit value of σ_{eq}^* . In this work we considered S_{crit} as the yield limit S_y and σ_{eq}^* represents an equivalent uniaxial stress value. In this work, we used as σ_{eq}^* the recovered von Mises stress field σ_{vm}^* evaluated from σ^* , the so called recovered stress field, more accurate than the stress field σ^h provided by the FEM. There are different procedures to obtain σ^* . Because of their accuracy, the most commonly used techniques are the Superconvergent Patch Recovery (SPR) technique (proposed by Zienkiewicz and Zhu [48]) and enhanced versions of this technique, like the SPR-C technique [49].

The use of the density field ρ in topology optimization implies, a particular definition of the stress field to keep consistency with the expression of the strain energy (compliance) in (10a). We can rewrite equation (10a) as:

$$\boldsymbol{\sigma}_e^{h\rho} = \mathbf{D}(\rho_e)\boldsymbol{\varepsilon}_e^h = \rho_e^p \mathbf{D}_0 \boldsymbol{\varepsilon}_e^h = \rho_e^p \boldsymbol{\sigma}_e^{h_0} \quad (12)$$

where $\boldsymbol{\sigma}_e^{h_0} = \mathbf{D}_0 \boldsymbol{\varepsilon}_e^h$ would represent the original FE stress field at the element, before considering the density correction. The penalization parameter p in (12) is consistent with equation (10b) [33, 50]. Taking into account equation (12), for the evaluation of the recovered stress field we propose to smooth the original stress field at elements, $\boldsymbol{\sigma}^{h_0}$, and then to modify the resulting recovered stress field using the density correction.

The steps to address the problem in (11) are presented in *Algorithm 2*. As previously mentioned, the structure of the problem is a nested optimization loop. The outer loop searches for the volume fraction whose corresponding maximum von Mises stress equals the yield limit, while the inner loop minimizes the compliance of the component subjected to the volume fraction defined in the outer loop. For the sake of simplicity, the updating scheme g in *Algorithm 2* consists of a quadratic curve fitting procedure. This method uses the information of the last 3 iterations, specifically the values of volume fractions \bar{v}_f and their corresponding stress $\overline{max(\sigma_{vm}^*)}$, to fit a surrogate model and infer the next value of v_f^{i+1} that would produce a $max(\sigma_{vm}^*) \equiv S_y$. A schematic representation of this strategy is show in Figure 24.

Algorithm 2: $\mathbb{T}\mathbb{O}(v_f(S_y))$. Stress scaling algorithm for evaluation of volume fraction for which $max(\sigma_{vm}^*) \equiv S_y$, with inner topology optimization loop based on the SIMP method.

```

Set  $S_y$ 
Initialize counter:  $i = 0$ 
Initialize volume fraction  $v_f^i$ 
Repeat = 1
while Repeat = 1 do
     $i = i + 1$ 
    Run Algorithm 1  $\mathbb{T}\mathbb{O}(v_f^i)$ 
    Obtain the stresses of the optimal layout distribution
    Evaluate the maximum von Mises stress:  $max(\sigma_{vm}^{*i})$ 
    if  $max(\sigma_{vm}^{*i}) \equiv S_y$  then
        | Repeat = 0
    end
    Update the volume fraction:  $v_f^{i+1} = g(\bar{v}_f, \overline{max(\sigma_{vm}^*)}, S_y)$ 
end

```

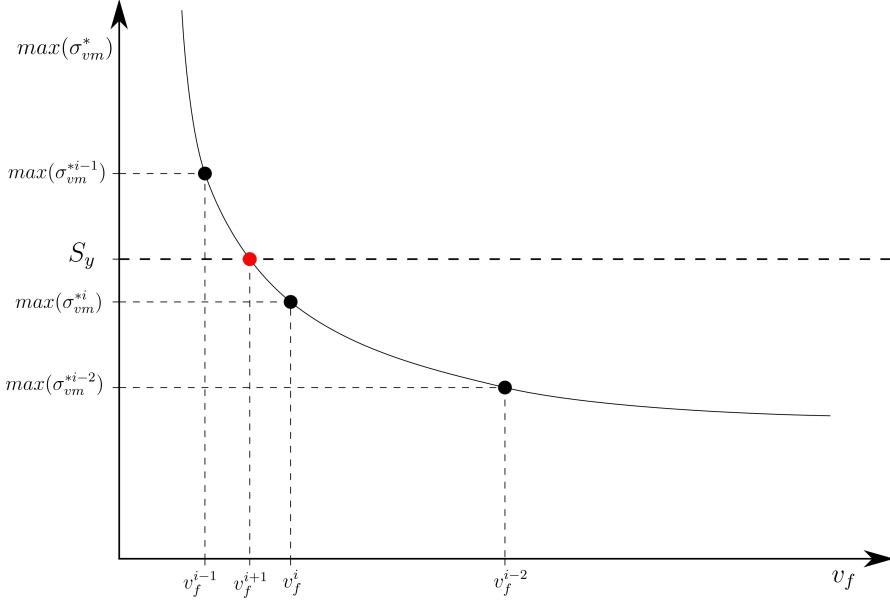


Figure 24: Schematic representation of the curve fitting procedure (g in *Algorithm 2*). Considering the volume fraction exploration algorithm, we use the value of the last three iterations and its corresponding maximum von Mises stress, and adjust a curve. The volume fraction value for which this curve will reach the value of the yield limit (S_y) corresponds to the next value of volume fraction.

A.2. Appendix: Shape Optimization

In this work we consider the parametrized shape optimization where the boundary is defined *a priori* by means of a set of parameters, also known as design variables \mathbf{a} , as shown in Figure 25.

The shape optimization formulation applied to the structural behaviour commonly uses the volume or mass as the objective function and a given measure of the stresses as a constraint, for instance to keep the maximum von Mises stress $max(\sigma_{vm}^*)$ below the yield stress limit S_y , as follows:

$$(\mathbb{S}\mathbb{O}_\sigma(S_y)) = \begin{cases} \min_a : & \text{Volume}(a) & (13a) \\ \text{subjected to:} & max(\sigma_{vm}^*(a)) \leq S_y & (13b) \end{cases}$$

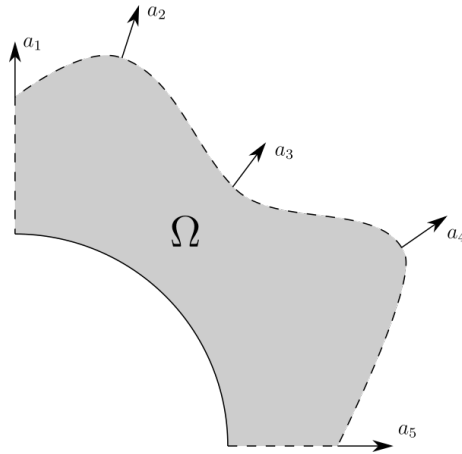


Figure 25: Parametrized boundary of the design domain.

A.3. Appendix: Manifold Learning

The data in most fields of science and engineering has high dimensionality. In order to manage high quantity of data and to handle it adequately, its dimension must be reduced. Manifold Learning (ML) techniques are a set of algorithms that transform the high-dimensional data into a reduced space. This manifold preserves the original structure of the high-dimensional space by extracting the main principal characteristics. The manifold learning eases the classification, visualization or even understanding of the high-dimensional data.

Additionally, in this work the reduced dimensions are used to generate new high-dimensional data, not existing in the original dataset. Linear techniques, such as Principal Component Analysis (PCA) were initially used to perform the dimensionality reduction. But in last decades, non-linear techniques have been developed to obtain the manifold space. The advantage of this techniques is that they are able to transform complex non-linear data. We propose the use of the Locally Linear Embedding (LLE). Figure 26 shows how it maintains the structure of a given dataset.

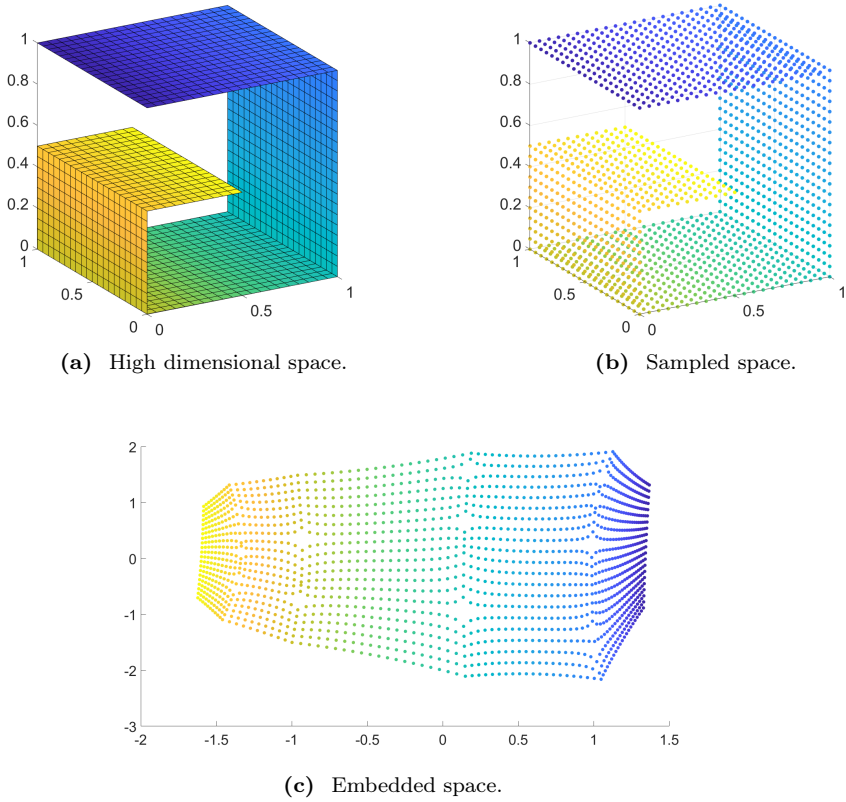


Figure 26: Example of the LLE algorithm, (a) represents the original high dimensional data, (b) shows a sampled space from the high dimensional space and (c) illustrates the embedded manifold provided by the LLE algorithm over the sampled high dimensional space.

A.4. Appendix: Cartesian grid Finite Element Method (*cgFEM*)

The accuracy of the FE analysis is a relevant factor in optimization processes but, as these are iterative algorithms, the computational efficiency of the FE analysis is critical. The use of meshes where all the elements have the same shape helps to improve the overall performance of the FE analysis. In these cases, the stiffness matrix evaluated for one element can be used for any other element having the same material properties simply considering a stiffness scaling factor evaluated as a function of the ratio of the element sizes. In fact, in most numerical examples shown in the literature of topology optimization, the domain used for the optimization is a rectangle (2D) or

a cuboid (3D), as these shapes can be easily meshed with Cartesian elements. However, practical applications cannot be restricted to this kind of domains. If standard boundary-conforming FE meshes were used, it would not be possible to ensure that all the elements have the same shape. The use of Fictitious Domain Methods (FDM), where the FE mesh is not necessarily conforming to the geometry, like the Finite Cell Method [26–28] or the Cartesian grid finite element method (*cgFEM*) [24, 25], both of them based on the use of Cartesian grids, is an alternative to solve this issue.

In particular, in *cgFEM* we embed the physical domain, Ω_{Phys} , in a cuboid defining the fictitious domain, Ω_{Fic} . The fictitious domain is meshed with elements of different levels. Considering the *Level-0* mesh as a single element embedding the cuboid, we split the mesh into 8 new Cartesian elements that structure the *Level-1* mesh. We repeat the same process recursively to create meshes with higher refinement levels, so they have a hierarchical structure. Then, the mesh for the FE analysis is created with elements of different levels of refinement. In order to impose C^0 continuity between contiguous elements from different level, we use multi-point constraints.

Figure 27a represents an example of physical domain, Ω_{Phys} , with a sufficiently smooth boundary Γ , embedded into the embedding domain Ω_{Fic} . The boundary Γ of Ω_{Phys} can be divided into two non-overlapping parts, Γ_D and Γ_N , where the Dirichlet and Neumann conditions are respectively imposed. Figure 27b, shows the embedding domain Ω_{Fic} , discretized with Cartesian elements. The following expression relates the different domains:

$$\Omega_{Phys} \subseteq \Omega_{Fic} = \bigcup_{e=1}^{n_e} \Omega^e \quad (14)$$

Figure 28 shows a 3D example analyzed with *cgFEM* that is used here to summarize the main characteristics of this methodology:

- *cgFEM* is an efficient FE analysis technique as it considers a Cartesian discretization of the embedding domain (see Figure 28a).
- The analysis mesh used by *cgFEM* to model the physical domain Ω_{Phys} can consider elements of different refinement levels. These elements include elements fully placed into Ω_{Phys} and elements cut by its boundary Γ . Elements fully outside of Ω_{Phys} are not considered in the analysis mesh (see Figure 28b).
- *cgFEM* uses a specifically designed integration mesh (Figure 28c), based on the NEFEM integration approach [51] that allows to consider the exact boundary representation given by, for instance, NURBS or T-Splines [52].

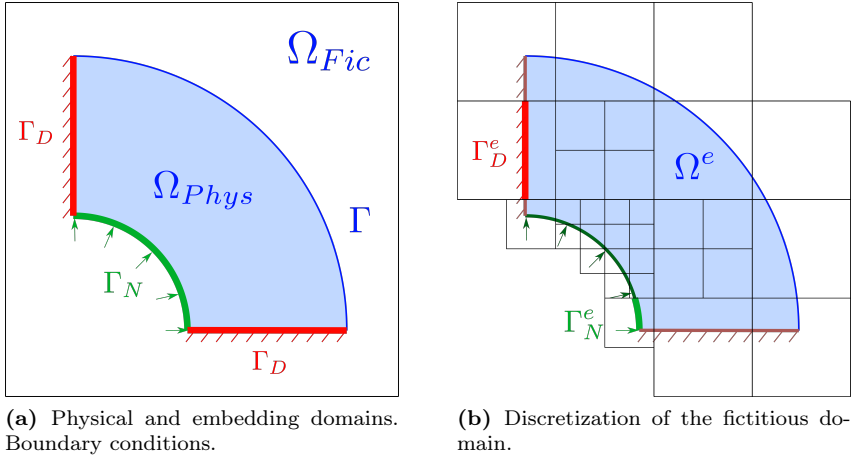
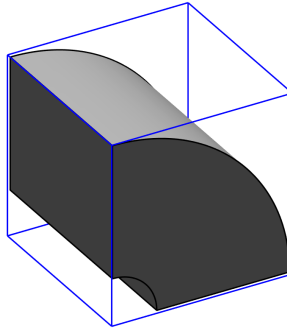
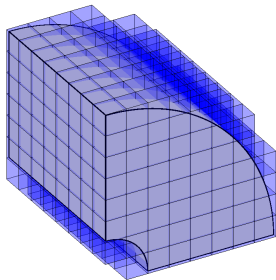


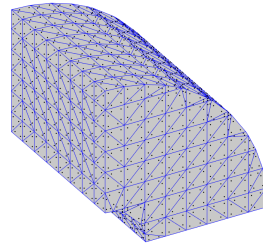
Figure 27: Cartesian grid finite element method (*cgFEM*). Representation of the physical domain and the discretization of the fictitious domain.



(a) Physical domain Ω_{Phys} (Cylinder) embedded in the fictitious domain Ω_{Fic} (cube).



(b) Discretization of the fictitious domain: analysis mesh.



(c) Integration Mesh.

Figure 28: *cgFEM*. Different domains involved in a finite element analysis.

A stabilized Lagrange multipliers formulation is used to impose boundary conditions in elements cut by the Dirichlet boundary. As a result, equation (10d) is replaced by the following equation,

$$a(\mathbf{u}, \boldsymbol{\nu}) + \frac{k}{h} \int_{\Gamma_D} \mathbf{u} \cdot \boldsymbol{\nu} d\Gamma = l(\boldsymbol{\nu}) + \frac{k}{h} \int_{\Gamma_D} \mathbf{g} \cdot \boldsymbol{\nu} d\Gamma + \int_{\Gamma_D} \mathbf{T}(\bar{\mathbf{u}}) \cdot \boldsymbol{\nu} d\Gamma \quad (15)$$

A detailed description of the derivation of this equation and the description of its behaviour, out of the scope of this paper, can be found in Reference [53]. The most relevant feature of the proposed stabilized Lagrange multipliers formulation is that the stabilization term \mathbf{T} is evaluated as a recovered [48, 49] traction field. As this traction field depends on the FE solution, an iterative process, i.e. Richardson iterations, is used to solve (15). The stabilization terms are not affected by ρ and do not play any role in the TO procedure.

Acknowledgements

The authors gratefully acknowledge the financial support of Conselleria d'Educació, Investigació, Cultura i Esport (Generalitat Valenciana, project Prometeo/2016/007), Ministerio de Economía, Industria y Competitividad (project DPI2017-89816-R) and Ministerio de Educación (FPU16/07121).

References

- [1] M. P. Bendsøe, "Optimal shape design as a material distribution problem," *Structural Optimization*, vol. 1, no. 4, pp. 193–202, 1989.
- [2] M. Zhou and G. I. Rozvany, "The COC algorithm, Part II: Topological, geometrical and generalized shape optimization," *Computer Methods in Applied Mechanics and Engineering*, vol. 89, no. 1-3, pp. 309–336, 1991.
- [3] H. P. Mlejnek, "Some aspects of the genesis of structures," *Structural Optimization*, vol. 5, no. 1-2, pp. 64–69, 1992.
- [4] M. Y. Wang, X. Wang, and D. Guo, "A level set method for structural topology optimization," *Computer Methods in Applied Mechanics and Engineering*, vol. 192, no. 1-2, pp. 227–246, 2003.

-
- [5] M. Y. Wang and X. Wang, "Color" level sets: A multi-phase method for structural topology optimization with multiple materials," *Computer Methods in Applied Mechanics and Engineering*, vol. 193, no. 6-8, pp. 469–496, 2004.
- [6] L. Shu, M. Yu Wang, and Z. Ma, "Level set based topology optimization of vibrating structures for coupled acoustic-structural dynamics," *Computers and Structures*, vol. 132, pp. 34–42, 2014.
- [7] L. Dedè, M. J. Borden, and T. J. Hughes, "Isogeometric Analysis for Topology Optimization with a Phase Field Model," *Archives of Computational Methods in Engineering*, vol. 19, no. 3, pp. 427–465, 2012.
- [8] A. L. Gain and G. H. Paulino, "Phase-field based topology optimization with polygonal elements: A finite volume approach for the evolution equation," *Structural and Multidisciplinary Optimization*, vol. 46, no. 3, pp. 327–342, 2012.
- [9] S. H. Jeong, G. H. Yoon, A. Takezawa, and D. H. Choi, "Development of a novel phase-field method for local stress-based shape and topology optimization," *Computers and Structures*, vol. 132, pp. 84–98, 2014.
- [10] M. Papadrakakis and B. H. Topping, *Innovative computational methods for structural mechanics*. Saxe-Coburg Publications, 1999.
- [11] P. S. Tang and K. H. Chang, "Integration of topology and shape optimization for design of structural components," *Structural and Multidisciplinary Optimization*, vol. 22, no. 1, pp. 65–82, 2001.
- [12] G. W. Jang, K. J. Kim, and Y. Y. Kim, "Integrated topology and shape optimization software for compliant MEMS mechanism design," *Advances in Engineering Software*, vol. 39, no. 1, pp. 1–14, 2008.
- [13] A. R. Yildiz, N. Öztürk, N. Kaya, and F. Öztürk, "Integrated optimal topology design and shape optimization using neural networks," *Structural and Multidisciplinary Optimization*, vol. 25, no. 4, pp. 251–260, 2003.
- [14] M. Bremicker, M. Chirehdast, N. Kikuchi, and P. Y. Papalambros, "Integrated topology and shape optimization in structural design," *Mechanics of Structures and Machines*, vol. 19, no. 4, pp. 551–587, 1991.
- [15] G. A. Méndez Algarra and A. Tovar Pérez, "Integrating topology and shape optimization: a way to reduce weight in structural ship design," *Ciencia y tecnología de buques*, vol. 3, pp. 83–92, 1 1.
- [16] M. P. Bendsøe and H. C. Rodrigues, "Integrated topology and boundary shape optimization of 2-D solids," *Computer Methods in Applied Mechanics and Engineering*, vol. 87, no. 1, pp. 15–34, 1991.

- [17] M. Zhou, N. Pagaldipti, H. L. Thomas, and Y. K. Shyy, “An integrated approach to topology, sizing, and shape optimization,” *Structural and Multidisciplinary Optimization*, vol. 26, no. 5, pp. 308–317, 2004.
- [18] A. N. Christiansen, J. A. Bærentzen, M. Nobel-Jørgensen, N. Aage, and O. Sigmund, “Combined shape and topology optimization of 3D structures,” *Computers and Graphics (Pergamon)*, vol. 46, pp. 25–35, 2015.
- [19] T. T. Nguyen, J. A. Bærentzen, O. Sigmund, and N. Aage, “Efficient hybrid topology and shape optimization combining implicit and explicit design representations,” *Structural and Multidisciplinary Optimization*, vol. 62, no. 3, pp. 1061–1069, 2020.
- [20] L. Jiang, S. Chen, and X. Jiao, “Parametric shape and topology optimization: A new level set approach based on cardinal basis functions,” *International Journal for Numerical Methods in Engineering*, vol. 114, no. 1, pp. 66–87, 2018.
- [21] N. Ferro, S. Micheletti, and S. Perotto, “An optimization algorithm for automatic structural design,” *Computer Methods in Applied Mechanics and Engineering*, vol. 372, p. 113335, 2020.
- [22] I. T. Jolliffe, “Principal Component Analysis, Second Edition,” *Springer Series in Statistics*, vol. 98, p. 487, 2002.
- [23] S. T. Roweis and L. K. Saul, “Nonlinear dimensionality reduction by locally linear embedding,” *Science*, vol. 290, no. 5500, pp. 2323–2326, 2000.
- [24] E. Nadal, J. J. Ródenas, J. Albelda, M. Tur, J. E. Tarancón, and F. J. Fuenmayor, “Efficient Finite Element Methodology based on Cartesian grids: Application to structural shape optimization,” *Abstract and Applied Analysis*, vol. 2013, pp. 1–19, 2013.
- [25] E. Nadal, “Cartesian grid FEM (cgFEM): High performance h-adaptive FE analysis with efficient error control. Application to structural shape optimization,” p. 312, 2014.
- [26] J. Parvizian, A. Düster, and E. Rank, “Finite cell method : h- and p-extension for embedded domain problems in solid mechanics,” *Computational Mechanics*, vol. 41, no. 1, pp. 121–133, 2007.
- [27] A. Düster, J. Parvizian, Z. Yang, and E. Rank, “The finite cell method for three-dimensional problems of solid mechanics,” *Computer Methods in Applied Mechanics and Engineering*, vol. 197, no. 45-48, pp. 3768–3782, 2008.
- [28] J. Parvizian, A. Düster, and E. Rank, “Topology optimization using the finite cell method,” *Optimization and Engineering*, vol. 13, no. 1, pp. 57–78, 2012.

-
- [29] J. E. Shigley, C. R. Mischke, and R. G. Budynas, *Shigley's mechanical engineering design - 9th Ed.* PhD thesis, 2002.
- [30] D. González, E. Cueto, and F. Chinesta, "Computational Patient Avatars for Surgery Planning," *Annals of Biomedical Engineering*, vol. 44, no. 1, pp. 35–45, 2016.
- [31] W. E. Lorensen and H. E. Cline, "Marching Cubes: A high resolution 3D surface construction algorithm.," *Computer Graphics (ACM)*, vol. 21, no. 4, pp. 163–169, 1987.
- [32] D. Muñoz, J. Albelda, J. J. Ródenas, and E. Nadal, "Improvement in 3D topology optimization with h-adaptive refinement using the Cartesian grid Finite Element Method," *International Journal for Numerical Methods in Engineering*, 2021.
- [33] C. Le, J. Norato, T. Bruns, C. Ha, and D. Tortorelli, "Stress-based topology optimization for continua," *Structural and Multidisciplinary Optimization*, vol. 41, no. 4, pp. 605–620, 2010.
- [34] D. Yang, H. Liu, W. Zhang, and S. Li, "Stress-constrained topology optimization based on maximum stress measures," *Computers and Structures*, vol. 198, pp. 23–39, 2018.
- [35] S. T. Roweis and L. K. Saul, "Nonlinear Dimensionality Reduction by Locally Linear Embedding," *Science*, vol. 290, pp. 2323–2326.
- [36] M. P. Bendsøe and N. Kikuchi, "Generating optimal topologies in structural design using a homogenization method," *Computer Methods in Applied Mechanics and Engineering*, vol. 71, no. 2, pp. 197–224, 1988.
- [37] Y. M. Xie and G. P. Steven, "A simple evolutionary procedure for structural optimization," *Computers and Structures*, vol. 49, no. 5, pp. 885–896, 1993.
- [38] P. Tanskanen, "The evolutionary structural optimization method: Theoretical aspects," *Computer Methods in Applied Mechanics and Engineering*, vol. 191, no. 47-48, pp. 5485–5498, 2002.
- [39] D. J. Munk, G. A. Vio, and G. P. Steven, "Topology and shape optimization methods using evolutionary algorithms: a review," *Structural and Multidisciplinary Optimization*, vol. 52, no. 3, pp. 613–631, 2015.
- [40] P. A. Vikhar, "Evolutionary algorithms: A critical review and its future prospects," in *2016 International Conference on Global Trends in Signal Processing, Information Computing and Communication (ICGTSPICC)*, pp. 261–265, IEEE, 2016.
- [41] M. Y. Wang, X. Wang, and D. Guo, "A level set method for structural topology optimization," *Computer Methods in Applied Mechanics and Engineering*, vol. 192, no. 1-2, pp. 227–246, 2003.

- [42] M. Y. Wang and X. Wang, "Color" level sets: A multi-phase method for structural topology optimization with multiple materials," *Computer Methods in Applied Mechanics and Engineering*, vol. 193, no. 6-8, pp. 469–496, 2004.
- [43] G. Allaire, F. De Gournay, F. Jouve, and A.-M. Toader, "Structural optimization using topological and shape sensitivity via a level set method," tech. rep., 2005.
- [44] S. Amstutz and H. Andrä, "A new algorithm for topology optimization using a level-set method," *Journal of Computational Physics*, vol. 216, no. 2, pp. 573–588, 2006.
- [45] T. Yamada, K. Izui, S. Nishiwaki, and A. Takezawa, "A topology optimization method based on the level set method incorporating a fictitious interface energy," *Computer Methods in Applied Mechanics and Engineering*, vol. 199, no. 45-48, pp. 2876–2891, 2010.
- [46] L. Dedè, M. J. Borden, and T. J. Hughes, "Isogeometric Analysis for Topology Optimization with a Phase Field Model," *Archives of Computational Methods in Engineering*, vol. 19, no. 3, pp. 427–465, 2012.
- [47] O. Sigmund, "A 99 line topology optimization code written in matlab," *Structural and Multidisciplinary Optimization*, vol. 21, no. 2, pp. 120–127, 2001.
- [48] O. C. Zienkiewicz and J. Z. Zhu, "The superconvergent patch recovery (SPR) and adaptive finite element refinement," *Computer Methods in Applied Mechanics and Engineering*, vol. 101, no. 1-3, pp. 207–224, 1992.
- [49] J. J. Ródenas, M. Tur, F. J. Fuenmayor, and A. Vercher, "Improvement of the superconvergent patch recovery technique by the use of constraint equations: The SPR-C technique," *International Journal for Numerical Methods in Engineering*, vol. 70, no. 6, pp. 705–727, 2007.
- [50] M. Bruggi, "On an alternative approach to stress constraints relaxation in topology optimization," *Structural and Multidisciplinary Optimization*, vol. 36, no. 2, pp. 125–141, 2008.
- [51] R. Sevilla, S. Fernández-Méndez, and A. Huerta, "NURBS-enhanced finite element method (NEFEM)," *International Journal for Numerical Methods in Engineering*, vol. 76, no. 1, pp. 56–83, 2008.
- [52] O. Marco, R. Sevilla, Y. Zhang, J. J. Ródenas, and M. Tur, "Exact 3D boundary representation in finite element analysis based on Cartesian grids independent of the geometry," *International Journal for Numerical Methods in Engineering*, vol. 103, no. 6, pp. 445–468, 2015.
- [53] M. Tur, J. Albelda, O. Marco, and J. J. Ródenas, "Stabilized method of imposing Dirichlet boundary conditions using a recovered stress field," *Computer Methods in Applied Mechanics and Engineering*, vol. 296, pp. 352–375, 2015.

PAPER C

Manifold learning for coherent design interpolation based on geometrical and topological descriptors

D. Muñoz, O. Allix, F. Chinesta, J. J. Ródenas and E. Nadal

Computer Methods in Applied Mechanics and Engineering

Volume 405, 2023

DOI: [10.1016/j.cma.2022.115859](https://doi.org/10.1016/j.cma.2022.115859)

Abstract

In the context of intellectual property in the manufacturing industry, know-how is referred to practical knowledge on how to accomplish a specific task. This know-how is often difficult to be synthesised in a set of rules or steps as it remains in the intuition and expertise of engineers, designers, and other professionals. Today, a new research line in this concern spot-up thanks to the explosion of Artificial Intelligence and Machine Learning algorithms and its alliance with Computational Mechanics and Optimisation tools. However, a key aspect with industrial design is the scarcity of available data, making it problematic to rely on deep-learning approaches. Assuming that the existing designs live in a manifold, in this paper, we propose a synergistic use of existing Machine Learning tools to infer a reduced manifold from the existing limited set of designs and, then, to use it to interpolate between the individuals, working as a generator basis, to create new and coherent designs. For this, a key aspect is to be able to properly interpolate in the reduced manifold, which requires a proper clustering of the individuals. From our experience, due to the scarcity of data, adding topological descriptors to geometrical ones considerably improves the quality of the clustering.

Thus, a distance, mixing topology and geometry is proposed. This distance is used both, for the clustering and for the interpolation. For the interpolation, relying on optimal transport appear to be mandatory. Examples of growing complexity are proposed to illustrate the goodness of the method.

Key words

Structural Optimisation, Machine Learning, Dimensionality Reduction, Locally Linear Embedding, Topological Data Analysis, Optimal Transport

Contents

1	Introduction	177
2	Methodology	178
2.1	Reference database	179
2.2	Geometry-based strategy	180
2.2.1	Overview of the original LLE algorithm	181
2.2.2	Application of the LLE to reference database: results and draw-backs	182
2.3	Geometry and Topology-based strategy	183
2.3.1	Topological Data Analysis overview	183
2.3.2	Modifications in LLE to consider geometry and topology	186
2.3.3	Optimal Transport-based interpolation to recover dimensionality	189
3	Numerical Example	191
3.1	Topological characterization	193
3.2	Influence of the weighting factor θ	194
3.3	Results	196
4	Conclusions	202
5	Future works	203
	Acknowledgements	203
	References	204

1. Introduction

In the context of intellectual property in the industry, know-how is referred to the practical knowledge about how to accomplish a specific task [1]. Most of this know-how resides in the intuition and expertise of engineers and designers, among a wide variety of professionals. Thus, it is extremely difficult to characterize by rules or steps. In order to not lose a given know-how, we would like to be able to extract it from the objects previously created.

For this, as it is done today in many other domains in engineering, we propose to ally tools emerging from Artificial Intelligence and Machine learning with techniques belonging to Computational Mechanics and Optimisation. But what could be a possible strategy? A key difficulty is scarcity in the number of designs in a given industry. This implies that it is not possible to properly use deep-learning approaches for this purpose [2]. Therefore, among the available tools, we have selected those allowing us to infer, if possible, a reduced manifold of the existing designs. Being its existence our main hypothesis. It will be possible if these techniques can adequately approximate the low dimensionality space where the current designs belong to. This is mandatory because, with few individuals, compared to deep-learning approaches, one can expect to interpolate, in a sense to be precised later, only in low dimensional space.

In our scientific context, a related question naturally arises: how to characterise the existing component designs? This first paper will consider the design as the objects' geometries. Clearly, in the future, we should include other characterisations, as the strains or stress fields, for instance, two crucial measures in the structural mechanics field. Even considering this restricted definition of design, one should be precise in characterising a geometry because there exist multiple ways to do it. In fact, it is our experience that this choice may significantly influence the dimensions of the reduced manifold. A criterion of choice is that the implicit space should be a manifold of possible designs. That is, we need to create appropriate designs when interpolating between existing designs.

The first part of the paper is devoted to finding a shape characterisation that allows obtaining an attractive latent space of existing designs and interpolating in this reduced space. The designs are characterized by their geometry and topology. The relevance of the geometrical information is evident. However, in the context of small data, topology play an important role since it is additional information than the algorithms may use. Among those descriptors, the easiest to manipulate are those based on fields. Thus, for the geometry, we employ the Level-set Functions [3,4]. For the topology we use the principle of persistent homology [5], which belongs to the field of Topological Data Analysis tools [6,7], to create a geometrical 2D image of the topology of the object, the so-called persistence image [8]. Mixing geometrical and

topological descriptors is thus possible. Then, we adopt the use of Manifold Learning techniques (ML) [9] to reduce the dimension of the data by extracting the latent structure stored in it. There exists an immense variety of techniques in the ML field, such as the Principal Component Analysis (PCA) [9], which finds the direction of maximum variation in the original dataset. To overcome the limit of this linear technique, non-linear extensions have been proposed. These techniques can preserve the non-linear nature of the original dataset. Among the different non-linear techniques such as Sammon mapping [10], k -PCA [11], Laplacian eigenmaps [12], Isomaps [13] and Autoencoders [14–16], we select the Locally Linear Embedding (LLE) [17]. This technique has been successfully used when data is highly non-linear [18], as in the case of the information coming from the component’s topology, and has shown good results in previous works [19, 20].

The second part of the paper is devoted to the interpolation of objects in the manifold of the existing designs. Apart from dimensionality reduction, rather than using the entire basis, LLE identifies the neighbours used to reconstruct an individual decreasing the computational cost. The evaluation of the vicinity needed for LLE is usually made employing the distances between individuals, which, in the standard LLE implementation, corresponds to the L_2 euclidean metric. As the scarcity of data is a usual situation in the context we work on, relying on the euclidean norm and the linear interpolation as a basis for the component generator could be ineffective and could also produce components with no physical sense and artefacts. Then, we propose to make use of Optimal Transportation tools (OT) [21–24], which include the Wasserstein metric [22, 23]. Additionally, we will consider this metric in the solution of the barycentre problem [25] to interpolate within the objects based on the vicinities defined by the LLE. As a reminder, solving the search of the barycentre problem considering the L_2 euclidean metric is equivalent of using the linear interpolation.

The outline of this article is established as follows. We intend to illustrate the basic ideas with a simple example in each section before applying them to a more complex numerical example of a car bumper. Then, we first try the standard procedure with the LLE algorithm, and in the following sections, we assess the improvements achieved when applying the techniques presented in this introduction. Later, we employ the selected strategy in the car bumper example. To finalise, we conclude the article by gathering some final thoughts.

2. Methodology

Figure 1 represents the main steps of the methodology presented. In summary, the main goal of this work is to define an interpolation procedure between existing

components living in a common manifold. The procedure has an offline and an online phase. The offline phase refers to gathering the dataset and the subsequent treatment that generates the reduced manifold, while the online phase involves the navigation within the manifold and the creation of new components through the interpolation scheme.

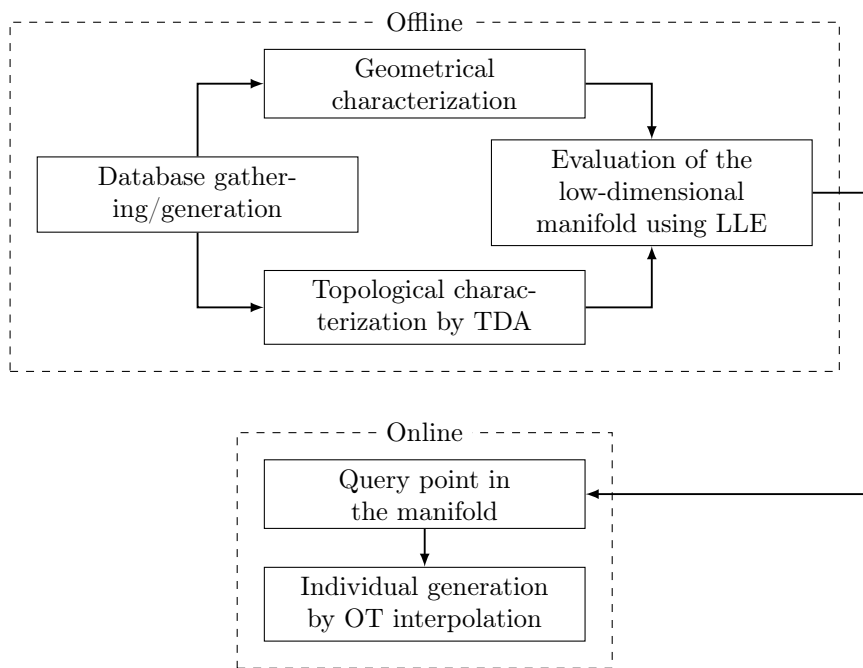


Figure 1: Simplified workflow of the methodology proposed.

2.1. Reference database

We will apply each of the strategies considered in this paper to an elementary academic problem. It consists of a dataset of 75 individuals, the geometry being a square including one, two and three holes, preserving the local shape, but modifying the position. Therefore, the geometry is defined with only 3 parameters: the horizontal position, the vertical position and the number of holes. The reference database is composed of the shape descriptors of each individual. In the introduction, we suggested that geometry descriptors based on domain fields are more convenient for our purpose. Thus, for the geometrical characterisation, we rely on the Level-set method [3, 4]. Among the variety of level-set functions available in the bibliography, we employ the Signed Distance Function (SDF), which has the particularity of storing the distance to the boundary of the component. Therefore, the zero-isovalue of

the level-set function corresponds to the boundary of the component [26–31]. In this example, each level-set function is discretized by 961 nodes. A subset of the database is shown in Figure 2. In this Figure, as in the rest of the paper, the geometry of each individual is defined by its SDF.

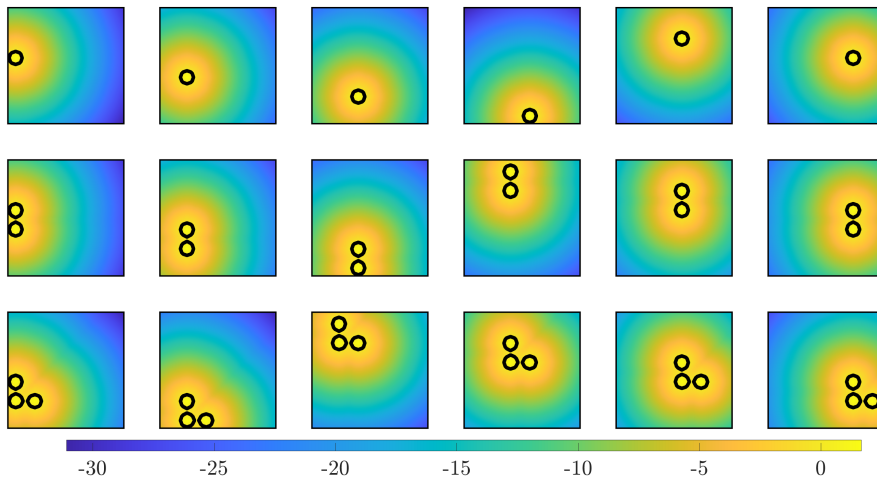


Figure 2: Signed Distance Function of a representative sampling of the complete database (75 individuals).

2.2. Geometry-based strategy

Following the steps illustrated in the workflow scheme, see Figure 1, the database is gathered and represented in the Figure 2. As we mentioned above, we consider an elementary academic example to describe the proposed strategy. In Figure 2, we show a sampling of the 75 individuals that compose the database. Each of the individuals is defined by its Signed Distance Function whose zero level (black contour in the images) represents their geometry. Each individual of the database consists of a set of circles of constant diameter that can be located at any position in a square domain. In the standard implementation of the strategy, no further preprocessing of the data is needed, that is, the topological characterization (step 3 in Figure 1) is not applied. Then, the next step is to reduce the dimensionality of the database. As we expect the manifold to be of a non-linear nature, we rely here on the Locally Linear Embedding (LLE) algorithm. We chose the LLE algorithm since it provides not only the manifold but a set of non-linear modes that could be used to move into the manifold.

2.2.1. Overview of the original LLE algorithm

Let \mathbf{X}_i be each sample of the training set in the high-dimensional space. The LLE algorithm hypothesize that any point in the database must be obtained as a weighted linear combination of k neighbours with w_{ij} , $j \in [1, k]$ as,

$$\mathbf{X}_i = \sum_j^k w_{ij} \mathbf{X}_j, \quad (1)$$

The neighbours that compose the vicinity of each individual are obtained by choosing the k individuals with smallest distance d_{ij} , evaluated as,

$$d_{ij} = \|\mathbf{X}_i - \mathbf{X}_j\| \quad (2)$$

where $\|\cdot\|$ is the Frobenius norm.

The number of neighbours k is user-defined, and the weights w_{ij} are obtained by minimising the functional represented in equation (3):

$$\varepsilon(\mathbf{w}) = \sum_i \|\mathbf{X}_i - \sum_j^k w_{ij} \mathbf{X}_j\|^2, \quad (3)$$

where w_{ij} are subjected to the constraint $\sum_j w_{ij} = 1$. The LLE entrust that these weights are invariant to space transformations. Hence the value of the weights is preserved when changing between spaces. Keeping the weights unchanged, the projection of \mathbf{X}_i on the reduced space, denoted \mathbf{Y}_i is defined by the minimisation of the functional in (4):

$$\epsilon(\mathbf{Y}) = \sum_i \|\mathbf{Y}_i - \sum_j^k w_{ij} \mathbf{Y}_j\|^2, \quad (4)$$

If all eigenvectors are kept, all the original information is stored, otherwise, we retain the eigenvectors associated to the d smallest eigenvalues and maintain the latent structure of the database. The number of eigenvalues is defined by the user and it is assumed to be small. In the reference example, if the technique succeed, it will be 3.

High-dimensional individuals may be obtained as a weighted linear combination of k neighbours, therefore, the reduced manifold of existing designs may be defined as the set of points \mathbf{Y} such that:

$$\mathbf{Y} = \left\{ \sum_j^k \bar{w}_{ij} \mathbf{Y}_j \in \mathbb{R}^d \mid \sum_j^k \bar{w}_{ij} = 1 \right\} \quad (5)$$

Even though this set is never constructed, an element $\bar{\mathbf{Y}}_i$ in \mathbf{Y} may be associated to the element $\bar{\mathbf{X}}_i$ of the original space as,

$$\bar{\mathbf{X}}_i = \sum_j^k \bar{w}_{ij} \mathbf{X}_j, \tag{6}$$

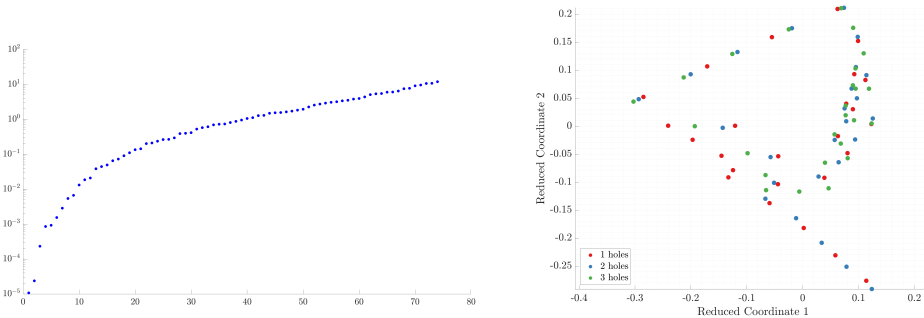
where the weights \bar{w}_{ij} are obtained by minimizing the following functional:

$$\bar{\epsilon}(\bar{\mathbf{w}}) = \|\bar{\mathbf{Y}}_i - \sum_j^k \bar{w}_{ij} \mathbf{Y}_j\|^2. \tag{7}$$

When seeking for a new individual, for example in order to optimise a product, one may search for the best element within the manifold. The technique to perform such a search will be the object of a companion paper.

2.2.2. Application of the LLE to reference database: results and drawbacks

We apply here the LLE algorithm to the reference database with the number of neighbours in the vicinity taken as $k = 4$. The resulting eigenvalues are represented in Figure 3a while, in Figure 3b, we illustrate the spatial distribution of the coordinates in the reduced space, where each individual is classified by its topology, that is, the number of holes is represented by the colour of the points.



(a) Eigenvalues obtained from minimizing (4). (b) Two first coordinates of the reduced latent space.

Figure 3: Resulting eigenvalue distribution (a) and reduced coordinates (b) by using the LLE technique with the original data.

On Figure 3a the eigenvalue spectrum of the problem in (4) is displayed. On this graph the 2 lowest eigenvalues are separated from the rest of the spectrum. This

information is used to retain a latent space of dimension 2. In this case, we know beforehand that the reduced space is of dimension 3 (horizontal and vertical position of the holes and number of holes), but the method fails in obtaining it. To evaluate the performance of this methodology, we design an experiment where one of the individuals is removed from the database. Then we try to recreate it by using the inverse mapping of the LLE. In Figure 4 we illustrate the original individual (on the left) along with the recovered one (on the right).

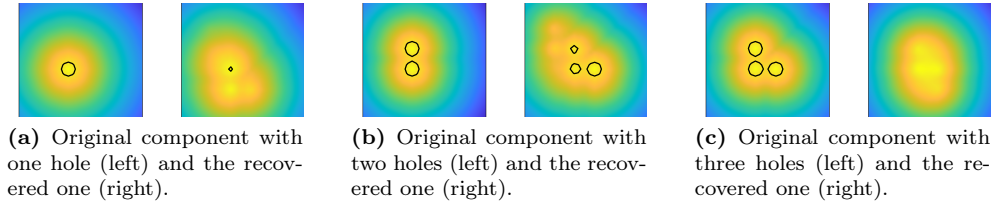


Figure 4: Examples of original components removed from the database and the recovered ones by the vicinity information.

Comparing the original individual with the recovered one, we could conclude that the performance of this strategy is unsatisfactory. Indeed, it cannot reconstruct any of the original individuals. One of the aspects that may improve the methodology’s performance is to add topological information to the strategy in order to obtain an appropriate clustering of the original database. As you can observe, the recovered individuals preserve the position of the holes in two scenarios (cases a and c) but never match the number of holes. Presumably, this behaviour is due to the reduced amount of information (small data). Therefore we propose to harness the available samples by extracting more information, i.e. the topology.

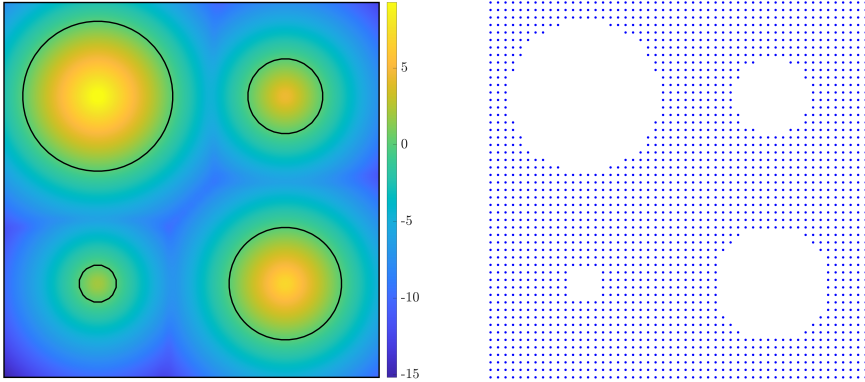
2.3. Geometry and Topology-based strategy

This section revisits the conclusions gathered in the previous section and develops a strategy to possibly improve the overall performance of the previous one. The first modification considered consists in the addition of topological information. This section explains how topology is characterized, how this information is obtained and how we propose to merge geometrical and topological information. The final objective is to cluster the data into its different topologies to aid the interpolation scheme to create pertinent individuals.

2.3.1. Topological Data Analysis overview

In this work, we consider that the number of holes defines the topology of an object, so we need a tool to automatically infer the number of holes and give some sense of its

size, but we also need to define a technique to properly compare different topologies. We propose to employ the Topological Data Analysis (TDA) [6,7] that encompasses a set of tools from high-dimensional data analysis which extract topological information from a group of points. These techniques are directly applicable as any SDF can be converted into a cloud of points employing the coordinates on the nodes in a Cartesian grid and its function value. The topological characterisation we use is based on the principle of persistent homology [5], which extracts the most relevant features in a point cloud; as mentioned, these features may be the number of holes and a sense of its size, for instance. In Figure 5a we show an synthetic example of a component's SDF, along with its boundary, while, in Figure 5b, we represent the resulting set of points considered for the TDA strategy, i.e. negative values of the SDF represent the domain of the geometry.



(a) Geometry descriptor of an individual composed by 4 circles.

(b) Equivalent point cloud.

Figure 5: Synthetic example for TDA (a) SDF (zero value corresponds to the boundary, in black) (b) the resulting points employed for the TDA tools.

Considering the resulting unconnected set of points $\in \mathbb{R}^2$, we define a circle with a radius r from each point. As the value of r increases, the connectivity of points changes. A connection is established when two or more points are inside of a circle of radius r . This change in connectivity allows the creation of geometrical entities such as edges or triangles, whose vertices are the set of points. At some moment, the connectivity of the points will create a set of edges that form a closed polygon. If we keep increasing r , the connectivity will create entities of higher dimensions, such as triangles that will cover the hole and then disappear. Persistent features detected with a wide range of spatial scales r are considered more likely to represent a true topological feature of the underlying point cloud instead of artefacts of the

sampling or noise. The value r in which a persistent feature appears and disappears is used to create the persistence diagram (PD), representing the birth x and death y of each topological feature found during the growth of r . As for any persistent feature, for instance, a hole, the birth precedes the death, all the points of the persistence diagram are located above the diagonal $y = x$, and any point (x, y) near the diagonal may represent noise or small scale features. Points far from the diagonal represent topological features that persist and may be considered to define the overall topology of the component.

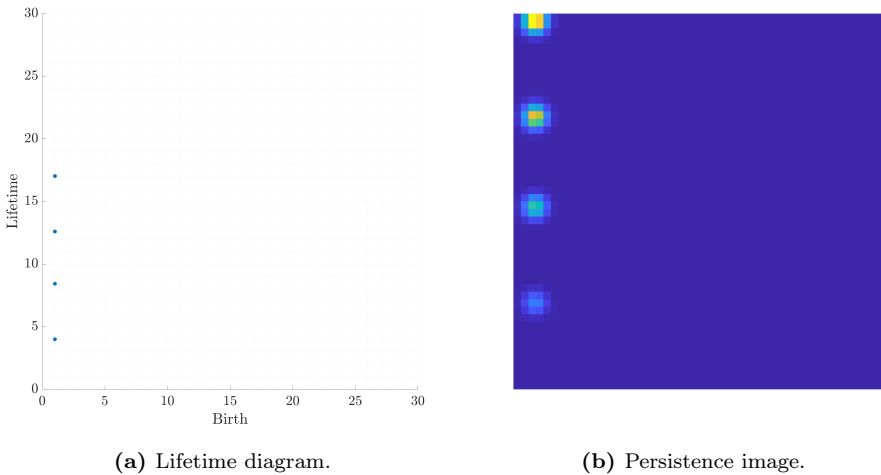


Figure 6: Space transformation of the persistent homology from the lifetime diagram (a) to the persistence image (b).

The persistence diagram belongs to a non-metric space, so comparing or evaluating a distance between different persistence diagrams is not directly possible. Different representations of the persistent homology are available that contain the same information but are displayed differently. We obtain the lifetime diagram (LD) (see Figure 6a) if we apply the mapping $f : (x, y) \rightarrow (x, y - x)$ to the persistence diagram (PD), as in the PD, points far from the x -axis represent more relevant topological features. The drawback of using those spaces is that they are not equipped with a norm, such as the L_2 metric commonly used in most Machine Learning applications. Thus, we need to apply space transformation to the current descriptor of topological features to a more appropriate representation equipped with a suitable norm. For that purpose, following the rationale in [8], we use the persistence surface, which is based on a Gaussian kernel evaluated in the space of the LD. The surface created is then reduced to a finite-dimensional discretised space. In particular, we fix a grid in the plane with $n \times n$ subdomains (pixels). The integration of the persistence surface over each pixel

gives, as a result, the so-called Persistence Image (PI) $\in \mathbb{R}^2$ (see Figure 6b) [8].

In Figure 6a, we illustrate how the four holes that appear in 5b are translated into the persistence diagram employing the persistent homology. Figure 6a represents one point per hole, and its coordinates correspond to the value of r when the hole is detected in x -axis and the total lifetime of the hole in y -axis. Notice that the birth of each feature is the same due to the uniformity of the grid used to describe the SDF. Figure 6b illustrates the resulting persistence image obtained from the space transformation of the persistence diagram.

2.3.2. Modifications in LLE to consider geometry and topology

The modification of the original strategy considers adding the persistence image (\mathbf{T}_i) of each individual to its geometrical description defined by its SDF (\mathbf{X}_i) as the topological descriptor into the manifold learning stage. So far, the information to feed the LLE algorithm corresponded to the geometrical representation of the components, i.e., the SDF. To feed the LLE algorithm with both geometrical and topological information we propose to make use of a weighted linear combination of the distances from each shape descriptor, topological and geometrical, as,

$$d_{ij}^2 = \frac{\theta}{\sum_i \sum_j \|\mathbf{X}_i - \mathbf{X}_j\|^2} \cdot \|\mathbf{X}_i - \mathbf{X}_j\|^2 + \frac{(1-\theta)}{\sum_i \sum_j \|\mathbf{T}_i - \mathbf{T}_j\|^2} \cdot \|\mathbf{T}_i - \mathbf{T}_j\|^2 \quad (8)$$

where θ is the weighting factor.

Additionally, we introduce the topological information in the LLE by modifying the equation (3), leading to:

$$\varepsilon(\mathbf{w}) = \sum_i \left[\frac{\theta}{\sum_i \sum_j \|\mathbf{X}_i - \mathbf{X}_j\|^2} \cdot \|\mathbf{X}_i - \sum_j^k w_{ij} \mathbf{X}_j\|^2 \right] + \sum_i \left[\frac{(1-\theta)}{\sum_i \sum_j \|\mathbf{T}_i - \mathbf{T}_j\|^2} \cdot \|\mathbf{T}_i - \sum_j^k w_{ij} \mathbf{T}_j\|^2 \right], \quad (9)$$

where \mathbf{X}_i is the level-set representation of the geometry, i.e., the SDF and \mathbf{T}_i is the corresponding persistence image. The optimal \mathbf{w} takes into account a mixture of the likeness of the geometry and topology.

2.3.2.1. Weighting factor selection

Considering the previously discussed modifications of the standard LLE implementation and the reference database, we compute the local vicinities of each individual considering the distance defined in equation (8). Later, we continue with the minimisation of the functional in equation (9). The next steps of the algorithm LLE are not modified. As in the previous example, we consider $k = 4$ neighbours with a randomly defined weighting factor of $\theta = 0.5$. In Figure 7a we show the distribution of the eigenvalues obtained from the LLE, and we conclude that the reduced dimensions are 2, again failing in obtaining the right number of dimensions. Figure 7b illustrates the projection of each individual to the reduced manifold of two dimensions.

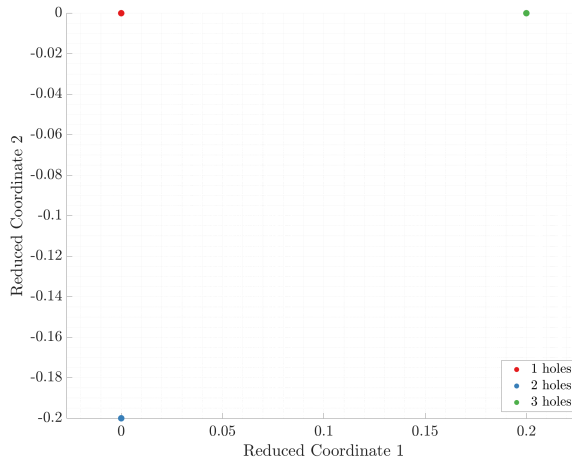
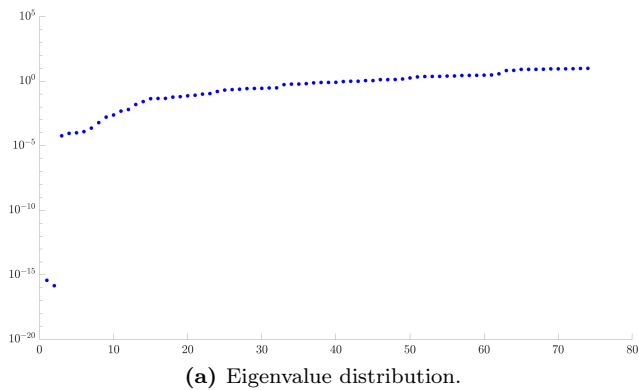
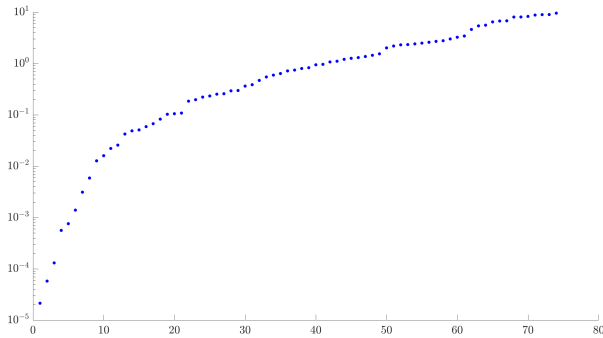
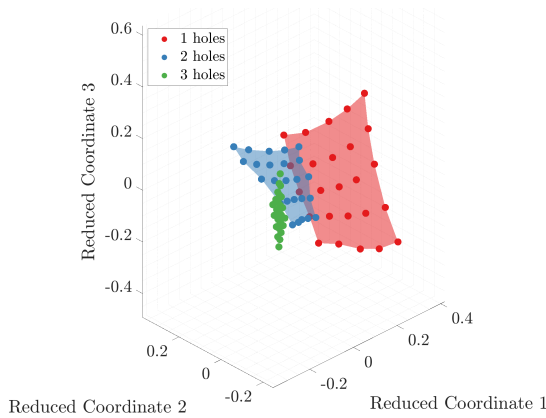


Figure 7: Resulting eigenvalue distribution (a) and reduced coordinates (b) by using the LLE technique including both, the original data and the persistence images.

In Figure 7 we see that each cluster is collapsed in one point in the reduced manifold, which prevents the extraction of geometrical modes, as well as the interpolation between individuals, indicating, perhaps that the topology information has too much influence. Hence, we modify the value of the weighting factor, in this case, $\theta = 0.8$. As in the previous example, Figure 8a shows the eigenvalues obtained, which suggests us that 3 reduced dimensions seem acceptable, as expected, in this case. In Figure 8b we also represent the spatial distribution of the projected individuals in the reduced manifold.



(a) Eigenvalue distribution.



(b) Three first coordinates of the reduced latent space.

Figure 8: Resulting eigenvalue distribution (a) and reduced coordinates (b) by using the LLE technique considering the original data and the persistence images.

With this value of the weighting factor θ , we improve the clusterisation with respect to the previous example. We could also extract geometrical information related to the horizontal and vertical location of the circles, which was impossible considering

the previous value of the weighting factor θ .

As in the previous experiment, we evaluate the method’s performance trying to recover several individuals removed from the dataset. Figure 9 shows the comparison between the original individual and the recovered one using the expression shown in (1). Even though the clusterisation is drastically improved, the recovered functions are far from the original ones, they match the position of the holes and slightly the topology but the results are not satisfactory so far. At this moment, our hypothesis here is that we have been able to properly organize the dataset in the reduced space, but that we lack of a proper interpolation approach to define the manifold.

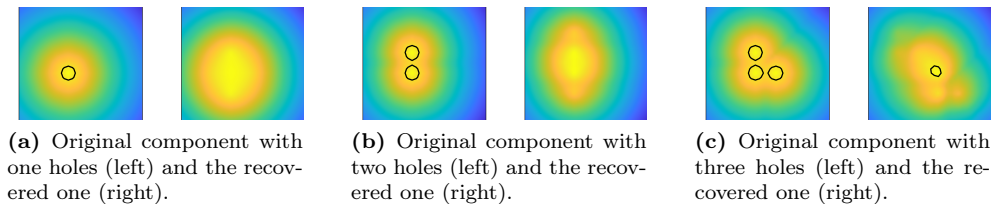


Figure 9: Examples of original components removed from the database and the recovered ones by the vicinity information.

The influence of the weighting factor may be seen as a regularization in the metric. This regularization enables the modification of the quantity of topological information added to the metric. However, the weighting factor is a hyperparameter and must be set by the user. The fulfilment of some criterion may guide the selection of its value. Different criteria may be considered, such as seeking a particular characteristic in the reduced manifold, for instance, the clusterization in topologies, or improving the quality of the recovered individuals.

2.3.3. Optimal Transport-based interpolation to recover dimensionality

A relevant characteristic of the LLE is that it allows to define one individual through the linear interpolation between the neighbours of its vicinity (1). Due to the scarcity of data this interpolation scheme, considering the original LLE technique is not appropriate, as seen before. This is why we propose to rely on an Optimal Transport approach for the objects’ interpolation [21–24].

2.3.3.1. Optimal Transport overview.

Optimal Transport techniques are based on the use of the Wassersteing distance W_2 between objects, also known as Earth Mover’s distance [22, 23]. These dis-

tances represent the geometric likeness between two objects by measuring the minimal amount of "work" needed to move the mass contained in one object onto the other. We may extrapolate this capability to tasks like geometric domain interpolation by solving the barycentre problem [25] stated as,

$$\mathbf{Z}_i^* = \arg \min_{\mathbf{Z}_i} \sum_{j=1}^k w_j W_2^2(\mathbf{Z}_i, \mathbf{Z}_j). \quad (10)$$

where, \mathbf{Z}_i and \mathbf{Z}_j correspond to the interpolated individuals and the individuals used for the interpolation, respectively. Also, W_2 corresponds to the Wasserstein metric and w_j are the interpolation weights. In Figure 10 we illustrate the resulting functions obtained from the linear and the optimal transport interpolation between two original functions.

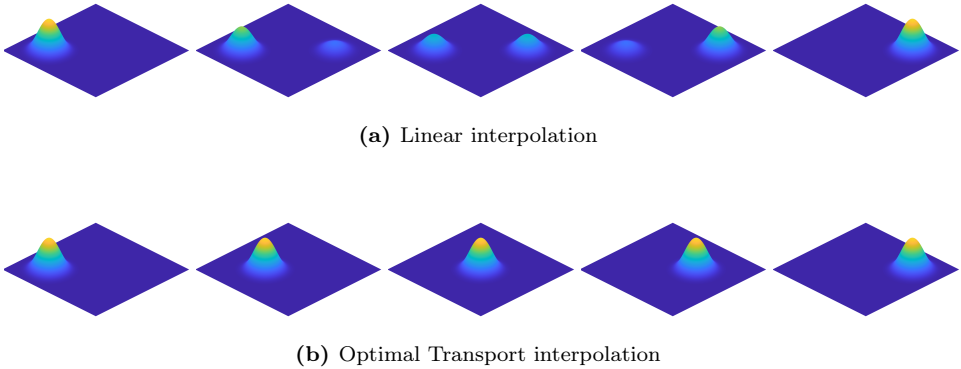


Figure 10: Comparison between linear and optimal transport interpolation. Figures on left and right are the original functions while the middle figures show their weighted interpolation.

2.3.3.2. Applying Optimal Transport-based interpolation to the reference database.

As seen in Section 2.3.3.1 the improvements achieved in the clustering task were not translated to the recovery performance. Considering the manifold obtained in Figure 8b, we modify the interpolation scheme, in this case, using the tools from OT. In Figure 11, we solve the barycentre problem considering the Wasserstein distance after transforming the original SDF into a probabilistic function which indicates the probability that a point is inside the geometry, being the implicit boundary described by the 0.5 value. Figure 11 shows that the original components and the recovered ones are virtually the same; thus, the modification in the interpolation scheme entail a relevant improvement in the reconstruction of objects.

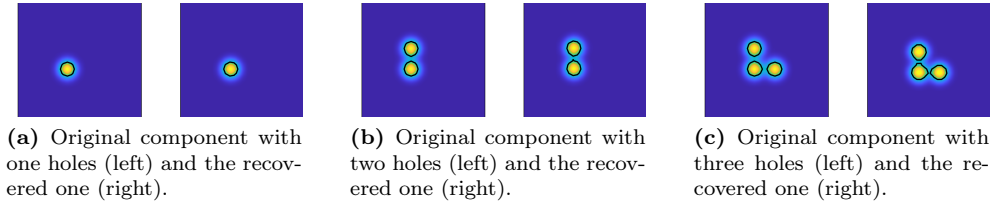


Figure 11: Examples of original components removed from the database and the recovered ones by the vicinity information.

It is interesting to get insight of the relative effect of optimal transport and the use of topological descriptors. For this, we apply the OT strategy without adding topological information (manifold shown in Figure 3b). This change the set of neighbours used to reconstruct individuals. From Figure 12 we can see that an OT strategy associated with a poor clustering does not lead to satisfactory results. Hence, from now on, in this paper we will rely on the simultaneous use of both strategies.

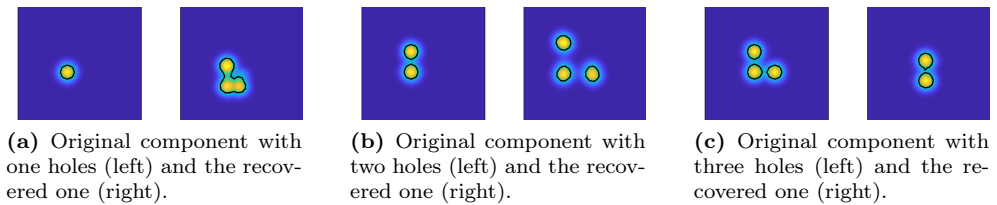


Figure 12: Examples of original components removed from the database and the recovered ones by the vicinity information, considering the OT strategy but not taking into account topology information.

3. Numerical Example

This section shows how the previous methodology is applied to an industrial example that mimics car's bumpers. Due to the impossibility of gathering actual data, we create the database artificially through a hybrid optimisation technique [20, 32]. We have generated a database that simulates the work of manufacturers, specifically those engaged in the car's bumper design. This example tries to mimic the actual designs of a car's bumper considering a simplified 2D domain. The design domain of the problem (see Figure 13) is characterized by variables h_1 , h_2 , and X , which define the region where the material is allowed to exist. The Dirichlet boundary conditions

are defined by the variables w and W , that specify the position where all displacements are restricted. Additionally, the variable P determines the value of the pressure applied; for all bumpers, we define the value of P in order to get the same resulting force applied to each bumper. This problem shows how the presented strategy works with more complex examples where the scarcity of data is also considered.

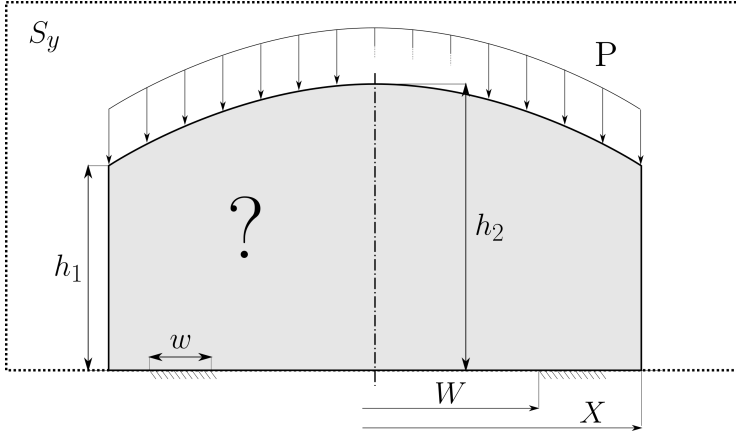


Figure 13: Parametrization of the variables that define the design domain and the boundary conditions of the hybrid optimisation algorithm.

Figure 14a shows an example of the resulting component obtained through the hybrid optimisation algorithm. This figure represents the SDF, with the boundary defined by its zero value. However, the input geometrical objects must be described by a probabilistic function to use the OT tools properly. In our case, we convert the SDF into a probabilistic function with its limits between 0 and 1 and the boundary described using the mid-value, 0.5. The value of the probabilistic function indicates the probability that a point belongs to the interior of the geometry, which, for a given kernel, is straightforward when the SDF is available. Then, Figure 14b illustrates the resulting function that describes the geometry of the component after its transformation.

Figure 15 shows a representative sampling of 9 individuals the database, which is composed of 83 individuals. Also, each individual is discretized by 10201 nodes. From now on, the standard geometrical descriptor will be the probabilistic function for representation purposes. Even though bumpers conform to the original dataset with various topologies, we neglect those with little importance. Then, the final database, as illustrated in Figure 15 consists of bumpers whose topology has 2 holes or none of them, as only a very reduced number of bumpers with more than 2 holes were obtained during the creation of the database.

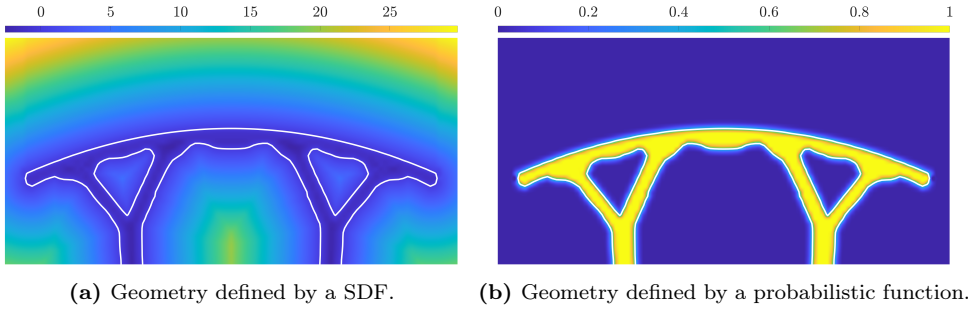


Figure 14: Conversion of the SDF (a) into a probabilistic distribution (b).

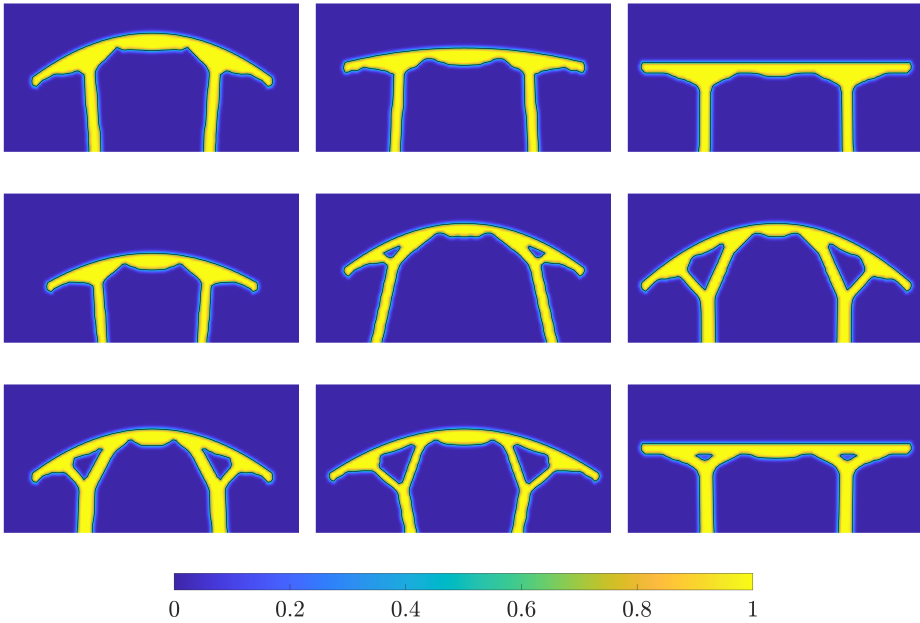


Figure 15: Probabilistic functions of sampled components from the database.

3.1. Topological characterization

As a reminder, the final proposed strategy considers the complete characterisation of the shape of a component, including its geometry and topology. Thus, the

next step is to obtain the persistent homology of each bumper in the database. Let's consider the bumper in Figure 14b, which presents two holes, to better illustrate the topological characterisation. We would compute the persistence image of each individual employing its persistent homology. The persistent homology, in this example (see Figure 16a), seems to capture one of the two holes, which may indicate that they are overlapped in the representation as the birth and lifetime are the same. This behaviour may be a source of issues in the clustering task, so we consider a different coordinate system to represent the persistent homology. As we use a uniform grid to represent the probabilistic function of each bumper, the birth of each hole is always the same (the spacing of the grid), so we assume that this coordinate is not that relevant and consider a different coordinate that includes the times a identical topological feature is repeated. So, the x -axis of the lifetime diagram, previously representing the birth, is replaced by the repeatability coordinate, providing the corresponding persistence image in Figure 16b, where two holes are now represented. As most of the image domain has 0 value, this image may be converted into a function over the whole domain, for instance, employing the level-set method (see Figure 16c).

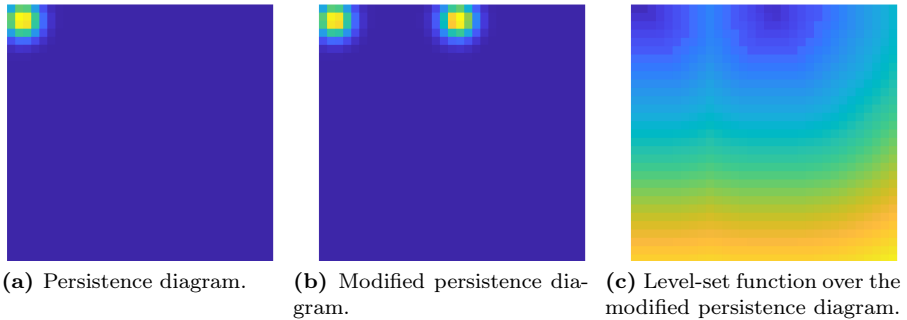
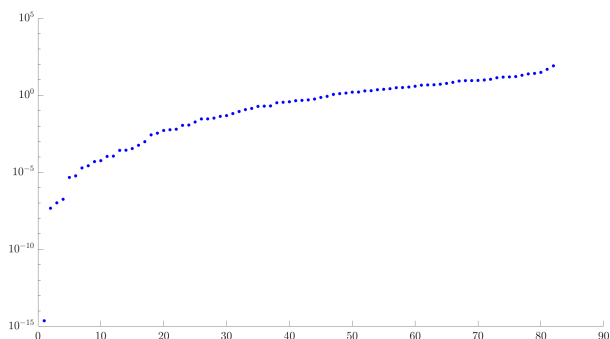


Figure 16: Persistent homology of the car's bumper in Figure 14 considering the repeatability of each persistent feature.

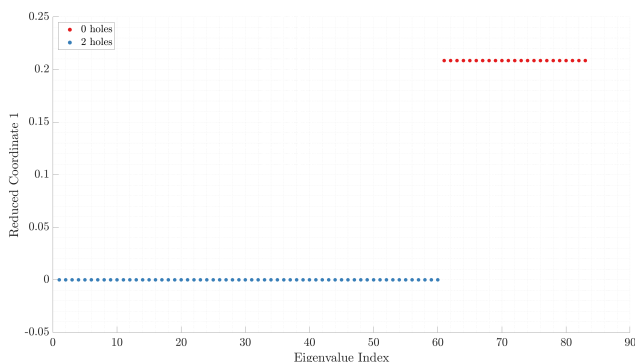
3.2. Influence of the weighting factor θ

Once the database has been processed, we have two shape descriptors for each component: a geometrical descriptor defined as a probabilistic function and a topological descriptor described with the persistence image. The next step within the proposed strategy consists in obtaining the reduced manifold containing the projection of each individual. For this problem, we used the modified version of the LLE that merges geometrical and topological information and use the euclidean distance to evaluate the local vicinities as in equation (8). The value of the weighting factor is arbitrarily set to $\theta = 0.5$, and the vicinity is set to 9 neighbours. Figure 17a shows the

eigenvalue distribution, where the smallest one is far from the rest, which implies that there is one dominant dimension in the reduced manifold. This seems strange as it is difficult to represent properly all the geometrical and topological details we described above with just one dimension. That is why we decided to modify the value of the weighting factor. Indeed, Figure 17b shows the representation of the components in the reduced manifold and we conclude that just the topology is inferred, so we must increase the contribution of the geometrical descriptor.



(a) Eigenvalue distribution.



(b) First coordinate of the reduced latent space.

Figure 17: Resulting eigenvalue distribution (a) and reduced coordinates (b) by using the LLE technique with the original data plus the persistence images.

For the next test, we set the value of the weighting factor to $\theta = 0.7$. Figure 18a shows the eigenvalue distribution where now more dimensions seem to characterize the database. In this example, we selected the 3 first dimensions, for representation purpose, as shown in Figure 18b, to describe the resulting reduced manifold. These results show that an appropriate selection of θ is required. In practice, the user should test several configurations of the hyperparameters θ and number of neighbours k until satisfied with the reduced space.

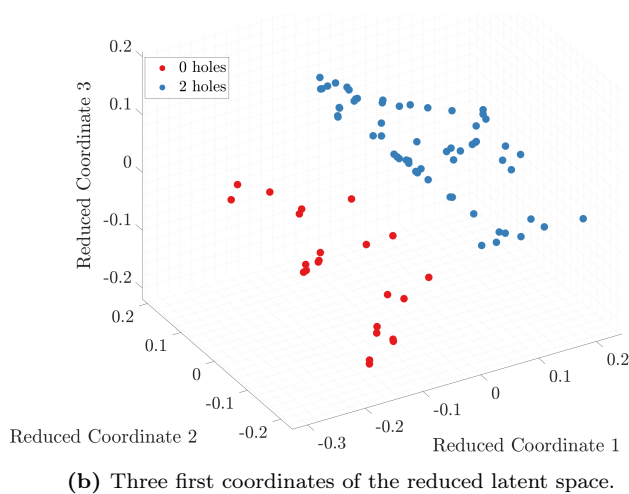
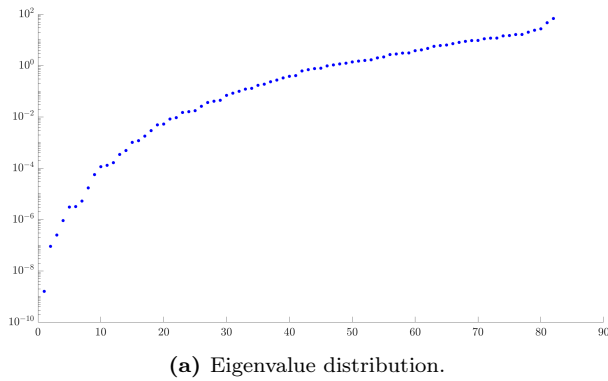
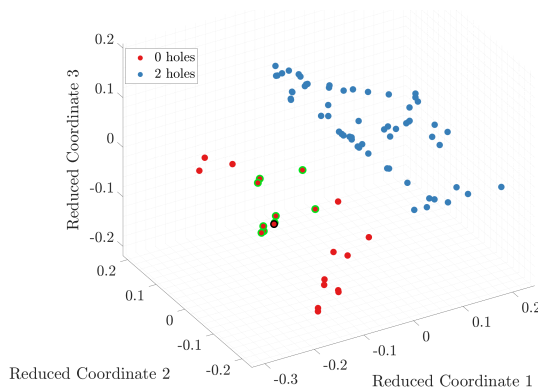


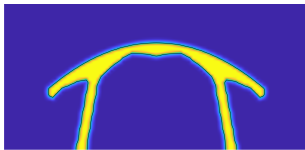
Figure 18: Resulting eigenvalue distribution (a) and reduced coordinates (b) by using the LLE technique with the original data plus the persistence images.

3.3. Results

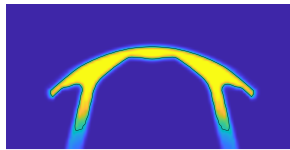
To check the feasibility of this methodology to produce components with physical sense and framed on the nature of the database, we repeat the same experiment as done with the moving circles example. This experiment consists of removing an individual from the database and trying to recover it using the inverse mapping of the LLE proposed in this paper. Figures 19 and 21 show examples of recovered individuals. Each Figure shows the recovery of one random individual selected from each of the clusters (cluster of topologies with 0 holes in Figure 19 and with 2 holes in Figure 21).



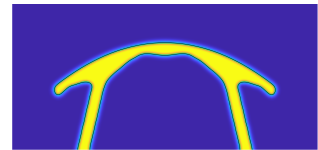
(a) Latent space where we highlight the reference individual (in black) and the neighbours used to recover it (in green).



(b) Reference bumper.



(c) Bumper recovered by linear interpolation.



(d) Bumper recovered by optimal transport-based interpolation.

Figure 19: Recovery of a bumper of the cluster with 0 holes removed from the database.

In each case, we present, using probabilistic functions, the original geometry to be recovered and the results obtained through linear interpolation and with the proposed strategy that computes the barycentre problem considering the Wasserstein distances. Some individuals are highlighted in these figures: the reference bumpers to be recovered, removed from the database, (highlighted with a black contour) and the neighbours used to recover the reference bumper (highlighted with a green contour). Analysing the recovered components, we conclude that the interpolation based on OT techniques provides components with physical sense, quite similar to the reference component and preserving the features in the database, while, on the contrary linear-based interpolation schemes seem to produce bumpers with artefacts and loss of features, that, consequently will prevent any successful numerical simulation.

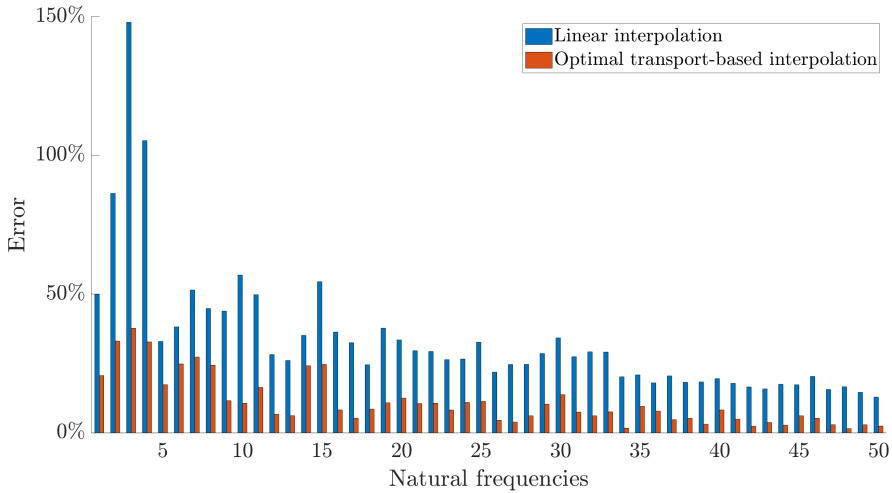
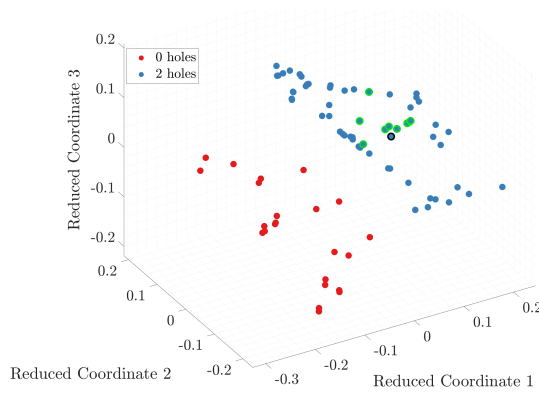


Figure 20: Error measure of each natural frequency for the reconstruction employing the linear interpolation (blue) and the optimal transport-based interpolation (orange).

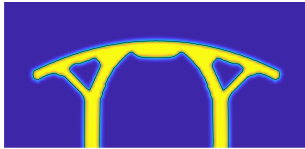
Additionally to the qualitative comparison in Figures 19 and 21, we compute a quantitative difference between the recovered bumpers and the reference one. As this component will fulfil certain structural criteria, we consider it interesting to compute an error metric based on its structural behaviour. Therefore, we carry out a modal analysis in each recovered component and then, we compare its first natural frequencies (removing those associated with the rigid solid movement) considering the following expression to measure its error,

$$Error_i = 100 \cdot \left| \frac{\hat{\omega}_i - \omega_i}{\omega_i} \right|, \quad (11)$$

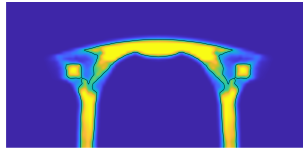
where, $\hat{\omega}_i$ and ω_i correspond to the i th natural frequency of the recovered bumper and the reference one, respectively. The error of the example in Figure 19 is illustrated in 20, while Figure 22 represents the error of the example pictured in Figure 19. In general terms, both Figures show that the bumper obtained employing the optimal transport-based interpolation presents lower error levels for the first 50 natural frequencies.



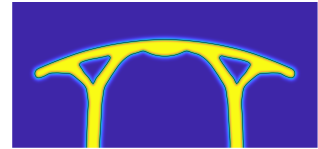
(a) Latent space where we highlight the reference individual (in black) and the neighbours used to recover it (in green).



(b) Reference bumper.



(c) Recovered bumper by linear interpolation.



(d) Recovered bumper by optimal transport-based interpolation.

Figure 21: Recovery of a bumper of the cluster with 2 holes removed from the database.

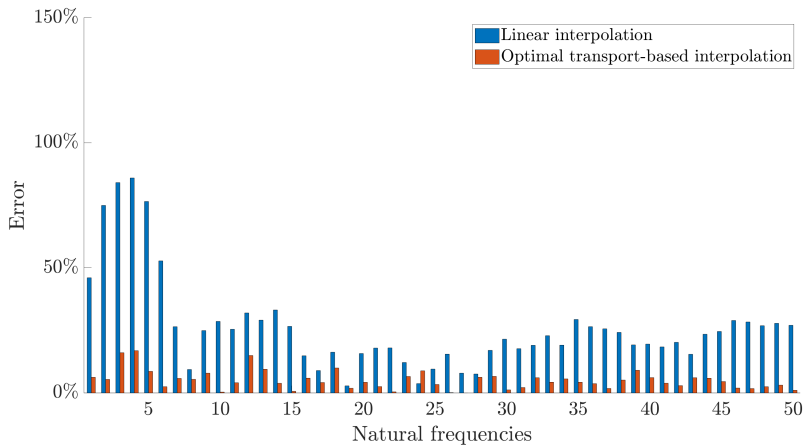


Figure 22: Error measure of each natural frequency for the reconstruction employing the linear interpolation (blue) and the optimal transport-based interpolation (orange).

With the creation of the reduced manifold, we are not limited to recover individuals in the database. Instead we are also able to navigate along this manifold being able to obtain the projection of the original high dimensional space corresponding to the points on the low dimensional manifold. The resulting projection of these points will entail the creation of new components non-existing in the original database, as we will be able to retrieve the geometrical and topological information. Figure 23a shows an arbitrary point in the reduced manifold located between the topological clusters, along with the neighbours, of different topologies, used for its interpolation. Figures 23b and 23c illustrate the resulting component obtained by linear and by optimal transport interpolations.

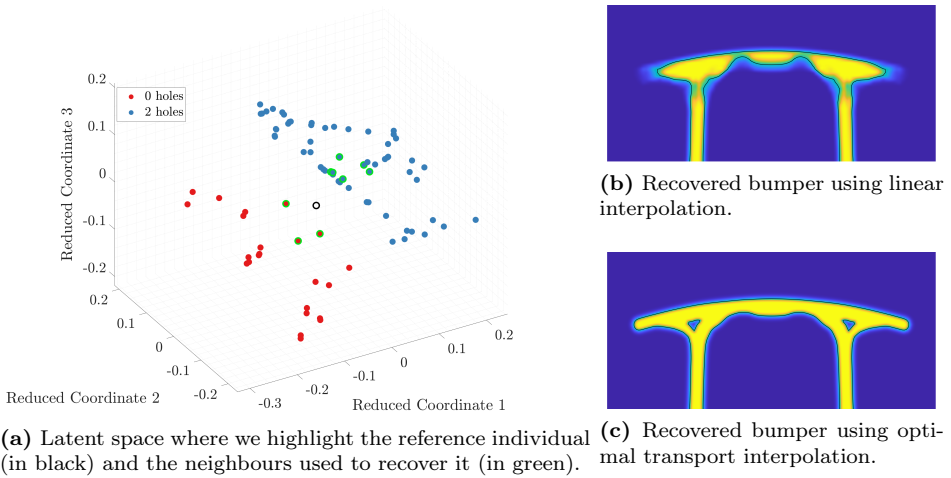
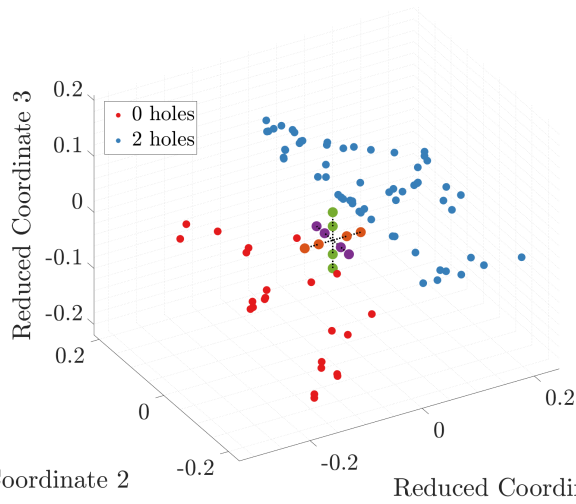
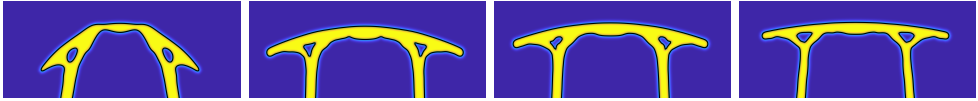


Figure 23: Creation of a new bumper employing the proposed methodology.

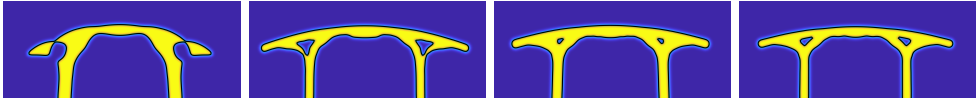
In order to illustrate the robustness and the generative capability of the methodology proposed, we extend this numerical example by adding a new experiment. Based on the previous example (Figure 23), this experiment navigates within the manifold and generates new bumpers that are non-existing in the original database. We use the bumper coordinates in Figure 23 as a reference. Then we define 3 directions, each corresponding to the axis of the coordinate system of the reduced parametric space. As a reminder, we use the LLE technique that extracts the non-linear structure of the high-dimensional data. In our example, these are a set of non-linear geometrical modes. The non-linearity means that each mode may influence the recovered data differently depending on its position in the manifold. Therefore, this experiment shows the local influence of each axis in the neighbourhood of the reference coordinates. Generally, we can conclude that the first dimension is in charge of the bumper’s curvature. In contrast, the second one seems more related to the topological change and the holes’ size. Finally, the third one may modify the bumper’s overall height and the holes’ size.



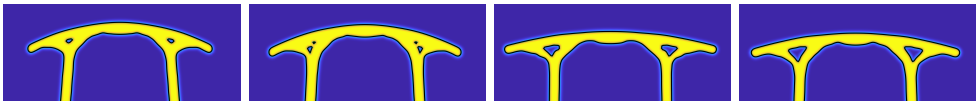
(a) Latent space where we highlight the query points, classified by the variation in its coordinates: reduced dimension 1 (orange points), reduced dimension 2 (purple points) and reduced dimension 3 (green points).



(b) Evolution of individuals according to the reduced dimension 1 (orange points).



(c) Evolution of individuals according to the reduced dimension 2 (purple points).



(d) Evolution of individuals according to the reduced dimension 3 (green points).

Figure 24: Creation of a set of new bumpers employing the proposed methodology.

Figure 24 illustrate this experiment where the reduced manifold along with the points of the study are represented in Figure Figure 24a. Also, Figures 24b, 24c and 24d show the resulting set of bumpers in each axis. Not all bumpers have the structural qualities we might expect, for instance, the first bumper of the second axis. It seems that this is a region where the topology of the bumper changes. The holes in the component get bigger until they reach the surface, therefore, modifying the

topology. However, we can still extract some conclusions about the influence of each axis on the characteristic of the generated bumper.

4. Conclusions

We have proposed a strategy to create a low dimensional manifold to describe an existing database of designs defined by their geometry and topology. We are able to navigate within this manifold not only to recover existing designs but, more interesting, to create new coherent designs. We have accomplished this goal using different tools such as the LLE, the TDA and the OT. To conclude the current work, we would like to synthesise some final thoughts:

- Manifold Learning (ML) strategies, such as the Locally Linear Embedding, are appropriate tools to visualise and manipulate high-dimensional data by extracting the inherent latent structure. The resulting dimensions may be considered a shape generator basis, employing the inverse mapping to recover the original dimensionality.
- The use of the level-set method seems to be a coherent framework to characterise the geometry of the components as it allows direct comparison between different shapes. We found the widely used Signed Distance Functions convenient for our purposes.
- Topological Data Analysis tools aid the clustering task carried out by the dimensionality reduction algorithm.
- We propose to adequately combine the geometrical description provided by the SDFs with topological information to obtain a synergetic effect. This requires the definition of θ , a parameter that weights the influence of these two different informations.
- The use of Optimal Transport tools in the ML strategy represents a definitive improvement with respect to the standard LLE algorithm implementation. Thanks to these techniques, the recovered individuals resemble the original database and have a physical sense from a structural point of view.
- Due to the computational cost of evaluating the Wasserstein distances, we propose a compromise strategy, where the Wasserstein distances are computed just when interpolating, instead of using them to create the reduced space.
- In the same way, using the LLE, allows to evaluate the Wasserstein distances among few neighbours instead of the full database.

- One of the limitations of the proposed methodology is its maturity. We still need to establish a metric that assesses the quality of the component reconstruction for any problem. For this reason, we cannot measure the influence of each hyperparameter appearing in the methodology, like the weighting factor or the number of neighbours, possibly leading to reduced manifolds not being able to extract the knowledge of the database.
- Once these limitations are surpassed, the potential applications of the methodology are several. For instance, it could be used for the development of a design tool able to propose, taking the know-how into account, predesigns characterized by the sets of parameters defined by the user. These predesigns may be then modified to meet other design requirements. Also, this methodology could be used for the development of an optimization algorithm that navigates the resulting reduced manifold to find the optimal component that maximizes/minimizes an objective function subject to a set of design constraints.

5. Future works

In this last section we would like to highlight some future developments from the current work:

- As we show with the last example, we are able to navigate the reduced manifold to obtain new components non-existing in the original dataset. This tools could be used, for instance, to obtain components defined in terms of geometrical and/or topological constraints or in terms of the structural behaviour of the component, for example.
- The selection of the weighting factor θ may be guided by and optimisation algorithm by looking for some specific characteristics of the resulting reduced manifold.

Acknowledgements

The authors gratefully acknowledge the financial support of Ministerio de Educación (FPU16/07121), Generalitat Valenciana (Prometeo/2021/046 and CIAICO/2021/226), Ministerio de Economía, Industria y Competitividad (DPI2017-89816-R) and FEDER. O. Allix would like to thank the French National University Council and ENS Paris-Saclay for supporting his sabbatical at UPV, which made it possible to closely interact

with the colleagues from I2MB-UPV.

Funding for open access charge: CRUE-Universitat Politècnica de València

References

- [1] UNIDO, “Manual on Technology Transfer Negotiation,” *General Studies Series. Vienna*, 1996.
- [2] A. Krizhevsky, I. Sutskever, and G. E. Hinton, “ImageNet classification with deep convolutional neural networks,” *Communications of the ACM*, vol. 60, no. 6, pp. 84–90, 2017.
- [3] R. Malladi, J. A. Sethian, and B. C. Vemuri, “Shape Modeling with Front Propagation: A Level Set Approach,” *IEEE Transactions on Pattern Analysis and Machine Intelligence*, vol. 17, no. 2, pp. 158–175, 1995.
- [4] T. Chan and W. Zhu, “Level set based shape prior segmentation,” in *Proceedings - 2005 IEEE Computer Society Conference on Computer Vision and Pattern Recognition, CVPR 2005*, vol. II, pp. 1164–1170, IEEE Computer Society, 2005.
- [5] A. Zomorodian and G. Carlsson, “Computing persistent homology,” *Discrete and Computational Geometry*, vol. 33, no. 2, pp. 249–274, 2005.
- [6] G. Carlsson, “Topology and data,” *Bulletin of the American Mathematical Society*, vol. 46, no. 2, pp. 255–308, 2009.
- [7] L. Wasserman, “Topological Data Analysis,” *Annual Review of Statistics and Its Application*, vol. 5, pp. 501–532, 2018.
- [8] H. Adams, T. Emerson, M. Kirby, R. Neville, C. Peterson, P. Shipman, S. Chepushtanova, E. Hanson, F. Motta, and L. Ziegelmeier, “Persistence images: A stable vector representation of persistent homology,” *Journal of Machine Learning Research*, vol. 18, pp. 1–35, 2017.
- [9] I. T. Jolliffe, “Principal Component Analysis, Second Edition,” *Springer Series in Statistics*, vol. 98, p. 487, 2002.
- [10] J. W. Sammon, “A Nonlinear Mapping for Data Structure Analysis,” *IEEE Transactions on Computers*, vol. C-18, no. 5, pp. 401–409, 1969.
- [11] B. Schölkopf, A. Smola, and K. R. Müller, “Nonlinear Component Analysis as a Kernel Eigenvalue Problem,” *Neural Computation*, vol. 10, no. 5, pp. 1299–1319, 1998.

-
- [12] M. Belkin and P. Niyogi, “Laplacian eigenmaps for dimensionality reduction and data representation,” *Neural Computation*, vol. 15, no. 6, pp. 1373–1396, 2003.
- [13] J. B. Tenenbaum, V. De Silva, and J. C. Langford, “A global geometric framework for nonlinear dimensionality reduction,” *Science*, vol. 290, no. 5500, pp. 2319–2323, 2000.
- [14] M. A. Kramer, “Nonlinear principal component analysis using autoassociative neural networks,” *AIChE Journal*, vol. 37, no. 2, pp. 233–243, 1991.
- [15] P. Vincent, H. Larochelle, I. Lajoie, Y. Bengio, and P. A. Manzagol, “Stacked denoising autoencoders: Learning Useful Representations in a Deep Network with a Local Denoising Criterion,” *Journal of Machine Learning Research*, vol. 11, pp. 3371–3408, 2010.
- [16] D. P. Kingma and M. Welling, “An introduction to variational autoencoders,” 2019.
- [17] S. T. Roweis and L. K. Saul, “Nonlinear dimensionality reduction by locally linear embedding,” *Science*, vol. 290, no. 5500, pp. 2323–2326, 2000.
- [18] D. González, E. Cueto, and F. Chinesta, “Computational Patient Avatars for Surgery Planning,” *Annals of Biomedical Engineering*, vol. 44, no. 1, pp. 35–45, 2016.
- [19] E. Nadal, D. Muñoz, N. Vivó, I. Lucas, and J. J. Ródenas, “Evaluation of hip fracture risk using a hyper-parametric model based on the Locally Linear Embedding technique,” 2019.
- [20] D. Muñoz, E. Nadal, J. Albelda, F. Chinesta, and J. Ródenas, “Allying topology and shape optimization through machine learning algorithms,” *Finite Elements in Analysis and Design*, vol. 204, p. 103719, 2022.
- [21] F. L. Hitchcock, “The Distribution of a Product from Several Sources to Numerous Localities,” *Journal of Mathematics and Physics*, vol. 20, no. 1-4, pp. 224–230, 1941.
- [22] L. Kantorovitch, “On the Translocation of Masses,” *Management Science*, vol. 5, no. 1, pp. 1–4, 1958.
- [23] L. V. Kantorovich, “Mathematical Methods of Organizing and Planning Production,” *Management Science*, vol. 6, no. 4, pp. 366–422, 1960.
- [24] C. Villani, *Topics in optimal transportation*. 2003.
- [25] J. Solomon, F. De Goes, G. Peyré, M. Cuturi, A. Butscher, A. Nguyen, T. Du, and L. Guibas, “Convolutional Wasserstein distances: Efficient optimal transportation on geometric domains,” in *ACM Transactions on Graphics*, vol. 34, pp. 1–11, Association for Computing Machinery, 2015.

- [26] E. Burman, S. Claus, P. Hansbo, M. G. Larson, and A. Massing, “CutFEM: Discretizing geometry and partial differential equations,” *International Journal for Numerical Methods in Engineering*, vol. 104, no. 7, pp. 472–501, 2015.
- [27] J. Parvizian, A. Düster, and E. Rank, “Finite cell method : h- and p-extension for embedded domain problems in solid mechanics,” *Computational Mechanics*, vol. 41, no. 1, pp. 121–133, 2007.
- [28] A. Düster, J. Parvizian, Z. Yang, and E. Rank, “The finite cell method for three-dimensional problems of solid mechanics,” *Computer Methods in Applied Mechanics and Engineering*, vol. 197, no. 45-48, pp. 3768–3782, 2008.
- [29] D. Schillinger and M. Ruess, “The Finite Cell Method: A Review in the Context of Higher-Order Structural Analysis of CAD and Image-Based Geometric Models,” *Archives of Computational Methods in Engineering*, vol. 22, no. 3, pp. 391–455, 2015.
- [30] J. J. Ródenas, O. A. González-Estrada, J. E. Tarancón, and F. J. Fuenmayor, “A recovery-type error estimator for the extended finite element method based on singular+smooth stress field splitting,” *International Journal for Numerical Methods in Engineering*, vol. 76, no. 4, pp. 545–571, 2008.
- [31] J. J. Ródenas, O. A. González-Estrada, P. Díez, and F. J. Fuenmayor, “Accurate recovery-based upper error bounds for the extended finite element framework,” *Computer Methods in Applied Mechanics and Engineering*, vol. 199, no. 37-40, pp. 2607–2621, 2010.
- [32] D. Muñoz, J. Albelda, J. J. Ródenas, and E. Nadal, “Improvement in 3D topology optimization with h-adaptive refinement using the Cartesian grid Finite Element Method,” *International Journal for Numerical Methods in Engineering*, 2021.

